UNIVERSITY OF CALIFORNIA
SANTA CRUZ

THE EFFECTS OF REGIONAL OCEANOGRAPHIC CONDITIONS ON THE GEOCHEMISTRY OF FERROMANGANESE CRUSTS FROM THE WEST-CENTRAL PACIFIC OCEAN

A dissertation submitted in partial satisfaction
of the requirements for the degree of

DOCTOR OF PHILOSOPHY

in

OCEAN SCIENCES

by

Kira Mizell

December 2019

The Dissertation of Kira Mizell is approved:

_____
Professor Phoebe J. Lam, chair

_____
Professor A. Christina Ravelo

_____
Professor Adina Paytan

_____
James R. Hein, PhD

_____
Quentin Williams
Acting Vice Provost and Dean of Graduate Studies

Table of Contents **Page**

	Title page	i
	Table of Contents	iii
	Thesis Abstract	vii
	Acknowledgements	ix
	Thesis Introduction	1
	References	4
	Chapter 1. Geographic and oceanographic influences on ferromanganese crust composition along a Pacific Ocean meridional transect, 14N to 14S	7
	Abstract	7
1.	Introduction	8
1.1	Ferromanganese Crusts	8
1.2	Geographic and Geologic Setting	9
1.3	Oceanographic Regimes	10
2.	Methods	12
2.1	Samples	12
2.2	Major and trace element concentrations	14
2.3	Statistical correlations and factor analysis	15
3.	Results	17
3.1	Overall Compositional Variation of FeMn Crusts	17
3.2	Geographic correlations within the dataset	17
3.3	Water Depth and Oxygen Correlations	18
3.4	Latitude Correlations	19
3.4.1	Equatorial Upwelling Signal	20
3.5	Longitude Correlations and Zonal Comparisons	21
3.5.1	Correlations with longitude from CCM	21
3.5.2	Comparison of latitude, water depth, and oxygen correlations within zonally offset MGT and HBT	21
3.5.3	MGT versus HBT zonal chemistry trends	22
3.6	Q-mode Factor Analysis of MGT	22
4.	Discussion	25
4.1	Controls on the major oxide phases	25
4.1.1	Fe and Mn associated elements	29
4.2	Productivity signatures	32
4.2.1	Basin-wide versus regional characteristics	35
4.3	Detrital sources interpreted from bulk compositions	36

		Page
5.	Summary and Conclusions	40
6.	Acknowledgements, Samples, and Data	44
7.	References	46
	Tables	54
	Figures	59
	Supplementary Tables and Figures	65
	Chapter 2. Mineral associations and speciation of Pb in phosphatized ferromanganese crusts from the Pacific Ocean	78
	Abstract	78
1.	Introduction	79
2.	Samples	82
3.	Methods	83
3.1	Preparation of Pb-sorbed end-member model compounds	83
3.2	Lead and major element concentration in bulk FeMn crust layers	85
3.3	X-ray diffraction mineralogy	86
3.4	Bulk x-ray absorption spectroscopy collection	86
3.5	Microfocused x-ray fluorescence mapping and x-ray absorption spectroscopy collection	87
3.6	XAS Data Analysis	88
4.	Results	89
4.1	Pb content and correlations in bulk non-phosphatized and phosphatized layers of FeMn crusts	89
4.2	Element correlations from μXRF maps	91
4.3	Pb speciation of bulk phosphatized FeMn crust layers from XANES	92
4.4	Characterization of non-phosphatized FeMn crust and synthesized mineral model compounds	93
4.5	Pb speciation of bulk phosphatized FeMn crust layers from EXAFS	94
4.6	Pb speciation in leached residuals from phosphatized FeMn crusts	95
5.	Discussion	96
5.1	Contribution of PbO to linear combination fits	96
5.2	Possibility of micro-scale changes in Pb speciation	97
5.3	Lead speciation related to the degree of phosphatization	98

		Page
5.4	Mass balance of Pb between mineral phases in phosphatized FeMn crusts	100
5.4.1	Lead speciation and enrichment in phosphatized layers	100
5.4.2	Potential for the formation of Pb-phosphates	101
5.4.3	Formation of other Pb-rich minerals	103
6.	Summary and Conclusions	104
7.	Acknowledgements	106
8.	References	107
	Tables	112
	Figures	118
	Chapter 3. Ferromanganese Crusts from the Tuvalu Exclusive Economic Zone: Composition, Evolution, and Critical-Metal Resource Considerations	125
	Abstract	125
1.	Introduction	126
1.1	Ferromanganese crust characteristics	126
1.2	Development of FeMn crust exploration	127
1.3	Geological and oceanographic features of Tuvalu seamounts	128
1.4	Previous studies	129
2.	Samples and Methods	130
2.1	Samples	130
2.2	Methods	132
2.2.1	Mineralogy	132
2.2.2	Chemical composition and element correlations	132
3.	Results	134
3.1	Mineralogy	134
3.2	Fe and Mn contents and genetic discrimination	134
3.3	Detrital elements	135
3.4	Phosphatization	136
3.5	Interelement relationships of the main mineral phases	137
3.6	Estimated growth rates	138
3.7	Geographic correlations from CCM	140
3.8	Metals traditionally of economic interest	140
3.9	Rare earth elements	141
3.10	Additional critical metals of interest	142

		Page
3.11	Hydrothermally mineralized Mn-oxide sample	143
4.	Discussion	145
4.1	Spatial controls on growth rates and Mn contents for Tuvalu crusts	145
4.2	Comparisons with Tuvalu crusts from shallower water depths	147
4.3	Comparisons with the Prime Crust Zone	149
4.4	Mechanism and potential distribution of hydrothermal mineralization	154
4.5	Resource considerations for FeMn crusts from the Tuvalu EEZ	156
5.	Summary and Conclusions	159
6.	Acknowledgements	161
7.	References	162
	Tables	171
	Figures	178
	Supplementary Tables and Figures	188

THE EFFECTS OF REGIONAL OCEANOGRAPHIC CONDITIONS ON THE GEOCHEMISTRY OF FERROMANGANESE CRUSTS FROM THE WEST-CENTRAL PACIFIC OCEAN

By

Kira Mizell

Thesis Abstract

Ferromanganese (FeMn) crusts are of interest and clear importance both as a unique paleoceanographic archive of seawater chemistry and as a potential resource for valuable and critical metals. Presently, there is a need to shift FeMn crust research from purely exploration-based studies to more targeted expeditions that can precisely locate FeMn crusts with characteristics of interest for scientific research and resource evaluation. Understanding the influence of general oceanographic conditions on FeMn crust formation is key to defining permissive regions. This thesis investigates variations in the geochemistry of FeMn crusts from the west-central Pacific that are associated with regional oceanographic conditions, including proximity to the oxygen minimum zone and high biological productivity maintained at the equator, as well as water depth controls and the effects of diagenetic phosphatization. Chemical analysis of over 60 FeMn crusts reveals that the oxygen minimum zones in the northern and southern tropics in the west Pacific exhibit strong controls on the composition of recent FeMn crust growth as well bulk FeMn crusts. Manganese contents are increased near the oxygen minimum zones, which is shown quantitatively for a broad region in this thesis for the first time. Iron is instead enriched in deeper waters where oxidation of iron is increased, which may be caused by higher carbonate ion

concentrations and pH at depth and the availability of deep sources of iron. High biological productivity in the equatorial upwelling zone enriches iron, magnesium, and barium in FeMn crusts that are forming below this zone due to increased efficiency of the biological pump. Diagenetic phosphatization is commonly observed in crusts from depths above 2000 meters, but does not exceedingly dilute manganese oxides or elements of economic interest. Synchrotron analyses of phosphatized FeMn crust layers indicate that phosphatization does not change the speciation of lead as hypothesized based on previous sequential leaching studies. Overall, is it shown that the general oceanographic parameters studied here influence FeMn crust composition based on their geographic location and water depth, and these parameters can help create criteria for future crust exploration.

Acknowledgements

I have received an overwhelming amount of support from the U.S. Geological Survey, specifically the Pacific Coastal and Marine Science Center here in Santa Cruz. They have provided funding for my research, travel, and stipend, which greatly reduced the stress associated with graduate school and for this I am extremely grateful. This support was spearheaded by my thesis advisor, Jim Hein, who saw my potential while working as a technician and encouraged me to pursue my PhD. I truly thank him for believing in me. Jim has been an incredible mentor, both scientifically and professionally. He has always generously shared ideas and introduced me to an incredible community of marine geologists, which has been priceless to developing my place in the field. I am honored to have been one of Jim's final PhD students, and I look forward to pulling him out of retirement from time to time to discuss the intricacies of ferromanganese crusts over a glass of wine. I also owe a huge amount of thanks to the Marine Minerals research team at USGS. Thank you to Mariah Mikesell, who seamlessly took over my job as technician when I started the program. Thank you to Sam Whisman, who provided analytical help but more importantly endless conversation and emotional support during some of the hardest days of my PhD. Finally, thank you to Amy Gartman, who has been an incredible support and role model and has created so much hope and excitement for the future of our team.

I am much obliged to my academic advisor Phoebe Lam. Taking on a PhD student with an adjacent research topic can be challenging, but Phoebe never made me feel left out of the Lam Lab Group. She has taught me so many things, from

synchrotron skills to having no fear in asking questions. Her work ethic and positive attitude are things I hope to emulate in my career, and I am excited to continue our search for deeper understanding of iron and manganese together. I have also learned so much from the members of the Lam Lab. I so valued the times I showed up to a Lam Lab meeting with a shell of a presentation and walked away with a brain full of ideas thanks to insights from Yang Xiang, Jong-Mi Lee, and Vinicius Amaral. I also truly enjoyed getting to know all of them and their families.

I'd also like to thank my thesis committee members, Christina Ravelo and Adina Paytan for their diverse perspectives and contributions to my thesis. They are both excellent scientists and mentors, and I was privileged to have had their guidance. The Ocean Sciences Department at UCSC was a wonderful place to study, and I am extremely appreciative to the professors and department staff who put much time and effort into my academic success and made this such a rewarding experience.

My cohort in the Ocean Sciences department has also been a great support and joy to me as. No one knows the tribulations of graduate school like your fellow students, and I was honored to go through this journey with Meredith McPherson, Yang Xiang, Katie Harding, Maria Hamilton, Hayley Neutzel, Bruce Laughlin, and Zach Stewart.

Finally, I have a deep gratitude for my family and friends for encouraging me throughout my PhD. My parents, my sisters, and most of all, my husband, have been patient, listened, and bolstered me up when I needed it most. I thank them wholeheartedly for believing in me and giving me space to pursue this dream.

Thesis Introduction

Ferromanganese (FeMn) crusts are a type of deep-ocean mineral deposit found ubiquitously throughout the world's oceans as coatings or encrustations on rock substrate. They principally occur on the flanks and tops of seamounts, plateaus, and ridges where low sedimentation rates and currents keep rock surfaces clear of sediment. FeMn crusts have been found in all of the major oceans but are more abundant in the Pacific Ocean due to the higher number of seamounts that result from hotspot volcanism across the Pacific Plate. FeMn crusts form at a variety of water depths, and have been recovered from a minimum of 400 to a maximum of 7000 m water depth (Hein et al. 2000). The mineral matrix of FeMn crusts is composed of turbostratically disordered manganese oxide (namely iron-rich δ-MnO_2, vernadite; Bolton et al. 1988; Varentsov et al. 1991; Koschinsky and Halbach 1995), amorphous iron oxyhydroxides (δ-FeOOH, feroxyhyte; Varentsov et al. 1991) and has an extremely high specific surface area (mean 300 m^2/g; Hein et al. 2000). Therefore, FeMn crusts are excellent trace-metal scavengers and are highly enriched in many trace elements compared to the surrounding seawater concentrations, especially Co, Ti, Te, Ce, P, Pb, and Pt (Hein et al. 1985; De Carlo, Mcmurtry, and Kim 1987; Hein et al. 1987; De Carlo et al. 1987; Halbach et al. 1989; Hein et al. 2003). FeMn crust are now considered of interest as a potential ore deposit for Co, Ni, Pt, Mn, Tl, Te, rare earth elements, and other metals (Hein et al. 2000). Currently, there are four contracts granted by the International Seabed Authority for exploration of FeMn

crusts in areas beyond national jurisdiction (international waters) in the west Pacific Ocean and one in the SW Atlantic Ocean.

FeMn crusts are accretionary deposits, growing layer by layer on the micrometer scale. Therefore, FeMn crusts are not only interesting due to high metal concentrations, but also as a layered record of seawater chemistry and global environmental changes, similar to corals and other accretionary deposits. Age dating of the upper layers of FeMn crusts using first U-series and Be isotopes (Hein and Koschinsky 2014) and later estimates using chronometric equations based on Co concentration (such as that of Manheim and Lane-Bostwick 1988) revealed extremely slow growth rates, most commonly from 1 to 6 mm/Ma (Hein et al. 2000). Using these growth rates, ages were extrapolated to the base of the thickest Pacific crusts, which dated crust growth initiation back to the Eocene and placed thinner crusts throughout the later Cenozoic (Hein et al. 2000; Klemm et al. 2005). Later, the full thickness of FeMn crusts were dated using Os isotopes revealing that FeMn crusts can serve as a record for seawater chemistry as far back as the Late Cretaceous (Klemm et al. 2005; Nielsen et al. 2009; Josso et al. 2019). Paleoceanographic investigations of FeMn crusts revealed their contribution to the reconstruction of past circulation patterns of the ocean and erosional input (Frank et al. 2002) as well as the opening and closure of various oceanic gateways (e.g., Burton et al. 1999; Frank et al. 1999), changes in the Antarctic bottom water (Xu et al. 2006), and others.

FeMn crusts are of interest and clear importance both as a unique paleoceanographic archive of seawater chemistry and as a potential resource for

valuable and critical metals. The solid foundation of research on FeMn crusts generated over the past 40 years confirms the wide distribution of crusts and demonstrates the potential to pinpoint particular element enrichments or characteristics of interest in FeMn crusts for scientific research or resource potential. For example, if a specific paleoceanographic event is of interest for research, a certain crust thickness will be required. In addition, if a specific metal is of interest as a mineral resource, predictions of where crusts will be enriched in the metal of interest are required. Thus, at present, there is a need to shift FeMn crust research from purely exploration-based studies to more targeted expeditions that can precisely locate FeMn crusts with the characteristics of interest. This shift requires research focused on determining the oceanographic conditions that influence FeMn crust formation. This will allow the growing repository of oceanographic data to be harnessed to define more precise permissive areas for FeMn crusts that possess the characteristic(s) of interest.

This thesis addresses the oceanographic influences on the formation of FeMn crusts in the Pacific Ocean that can be used to define permissive criteria for the targeted collection of FeMn crusts in the future. Chapter 1 examines whether the upper-most layers of FeMn crusts from a meridional transect in the western equatorial Pacific change in composition with proximity to the oxygen minimum zone and high biological productivity maintained at the equator as well as water depth. The study, in effect, calibrates the ability of FeMn crusts to record regional changes in seawater composition by comparing recent crust growth with modern seawater measurements.

Chapter 2 examines the effects of phosphatization, the only widespread diagenetic influence on FeMn crusts, on the speciation of Pb in FeMn crusts. Determining how the process of phosphatization modifies metal concentration and mobility in crusts improves the genetic model and facilitates our understanding of mass balance in FeMn crusts. This study also informs the broader context of how phosphatization should influence the development of permissive criteria for FeMn crusts. Chapter 3 examines variability in FeMn crusts from the Tuvalu Exclusive Economic Zone (EEZ) in the southern equatorial Pacific. This study provides an example of how FeMn crusts collected from reconnaissance expeditions can determine oceanographic influences on crusts in that region and help define permissive regions for future interest. This study also examines bulk crusts, which integrate crust composition over millions of years, and their correlations with oceanographic parameters can be compared with recent crust growth from the same region reported in Chapter 1.

As interest in FeMn crusts continues to grow, so will the need to define the criteria for how to find deposits with specific characteristics, and the following thesis contributes to that definition.

References

Bolton, B. R., Exon, N. F., Ostwald, J., and Kudrass, H. R. 1988. "Geochemistry of Ferromanganese Crusts and Nodules from the South Tasman Rise, Southeast of Australia." *Marine Geology* 84: 53–80. https://doi.org/10.1016/0025-3227(88)90125-9.

Burton, K. W., Bourdon, B., Birck, J. L., Allègre, C. J., and Hein, J. R. 1999. "Osmium Isotope Variations in the Oceans Recorded by Fe-Mn Crusts." *Earth and Planetary Science Letters* 171 (1): 185–97. https://doi.org/10.1016/S0012-

821X(99)00139-9.

De Carlo, E. H., Pennywell, P. A., and Fraley, C. M. De. 1987. "Geochemistry of Ferromanganese Deposits from the Kiribati and Tuvalu Region of the West Central Pacific Ocean." *Marine Mining* 6: 301 pp.

De Carlo, E. H., Mcmurtry, G. M., and Kim, K. H. 1987. "Geochemistry of Ferromanganese Crusts from the Hawaiian Archipelago I. Northern Survey Areas." *Deep-Sea Re.~earch* 3487 (3): 441–67. https://ac.els-cdn.com/0198014987901476/1-s2.0-0198014987901476-main.pdf?_tid=937371d9-4f3f-4f78-9d3d-bf6c0b91ca54&acdnat=1529346943_410c4f6db45753bdbf520794934a98f0.

Frank, M., O'Nions, R. K., Hein, J. R., and Banakar, V. K. 1999. "60 Myr Records of Major Elements and Pb-Nd Isotopes from Hydrogenous Ferromanganese Crusts: Reconstruction of Seawater Paleochemistry." *Geochimica et Cosmochimica Acta* 63 (11–12): 1689–1708. https://doi.org/10.1016/S0016-7037(99)00079-4.

Frank, M., Whiteley, N., Kasten, S., Hein, J. R., and O'Nions, K. 2002. "North Atlantic Deep Water Export to the Southern Ocean over the Past 14 Myr: Evidence from Nd and Pb Isotopes in Ferromanganese Crusts." *Paleoceanography* 17 (2): 1–9. https://doi.org/10.1029/2000PA000606.

Halbach, P., Sattler, C.-D., Teichmann, F., and Wahsner, M. 1989. "Cobalt-Rich and Platinum-Bearing Manganese Crust Deposits on Seamounts: Nature, Formation and Metal Potential." *Marine Mining* 8 (1): 23–39.

Hein, J. R., Manheim, F. T., Schwab, W. C., Davis, A. S., Daniel, C. L., Bouse, R. M., Morgenson, L.A., Sliney, R. E., Clague, D., Tate, G. B., and Cacchione, D. A. 1985. "Geologic and Geochemical Data for Seamounts and Associated Ferromanganese Crusts in and near the Hawaiian, Johnston Island, and Palmyra Island Exclusive Economic Zones."

Hein, J. R., Morgenson, L.A., Clague, D. A., and Koski, R. A. 1987. "Cobalt-Rich Ferromanganese Crusts from the Exclusive Economic Zone of the United States and Nodules from the Oceanic Pacific." In *Geology and Resource Potential of the Continental Margin of Western North America and Adjacent Ocean Basins-Beaufort Sea to Baja California*, edited by J. G. Scholl, D. W., Grantz, A., and Vedder, Circum-Pac, 753–71. Houston, TX.

Hein, J. R., and Koschinsky, A. 2014. *Deep-Ocean Ferromanganese Crusts and Nodules*. *Treatise on Geochemistry: Second Edition*. 2nd ed. Vol. 13. Published by Elsevier Inc. https://doi.org/10.1016/B978-0-08-095975-7.01111-6.

Hein, J. R., Koschinsky, A., Bau, M., Manheim, F. T., Kang, J.-K., and Roberts, L. 2000. “Cobalt-Rich Ferromanganese Crusts in the Pacific.” *CRC Marine Science Series* 17.

Hein, J. R., Koschinsky, A., and Halliday, A. N. 2003. “Global Occurrence of Tellurium-Rich Ferromanganese Crusts and a Model for the Enrichment of Tellurium.” *Geochimica et Cosmochimica Acta* 67 (6): 1117–27. https://doi.org/10.1016/S0016-7037(00)01279-6.

Josso, P., Parkinson, I., Horstwood, M., Lusty, P., Chenery, S., and Murton, B. 2019. “Improving Confidence in Ferromanganese Crust Age Models: A Composite Geochemical Approach.” *Chemical Geology* 513: 108–19. https://doi.org/10.1016/j.chemgeo.2019.03.003.

Klemm, V., Levasseur, S., Frank, M., Hein, J. R., and Halliday, A. N. 2005. “Osmium Isotope Stratigraphy of a Marine Ferromanganese Crust.” *Earth and Planetary Science Letters* 238 (1–2): 42–48. https://doi.org/10.1016/j.epsl.2005.07.016.

Koschinsky, A., and Halbach, P. 1995. “Sequential Leaching of Marine Ferromanganese Precipitates: Genetic Implications.” *Geochimica et Cosmochimica Acta* 59 (24): 5113–32. https://doi.org/10.1016/0016-7037(95)00358-4.

Manheim, F. T. and Lane-Bostwick, C. M. 1988. “Cobalt in Ferromanganese Crusts as a Monitor of Hydrothermal Discharge on the Pacific Sea Floor.” *Nature 1988 335:6185* 335 (6185): 59. https://doi.org/10.1038/335059a0.

Nielsen, S. G., Mar-Gerrison, S., Gannoun, A., LaRowe, D., Klemm, V., Halliday, A. N., Burton, K. W., and Hein, J. R. 2009. “Thallium Isotope Evidence for a Permanent Increase in Marine Organic Carbon Export in the Early Eocene.” *Earth and Planetary Science Letters* 278 (3–4): 297–307. https://doi.org/10.1016/j.epsl.2008.12.010.

Varentsov, I.M. M., Drits, V.A. A., Gorshkov, A.I. I., Sivtsov, A.V. V., and Sakharov, B.A. A. 1991. “Mn-Fe Oxyhydroxide Crusts from Krylov Seamount (Eastern Atlantic): Mineralogy, Geochemistry and Genesis.” *Marine Geology* 96 (1–2): 53–70. https://doi.org/10.1016/0025-3227(91)90201-E.

Xu, Z., Li, A., Jiang, F., and Li, T. 2006. “Paleoenvironments Recorded in a New-Type Ferromanganese Crust from the East Philippine Sea.” *Journal of China University of Geosciences* 17 (1): 34–42. https://doi.org/10.1016/S1002-0705(06)60004-6.

Chapter 1.

Geographic and oceanographic influences on ferromanganese crust composition along a Pacific Ocean meridional transect, 14N to 14S

Abstract

The major controls on the variability of ferromanganese crust composition have been generally described over the past 40 years, however most compilation studies lack quantitative statistics and are limited to a small region of several seamounts or compare FeMn crusts from disparate areas of the global oceans. This study provides the first detailed research to address the geographic and oceanographic controls of FeMn crust composition from a line of seamounts across 30° of latitude in the west central Pacific. Element concentrations from the uppermost layer (<15mm) of 57 FeMn crusts were evaluated for statistically significant variance and correlation with a variety of oceanographic and geographic parameters. Manganese, Co, Ni, Mo, and Zn concentrations in crusts in this region are highly correlated with seawater oxygen concentrations, suggesting oxygen as the dominant controlling factor for these elements. Iron instead correlates with water depth, which we attribute to increased carbonate ion concentration with increasing water depth. Silicon and Al content in crusts demonstrate a potential meridional variance of detrital inputs and sources in the region. Iron, Ba, and Mg are enriched in FeMn crusts below the equatorial upwelling zone which is related to biological productivity. Fluctuations in the four oceanographic and geographic parameters, seawater oxygen content, detrital input, surface productivity, and deep sources of iron, are robustly recorded by FeMn crusts.

Modern measurements of these primary parameters, as well as paleoceanographic reconstructions, can be used to define regions of interest for FeMn crust exploration.

1. Introduction

1.1 Ferromanganese Crusts

Ferromanganese (FeMn) crusts are chemical sedimentary rocks composed predominantly of iron and manganese oxide minerals. These deposits grow on the flanks and summits of seamounts and other midplate volcanic edifices throughout the global ocean. They are a hydrogenetic mineral deposit, forming by the precipitation of iron and manganese oxides from seawater, and accumulate a remarkable list of elements over time through a variety of sorption reactions. FeMn crust composition is thus dependent on seawater composition, which can vary based on: geographic location and water depth, especially with proximity to coastal and aeolian input of detritus or to hydrothermal activity; with changes in atmospheric circulation and surface productivity; and as different water masses circulate and mix. The capacity of fluctuations in these oceanographic and geographic controls on seawater composition to be recorded and archived by FeMn crusts must be calibrated, and many studies have done so using isotopes of specific elements like Pb (e.g. Christensen et al., 1997; Klemm et al., 2007), Nd and Hf (van de Flierdt et al., 2004), Os (e.g. Klemm et al., 2005), Ni (e.g. Gall et al., 2013), Tl (e.g. Nielsen et al., 2009), and others. Some studies have also looked at water depth controls on crust composition, for example

variability along a single seamount (Usui et al., 2017) and variability of rare earth elements plus yttrium (REY) with water depth (Azami et al., 2018).

However, few studies have included seawater changes recorded by FeMn crusts along a large, continuous geographic feature where changes with latitude and water depth can covary and systematic investigations are required to separate the fundamental controls of each variable on crust compositions. Hein et al., (2016) performed one of the few such studies, reporting FeMn crust variability along the 5000 km long Ninetyeast Ridge in the Indian Ocean, including changes in growth rates explained by changes in the depth of the oxygen minimum zone and supply of deep-sourced iron; however, that study included only 12 crusts from 9 locations along the ridge due to limited sample availability. The research presented here provides another opportunity, but with a much higher sample density, through the examination of 57 FeMn crust samples along a chain of seamounts in the Pacific Ocean that spans from 14°N to 14°S and from 171°W to 168°E (Figure 1). In addition, the current study compares recent growth-layer composition with modern seawater parameters that are easily observed or measurable at the current crust locations, which aids in the development of successful exploration criteria for these deposits by improving the ability to predict FeMn crust composition within large-scale, contemporary, oceanographic and geographic settings.

1.2 Geographic and Geologic Setting

The Pacific plate hosts several linear volcanic chains composed of a multitude of seamounts as a result of hotspot volcanism and plate movement through time. The central West Pacific Ocean contains the "Hotspot Highway", a region where four hotspot tracks (Rurutu, Macdonald, Rarotonga, and Samoa) overlap resulting in seamounts of varying composition and ages (Finlayson et al., 2018). FeMn crusts from this study were sampled from a linear chain of seamounts along the Rurutu, Macdonald, and Samoa hotspot tracks, including the Marshall Island, Gilbert Island, Tuvalu, and Tokelau chains, seamounts near Howland and Baker Islands, and the eastern and western Samoan seamounts (Finlayson et al., 2018; Jackson et al., 2010). These seamounts range in age from 10 to 90 million years old and present vast areas of rock outcrops that allow for significant accretion of FeMn crusts (Finlayson et al., 2018).

1.3 Oceanographic Regimes

The FeMn crust sample set spans not only a wide range of latitudes (14°N to 14°S) and longitudes (168°E to 171°W) but also water depths (1399 to 4354 m), allowing for the samples to be situated within a variety of water masses (Bostock et al., 2010) and oceanographic environments. The most prominent oceanographic feature in this region is the equatorial upwelling zone (hereafter called EUZ) where upwelled nutrient-rich waters along the equator spur increased biological productivity in surface waters. This results in increased surface chlorophyll-a values occurring along the equator from 3°N to 2.7°S at the western margin of the sample region and

from 7°N to 8.8°S at the eastern margin (NASA MODIS Aqua, April 2019; Figure 1). Although the EUZ is a feature at the sea surface and FeMn crusts in this study are found below 1000 m, biogenic particle flux from the surface to deeper levels in the water column is increased under the EUZ (Smith et al., 1997). Scavenged elements like Co, and organic-matter related elements like Ba, can be delivered to deeper parts of the water column when particles are remineralized (Hawco et al., 2018; Paytan and Kastner 1996). Carbonate particles will also dissolve as they approach the aragonite and calcite compensation depths (ACD and CCD), and biogenic silica particles will dissolve due to its undersaturation everywhere in the oceans. These dissolution processes can return metals to the dissolved phase, making them available for incorporation into adjacent FeMn crusts (Halbach & Puteanus, 1984; Twining & Baines, 2013). In addition, increased carbonate ion concentrations increase pH, which can affect Fe-oxide precipitation (King et al., 1998).

Beyond productivity-related chemical signals, the water depth at which each FeMn crust was located also determines which of the larger-scale oceanic water masses advected to the region influence each crust. The shallowest and northernmost samples will be influenced by the Eastern Tropical North Pacific (ETNP) subsurface oxygen minimum zone (OMZ); for example, two of the FeMn crusts were growing in waters currently containing approximately 90 µmol/l oxygen (Garcia et al., 2014a). On the other hand, the deepest samples formed in more oxygen-rich Circumpolar Deep Water (~200 µmol/l; Garcia et al., 2014a; Figure 2). In general in this region, oxygen concentration increases with water depth, making oxygen a likely control on

variation in FeMn crust composition with water depth because of the many redox processes (Hein et al., 1997) that characterize the formation and composition of crusts.

Samples along this meridional transect may also be influenced by multiple detrital inputs. For example, wind-blown loess from Mongolia is known to reach the equatorial north Pacific through the washing-out of dust particles from the atmosphere within the Intertropical Convergence Zone (Hyeong et al., 2005) and thus the northernmost and westernmost FeMn crusts may reflect chemical signatures of this detrital source. Samples in the southeastern region are much closer to the Tonga-Kermadec Volcanic Arc system and may receive more terrestrial/volcanic input, as well as wind-blown loess from Australia as found in nearby deep-ocean sediment cores (Zhou & Kyte, 1992). Another potential influence on crust compositions in the southern part of the study region is hydrothermal activity from the nearby volcanic arcs, back-arcs, and hotspot volcanic activity. In our study, we decipher detrital signatures from bulk FeMn crust compositions to assess this technique, but we acknowledge that isolating the detrital grains and measuring their detailed isotopic (Nd, Pb, Hf) compositions would better identify these detrital sources.

2. Methods

2.1 Samples

Samples analyzed in this study (n=57) were collected via dredge on four research cruises (Table 1). Each dredge latitude, longitude, and water depth were calculated

from shipboard dredge log records to account for the length of wire out, movement by the ship, approximate seamount slope, and multiple "bites" of the dredge in order to maximize location accuracy. For simplicity in data interpretation, samples were grouped into 3 main transects based on location and named for the nearby islands as follows: Marshall-Gilbert-Tuvalu (MGT), Howland-Baker-Tokelau (HBT), and Samoa (Figure 1). The MGT transect is considered the primary transect of the study since it spans the greatest latitudinal range and is continuous along a straight line. The Samoa transect occurs after the bend in the hotspot track and aligns more east-west allowing for the study of zonal effects, and the HBT transect offers a parallel and longitudinally offset sample group to the MGT transect, which is also ideal for examining zonal changes in FeMn crust composition.

This study would be best performed with FeMn crust subsamples of only the uppermost 0.5-1 mm of crust in order to minimize the number of years of seawater chemistry that are integrated over each crust sample and for better comparison with modern seawater parameters; however, data from the upper 0.5-1 mm or less was very limited since we compiled previously analyzed samples. In order to maximize the number of samples included in the dataset for the best statistics and geographic coverage, we therefore include FeMn crusts and uppermost crust sublayers of up to 15 mm thick. The typical growth rates of FeMn crusts in the open ocean range from 1-10 mm/ Myr (Hein and Koschinsky, 2014). If a slow growth rate of 1.5 mm/ Myr is assumed for samples with the maximum allowed thickness of 15 mm, this would encompass a maximum of 10 Myr of crust growth. Based on models of Pacific Plate

movement, a seamount in the study region would have moved ~1 degree or ~100 km northwest in 10 Myr (Van Hinsbergen et al., 2015). Ten Myr at an average subsidence rate of 2 cm/10^3 yr (Menard, 1969) results in ~200 m of total subsidence. Thus, limiting the thickness to 15 mm still eliminates major variations that might otherwise be attributed to movement of the Pacific plate and associated thermal subsidence, such as movement into or out of the EUZ (latitude) or further below the OMZ (depth). Our data indicate that chemical variations are still interpretable using modern general geographic and oceanographic parameters, but would be even more robust using thinner crusts to minimize the amount of time integrated within each crust layer. We also acknowledge that some correlations may be stronger if crust layers from a uniform time-frame were used.

2.2 Major and trace element concentrations

The uppermost layer of each FeMn crust was sampled with a knife and then ground to 75 μm with an agate mortar and pestle. The chemical composition of the Fe-Mn crusts was determined at SGS Labs, Canada (previously XRAL). The 10 major elements were determined by X-Ray Fluorescence (XRF) on borate fused disks, and the minor elements by inductively coupled plasma mass spectrometry and atomic emission spectroscopy (ICP-MS and ICP-AES) following a 4-acid digestion, except the Tuvalu (cruise RR1310) samples for which Cu, Mo, Ni, V, and Y were prepared for ICP-MS using lithium-metaborate fused disks. The water content (H_2O^-) of each FeMn crust was determined by gravimetric analysis, and the weight percent

water was then used to correct element concentrations in each sample to sorbed-water-free values. Reproducibility measured from duplicate analyses of the sample was better than 7% for all elements except for As and Cd, which were 9.3% and 17%, respectively, for one batch out of six separate batches of analyses for which duplicate analyses were measured. Accuracy was determined for four of the seven batches of analyses by calculating the percent difference between published recommended values and measured values for certified reference materials. Accuracy was better than 7% for Fe, Si, Al, Na, K, Ti, P, As, Cd, Cu, Sr; 8-15% for Pb, Mo, Mg, Mn, Zn, Ba; 15-25% for Y, Ca, Cr, Co; 27% for V; and 34% for Ni. Certified reference materials used to determine accuracy included: SY-4, NODA-1, NODP-1, OREAS 171, OREAS 405, OREAS 903, SARM42, and RTS-3A. Note that some certified standards measured for accuracy calculations are dissimilar to FeMn crust matrix and may not closely reflect the accuracy for the FeMn crust measurements presented here. For dredge sites with multiple individual FeMn crust samples, the chemistry from the uppermost layers of these samples was averaged and represents the mean chemical composition of the upper <15mm of FeMn crusts at the particular latitude, longitude, and depth of the dredge site.

2.3 Statistical correlations and factor analysis

To determine statistically significant variance in major and trace element concentrations for FeMn crust samples from different locations along the seamount chains, and to determine correlations for concentration variations with geographic and

oceanographic parameters, several statistical methods were employed. Variance between samples was first determined using basic parameters such as mean and standard deviation. Pearson correlation coefficient matrices (CCM) were generated using MatLab to determine element concentration correlations with geographic and oceanographic parameters that could be quantified, such as latitude, longitude, water depth, and oxygen concentration. Longitudes were all converted to eastings, so that longitude increases toward the east. To investigate all geographic factors and identify possible inherent location biases in the dataset, CCM were run separately for the whole dataset (n=57), the primary MGT transect (n=33), HBT transect (n=9), MGT samples within the latitude bounds of the HBT transect (n=15), Samoa transect (n=15), as well as all samples north of the equator (n=12), all samples south of the equator (n=45), and samples north and south of the equator within the MGT transect (n=10 and n=23, respectively) in order to account for the larger overall number of samples south of the equator. Note that all correlations reported in subsequent sections are significant at the 95% confidence level (CL) or higher, with specific confidence levels (95% or 99%) defined when important. Q-mode factor analysis of the major and trace element data was also run for the primary MGT transect (n=33) in MatLab (Pisias, Murray, & Scudder, 2013) to identify common groups of elements, referred to as factors, and determine which of these factors reflect geographic and oceanographic parameters along this primary transect. For Q-mode factor analysis, each variable percentage was scaled to the percent of the maximum value before the values were row-normalized and cosine-theta coefficients calculated. Factors were

derived from orthogonal rotations of principal component eigenvectors using the Varimax method (Klovan & Imbrie, 1971). All but three samples have communalities greater than 0.9 with an overall average communality for the 33 samples of 0.94; communality is an index of the efficiency of a reduced set of factors to account for the original variance.

3. Results

3.1 Overall Compositional Variation of FeMn Crusts

The concentrations of major and trace elements in the 57 FeMn crusts in this study show a large variation, providing the foundation for the hypothesis that crust composition will vary when distributed through an area with different oceanographic conditions and geographic locations. Iron and Mn, which comprise the main mineral phases of FeMn crusts, each vary overall by 21 wt. %, ranging from 15-36 and 12-33 wt. % and having relative standard deviations (RSD) of 22% and 26%, respectively (Table 2; Supplementary Table 1). Silicon and Al, which typically represent minor detrital phases found in FeMn crusts, exhibit overall ranges of 6.9 and 2.9 wt. % and have RSDs of 32% and 52%, respectively. Ba varies overall by 2633 ppm, with a RSD of 37%. The RSDs for Cu, Cr, and Co are all above 60%, with Co exhibiting the largest overall range in concentration for the trace metals of 1.75 wt. %, from the minimum value of 0.14 to the maximum of 1.89 wt. % (Table 2).

3.2 Geographic correlations within the dataset

Several of the geographic parameters being examined covary, which affects the proper interpretation of element correlations with those parameters. First, the MGT and HBT seamount chain transects are oriented northwest- southeast (Figure 1), and the magnitude of the change in latitude between sample locations along these two sample transects is much more than the change in longitude; therefore, zonal variations in crust composition within each of these individual sample transects are likely to be less significant than meridional variations, or may be entirely caused by meridional controls. In addition, sample water depths anticorrelate with latitude within the whole dataset (R=0.3801, n=57) and especially within the MGT transect (R=0.5863, n=33). Oxygen has a very strong correlation with water depth for the whole dataset (R=0.9046, n=57) and even stronger for the primary MGT transect (R=0.9390, n=33). Therefore, element correlations with water depth and latitude may be mostly or completely attributable to correlation with oxygen concentration, however we investigated each separately (Table 3).

3.3 Water Depth and Oxygen Correlations

CCM reveal positive Fe, Fe/Mn, and Cu correlations with water depth for the whole dataset, MGT, and north of the equator, but not within groups that are all or mostly south of the equator. The exception is Fe, which is also positively correlated with water depth in Samoa (Table 3; Supplementary Tables 2 and 3). Si correlates with depth at the 95% CL for the whole dataset and for the MGT transect. Barium correlates with water depth for the whole dataset, in HBT and north of the equator.

Titanium shows positive correlations with water depth in the whole sample set, MGT, and south of the equator, which are the groups with the highest number of samples. Lead, Ni, and Co anticorrelate with water depth for the whole dataset, MGT, and north of the equator, and one or more of Pb, Ni, and Co anticorrelate with water depth in most sample groups, except south of the equator. Zinc also anticorrelates with water depth in the whole dataset and MGT. Phosphorous is anticorrelated with water depth in all of the sample groups that dominate south of the equator, except HBT, which is likely due to the small number of samples.

Despite oxygen and water depth being highly correlated, and many element correlations with these two parameters being similar, some element correlations with oxygen differ from those with water depth. Manganese, for example, shows a significant anticorrelation with oxygen for the whole dataset, MGT, and Samoa, while Mn did not show significant anticorrelations with water depth in any of these sample groups. Al is correlated with oxygen for MGT but is not correlated with depth in any transect. Cadmium anticorrelates with oxygen south of the equator, including in HBT and the 'MGT within HBT' groups. Sodium anticorrelates with oxygen for the whole dataset and within MGT, but did not have significant correlations with depth in these transects.

3.4 Latitude Correlations

The Fe/Mn ratio anticorrelates with latitude (increases to the south) in all data groups except Samoa, HBT, and 'MGT within HBT' (Table 3). Iron anticorrelates

with latitude in MGT and in groups north of the equator and correlates with latitude south of the equator, whereas Mn correlates with latitude, especially for the MGT samples and even more strongly in the southern portion of the MGT transect. Cobalt, Mo, Ni, Pb, and V follow the behavior of Mn, correlating with latitude. Zinc correlates with latitude for all samples and MGT but anticorrelates with latitude south of the equator.

Silicon and Al anticorrelate with latitude overall and especially in the MGT transect samples, and Al also anticorrelates with latitude in all sample groups north of the equator. The Si/Al ratio, however, correlates with latitude in sample groups north of the equator and in MGT. Phosphorous is correlated with latitude in sample groups that are dominantly located south of the equator. The HBT transect includes only nine samples, so very few element correlations are significant.

Singling out the MGT transect samples, to consider the effect of latitude on samples north versus south of the equator, few differences occur from the overall dataset correlations; however, Mn, Co, Ni, Zn and Mo correlations with latitude are no longer observed when only MGT samples north of the equator are included in the CCM. Titanium, V, Cd, and P correlate with latitude when just MGT samples south of the equator are included (Table 3).

3.4.1 Equatorial Upwelling Signal

Barium, Mg, and Fe all anticorrelate with latitude north of the equator and correlate with latitude south of the equator. The concentrations of Ba, Mg, and Fe are

relatively high in FeMn crusts located within the EUZ compared to those outside the EUZ, which show a clear relationship with the high biological productivity in that region (Figure 3).

3.5 Longitude Correlations and Zonal Comparisons

3.5.1 Correlations with longitude from CCM

Within the whole dataset, Fe correlates with longitude (more Fe to the east), whereas Mn, Pb, Co, Ni, and Mo anticorrelate with longitude (Table 3). For MGT samples, similar correlations are observed as with the whole dataset, and As, Zn, and Si/Al additionally anticorrelate with longitude. In the Samoa region, Cr correlates with longitude while Cu anticorrelates with longitude.

3.5.2 Comparison of latitude, water depth, and oxygen correlations within zonally offset MGT and HBT transects

To further investigate changes in FeMn crust composition with longitude, we compared the element correlations with latitude, depth, and oxygen for HBT crusts to those of crusts from a sub-transect of the MGT that is within the latitude range of and parallel to HBT but offset by approximately 8 degrees of longitude. Within both HBT and the sub-transect of MGT, Ba correlates with latitude; however, in HBT, Mo also correlates with latitude, and Co anticorrelates with latitude, which is not seen in the MGT sub-transect. The MGT sub-transect reveals positive correlations for Fe and Mn as well as Mg, Ca, and P with latitude that are not seen in HBT. When element

correlations with water depth and oxygen within these two regions are compared, Cd anticorrelates with water depth and oxygen in both regions. For HBT samples, Ca and Mg anticorrelate with oxygen and depth, while Ba correlates with both water depth and oxygen, none of which are observed in the MGT sub-transect (Table 3). Lead and P anticorrelate with water depth oxygen in the MGT sub-transect but not in HBT.

3.5.3 MGT versus HBT zonal chemistry trends

FeMn crusts from HBT contain more Fe and Mn than crusts from MGT within the same latitude range, but Fe/Mn ratios are similar, so the Fe and Mn enrichments are nearly equal (Figure 4). Generally, there is more Al in the samples from the MGT sub-transect than in the HBT samples, but Si is similar. It is important to note that for the HBT transect and MGT sub-transect, the distribution of samples with water depth and surrounding oxygen concentrations are fairly uniform, which means that zonal variations are likely independent of oxygen concentration in seawater. The exception is for the northernmost samples of this subset (~0° - 1°N) where samples from the HBT transect are much deeper than the MGT samples at this latitude and are exposed to higher seawater oxygen concentrations, therefore water depth and oxygen are likely controlling the Fe and Mn concentrations in these three samples (Figure 4).

3.6 Q-mode Factor Analysis of MGT

Q-mode factor analysis, based on the 33 samples within the MGT sample group, produced four factors that account for 93.8% of the variance, with Factors 1-4 accounting for 34.9%, 19.2%, 29.5%, and 10.3% of the variance respectively (Table 4). The factor loadings for Factor 1 for each sample are correlated with oxygen at the 99% confidence level (CL) with an R value of 0.5870, however the trend is not described entirely by oxygen concentration (Figure 5; note that the correlation appears negative since oxygen is decreasing to the north). Therefore, Factor 1 is interpreted to represent elements that vary due to the oxygen concentration in seawater at each sample location while recognizing that other influences are evident. Factor 1 describes the variance in the following elements, in order of decreasing factor scores, Ni, Pb, Co, Mn, Zn, Na, and Mo. Most of these elements, especially Ni, Co, and Mo, are known to be enriched in the Mn-oxide phase of FeMn crusts, so it is likely that when more Mn-oxide is precipitated in relatively lower oxygen concentrations, the other elements also become more enriched as they sorb onto the Mn-oxide phase.

Factor 2 is interpreted to represent a mixed influence of detrital input and increasing carbonate ion concentrations with water depth, since many of the elements with high factor scores for factor 2 (Table 4) have significant correlations with water depth in CCM (Fe, Cu, Si), or are elements typically associated with the detrital fraction of FeMn crusts (Si, Al, K, Na, Mg, Cr, Zn). The factor loadings for each sample for factor 2 have a weak but significant correlation (95% CL) with the estimated dissolved carbonate ion concentration at each sample location

(Supplementary Table 1; Key, R.M. et al., 2004; Figure 5). Colloidal Fe has been shown to be released during biogenic carbonate dissolution (Palmer 1985; Halbach and Puteanus 1984), and increased carbonate ion concentrations elevate pH and increase the oxidation rate of Fe(II) in seawater (King et al., 1998). In addition, Cu is highly enriched in the Fe-oxyhydroxide phase of FeMn crusts. Therefore, higher iron-oxide formation at depth where carbonate ion concentration is higher is a plausible interpretation for Factor 2. Silicon and Al have no relationship with carbonate ion concentrations yet have high scores for Factor 2. Detrital flux may also increase with depth due to weathering and mass movement of debris down the slopes of seamounts. Thus, Factor 2 likely reflects these two correlated depth-related phases.

Elements with high factor scores for Factor 3 include Y, Ca, Si, Al, Fe, V, As, Sr, and P (Table 4). The high factor scores for Si and Al indicate that like Factor 2, Factor 3 also partially represents detrital input to FeMn crusts. The plot of Factor 2 scores versus Factor 3 scores (Figure 5A) show that these factors are generally correlated (negative correlation) except for Si and Al, which supports that detrital inputs are distinguishing these factors. Additionally, the factor loadings for Factor 3 anticorrelate with latitude at the 99% CL. Latitude is interpreted here to indicate changes in detrital-associated elements (Si, Al, K) and their ratios with latitude as presented in the previous section, which imply the possibility of differing detrital provenance or flux along the meridional transect (Table 3; see discussion section). Due to the presence of P, Sr, V, As, and Y in this factor, a biogenic signal may also exist in this factor. The enrichment of these elements in seawater can be linked to

high productivity and biogenic particle flux because they are bioessential elements (V and P) or preferentially sorb to organic matter (Sr, Y, and As).

Factor 4 is characterized by elements related by the EUZ, and factor loadings for each sample correlate at higher than the 99% CL (R=0.6757, n=33) with surface chlorophyll-a values (NASA MODIS Aqua, April 2019; Figure 5; Supplementary Table 1) at each sample latitude/longitude. The elements with the highest factor scores for Factor 4 in decreasing order are Ba, Fe, and Mg (Table 4), which were also the elements most strongly associated with the EUZ in CCM results (Table 3).

4. Discussion

4.1 Controls on the major oxide phases

It is well established that thicker and more Mn- and Co-rich FeMn crusts are associated with proximity to oxygen minimum zones (OMZ) due to the high dissolved Mn contents within the OMZ, and permissive depths for such metal-rich FeMn crusts have been described based on the depth of the OMZ (Cronan 1984; Hein et al., 2000). This trait is well demonstrated by the sample transect here, which shows higher Mn and Co concentrations in the northern samples that were forming just below the lowest oxygen concentration observed in this region, at approximately 600-1000 m water depth, which is the western portion of the Eastern Tropical North Pacific OMZ originating offshore of Mexico (Figure 2). The strong anticorrelation of Mn with seawater oxygen, as well as high scores for Mn in Factor 1 and correlations of Factor 1 loadings with seawater oxygen, substantiates that seawater oxygen

concentration is the oceanographic property that has the most influence on Mn concentration in FeMn crusts (Table 3; Table 4; Figure 5). Unlike previous studies of crusts in the Pacific (e.g. Hodkinson and Cronan, 1991) that inferred OMZ locations from limited oceanographic data, this study uses measured oxygen concentrations interpolated to each sample's specific location to account for fluctuations in oxygen concentration with depth as well as proximity to a stronger or weaker OMZ.

In contrast to Mn, Fe concentration as well as the Fe/Mn ratio in FeMn crusts in this study increase with water depth, as seen in many other Pacific Ocean crust compilation studies (e.g. De Carlo, Mcmurtry, and Kim 1987 and Hodkinson and Cronan 1991). The cause of increased Fe contents in crusts with depth is attributed to either a lessening contribution of Mn because crust growth is occurring further from the Mn-rich OMZ, or a deep-water source of iron. Halbach and Puteanus (1984) suggested that the increased dissolution of the carbonate tests of plankton with depth is a likely a source of Fe to FeMn crusts. Additionally, kinetic experiments have shown that increased carbonate ion concentration in synthetic seawater increases the pH and increases the oxidation rate of Fe(II) in seawater (King et al., 1998). An increase in deepwater pH would also decrease the solubility of Fe(III), which has a solubility minimum around pH 8 (e.g., Liu and Millero 2002). These or similar pH-dependent processes could potentially also augment the Fe-(oxyhydr)oxide content in FeMn crusts. Dissolved carbonate ion concentrations correlate (95% CL) with the factor loadings of Factor 2, which has a high factor score for Fe. This suggests that the release of dissolved Fe from the dissolution of carbonate, and/ or increased pH

from high carbonate ion concentrations, leads to increased precipitation of Fe-oxyhydroxides in FeMn crusts. The carbonate compensation depth (CCD) in the equatorial Pacific is estimated at ~4650 m in the modern Pacific and has risen to 4100 m within the past 5 million years (Pälike et al., 2012), which is the average age of the upper layers of FeMn crusts in this study as calculated from their estimated crust growth rates (average 3.14 mm/Myr) using the cobalt-based chronometric equations of Manheim and Lane-Bostwick (1988; growth rate calculations discussed further in 4.1.1). The mean depth of samples in this study is 2900 m with a maximum depth of 4354 m, therefore none of the samples occur below the modern CCD and only four occur below the paleo CCD of 4100 m. However, the dissolved carbonate ion concentration in this region of the modern ocean nonetheless generally increases with depth below 2000 m because of deep and bottom waters that are more recently ventilated. This argues in favor of a pH-dependent process rather than the dissolution of biogenic carbonate tests as a more likely source of the correlation between Fe and depth.

Isotopic studies reveal that hydrothermal emissions and sediment redox cycling can be significant sources of Fe to the deep ocean (Horner et al., 2015), which may also explain increased Fe contents in FeMn crusts with depth. The trace element composition of water masses in the Indian Ocean show that Fe concentration in seawater is elevated in deep waters due to hydrothermal contribution at specific depths (Nishioka et al., 2013), and Hein et al., (2016) attributed increased Fe concentration in FeMn crusts from the same depths along the Ninetyeast Ridge to

their growth from this Fe-rich Indian Ocean water mass. However, the region studied here does not have a hydrothermal source that is likely to supply the entire line of seamounts at a consistent depth; only the southern portion of the sample region is close enough to known hydrothermal sources (Tonga-Kermadec Arc and Back-arc), but the depth trend for Fe is consistent for all crusts in the region. Also, a proxy to determine whether dissolved carbonate ion concentrations or hydrothermal input is the dominant contributor to enriched Fe concentration in FeMn crusts, that can be interpreted using bulk element concentrations of FeMn crusts alone, is not known.

A third explanation for an increase in Fe content in FeMn crusts with depth is increased entrained detrital material. As seen in the CCM results (Table 3), Si also increases with depth and both Si and Al, which are detrital elements, have strong factor scores in depth-related Factor 2 of the Q-mode factor analysis. Iron is a major component of the majority of the aluminosilicate minerals found in the deep ocean, therefore, if detrital input to FeMn crusts is increasing with depth, Fe concentration should also increase. Detrital input to crusts likely increases with depth due to the downslope movement of materials as the seamounts are eroded and debris is re-worked. However, mass-balance calculations for Fe associated with the estimated detrital contribution to total FeMn crust mass do not favor this source for most of the increased Fe (Hein & Koschinsky, 2003). The ultimate cause of the increase of Fe in FeMn crusts with water depth is likely associated with all of these factors; however, in this study we are only able to test the dissolved carbonate ion concentration hypothesis quantitatively, and determine that it is consistent with our data.

4.1.1 Fe and Mn associated elements

Most of the trace elements analyzed in this study have a typical association with either the Mn-oxide or Fe-oxyhydroxide phases in FeMn crusts based on their speciation in seawater, and these associations have been substantially confirmed by sequential leaching studies (Koschinsky and Halbach, 1995; Koschinsky and Hein, 2003). Cobalt and Ni are strongly associated with the Mn phase in crusts throughout the global ocean, and both follow the geographic and oceanographic correlations of Mn in this study. Notably however, the anticorrelations of Ni and Co with water depth are significant at the 99% CL, while Mn was not anticorrelated with water depth at even the 95% CL. Manganese might be expected to anticorrelate with water depth in the Pacific, however, since oxygen concentrations are lower at shallower depths. The fact that Co and Ni show strong anticorrelations with water depth independent of Mn but the same strong anticorrelations with oxygen as Mn, suggests that Co and Ni either experience additional water depth-related controls on their concentration in crusts, or their enrichment is not as strongly controlled by oxygen concentrations in seawater as for Mn. Cobalt has a scavenged-type vertical profile in the Pacific Ocean, while Ni has a nutrient-like vertical profile on average in the Pacific (Bruland, 1983). However, both Co and Ni have fairly uniform concentrations in seawater below ~1500 m where the crusts studied here occur, so metal supply is not the cause of the discrepancy between Mn and Ni and Co with water depth. The high Co enrichment in FeMn crusts has been explained by its surface oxidation from Co^{2+} to less soluble Co^{3+} at the surface of crusts, however this has not been identified

as a surface reaction for Ni (Hein et al., 2000; Hem, 1978; Manceau et al., 1997). The probable control for both the Ni and Co concentrations is the growth rates of the crusts. Growth rates tend to increase with water depth in general, and therefore crusts with slower growth rates commonly occur at shallower depths and have higher Co and Ni concentrations (Halbach and Puteanus 1984; Hein et al., 2000). Growth rates estimated for FeMn crusts in this study using the Manheim and Lane-Bostwick (1988) equations do anticorrelate strongly with Co and even more strongly with Ni (R= -0.6914 and -0.8028, respectively for n=57). While these growth rates are estimates and would be more informative if calculated from absolute ages determined by isotope measurements, these results do indicate that slower growth rates at shallower depths allow for increased accumulation of Ni and Co. This change in growth rate with water depth has been clearly verified for continental-margin crusts (Conrad et al., 2017) and has been inferred to also characterize open-ocean crusts, but may not always be invariably true. For example, (Usui et al., 2017) showed that growth rates of crusts do not change with water depth over a detailed sampling from the base to the summit of a West Pacific seamount. However, the data presented here support that growth rates in FeMn crusts do change with water depth in Pacific open-ocean crusts, and that growth rates also affect the accumulation of Mn-oxide associated elements.

Zinc and Mo also have the same geographic and oceanographic correlations as Mn, and Cu and Ti align with those of Fe, which are expected phase associations based on element correlations, sequential leaching, and/ or x-ray absorption studies,

and confirm that the concentrations of these trace elements are controlled by the amount of the major oxide to which they sorb (Hein, Koschinsky, and Halliday 2003; Kashiwabara et al., 2011; Koschinsky and Hein, 2003). Lead and As, however, are thought to dominantly associate with the Fe-oxyhydroxide phase based on sequential leaching (Koschinsky & Hein, 2003) but instead correlate at the 99% CL with Mn and follow the geographic and oceanographic correlations of Mn in CCMs for all samples and for samples within the MGT transect. Lead has a very short residence time in seawater (Flegal & Patterson, 1983), so local and temporal changes in dissolved Pb distribution in the water column can affect its concentration in FeMn crusts. Dissolved Pb data from the Pacific equatorial region shows a strong subsurface maximum from 20°N to 50°N at the 160°W meridian, attributed to aerosol material that sinks just fast enough to avoid scavenging by biogenic particles in the surface and is then distributed to the equatorial region via the subtropical gyres (Zheng et al., 2019). This suggests that modern increased concentrations of Pb in the subsurface from leaching of aeolian dust along the northern portion of the sample region, that coincidentally mirror those of Co and Mn due to the stronger OMZ in the north, can explain the grouping of Pb with the geographic-oceanographic correlations of Co and Mn in this study. Additionally, Pb does show statistical correlations with both Mn and Fe in other regions of the Pacific (Hein et al., 2003), and the surface binding mechanisms allows for sorption of Pb to both the Fe and the Mn phase, as demonstrated by (Takahashi et al., 2007).

Arsenic has a nutrient-like distribution in the Pacific, with little fluctuation in concentration from 1000 – 5000 m water depth, so variation in the concentration of As in crusts is not due to changes in the As supply throughout the water column (Cutter & Cutter, 2006). Arsenic in seawater is most commonly in the form of As(V) arsenates (e.g. $H_2AsO_4^-$/ $HAsO_4^{2-}$/AsO_4^{3-}; Byrne, 2002), and As in FeMn crusts was confirmed with x-ray absorption spectroscopy to also have an oxidation state of As(V) (Kashiwabara et al., 2008). Therefore, the oxidation of As at the surface of the Mn oxide is not a likely mechanism for its association with Mn in the FeMn crusts here. However, As(V) arsenates can adsorb to Mn(IV) vacancy sites of synthetic Mn-oxides (Foster, Brown Jr., & Parks, 2003), which may be a reaction occurring here, or through co-precipitation reactions, either of which need to be confirmed using micro x-ray absorption spectroscopy. The elements Ti, Cd, Cr, V, and Y did not show consistent correlations with the oceanographic and geographic properties analyzed in this study and therefore are not discussed.

4.2 Productivity signatures

Barium, Fe, and Mg show significant increases in concentration within the EUZ region and thus their concentrations appear to be linked to surface productivity (Figure 1 and Figure 3). Barium in FeMn crusts is dominantly found in the Mn-oxide phase during sequential leaching of non-phosphatized crusts, thus Ba is likely sorbed to the Mn-oxide phase as a hydrated cation, Ba^{2+} (Koschinsky & Hein, 2003). Throughout the open ocean, dissolved Ba has a nutrient-like distribution and is thus

dominantly controlled by biological uptake in surface waters and subsequent release during remineralization of biogenic debris as it sinks to deeper waters (Chow and Goldberg 1960; Paytan and Kastner 1996), so the general increase of the biogeochemical cycling of Ba in the EUZ may provide increased dissolved Ba to FeMn crusts there. In addition, particulate barite flux to the deep ocean is increased when the productivity of overlying surface waters increases (Dymond, Suess, & Lyle, 1992). Although barite is not a major contributor to FeMn crust mineralogy, individual micrometer-scale barite grains are often seen using SEM analysis of FeMn crusts, so particulate barite can provide a small component of the increased Ba contents in crusts. Further, Paytan and Kastner (1996) found that, although sedimentary barite has low solubility, there is flux of dissolved barium to benthic waters from barite dissolution in oxic sediments in areas of high surface productivity, which may also supply dissolved Ba to FeMn crusts in the EUZ. Thus, the increased Ba content in FeMn crusts in the EUZ is reasonable and can be expected for similar regions of elevated productivity.

Iron is also highly associated with biogenic flux to the deep ocean; it is a micronutrient for most plankton so is taken up at the surface. Because it is particle reactive, only a portion is released back to the dissolved iron pool during remineralization of sinking biogenic particles, and the rest is scavenged back onto sinking particles (Twining et al., 2014). The EUZ, specifically, is a region of high productivity and has a highly efficient biological pump with particles raining at a high rate to the deep ocean (Kiko et al., 2017). The EUZ also receives high dissolved iron

from the equatorial undercurrent originating from the Western Pacific (Slemons et al., 2010). Biogenic and scavenged iron may thus be efficiently transferred from the relatively high iron supplied from the equatorial undercurrent to regions of FeMn crust formation in the EUZ.

Increased Mg in FeMn crusts below the in EUZ region is less straightforward. Dissolved Mg is highly concentrated in ocean water, has a conservative profile with depth, and occurs mostly as Mg^{2+} in the dissolved phase, which sorbs to the surface of negatively charged MnO_2 (Koschinsky & Hein, 2003); however, Mn is not more highly concentrated in crusts from the EUZ region (discussed below). Magnesium has been shown to preferentially sorb to the surface of biogenic opaline sediments over the other major cations, Na and K, in some regions of the equatorial Pacific (Donnelly & Merrill, 1977), and diatoms, which have opaline frustules, can dominate the phytoplankton population in equatorial divergence zones, such as the Pacific EUZ examined here (Estrada et al., 2016). Therefore, one possible explanation for the enrichment of Mg in FeMn crusts below the EUZ is biogenic opal flux to deep waters and Mg desorption/sorption from opaline sediments to nearby FeMn crusts. Alternatively, Mg is also moderately high in the easily leached phase of FeMn crusts, which is predominantly carbonates (Koschinsky & Hein, 2003), and Mg is incorporated into the calcite tests of foraminifera and nanoplankton. Thus, increased Mg in these FeMn crusts may also reflect greater amounts of carbonate tests incorporated into them as marine snow during their slow growth below the productive surface waters of the EUZ.

Phosphorous flux to the deep ocean from the degradation of sinking organic matter is greater in regions with high surface productivity, and P is highly scavenged by Fe-oxyhydroxide particles (Filippelli & Delaney, 1996). However, P concentrations are not elevated in the FeMn crusts in the study region below the EUZ, as might be expected. P does correlate with Fe for all samples (99% CL) and within the MGT transect (95% CL), however P concentrations in the FeMn crusts do not correlate with the phosphate concentrations in seawater (Garcia et al., 2014b; Supplementary Table 1) at each sample location within the primary MGT transect. The decoupling of P concentration in crusts and productivity occurs throughout the central Pacific (Hein et al., 2000), and requires further investigation into the surface chemistry of P in FeMn crusts and the controls on the accumulation of P in non-phosphatized crust layers.

4.2.1 Basin-wide versus regional characteristics

Hodkinson and Cronan (1991) compiled data for FeMn crusts from much of the Pacific Ocean (~25°N to ~25°S and 175°E to 150°W) and reported general trends in the chemical composition of crusts with location. For that large area, some correlations differed from our results. Most strikingly, Hodkinson and Cronan (1991) found that Mn increased near the equator which they attributed to surface productivity due to equatorial upwelling. In contrast, when restricted to our specific sample region and with more detailed sampling of the younger, uppermost crust layers, it was Fe, not Mn, that was more enriched within the EUZ. Although there is a subsurface

minimum in oxygen along the EUZ when sinking organic matter is respired below the photic zone, subsurface EUZ oxygen concentrations are not low enough to strongly affect Mn concentrations in the FeMn crusts for the sample area examined here. The Mn trend observed by Hodkinson and Cronan (1991) was due to the strong OMZs further east in the tropical Pacific, including the poorly ventilated Eastern Tropical Pacific oxygen deficient zones that propagate westward from the west coasts of Mexico and Peru.

These regional variations show that a more nuanced view of environmental conditions is required for choosing regions of interest for potentially economic FeMn crusts. While the larger-scale studies point to the equatorial region for higher Mn and therefore more Co-rich crusts (Co being the main metal of economic interest in crusts), it is clear from this study that for island nations looking for resources within their Exclusive Economic Zones, shallower-water crusts from the northern subtropical region should be the area of focus in order to collect FeMn crusts growing beneath or near the strongest modern OMZ. In addition, for FeMn crust exploration in areas beyond national jurisdictions and for thicker crusts from older seamounts, current OMZs as well as past OMZ reconstructions can be used to locate the most Mn- and Co-rich bulk crusts.

4.3 Detrital sources interpreted from bulk compositions

Sourcing the detritus in FeMn crusts is best done by isolating the detrital fraction of the crust material using reductive leaches of the Fe- and Mn-oxide phases, and then

measuring element (Pb, Nd, Hf, Sr) isotopes of the detrital material (e.g. Dausmann et al., 2015). However, this process requires large amounts of sample material, chemical reagents, and time, so it is useful to understand how much detrital source information can be interpreted from the bulk chemical composition of FeMn crusts. Silicon, Al, and especially Si/Al ratios have been used as the signature elements of the detrital phase in FeMn crusts not only because they are the major components of most terrestrial detritus, such as clays, feldspars, and quartz, but also based on correlations, factor analyses, and sequential leaching studies of FeMn crusts (Hein et al., 2000). Silicon and Al consistently anticorrelate with Mn, and are grouped in factor analyses with other elements that make up detrital minerals, like K, Mg, Ca, Cr, Zn, Li, Cs, and/or Se (Hein et al., 2000; Hein and Koschinsky 2014). The other major elements found in aluminosilicate minerals, like Mg, Ca, and K, are used in ratio to Al and Si to discriminate type and source of detritus in marine particles and sediments; however, in bulk FeMn crust samples, this method can be confounded due to the fact that Mg, Ca, and K cations can sorb to the negatively charged Mn-oxide surfaces of FeMn crusts. Therefore an undetermined portion of their concentration in bulk crusts is due to sorption and only the remaining portion comprises their contribution from aluminosilicate minerals. However, in this study, K did not correlate well with Mn or Fe (R is 0.2100 and 0.0877, respectively for n=57), and normalizing K to the sum of Fe and Mn concentrations did not improve the efficacy. Thus, we have used K as a third element in conjunction with Si and Al to aid in determining the variance of detrital sources along our sample transect, although we acknowledge that the absolute

concentrations of K, and even Si and Al, can be influenced by sorption of their dissolved species onto the charged surfaces of the oxides.

A ternary plot for Si, Al, and K concentrations (K multiplied by 10 to spread out the data) for all of the samples in this study shows that the FeMn crust samples align along a linear trend coinciding with their location along the meridional transect (Figure 6). The northernmost samples (Gilbert) plot at the highest K and low Al region of the line, followed by the HBT samples; Gilbert and Tuvalu intermix next along the linear progression, and Samoa completes the line toward the highest Si and higher relative Al section of the ternary plot. Although these values cannot be directly compared with the Si, Al, and K concentrations and ratios of potential source detritus due to the dilution and sorption factors in FeMn crusts discussed, it is clear from the linear separation that the detrital sources in the crust do vary from the northern to southern ends of the sample transect. This result was corroborated by the Q-mode factor analysis in which Factor 3, interpreted to partially represent detrital flux and provenance, showed a strong correlation of factor loadings with latitude. Latitude is not an actual proxy for detrital provenance or flux; thus, further evidence that detrital sources vary along the meridional transect in this region follows.

The Si and Al absolute concentrations in crusts both decrease toward the north for all samples and within the MGT group (99% CL anticorrelations with latitude), however the Si/Al ratio increases toward the north (95% CL within the MGT transect), which indicates that although more detrital material is being delivered to the southern portion of the MGT transect, more silica-rich detritus characterizes the

crusts to the north. However, when the Si/Al ratios for the entire sample set are considered with respect to latitude, the Samoa samples have Si/Al ratios similar to those of the mid to north sectors of the MGT transect, suggesting that a silica-rich, aluminum-poor detrital source also prevails near Samoa (Supplementary Table 1). Average loess from New Zealand has the highest Si/Al value of any of the potential detrital sources to this region (4.30; Taylor, McLennan, and McCulloch, 1983) followed closely by the average loess from China (4.25; Gallet, Jahn, and Torii 1996), which could indicate that the northern and southern segments are supplied by more Si-rich wind-blown detrital material from the closest dust sources, yet 25 of the 57 FeMn crust samples have Si/Al that are still higher than the loess values. These high Si/Al ratios are likely caused by low Al concentrations, especially three samples within the HBT sample group that had Al values less than 0.01%; these may be errors in the analytical data and we will not emphasize those data here. Some samples may also be slightly enriched in Si due to the sorption of dissolved silicate to the slightly positively charged Fe-oxyhydroxide phase, although Si concentrations in the crusts do not correlate with dissolved silicate concentrations in the seawater at each sample location within the primary MGT transect (Supplementary Table 1; Garcia et al., 2014b).

The majority of the Tuvalu and Gilbert crust samples have lower Si/Al ratios that are closer to basaltic source rocks (average 3.95 and 3.67, respectively), such as average ocean island basalt (3.37; Dasgupta, Jackson, and Lee, 2010), Samoa Island basalt (3.33; Dasgupta, Jackson, and Lee, 2010), and average oceanic arc basalt (2.80;

Arculus, 1981). Several samples from the Gilbert Islands clump at the lowest end of the Si/Al spectrum (minimum 1.12), which are closest to tholeiitic basalts from seamounts of the Tonga-Kermadec Arc (2.09; Brothers et al., 1980), however this detrital source is unlikely due to the large distance between the Gilbert Islands and the Tonga-Kermadec Arc. The low Si/Al ratios seen in the Gilbert chain occur within the EUZ, which suggest that perhaps higher Al is being delivered to crusts here due to biological particle flux to the deep ocean as observed by (Murray & Leinen, 1996). Conversely, the adjacent HBT samples are also situated within the EUZ and have the highest Si/Al ratios. The high Si/Al ratios in the HBT samples are supported by the 95% CL correlation of excess silica (Si_{ex}) for each crust sample in the EUZ (Supplementary Table 1; calculated based on the Si/Al ratio for average ocean island basalt; 3.37; Dasgupta, Jackson, and Lee 2010) with corresponding surface chlorophyll-a values (R = 0.8113, n=10; Supplementary Figure 1). Increased biogenic silica input to FeMn crusts within the EUZ, especially for the HBT samples where surface productivity is the highest for the entire dataset (Figure 1), may explain the Si_{ex} beyond the proposed detrital inputs. These data demonstrate that bulk major element concentrations in crusts along these transects have complex local distributions that make it difficult to constrain specific detrital sources.

5. Summary and Conclusions

The uppermost layers (<15 mm) of 57 FeMn crusts along a linear chain of seamounts in the western equatorial Pacific, from 14°N to 14°S, show a wide

variation in the concentrations of 23 major and trace elements, and the majority of the compositional variation can be attributed to several key modern oceanographic and geographic characteristics in the region. Oxygen concentrations throughout the water column control variations in FeMn crust composition with both latitude and water depth. Meridional changes in oxygen concentration are predominantly due to the presence of a stronger OMZ in the northern subtropical portion of the sample area, while depth controls are caused by the stratified, increasing oxygen concentrations with depth. The oxygen concentration of seawater has the strongest influence on Mn concentration in FeMn crusts. Mn concentrations anticorrelate with dissolved oxygen at the 99% CL at each sample location. Q-mode factor analysis of samples along the main MGT transect produced an oxygen-related factor with a high factor score for Mn; both of these quantitative statistics linking Mn content in FeMn crusts to seawater oxygen concentration are presented here for the first time. Elements known to associate with the Mn-oxide phase of FeMn crusts, like Co, Ni, Mo, and Zn, all exhibit similar geographic-oceanographic correlations as Mn. However, Co, Ni, and Zn are not as sensitive to oxygen concentrations as Mn, and they have significant anticorrelations with water depth that are attributable to increasing growth rates with water depth, which Mn does not.

The iron content of FeMn crusts in this study increases with water depth, which has been attributed to the following factors in previous works: decreasing Mn concentrations in the crust with increasing oxygen concentrations in seawater at depth, increased dissolved Fe concentrations in seawater with depth due to the

dissolution of carbonate particles, deep hydrothermal sources, release from sediments, and increases in Fe-bearing aluminosilicate detritus. Q-mode factor analysis in this study show a factor with a high Fe factor score for which dissolved carbonate ion concentrations at each sample location correlate at the 95% CL with factor loadings. This result offers the first quantitative statistic to support the hypothesis that an increase in carbonate ion concentration with increasing water depth from younger water masses or biogenic carbonate dissolution can increase the Fe content of FeMn crusts with increasing water depth. We attribute this mainly to increased pH with increased carbonate ion concentration. However, we acknowledge that deep Fe sources as well as decreasing Mn precipitation also contribute to this increase in Fe with water depth. Copper, and in some cases Ti, have higher concentrations when Fe concentration is higher, as expected, due to their preferential enrichment in the Fe-oxyhydroxide phase of FeMn crusts. Lead, on the other hand, can be enriched in the iron phase, but instead has the same geographic-oceanographic correlations as Mn. The variance in Pb content in FeMn crusts in this region may be attributed to local fluctuations in seawater concentrations, which is a unique characteristic among the trace elements reported here.

The higher surface productivity seen within the EUZ (~5°N to ~5°S) is another meridional control on FeMn crust composition in this region, causing elevated Fe and Ba concentrations in crusts due to their association with efficient biogenic particle flux, which transports elevated Fe and Ba to depth where it can be incorporated into FeMn crusts. Magnesium is also more concentrated in FeMn crusts within the EUZ

region, and the cause of its enrichment is also likely the result of higher flux of Mg-rich carbonate and opal particles as marine snow.

Silicon and Al concentrations in crusts both decrease significantly with latitude and increase with oxygen concentrations in seawater, showing unequal entrainment of detrital material along the seamount chains as well as increased detritus in crusts with water depth, likely the result of weathering and mass movement of debris down the flanks of seamounts. The bulk concentrations of Si, Al, and K, in the crusts were not sufficient to directly compare with those of source regions to deduce provenance of detritus in the crusts, due to the additional sorption of each, especially K, onto the surfaces of the Fe- and Mn-oxides. Excess Si is correlates with chlorophyll-a concentrations within the EUZ, demonstrating that Si enrichment in crusts due to biogenic input can also influence Si/Al ratios for crusts in this region, especially in the HBT transect where productivity is highest. However, Si/Al ratios as well as a ternary plot of Si, Al, and K reveal a meridional variation, which can be interpreted as different detrital sources dominating in different regions along the seamount chain from north to south. The northernmost (Marshall and Gilbert Islands) and southernmost (Samoa) portions of the chain receive detritus that is more Si-rich relative to Al, which is a signature of aeolian sources that are likely supplied from China in the north and from New Zealand or Australia in the south. The central part of the sample region has lower Si/Al ratios that can be attributed to increased locally-supplied detritus from the many basaltic islands nearby. However, more definitive and detailed results as to provenances for the detrital fraction of crusts would require

separating the detritus and analyzing it for isotopic compositions of Pb, Nd, Sr, and Hf.

Zonal variations in FeMn crust composition are minimal, and the majority of the element correlations with longitude are also caused by changes in oxygen concentration. Overall, this study confirms that FeMn crusts are highly heterogeneous in composition in the region studied and demonstrates with novel statistical significance that the oxygen concentration in seawater, carbonate ion concentration and sources of dissolved Fe in the deep ocean, the productivity of overlying surface waters, and detrital sources and contents of crusts exhibit the predominant controls on their chemical composition. Modern measurements, as well as paleo reconstructions, of these five oceanographic and geographic properties should be used to quantitatively define the permissive regions for FeMn crust exploration and to establish which regions contain crusts of potential economic value.

6. Acknowledgements, Samples, and Data

The oceanographic research cruises during which samples were collected for this study were funding by the following research grants: NSF grant #1154070 (cruise RR1310), OCE-9730394 (cruise AVON02), and OCE-0351437 (cruise KM0506); Cruise L9-84-CP was funded by the U.S. Geological Survey. We thank Scripps Institute of Oceanography and the Marine and Geology Repository, College of Earth, Ocean, and Atmospheric Sciences, Oregon State University for providing rock samples. We thank Dr. Adina Paytan, Dr. Christina Ravelo, Dr. Jong-Mi Li, and

Yang Xiang for valuable discussions regarding the oceanographic component of this study. We thank USGS Marine Minerals Lab technicians for past sample processing. We thank Thomas Lorenson for the internal USGS review. The geochemical dataset used in this paper is currently being archived in the USGS data repository, ScienceBase.gov. This chapter has been submitted to the scientific journal Geochemistry, Geophysics, Geosystems for publication, but was not accepted for publication at the time this thesis was submitted. That version of this manuscript includes the authors, James R. Hein (thesis advisor and provided scientific input), Phoebe J. Lam (thesis advisor and provided scientific input), Anthony A.P. Koppers (provided samples and organizational input), and Hubert Staudigel (provided samples and organization input).

7. References

Arculus, R. J. (1981). Island arc magmatism in relation to the evolution of the crust and the mantle. *Tectonophysics*, *75*, 113–133.

Azami, K., Hirano, N., Machida, S., Yasukawa, K., & Kato, Y. (2018). Rare earth elements and yttrium (REY) variability with water depth in hydrogenetic ferromanganese crusts. *Chemical Geology*, *493*, 224–233. https://doi.org/10.1016/J.CHEMGEO.2018.05.045

Bostock, H. C., Opdyke, B. N., & Williams, M. J. M. (2010). Characterising the intermediate depth waters of the Pacific Ocean using δ 13 C and other geochemical tracers. *Deep-Sea Research Part I: Oceanographic Research Papers*, *57*(7), 847–859. https://doi.org/10.1016/j.dsr.2010.04.005

Brothers, R. N., Heming, R. F., Hawke, M. M., & Davey, F. J. (1980). Tholeiitic basalt from the Monowai seamount, Tonga-Kermadec ridge (note). *New Zealand Journal of Geology and Geophysics*, *23*(4), 537–539. https://doi.org/10.1080/00288306.1980.10424125

Bruland, K. (1983). Trace elements in seawater. In J. P. Riley & R. Chester (Eds.), *Chemical Oceanography* (2nd Editio, pp. 147–220). London: Academic.

Byrne, R. H. (2002). Inorganic speciation of dissolved elements in seawater: The influence of pH on concentration ratios. *Geochemical Transactions*, *3*(1), 11–16. https://doi.org/10.1039/b109732f

Chow, T. J., & Goldberg, E. D. (1960). On the marine geochemistry of barium. *Geochimica Et Cosmochimica Acta*, *20*, 192–198.

Christensen, J. N., Halliday, A. N., Godfrey, L. V., Hein, J. R., & Rea, D. K. (1997). Climate and ocean dynamics and the lead isotopic records in pacific ferromanganese crusts. *Science*, *277*(5328), 913–918. https://doi.org/10.1126/science.277.5328.913

Conrad, T., Hein, J. R., Paytan, A., & Clague, D. A. (2017). Formation of Fe-Mn crusts within a continental margin environment. *Ore Geology Reviews*, *87*, 25–40. https://doi.org/10.1016/j.oregeorev.2016.09.010

Cronan, D. S. (1984). Criteria for the recognition of areas of potentially economic manganese nodules and encrustations in the CCOP/SOPAC region of the central and southwestern tropical Pacific. *South Pacific Marine Geological Notes, CCOP/SOPAC*, *3*(1).

Cutter, G. A., & Cutter, L. S. (2006). Biogeochemistry of arsenic and antimony in the North Pacific Ocean. *Geochemistry, Geophysics, Geosystems*, *7*(5). https://doi.org/10.1029/2005GC001159

Dasgupta, R., Jackson, M. G., & Lee, C. T. A. (2010). Major element chemistry of ocean island basalts - Conditions of mantle melting and heterogeneity of mantle source. *Earth and Planetary Science Letters*, *289*(3–4), 377–392. https://doi.org/10.1016/j.epsl.2009.11.027

Dausmann, V., Frank, M., Siebert, C., Christl, M., & Hein, J. R. (2015). The evolution of climatically driven weathering inputs into the western Arctic Ocean since the late Miocene: Radiogenic isotope evidence. *Earth and Planetary Science Letters*, *419*, 111–124. https://doi.org/10.1016/j.epsl.2015.03.007

De Carlo, E. H., Mcmurtry, G. M., & Kim, K. H. (1987). Geochemistry of ferromanganese crusts from the Hawaiian Archipelago I. Northern survey areas. *Deep-Sea Re.~earch*, *3487*(3), 441–467. Retrieved from https://ac.els-cdn.com/0198014987901476/1-s2.0-0198014987901476-main.pdf?_tid=937371d9-4f3f-4f78-9d3d-bf6c0b91ca54&acdnat=1529346943_410c4f6db45753bdbf520794934a98f0

Donnelly, T. W., & Merrill, L. (1977). tendency of opal to adsorb Mg more readily than Na and both of these more than K . Although a hiatus in sedimentation is inferred to be an important requirement for this process , a simple application of diffusion calculations suggests that this process i, *19*, 167–186.

Dymond, J., Suess, E., & Lyle, M. (1992). Barium in Deep-Sea Sediment: A Geochemical Proxy for Paleoproductivity. *Paleoceanography*, *7*(2), 163–181. https://doi.org/10.1029/92PA00181

Estrada, M., Delgado, M., Blasco, D., Latasa, M., Cabello, A. M., Benítez-Barrios, V., … Vidal, M. (2016). Phytoplankton across tropical and subtropical regions of the Atlantic, Indian and Pacific oceans. *PLoS ONE*, *11*(3), 1–29. https://doi.org/10.1371/journal.pone.0151699

Filippelli, G. M., & Delaney, M. L. (1996). Phosphorus geochemistry of equatorial Pacific sediments. *Geochimica et Cosmochimica Acta*, *60*(9), 1479–1495. https://doi.org/10.1016/0016-7037(96)00042-7

Finlayson, V. A., Konter, J. G., Konrad, K., Koppers, A. A. P., Jackson, M. G., & Rooney, T. O. (2018). Sr–Pb–Nd–Hf isotopes and 40Ar/39Ar ages reveal a Hawaii–Emperor-style bend in the Rurutu hotspot. *Earth and Planetary Science Letters*, *500*, 168–179. https://doi.org/10.1016/j.epsl.2018.08.020

Flegal, A. R., & Patterson, C. C. (1983). Vertical concentration profiles of lead in the Central Pacific at 15°N and 20°S. *Earth and Planetary Science Letters*, *64*(1), 19–32. https://doi.org/10.1016/0012-821X(83)90049-3

Foster, A. L., Brown Jr., G. E., & Parks, G. A. (2003). X-ray absorption fine structure study of As(V) and Se(IV) sorption complexes on hydrous Mn oxides. *Geochimica et Cosmochimica Acta*, *67*(11), 1937–1953. https://doi.org/10.1016/S0016-7037(02)01301-7

Gall, L., Williams, H. M., Siebert, C., Halliday, A. N., Herrington, R. J., & Hein, J. R. (2013). Nickel isotopic compositions of ferromanganese crusts and the constancy of deep ocean inputs and continental weathering effects over the Cenozoic. *Earth and Planetary Science Letters*, *375*, 148–155. https://doi.org/10.1016/J.EPSL.2013.05.019

Gallet, S., Jahn, B. M., & Torii, M. (1996). Geochemical characterization of the Luochuan loess-paleosol sequence, China, and paleoclimatic implications. *Chemical Geology*, *133*(1–4), 67–88. https://doi.org/10.1016/S0009-2541(96)00070-8

Garcia, H. E., Locarnini, R. A., Boyer, T. P., Antonov, J. I., Baranova, O. K., Zweng, M. M., … Johnson, D. R. (2014a). *World Ocean Atlas 2013, Volume 3: Dissolved Oxygen, Apparent Oxygen Utilization, and Oxygen Saturation*. (S. (Ed. . Levitus & A. (Technical E. . Mishonov, Eds.). NOAA Atlas NESDIS 75.

Garcia, H. E., Locarnini, R. A., Boyer, T. P., Antonov, J. I., Baranova, O. K., Zweng, M. M., … Johnson, D. R. (2014b). *World Ocean Atlas 2013, Volume 4: Dissolved Inorganic Nutrients (phosphate, nitrate, silicate)*. (S. (Ed. . Levitus & A. (Technical E. . Mishonov, Eds.). NOAA Atlas NESDIS 76.

Halbach, P., & Puteanus, D. (1984). The influence of the carbonate dissolution rate on the growth and composition of Co-rich ferromanganese crusts from Central Pacific seamount areas. *Earth and Planetary Science Letters*, *68*(1), 73–87. https://doi.org/10.1016/0012-821X(84)90141-9

Hawco, N. J., Lam, P. J., Lee, J. M., Ohnemus, D. C., Noble, A. E., Wyatt, N. J., … Saito, M. A. (2018). Cobalt scavenging in the mesopelagic ocean and its influence on global mass balance: Synthesizing water column and sedimentary fluxes. *Marine Chemistry*. https://doi.org/10.1016/j.marchem.2017.09.001

Hein, J. R., & Koschinsky, A. (2014). *Deep-Ocean Ferromanganese Crusts and Nodules*. *Treatise on Geochemistry: Second Edition* (2nd ed., Vol. 13). Published by Elsevier Inc. https://doi.org/10.1016/B978-0-08-095975-7.01111-6

Hein, James R., Conrad, T., Mizell, K., Banakar, V. K., Frey, F. A., & Sager, W. W. (2016). Controls on ferromanganese crust composition and reconnaissance resource potential, Ninetyeast Ridge, Indian Ocean. *Deep Sea Research Part I: Oceanographic Research Papers*, *110*, 1–19. https://doi.org/10.1016/J.DSR.2015.11.006

Hein, James R., Koschinsky, A., Bau, M., Manheim, F. T., Kang, J.-K., & Roberts, L. (2000). Cobalt-Rich Ferromanganese Crusts in the Pacific. In *Handbook of Marine Mineral Deposits* (Vol. 17, pp. 239–279).

Hein, James R., Koschinsky, A., & Halliday, A. N. (2003). Global occurrence of tellurium-rich ferromanganese crusts and a model for the enrichment of tellurium. *Geochimica et Cosmochimica Acta*, *67*(6), 1117–1127. https://doi.org/10.1016/S0016-7037(00)01279-6

Hein, James R, Koschinsky, A., Halbach, P., Manheim, F. T., Bau, M., Kang, J.-K., & Lubick, N. (1997). Iron and manganese oxide mineralization in the Pacific. *Geological Society, London, Special Publications*, *119*(1), 123 LP – 138. https://doi.org/10.1144/GSL.SP.1997.119.01.09

Hem, J. D. (1978). Redox processes at surfaces of manganese oxide and their effects on aqueous metal ions. *Chemical Geology*, *21*, 199–218.

Hodkinson, R. A., & Cronan, D. S. (1991). Regional and depth variability in the composition of cobalt-rich ferromanganese crusts from the SOPAC area and adjacent parts of the central equatorial Pacific. *Marine Geology*, *98*(2–4), 437–447. https://doi.org/10.1016/0025-3227(91)90115-K

Hyeong, K., Park, S. H., Yoo, C. M., & Kim, K. H. (2005). Mineralogical and geochemical compositions of the eolian dust from the northeast equatorial Pacific and their implications on paleolocation of the Intertropical Convergence Zone. *Paleoceanography*, *20*(1), 1–11. https://doi.org/10.1029/2004PA001053

Jackson, M. G., Hart, S. R., Konter, J. G., Koppers, A. A. P., Staudigel, H., Kurz, M. D., … Sinton, J. M. (2010). Samoan hot spot track on a "hot spot highway": Implications for mantle plumes and a deep Samoan mantle source. *Geochemistry, Geophysics, Geosystems*, *11*(12). https://doi.org/10.1029/2010GC003232

Kashiwabara, T., Mitsunobu, S., Das, A., Itai, T., Tanimizu, M., & Takahashi, Y. (2008). Oxidation States of Antimony and Arsenic in Marine Ferromanganese Oxides Related to Their Fractionation in Oxic Marine Environment. *Chemistry Letters*, *37*(7), 756–757. https://doi.org/10.1246/cl.2008.756

Kashiwabara, T., Takahashi, Y., Tanimizu, M., & Usui, A. (2011). Molecular-scale mechanisms of distribution and isotopic fractionation of molybdenum between seawater and ferromanganese oxides. *Geochimica et Cosmochimica Acta*, *75*(19), 5762–5784. https://doi.org/10.1016/j.gca.2011.07.022

Key, R.M., Kozyr, A., Sabine, C. L., Lee, K., Wanninkhof, R., Bullister, J., … Pen, T.-H. (2004). A global ocean carbon climatology: Results from GLODAP. *Global Biogeochemical Cycles*, *18*(GB4031).

Kiko, R., A. Biastoch, P. Brandt, S. Cravatte, H. Hauss, R. Hummels, I. Kriest, F. Marin, A. M. P. McDonnell, A. Oschlies, M. Picheral, F. U. Schwarzkopf, A. M. Thurnherr, and L. Stemmann. (2017). Biological and physical influences on marine snowfall at the equator. *Nature Geoscience, 10,* 852–858.

King, W. D. (1998). Role of carbonate speciation on the oxidation rate of Fe(II) in aquatic systems. *Environmental Science Technology*, *32*, 2997-3003.

Klemm, V., Levasseur, S., Frank, M., Hein, J. R., & Halliday, A. N. (2005). Osmium isotope stratigraphy of a marine ferromanganese crust. *Earth and Planetary Science Letters*, *238*(1–2), 42–48. https://doi.org/10.1016/j.epsl.2005.07.016

Klemm, V., Reynolds, B., Frank, M., Pettke, T., & Halliday, A. N. (2007). Cenozoic changes in atmospheric lead recorded in central Pacific ferromanganese crusts. *Earth and Planetary Science Letters*, *253*(1–2), 57–66. https://doi.org/10.1016/j.epsl.2006.10.018

Klovan, J. E., & Imbrie, J. (1971). An algorithm and Fortran-iv program for large-scale Q-mode factor analysis and calculation of factor scores. *Journal of the International Association for Mathematical Geology*, *3*(1), 61–77. https://doi.org/10.1007/BF02047433

Koschinsky, A., & Halbach, P. (1995). Sequential leaching of marine ferromanganese precipitates: Genetic implications. *Geochimica et Cosmochimica Acta*, *59*(24), 5113–5132. https://doi.org/10.1016/0016-7037(95)00358-4

Koschinsky, A., & Hein, J. R. (2003). Uptake of elements from seawater by ferromanganese crusts: Solid-phase associations and seawater speciation. *Marine Geology*, *198*(3–4), 331–351. https://doi.org/10.1016/S0025-3227(03)00122-1

Manceau, A., Drits, V. A., Silvester, E., Bartoli, C., & Lanson, B. (1997). Structural mechanism of Co2+ oxidation by the phyllomanganate buserite. *American Mineralogist*, *82*(11–12), 1150–1175. https://doi.org/10.2138/am-1997-11-1213

Manheim, F. T., & Lane-Bostwick, C. M. (1988). Cobalt in ferromanganese crusts as

a monitor of hydrothermal discharge on the Pacific sea floor. *Nature 1988 335:6185*, *335*(6185), 59. https://doi.org/10.1038/335059a0

Menard, H. W. (1969). Elevation and subsidence of oceanic crust. *Earth and Planetary Science Letters*, *6*(4), 275–284. https://doi.org/10.1016/0012-821X(69)90168-X

Murray, R. W., & Leinen, M. (1996). Scavenged excess aluminum and its relationship to bulk titanium in biogenic sediment from the central equatorial Pacific Ocean. *Geochimica et Cosmochimica Acta*, *60*(20), 3869–3878. https://doi.org/10.1016/0016-7037(96)00236-0

NASA Goddard Space Flight Center, Ocean Ecology Laboratory, Ocean Biology Processing Group. Moderate-resolution Imaging Spectroradiometer (MODIS) Aqua, Level 3, 4km mission composite, default chlorophyll algorithm data; NASA OB. DAAC, Greenbelt, MD, USA. Accessed on 04/16/2019.

Nielsen, S. G., Mar-Gerrison, S., Gannoun, A., LaRowe, D., Klemm, V., Halliday, A. N., … Hein, J. R. (2009). Thallium isotope evidence for a permanent increase in marine organic carbon export in the early Eocene. *Earth and Planetary Science Letters*, *278*(3–4), 297–307. https://doi.org/10.1016/j.epsl.2008.12.010

Nishioka, J., Obata, H., & Tsumune, D. (2013). Evidence of an extensive spread of hydrothermal dissolved iron in the Indian Ocean. *Earth and Planetary Science Letters*, *361*, 26–33. Retrieved from https://doi.org/10.1016/j.epsl.2012.11.040

Pälike, H., Lyle, M. W., Nishi, H., Raffi, I., Ridgwell, A., Gamage, K., … Zeebe, R. E. (2012). A Cenozoic record of the equatorial Pacific carbonate compensation depth. *Nature*, *488*(7413), 609–614. https://doi.org/10.1038/nature11360

Palmer, M. R. (1985). Rare earth elements in foraminifera tests. *Earth and Planetary Science Letters*, *73*(2–4), 285–298. https://doi.org/10.1016/0012-821X(85)90077-9

Paytan, A., & Kastner, M. (1996). Benthic Ba fluxes in the central Equatorial Pacific, implications for the oceanic Ba cycle. *Earth and Planetary Science Letters*, *142*, 439–450. https://doi.org/10.1016/0012-821X(96)00120-3

Pisias, N. G., Murray, R. W., & Scudder, R. P. (2013). Multivariate statistical analysis and partitioning of sedimentary geochemical data sets: General principles and specific MATLAB scripts. *Geochemistry, Geophysics, Geosystems*, *14*(10), 4015–4020. https://doi.org/10.1002/ggge.20247

Schlitzer, R., Ocean Data View, odv.awi.de, 2018.

Slemons, L. O., Murray, J. W., Resing, J., Paul, B., and Dutrieux, P. (2010). Western Pacific coastal sources of iron, manganese, and aluminum to the Equatorial Undercurrent. *Global Biogeochem. Cycles*, *24*(GB3024). 1-16. doi:10.1029/2009GB003693.

Smith, C. R., Berelson, W., Demaster, D. J., Dobbs, F. C., Hammond, D., Hoover, D. J., … Stephens, M. (1997). Latitudinal variations in benthic processes in the abyssal equatorial Pacific: Control by biogenic particle flux. *Deep-Sea Research Part II: Topical Studies in Oceanography*. https://doi.org/10.1016/S0967-0645(97)00022-2

Takahashi, Y., Manceau, A., Geoffroy, N., Marcus, M. A., & Usui, A. (2007). Chemical and structural control of the partitioning of Co, Ce, and Pb in marine ferromanganese oxides. *Geochimica et Cosmochimica Acta*, *71*(4), 984–1008. https://doi.org/10.1016/j.gca.2006.11.016

Taylor, S. R., McLennan, S. M., & McCulloch, M. T. (1983). Geochemistry of loess, continental crustal composition and crustal model ages. *Geochimica et Cosmochimica Acta*, *47*(11), 1897–1905. https://doi.org/10.1016/0016-7037(83)90206-5

Twining, B. S., & Baines, S. B. (2013). The Trace Metal Composition of Marine Phytoplankton. *Annual Review of Marine Science*, *5*(1), 191–215. https://doi.org/10.1146/annurev-marine-121211-172322

Twining, B. S., Nodder, S. D., King, A. L., Hutchins, D. A., LeCleir, G. R., DeBruyn, J. M., Maas, E. W., Vogt, ., Wilhelm, S. W., & Boyd, P. W. (2014). Differential remineralization of major and trace elements in sinking diatoms. *Limnology and Oceanography*, *59*(3), 689-704. doi: 10.4319/lo.2014.59.3.0689.

Usui, A., Nishi, K., Sato, H., Nakasato, Y., Thornton, B., Kashiwabara, T., … Urabe, T. (2017). Continuous growth of hydrogenetic ferromanganese crusts since 17 Myr ago on Takuyo-Daigo Seamount, NW Pacific, at water depths of 800–5500 m. *Ore Geology Reviews*, *87*, 71–87. https://doi.org/10.1016/J.OREGEOREV.2016.09.032

van de Flierdt, T., Frank, M., Lee, D. C., Halliday, A. N., Reynolds, B. C., & Hein, J. R. (2004). New constraints on the sources and behavior of neodymium and hafnium in seawater from Pacific Ocean ferromanganese crusts. *Geochimica et Cosmochimica Acta*, *68*(19), 3827–3843. https://doi.org/10.1016/j.gca.2004.03.009

Van Hinsbergen, D. J. J., De Groot, L. V., Van Schaik, S. J., Spakman, W., Bijl, P. K., Sluijs, A., … Brinkhuis, H. (2015). A paleolatitude calculator for paleoclimate studies. *PLoS ONE*, *10*(6), 1–21. https://doi.org/10.1371/journal.pone.0126946

Zheng, L., Minami, T., Konagaya, W., Chan, C. Y., Tsujisaka, M., Takano, S., … Sohrin, Y. (2019). Distinct basin-scale-distributions of aluminum, manganese, cobalt, and lead in the North Pacific Ocean. *Geochimica et Cosmochimica Acta*, *254*, 102–121. https://doi.org/10.1016/j.gca.2019.03.038

Zhou, L., & Kyte, F. T. (1992). Sedimentation history of the south Pacific pelagic clay province over the last 85 million years inferred from the geochemistry of Deep Sea Drilling Project Hole 596. *Palaeogeography*, *7*(4), 441–465.

Table 1. Information for the four research expeditions from which samples were compiled for this study

Cruise ID	Year	Vessel	Island Region
L9-84-CP	1984	S.P. LEE	Marshall
AVON2	1999	Melville	Gilbert, Howland, Baker, Tokelau
RR1310	2013	Roger Revelle	Tuvalu and Samoa
KM0506	2005	Kilo Moana	Samoa

Table 2. Statistics for FeMn crust chemistry (n=57)

	Mean	Standard Deviation	Relative Standard Deviation	Max	Min	Range
Fe (wt. %)	24	5.2	22%	36	15	21
Mn	22	5.8	26%	33	12	21
Si	4.7	1.5	32%	8.8	1.9	6.9
Al	1.1	0.60	52%	2.9	0.01	2.9
Mg	1.2	0.19	15%	1.7	0.93	0.79
Ca	2.8	0.51	18%	4.3	1.5	2.8
Na	1.5	0.40	27%	2.2	0.38	1.8
K	0.5	0.13	27%	0.89	0.29	0.60
Ti	1.2	0.35	28%	2.2	0.79	1.4
P	0.5	0.09	17%	0.81	0.30	0.51
As (ppm)	266	50	19%	408	144	264
Ba	1760	659	37%	3707	1074	2633
Cd	4.0	0.85	21%	6.2	2.5	3.7
Co	5172	3540	68%	18879	1405	17474
Cr	17	17	101%	108	0.75	107
Cu	930	584	63%	3775	286	3489
Mo	427	143	33%	780	148	632
Ni	3305	1268	38%	6520	734	5786
Pb	1198	373	31%	2142	728	1414
Sr	1620	182	11%	2258	1230	1028
V	717	104	14%	1118	483	635
Zn	639	77	12%	841	503	339
Y	197	25	13%	234	103	131
Fe/Mn (ratio)	1.1	0.34	30%	2.1	0.47	1.7
Si/Al	36	136	378%	710	1.1	709
K/Al	4.8	19	389%	96	0.17	96

Table 3. Tabulated results from correlation coefficient matrices generated for each of the sample groups [1]

Latitude Correlations									
All Samples n = 57		MGT n = 33		Samoa n = 15		HBT n = 9		MGT within HBT n = 15	
(+)	(-)	(+)	(-)	(+)	(-)	(+)	(-)	(+)	(-)
Pb	**Fe/Mn**	**Pb**	**Fe/Mn**	**Ca**	*Cr*	**Ba**	*Co*	**Ba**	
Co	**Si**	**Na**	**Al**			*Mo*		**Mn**	
Ni	**Al**	**Co**	**Si**					**P**	
Mn		**Mn**	*Cu*					**Ca**	
Na		**Ni**	*Fe*					**Fe**	
Mo		**Zn**						**Mg**	
As		**As**						*Na*	
Cd		**Mo**						*V*	
Mg		*Si/Al*							
Zn									
K									
Longitude Correlations									
All Samples n = 57		MGT n = 33		Samoa n = 15		HBT n = 9		MGT within HBT n = 15	
(+)	(-)	(+)	(-)	(+)	(-)	(+)	(-)	(+)	(-)
Fe/Mn	**Pb**	**Fe/Mn**	**Pb**	**Cr**	*Cu*	*Sr*	*Ba*		*V*
Fe	**Ni**	**Si**	**Co**				*Mo*		*Ba*
Si	**Co**	**Al**	**Na**						
Ti	**Mn**	*Fe*	**Mn**						
Y	**Mo**	*Cu*	**Ni**						
	Cd		**Zn**						
	Na		**As**						
			Mo						
			Si/Al						
Water Depth Correlations									
All Samples n = 57		MGT n = 33		Samoa n = 15		HBT n = 9		MGT within HBT n = 15	
(+)	(-)	(+)	(-)	(+)	(-)	(+)	(-)	(+)	(-)
Fe	**Pb**	**Cu**	**Pb**	*Fe*	**Ca**	**Ba**	**Ca**		*Cd*
Ba	**Co**	*Fe*	**Co**		**V**		**Cd**		*Pb*
Ti	**Ni**	*Fe/Mn*	**Zn**		**Sr**		*Ni*		*P*
Fe/Mn	**Zn**	*Si*	**Ni**		*Ni*		*Co*		
Cu		*Ti*	**As**		*P*		*Sr*		
Si			*P*		*Pb*		*Mg*		
Oxygen Correlations									
All Samples n = 57		MGT n = 33		Samoa n = 15		HBT n = 9		MGT within HBT n = 15	
(+)	(-)	(+)	(-)	(+)	(-)	(+)	(-)	(+)	(-)
Fe/Mn	**Pb**	**Fe/Mn**	**Pb**	*Fe/Mn*	**Sr**	*Ba*	**Cd**		*P*
Fe	**Co**	**Cu**	**Co**	*Ti*	*Ni*		*Ca*		*Cd*
Si	**Ni**	**Si**	**Zn**		*As*		*Mg*		*Pb*
Ti	**Zn**	*Fe*	**Ni**		*Ca*				
Cu	**Na**	*Al*	**Na**		*Mo*				
	Mn		**Mn**		*P*				
	Cd		**As**		*Mn*				
	As		*Cd*		*Ni*				
	Mo								

Table 3. Continued

Latitude Correlations							
N. of Equator n = 12		S. of Equator n = 45		N. of Equator (MGT) n = 10		S. of Equator (MGT) n = 23	
(+)	(-)	(+)	(-)	(+)	(-)	(+)	(-)
Pb	**Mg**	**Mn**	**Fe/Mn**	**Pb**	**Ba**	**Ba**	*Fe/Mn*
Na	**Fe**	**Mg**	**Zn**	**Na**	**Mg**	**Mn**	
Co	**Ba**	**Ba**		*Si/Al*	**Al**	**Mg**	
Ni	**Fe/Mn**	**Mo**		*As*	**Fe**	**Na**	
Si/Al	**Al**	**Cd**			*Fe/Mn*	**Ti**	
		Co			*Cr*	**Fe**	
		Ni				*V*	
		Fe				*Co*	
		Ca				*Mo*	
		Na				*P*	
		K				*Cd*	
		P				*Pb*	
		Cu					
		Pb					
		Sr					
Longitude Correlations							
N. of Equator n = 12		S. of Equator n = 45		N. of Equator (MGT) n = 10		S. of Equator (MGT) n = 23	
(+)	(-)	(+)	(-)	(+)	(-)	(+)	(-)
Fe	**Pb**	**Fe/Mn**	**Ni**	**Mg**	**Pb**	*Fe/Mn*	**Ba**
Ba	*Co*	**Y**	**Cu**	**Ba**	**Na**		**Mn**
Mg	*Ni*	**Zn**	**Co**	*Al*	*Si/Al*		**Cd**
Fe/Mn	*Na*		*Al*	*Fe*	*As*		*V*
			Mo				*Pb*
							Co
							Mg
							Na
							Mo
Water Depth Correlations							
N. of Equator n = 12		S. of Equator n = 45		N. of Equator (MGT) n = 10		S. of Equator (MGT) n = 23	
(+)	(-)	(+)	(-)	(+)	(-)	(+)	(-)
Fe	**Pb**	*Ti*	*P*	*Ba*	**Pb**		*P*
Ba	**Na**			*Fe*	*Na*		
Mg	**Co**						
Fe/Mn	*Ni*						
Cu							
Oxygen Correlations							
N. of Equator n = 12		S. of Equator n = 45		N. of Equator (MGT) n = 10		S. of Equator (MGT) n = 23	
(+)	(-)	(+)	(-)	(+)	(-)	(+)	(-)
Fe	**Pb**		**Cd**	*Ba*	**Pb**		*P*
Ba	**Na**		**P**	*Fe*	*Na*		*Cd*
Mg	*Co*		*Co*				
Fe/Mn	*Ni*		*Ca*				
Cu			*Ni*				
			Pb				

[1] Correlations at the 99% Confidence Level are in bold and correlations at the 95% Confidence Level are in italics; elements are listed from strongest to weakest correlation (highest to lowest absolute value)

Table 4. Rotated VARIMAX factor scores for elements included in the Q-mode factor analysis of samples within the MGT transect [1]

Factor 1		Factor 2		Factor 3		Factor 4	
34.9%		19.2%		29.5%		10.3%	
Pb	0.4076	K	0.4024	Y	0.4680	Ba	0.5349
Ni	0.4063	Si	0.3865	Ca	0.3694	Fe	0.3473
Co	0.3204	Al	0.3271	Si	0.3517	Mg	0.3355
Zn	0.3108	Ti	0.3155	Al	0.3172	Ti	0.2779
Mn	0.3071	Na	0.2921	V	0.2748	Mn	0.2600
Na	0.2771	Ba	0.2804	As	0.2568	V	0.1942
Mo	0.2471	Zn	0.2530	P	0.2243	Sr	0.1796
Cd	0.2354	Cu	0.2487	Sr	0.2224	Mo	0.1775
As	0.2033	Mg	0.2178	Fe	0.2187	P	0.1511
Y	0.1653	Fe	0.1617	Mo	0.0902	Y	0.1081
V	0.1275	Cr	0.1595	Cu	0.0834	As	0.0612
Sr	0.1189	Ni	0.1344	Cd	0.0706	Cd	0.0283
K	0.0721	Cd	0.0513	Cr	0.0375	Na	0.0244
Ca	0.0647	Mn	0.0102	Na	0.0255	Cu	-0.0002
P	0.0465	Ca	0.0078	K	-0.0022	Ca	-0.0029
Ti	0.0359	Co	-0.0008	Zn	-0.0443	Pb	-0.0112
Mg	0.0172	Pb	-0.0270	Pb	-0.0708	Cr	-0.0447
Cr	0.0025	P	-0.0402	Mn	-0.0826	Co	-0.0725
Cu	-0.0636	Sr	-0.0992	Co	-0.1036	Al	-0.1457
Ba	-0.0839	V	-0.1050	Mg	-0.1263	K	-0.1519
Si	-0.1252	Mo	-0.1240	Ni	-0.1269	Ni	-0.1707
Al	-0.1351	Y	-0.1295	Ti	-0.1397	Si	-0.2296
Fe	-0.1574	As	-0.1308	Ba	-0.1812	Zn	-0.2474

[1] Scores and associated elements are listed from highest to lowest score for each factor

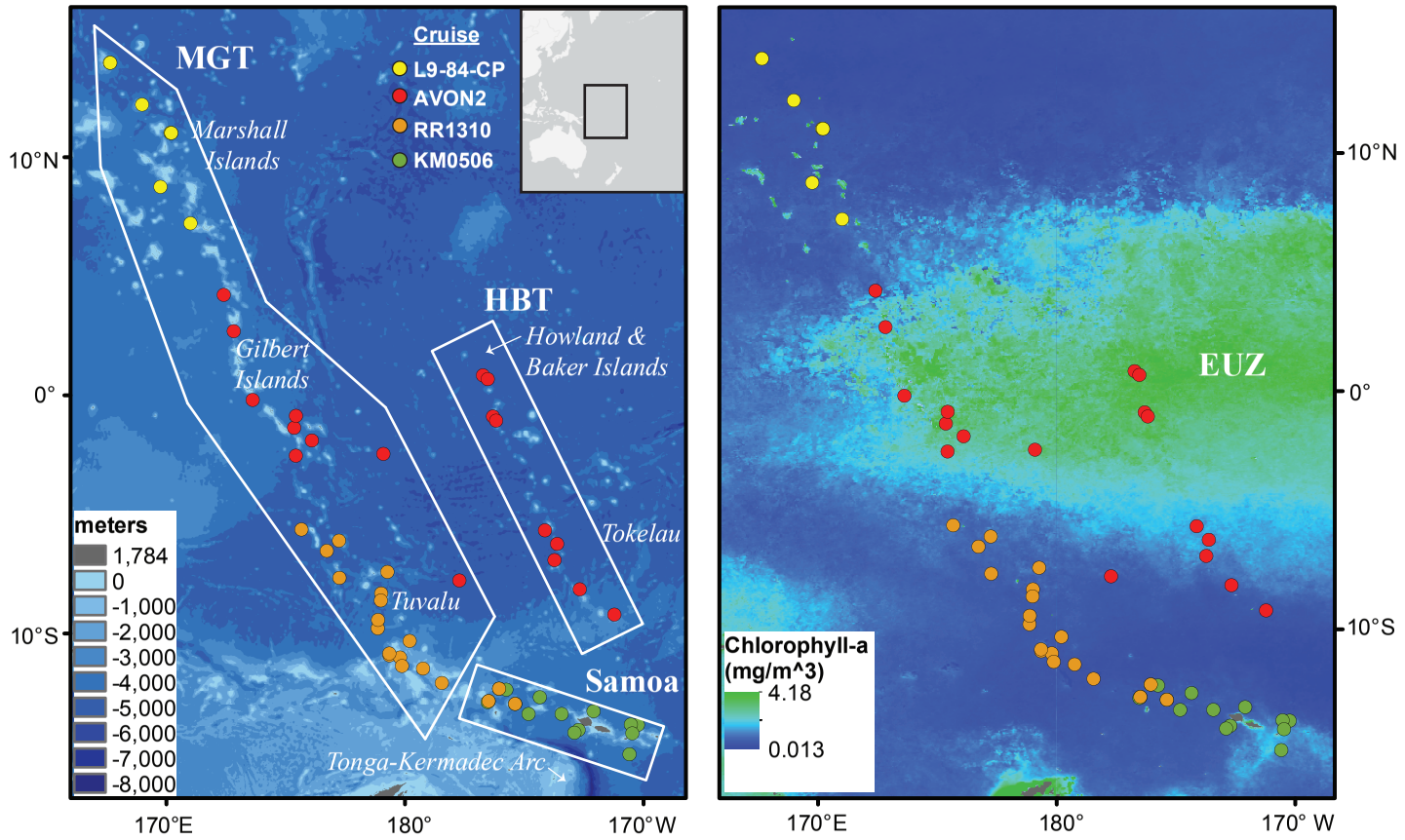

Figure 1. Maps of the western equatorial Pacific region studied here including FeMn crust dredge locations. Left: Inset in the upper right shows the general region of the sample area; different colors for dredge locations indicate the four cruises included in this study, and the areas outlined in white show the samples included in each of the three main sample transects, Marshall-Gilbert-Tuvalu (MGT), Samoa, and Howland-Baker-Tokelau (HBT); this map was created in ArcGIS and includes GEBCO 2014 bathymetry. Right: Dredge locations shown with respect to surface chlorophyll-a values (NASA MODIS Aqua, April 2019) to show sample locations with respect to increased surface productivity in the equatorial upwelling zone (EUZ).

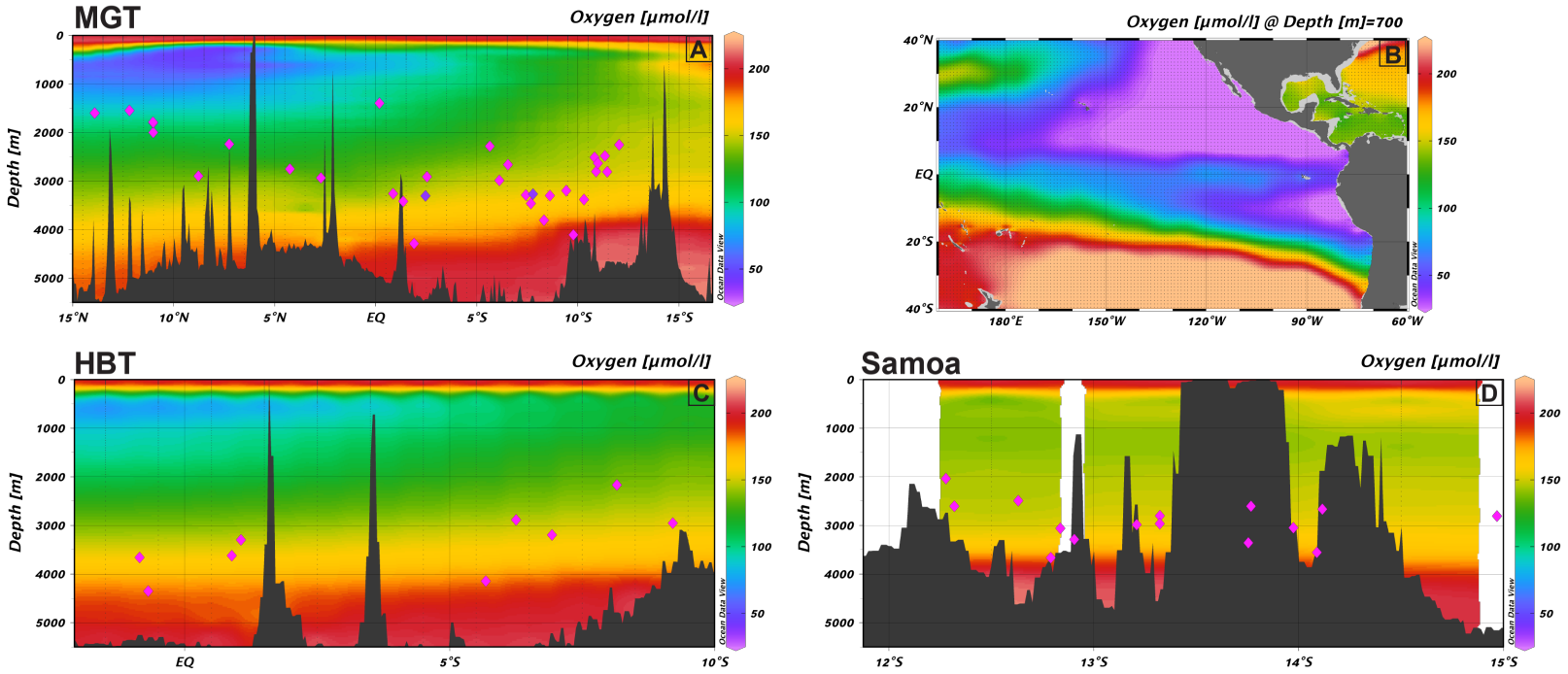

Figure 2. Depth sections of seawater oxygen concentrations for the main sample transects (A, C, D) as well as an isosurface plot of seawater oxygen concentration at a depth of 700 m (B). All plots were created in Ocean Data View (Schlitzer 2018) using oceanographic data from the World Ocean Atlas (Garcia et al., 2014). Scale bars for oxygen have a minimum value of 25 µmol/l and a maximum value of 225 µmol/l.

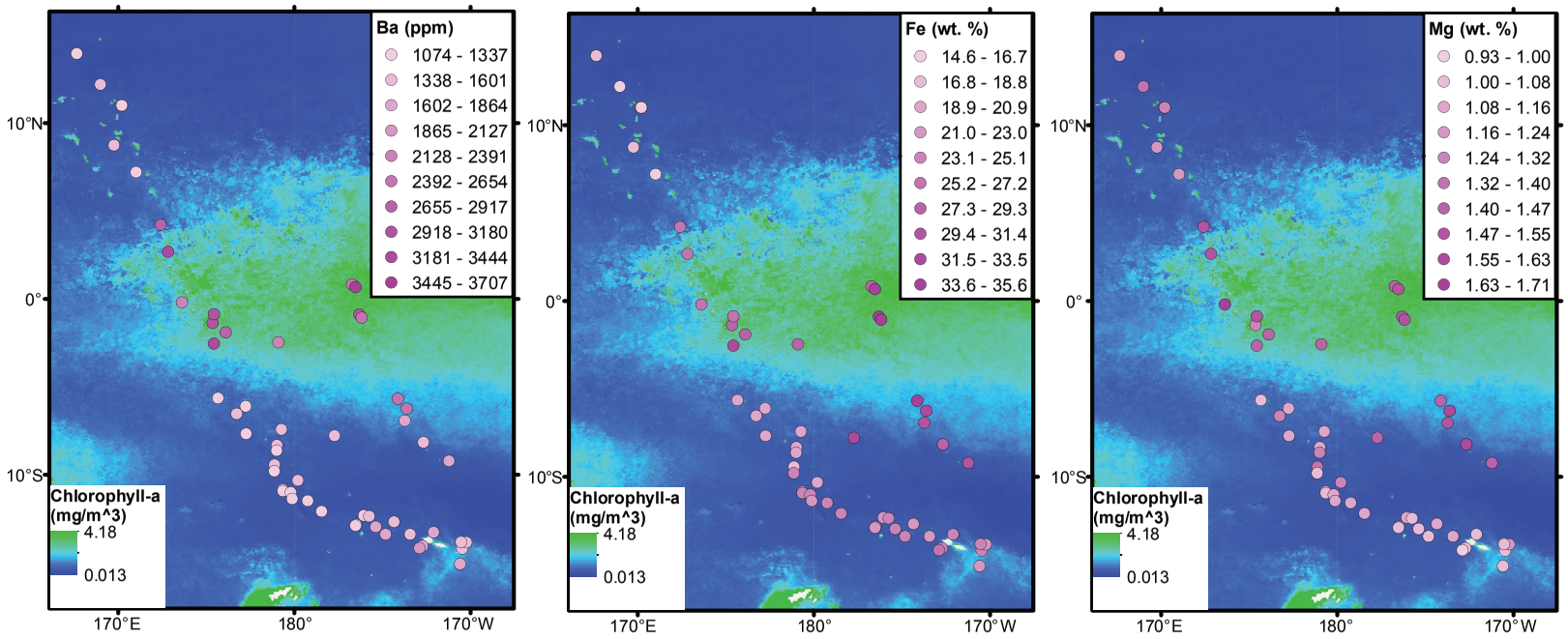

Figure 3. The Ba (left), Fe (middle), and Mg (right) concentration at each dredge location, with the color darkening as concentration increases, overlying a map of surface chlorophyll-a concentrations (NASA MODIS Aqua, April 2019).

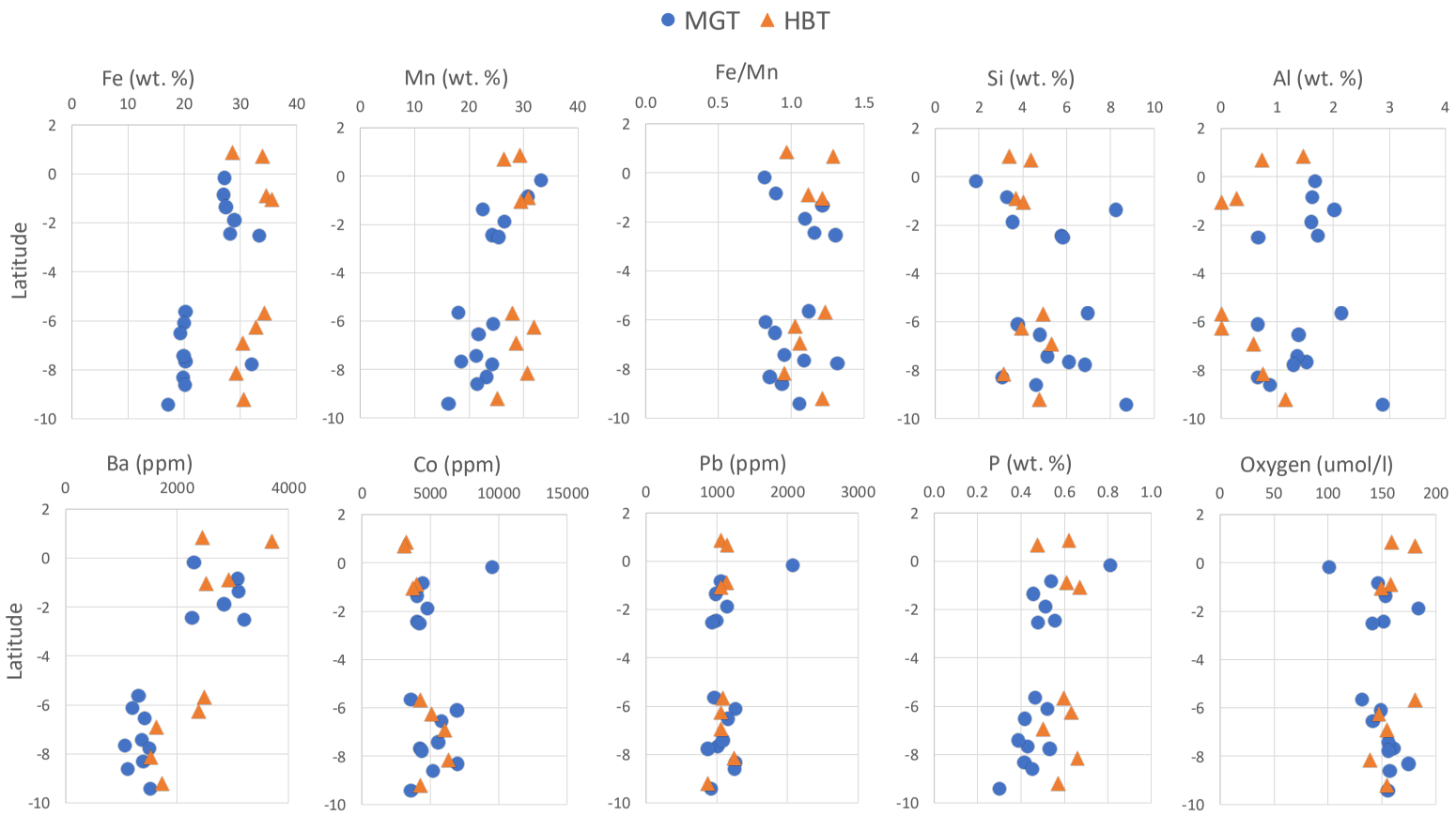

Figure 4. Concentrations of elements in FeMn crusts as well as seawater oxygen concentrations at sample locations within the HBT transect (blue circles) compared to those from the subsection of the MGT transect (orange triangles) within the same latitude range of 2°N to 10°S.

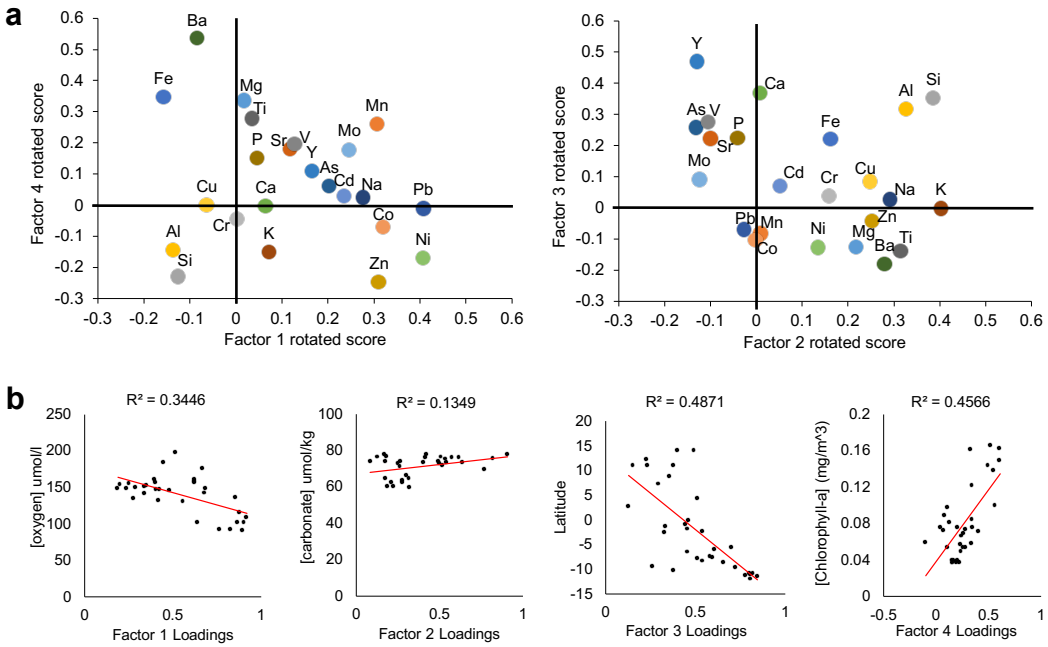

Figure 5. a) Plots of rotated VARIMAX factor scores for Factor 1 versus Factor 4 and for Factor 3 vs Factor 2. b) Plots of factor loadings for each factor versus the numerical values for the controlling oceanographic or geographic parameter or proxy to which the factor is mainly attributed. Correlations in the factor loading plots are significant at the 99% confidence level for factors 1, 3, and 4, and the correlation for factor 2 is significant at the 95% confidence level.

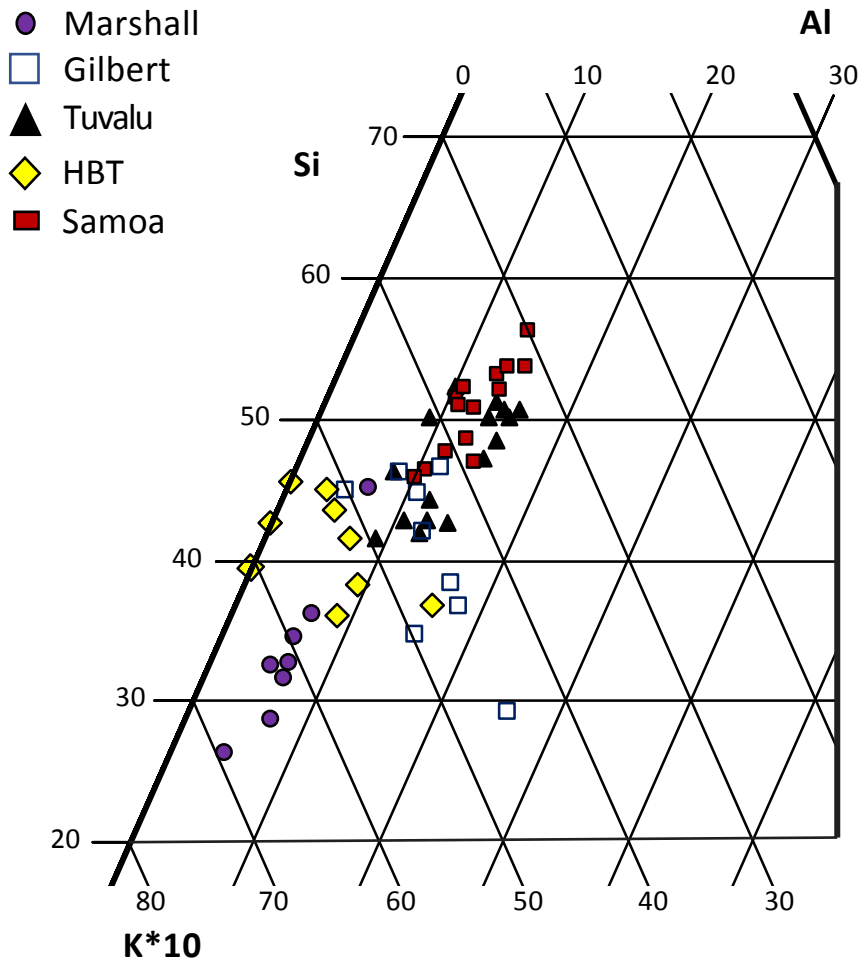

Figure 6. A truncated ternary diagram of Si, Al, and K (multiplied by ten) concentrations in FeMn crusts with symbols representing samples from seamounts in proximity to the listed islands, Marshall, Gilbert, Tuvalu, Samoa, and the group of Howland, Baker, and Tokelau (HBT).

Supplementary Table 1. Sorbed-water (H_2O^-) corrected chemistry for all samples

Island Region [1]	Marshall	Marshall	Marshall	Marshall	Marshall	Marshall	Marshall
Cruise ID	L9-84-CP	L9-84-CP	L9-84-CP	L9-84-CP	L9-84-CP	L9-84-CP	L9-84-CP
Sample/Dredge ID	D1	D6	D12-1-A	D13	D14-1-A	D15	D17-2-A
Layer Interval (mm) [2]	Mean	Mean	0-5	Mean	0-5	Mean	0-5
Latitude	7.245	8.768	11.018	11.008	11.009	12.181	13.904
Longitude	171.012	169.754	170.172	170.201	170.208	168.983	167.633
Water Depth (m)	2240	2900	1788	2000	1800	1550	1600
Oxygen (µmol/l) [3]	116	136	101	109	102	91	92
Cholophyll-a (mg/m^3) [4]	0.098	0.049	0.040	0.040	0.040	0.037	0.037
Carbonate (µmol/kg) [5]	64.7	71.0	62.2	63.4	62.2	59.4	59.9
Silicate (µmol/l) [3]	149	153	141	145	141	134	138
Excess Silica (wt. %) [6]	0.90	1.19	0.96	0.86	1.22	0.47	2.38
Phosphate (µmol/l) [3]	2.79	2.71	2.85	2.84	2.85	2.92	2.91
Fe (wt. %)	16	18	18	15	16	16	18
Mn	29	28	29	31	29	29	25
Si	2.9	2.8	2.8	1.9	2.5	2.3	4.6
Al	0.61	0.47	0.55	0.32	0.38	0.55	0.67
Mg	1.2	1.2	1.2	1.2	1.2	1.3	1.2
Ca	3.0	2.8	2.8	2.7	2.7	2.9	3.1
Na	2.0	1.9	1.8	2.0	1.9	2.1	2.1
K	0.58	0.48	0.52	0.51	0.48	0.52	0.50
Ti	1.1	1.1	0.99	1.3	1.3	1.1	0.79
P	0.46	0.44	0.48	0.37	0.39	0.49	0.70
H_2O^-	27	26	25	27	29	27	25
As (ppm)	288	313	334	261	295	295	348
Ba	1170	1519	1335	1318	1392	1447	1225
Cd	4.4	4.3	4.0	5.8	4.9	5.0	3.5
Co	13987	8974	10147	18879	15612	11549	8032
Cr	5.2	12	4.7	4.7	9.6	9.3	4.0
Cu	286	645	654	357	366	880	388
Mo	454	559	614	514	464	569	562
Ni	5810	5385	5340	5968	5485	6520	4150
Pb	1633	1764	2003	2059	1969	1989	2142
Sr	1541	1655	1736	1578	1547	1543	1606
V	662	737	788	611	647	686	763
Zn	812	750	774	782	759	841	643
Y	199	198	200	192	197	175	187
Fe/Mn (ratio)	0.55	0.65	0.62	0.47	0.56	0.56	0.69
Si/Al	4.8	5.9	5.1	6.1	6.6	4.2	6.9
K/Al	0.95	1.0	0.95	1.6	1.3	0.95	0.74

Supplementary Table 1. Continued

Island Region [1]	Marshall	Gilbert	Gilbert	Gilbert	Gilbert	Gilbert	Gilbert	Gilbert	Gilbert	Gilbert
Cruise ID	L9-84-CP	AVON2	AVON2	AVON2	AVON2	AVON2	AVON2	AVON2	AVON2	AVON2
Sample/Dredge ID	D18	03-2B	04-37B	11-A	D13	17-41B	22-10B	25-15B	40-19B	54-10B
Layer Interval (mm) [2]	Mean	0-15	0-9	0-9	Mean	0-12	0-9	0-10	0-11	0-6
Latitude	13.900	4.241	2.710	-0.188	-0.864	-1.364	-1.900	-2.466	-2.541	-7.785
Longitude	167.648	172.404	172.826	173.615	175.430	175.355	176.100	179.092	175.426	-177.723
Water Depth (m)	1600	2755	2938	1399	3261	3422	4290	3307	2913	3269
Oxygen (µmol/l) [3]	92	131	134	101	146	154	184	152	141	156
Cholophyll-a (mg/m^3) [4]	0.037	0.100	0.122	0.165	0.162	0.162	0.149	0.144	0.138	0.075
Carbonate (µmol/kg) [5]	59.9	66.3	69.6	64.6	73.3	75.5	78.0	75.2	73.2	76.2
Silicate (µmol/l) [3]	138	153	151	113	146	144	135	145	146	145
Excess Silica (wt. %) [6]	1.30	-1.71	0.80	-3.76	-2.22	1.43	-1.90	-0.06	3.60	2.51
Phosphate (µmol/l) [3]	2.91	2.35	2.43	2.88	2.61	2.60	2.43	2.58	2.64	2.52
Fe (wt. %)	18	26	25	27	27	27	29	28	33	32
Mn	27	31	17	33	31	23	27	24	26	24
Si	3.1	3.5	5.7	1.9	3.3	8.3	3.6	5.8	5.8	6.9
Al	0.55	1.6	1.5	1.7	1.6	2.0	1.6	1.7	0.66	1.3
Mg	1.1	1.5	1.5	1.7	1.5	1.3	1.4	1.4	1.4	1.4
Ca	3.0	3.2	1.5	3.7	3.2	2.7	3.3	2.9	2.9	3.0
Na	1.9	1.6	1.5	1.7	1.6	1.8	1.6	1.9	1.9	1.7
K	0.50	0.41	0.51	0.29	0.40	0.82	0.51	0.62	0.65	0.67
Ti	1.1	1.2	1.1	1.1	1.5	1.8	1.7	1.4	1.8	1.5
P	0.59	0.62	0.41	0.81	0.54	0.46	0.51	0.56	0.48	0.53
H_2O^-	27	20	22	25	21	18	21	20	21	23
As (ppm)	322	312	194	408	276	163	293	274	175	206
Ba	1305	2724	3210	2306	3091	3113	2850	2268	3211	1498
Cd	3.8	5.0	2.5	6.2	5.0	3.1	3.9	3.0	5.1	3.9
Co	12595	4428	3940	9571	4467	4093	4792	4073	4251	4429
Cr	19	16	54	55	37	11	5.0	8.8	15	12
Cu	296	546	876	375	1231	3775	1513	885	2145	1110
Mo	475	614	216	780	580	225	652	432	296	374
Ni	4387	3383	3680	4223	3519	2843	3203	2707	2995	3491
Pb	2139	1393	1420	2078	1063	993	1145	997	934	879
Sr	1618	1791	1230	2078	1587	1434	1904	1579	1599	1524
V	688	789	486	916	800	625	840	650	780	638
Zn	664	586	686	597	561	651	566	503	641	657
Y	206	233	125	210	216	151	182	197	162	189
Fe/Mn (ratio)	0.67	0.84	1.5	0.82	0.90	1.2	1.1	1.2	1.3	1.3
Si/Al	5.8	2.3	3.9	1.1	2.0	4.1	2.2	3.3	8.8	5.3
K/Al	0.91	0.27	0.35	0.17	0.25	0.41	0.32	0.36	0.98	0.52

Supplementary Table 1. Continued

Island Region [1]	Tuvalu	Tuvalu	Tuvalu	Tuvalu	Tuvalu	Tuvalu	Tuvalu	Tuvalu	Tuvalu	Tuvalu
Cruise ID	RR1310	RR1310	RR1310	RR1310	RR1310	RR1310	RR1310	R1310	RR1310	RR1310
Sample/Dredge ID	D04-02	D08-10	D09-12	D10-54	D16	D17-30	D18-20	D19-33	D20-54	D22
Layer Interval (mm) [2]	0-10	0-2	0-10	0-5	Mean	0-10	0-1	0-13	0-3	Mean
Latitude	-5.648	-6.117	-6.542	-7.677	-7.428	-8.328	-8.622	-9.430	-9.782	-10.306
Longitude	175.661	177.234	176.724	177.255	179.262	179.005	178.990	178.871	178.859	-179.803
Water Depth (m)	2286	2989	2665	3463	3289	3808	3302	3202	4110	3384
Oxygen (µmol/l) [3]	132	149	142	161	156	175	158	156	198	161
Cholophyll-a (mg/m^3) [4]	0.089	0.085	0.082	0.073	0.075	0.072	0.073	0.059	0.058	0.057
Carbonate (µmol/kg) [5]	71.7	74.1	73.8	76.6	76.0	77.6	76.8	77.4	76.4	75.8
Silicate (µmol/l) [3]	141	145	145	143	145	137	143	143	127	141
Excess Silica (wt. %) [6]	-0.30	1.60	0.11	0.97	0.54	0.85	1.65	-0.98	1.73	0.09
Phosphate (µmol/l) [3]	2.63	2.54	2.52	2.50	2.51	2.42	2.51	2.53	2.30	2.51
Fe (wt. %)	20	20	19	20	20	20	20	17	23	19
Mn	18	24	22	19	21	23	22	16	20	22
Si	7.0	3.8	4.8	6.1	5.1	3.1	4.6	8.8	4.3	4.4
Al	2.2	0.65	1.4	1.5	1.4	0.66	0.88	2.9	0.76	1.3
Mg	1.1	1.2	1.3	1.1	1.1	1.1	1.3	1.3	1.1	1.3
Ca	2.5	2.9	2.6	2.8	2.5	2.6	3.0	2.4	2.4	2.6
Na	1.5	0.87	1.2	1.3	1.4	1.2	0.87	1.6	1.4	1.1
K	0.56	0.37	0.50	0.66	0.51	0.36	0.33	0.89	0.35	0.48
Ti	0.87	0.96	0.95	1.1	0.96	1.2	0.84	1.5	0.83	1.5
P	0.47	0.52	0.42	0.43	0.39	0.42	0.45	0.30	0.50	0.37
H_2O^-	22	27	25	21	23	23	23	19	24	21
As (ppm)	237	308	217	256	241	263	281	144	288	217
Ba	1320	1198	1424	1074	1376	1399	1118	1527	1192	1523
Cd	3.7	4.3	4.6	3.9	4.2	4.2	4.8	4.1	3.4	4.4
Co	3625	6969	5862	4260	5611	7037	5212	3592	3229	5697
Cr	13	6.8	9.4	108	8.5	5.2	30	32	1.3	29
Cu	1094	608	1521	769	1546	1141	554	2520	903	1365
Mo	399	609	447	377	494	555	470	233	457	412
Ni	3566	4191	5416	3039	4390	3880	3595	4373	2377	4766
Pb	967	1274	1165	1014	1094	1274	1259	927	1246	1068
Sr	1442	1741	1478	1447	1561	1675	1631	1242	1535	1542
V	735	824	632	626	758	665	703	483	811	593
Zn	585	569	691	558	594	507	575	721	558	709
Y	169	202	171	175	173	218	199	103	219	165
Fe/Mn (ratio)	1.1	0.82	0.89	1.1	0.95	0.85	0.94	1.1	1.2	0.89
Si/Al	3.2	5.8	3.5	4.0	3.9	4.7	5.3	3.0	5.6	3.4
K/Al	0.26	0.58	0.36	0.44	0.37	0.56	0.38	0.31	0.46	0.38

Supplementary Table 1. Continued

Island Region [1]	Tuvalu	Tuvalu	Tuvalu	Tuvalu	Tuvalu	Tuvalu	Samoa	Samoa	Samoa	Samoa	Samoa
Cruise ID	RR1310	RR1310	RR1310	RR1310	RR1310	RR1310	RR1310	RR1310	RR1310	KM0506	KM0506
Sample/Dredge ID	D25-27	D26-04	D27-04	D28B-01	D30-02	D33	D38-26	D39	D41-33	ALIA 110	ALIA 111
Layer Interval (mm) [2]	0-15	0-10	0-10	0-5	0-15	Mean	0-10	Mean	0-7	Mean	Mean
Latitude	-10.827	-10.903	-10.992	-11.341	-11.451	-12.047	-12.791	-12.279	-12.905	-13.768	-13.755
Longitude	179.342	179.351	179.792	179.875	-179.246	-178.455	-176.495	-176.057	-175.383	-170.240	-170.534
Water Depth (m)	2513	2806	2636	2485	2812	2257	3666	2040	3290	2607	3361
Oxygen (µmol/l) [3]	147	150	148	148	151	147	179	144	155	152	165
Cholophyll-a (mg/m^3) [4]	0.068	0.066	0.075	0.054	0.053	0.054	0.054	0.055	0.052	0.048	0.050
Carbonate (µmol/kg) [5]	73.0	74.1	73.1	73.3	74.2	NA	NA	NA	NA	NA	NA
Silicate (µmol/l) [3]	138	141	139	137	140	131	NA	NA	NA	NA	NA
Excess Silica (wt. %) [6]	0.47	0.20	-0.38	-0.21	0.39	-0.28	0.64	-0.15	0.93	0.97	1.19
Phosphate (µmol/l) [3]	2.59	2.58	2.59	2.61	2.59	2.61	NA	NA	NA	NA	NA
Fe (wt. %)	23	24	24	22	23	23	24	23	25	21	23
Mn	19	17	14	16	17	17	15	17	16	19	18
Si	5.2	4.5	7.2	6.7	5.1	5.0	6.3	5.2	5.4	4.0	4.5
Al	1.4	1.3	2.2	2.1	1.4	1.6	1.7	1.6	1.3	0.90	0.97
Mg	1.1	1.1	1.1	1.2	1.2	1.1	1.1	1.1	1.1	1.2	1.0
Ca	2.6	4.3	4.0	2.5	3.3	2.9	2.3	3.0	2.2	2.4	2.2
Na	0.91	0.38	1.2	1.2	1.1	1.0	1.3	1.0	1.1	2.2	1.0
K	0.36	0.31	0.47	0.46	0.36	0.38	0.41	0.43	0.35	0.39	0.33
Ti	0.87	0.98	0.90	0.86	0.93	0.91	1.5	1.0	1.2	1.1	1.3
P	0.51	0.48	0.46	0.47	0.51	0.53	0.45	0.52	0.46	0.53	0.50
H_2O^-	21	19	21	23	25	24	22	22	21	20	19
As (ppm)	270	263	224	228	272	273	241	265	259	256	262
Ba	1341	1264	1167	1316	1189	1246	1490	1307	1626	1344	1365
Cd	3.6	3.8	3.3	3.5	3.0	3.3	3.1	3.3	3.3	4.0	3.2
Co	3201	3644	2423	2337	2437	3101	2659	3814	2593	3589	3139
Cr	5.1	6.2	20	10	7.9	9.8	19	13	7.6	26	25
Cu	994	801	807	1350	1270	1256	835	798	1085	631	516
Mo	373	284	224	280	385	364	278	366	362	338	328
Ni	2794	2543	2288	2289	2494	2543	1502	2612	1942	2728	1847
Pb	985	880	891	728	799	1074	1093	1291	1037	1124	990
Sr	1622	1650	1444	1490	1572	1615	1448	1653	1589	1564	1526
V	697	610	592	628	699	719	722	1118	696	719	678
Zn	612	557	593	616	564	610	603	605	665	722	592
Y	230	192	175	177	216	211	207	227	176	202	210
Fe/Mn (ratio)	1.2	1.4	1.7	1.4	1.4	1.4	1.6	1.3	1.5	1.1	1.3
Si/Al	3.7	3.5	3.2	3.3	3.7	3.3	3.8	3.3	4.1	4.5	4.6
K/Al	0.25	0.24	0.21	0.22	0.26	0.24	0.25	0.27	0.26	0.43	0.34

Supplementary Table 1. Continued

Island Region [1]	Samoa	Samoa	Samoa	Samoa	Samoa	Samoa	Samoa	Samoa	Samoa
Cruise ID	KM0506	KM0506	KM0506	KM0506	KM0506	KM0506	KM0506	KM0506	KM0506
Sample/Dredge ID	ALIA 112-02	ALIA 114-13A	ALIA 115-26A	ALIA 118	ALIA 119-02A	ALIA 120-11A	ALIA 121-02A	ALIA 122-12A	ALIA 128-20A
Layer Interval (mm) [2]	0-1	0-7	0-8	Mean	0-12	0-8	0-10	0-5	0-10
Latitude	-14.117	-13.975	-14.090	-13.322	-12.632	-13.323	-12.320	-12.837	-13.21
Longitude	-170.474	-172.724	-172.898	-173.434	-174.349	-174.823	-175.755	-176.531	-172.1
Water Depth (m)	2668	3050	3557	2967	2494	2805	2607	3062	2986
Oxygen (µmol/l) [3]	152	157	176	154	147	150	147	152	156
Cholophyll-a (mg/m^3) [4]	0.055	0.058	0.055	0.055	0.054	0.055	0.061	0.054	0.053
Carbonate (µmol/kg) [5]	NA	NA	NA	NA	NA	NA	NA	NA	NA
Silicate (µmol/l) [3]	NA	NA	NA	NA	NA	NA	NA	NA	NA
Excess Silica (wt. %) [6]	1.33	0.91	1.08	0.74	0.53	1.56	0.97	1.29	0.32
Phosphate (µmol/l) [3]	NA	NA	NA	NA	NA	NA	NA	NA	NA
Fe (wt. %)	24	24	26	21	22	25	24	23	23
Mn	18	13	12	20	18	16	17	19	14
Si	4.5	6.6	6.7	4.3	4.8	5.2	5.5	4.5	6.5
Al	0.93	1.7	1.7	1.1	1.3	1.1	1.3	0.95	1.8
Mg	1.0	1.1	0.93	1.1	1.1	1.0	1.1	1.1	1.0
Ca	2.3	2.1	2.1	2.4	2.7	2.3	2.5	2.4	2.4
Na	1.1	1.9	1.0	1.4	1.2	1.6	1.6	1.5	1.1
K	0.33	0.41	0.35	0.37	0.38	0.37	0.40	0.32	0.38
Ti	1.1	2.1	2.2	1.2	1.1	1.1	0.97	0.95	2.2
P	0.57	0.49	0.45	0.47	0.50	0.51	0.51	0.52	0.47
H_2O^-	19	16	15	19	18	18	21	19	16
As (ppm)	267	199	197	264	276	282	276	269	220
Ba	1352	1790	1960	1416	1557	1652	1506	1312	1838
Cd	3.4	3.3	2.8	3.6	3.1	2.9	3.1	3.2	3.2
Co	2382	1575	1405	4168	3479	2179	2443	2970	2029
Cr	24	31	31	17	19	15	18	14	27
Cu	440	650	458	656	697	558	744	621	473
Mo	305	148	152	402	388	333	333	360	189
Ni	1923	1036	734	2781	2640	1652	2089	2339	1277
Pb	1005	893	914	1026	1173	1050	1006	963	736
Sr	1538	1504	1499	1668	1691	1542	1570	1547	1468
V	712	616	671	691	757	782	746	717	625
Zn	661	729	695	576	661	692	672	606	733
Y	213	192	205	206	223	220	203	207	206
Fe/Mn (ratio)	1.3	1.9	2.1	1.1	1.3	1.5	1.4	1.2	1.6
Si/Al	4.8	3.9	4.0	4.1	3.8	4.8	4.1	4.7	3.5
K/Al	0.35	0.24	0.21	0.35	0.30	0.34	0.30	0.34	0.21

Supplementary Table 1. Continued

Island Region [1]	Samoa	HBT	HBT	HBT	HBT	HBT	HBT	HBT	HBT	HBT
Cruise ID	KM0506	AVON2	AVON2	AVON2	AVON2	AVON2	AVON2	AVON2	AVON2	AVON2
Sample/Dredge ID	ALIA 129-05A	26-55B	28-48B	33-33B	34-64B	44-25B	47-08B	D51	58-03B	62-13B
Layer Interval (mm) [2]	0-15	0-10	0-4	0-15	0-15	0-9	0-8	Mean	0-5	0-11
Latitude	-14.968	0.851	0.690	-0.888	-1.062	-5.684	-6.254	-6.932	-8.156	-9.211
Longitude	-170.592	-176.733	-176.534	-176.313	-176.182	-174.132	-173.625	-173.734	-172.675	-171.227
Water Depth (m)	2809	3661	4354	3625	3299	4149	2889	3197	2168	2955
Oxygen (µmol/l) [3]	154	158	181	158	149	181	147	155	139	154
Cholophyll-a (mg/m^3) [4]	0.053	0.178	0.182	0.173	0.170	0.105	0.101	0.093	0.079	0.071
Carbonate (µmol/kg) [5]	NA	NA	NA	NA	NA	NA	NA	NA	NA	NA
Silicate (µmol/l) [3]	NA	NA	NA	NA	NA	NA	NA	NA	NA	NA
Excess Silica (wt. %) [6]	0.95	-1.54	1.91	2.76	4.00	4.88	3.91	3.41	0.60	0.92
Phosphate (µmol/l) [3]	NA	NA	NA	NA	NA	NA	NA	NA	NA	NA
Fe (wt. %)	22	28	34	35	36	34	33	30	29	31
Mn	19	29	26	31	29	28	32	29	31	25
Si	4.3	3.4	4.4	3.7	4.0	4.9	3.9	5.3	3.1	4.8
Al	1.0	1.5	0.74	0.27	0.01	0.01	0.01	0.58	0.75	1.1
Mg	1.0	1.5	1.5	1.5	1.5	1.5	1.6	1.5	1.6	1.5
Ca	2.3	3.4	2.9	3.2	3.2	3.2	3.5	3.3	3.5	3.4
Na	1.1	1.8	1.5	1.7	1.8	1.8	1.8	2.2	1.9	1.8
K	0.40	0.44	0.54	0.42	0.48	0.66	0.60	0.63	0.48	0.65
Ti	1.5	1.0	1.6	1.4	1.2	1.5	1.3	1.8	1.4	1.3
P	0.44	0.62	0.48	0.61	0.67	0.60	0.63	0.50	0.66	0.57
H_2O^-	17	21	22	25	24	23	24	24	22	20
As (ppm)	240	354	279	363	319	311	316	189	264	255
Ba	1775	2459	3707	2927	2523	2480	2395	1634	1527	1740
Cd	3.4	4.4	3.6	4.2	5.8	3.7	4.7	4.0	5.8	5.3
Co	4034	3266	3153	4040	3745	4256	5145	6100	6312	4280
Cr	19	5.0	9.0	4.0	0.75	10	14	7.3	6.4	5.0
Cu	752	475	1583	788	744	880	984	1193	484	1131
Mo	339	662	561	666	564	540	618	442	490	419
Ni	2862	3190	3282	2874	3035	2755	3987	4042	4144	3504
Pb	1019	1061	1149	1138	1059	1091	1062	1056	1251	870
Sr	1594	1803	1712	1748	1787	1723	1816	1678	2258	2190
V	713	794	807	885	827	819	849	629	729	670
Zn	704	520	696	600	578	565	596	676	576	593
Y	202	211	175	213	234	232	220	172	225	205
Fe/Mn (ratio)	1.2	0.97	1.3	1.1	1.2	1.2	1.0	1.1	0.95	1.2
Si/Al	4.3	2.3	6.0	14	537	710	564	9.3	4.2	4.2
K/Al	0.40	0.30	0.74	1.6	64	96	86	1.1	0.64	0.57

[1] HBT includes samples near Howland, Baker, and Tokelau islands

[2] Samples with mean listed for the layer interval represent the mean chemistry for the uppermost crust layers (<15mm) from multiple individual FeMn crusts recovered from the listed dredge location

[3] Oxygen values (Garcia et al. 2014a) and silicate and phosphate values (Garcia et al. 2014b) are interpolated from World Ocean Atlas 2013 1.00 degree data using 2-D estimation in Ocean Data View (Schlitzer 2018) at each sample location and depth

[4] Chlorophyll-a values are interpolated from satellite data (NASA MODIS Aqua, April 2019) at each sample location and depth

[5] Dissolved carbonate values are interpolated from GLODAP data (Key et al. 2004) using 2-D estimation in Ocean Data View (Schlitzer 2018) at each sample location and depth

[6] Excess silica was calculated by multiplying the Si/Al for average ocean island basalt (3.37; Dasgupta, Jackson, and Lee 2010) by the Al concentration for each FeMn crust and then subtracting this theoretical Si concentration from the measured Si concentration for each FeMn crust

Supplementary Table 2. Correlation coefficient matrix for all 57 FeMn crust samples analyzed in this study [1]

	Latitude	Longitude	Depth	[Oxy]	Fe	Mn	Fe/Mn	Si	Al	Si/Al
Latitude	1.0000	-0.8299	-0.3801	-0.6979	-0.2100	0.7127	-0.7297	-0.5250	-0.3975	0.0280
Longitude	-0.8299	1.0000	0.4210	0.6572	0.4742	-0.4123	0.6529	0.3173	0.0661	0.1988
Depth	-0.3801	0.4210	1.0000	0.9046	0.5034	-0.1371	0.3842	0.3006	0.0612	0.2083
[Oxy]	-0.6979	0.6572	0.9046	1.0000	0.4604	-0.3955	0.5876	0.4187	0.1992	0.1413
Fe	-0.2100	0.4742	0.5034	0.4604	1.0000	0.2319	0.4265	0.1612	-0.1252	0.4632
Mn	0.7127	-0.4123	-0.1371	-0.3955	0.2319	1.0000	-0.7450	-0.6948	-0.5865	0.2944
Fe/Mn	-0.7297	0.6529	0.3842	0.5876	0.4265	-0.7450	1.0000	0.6955	0.4545	0.0168
Si	-0.5250	0.3173	0.3006	0.4187	0.1612	-0.6948	0.6955	1.0000	0.6750	-0.0620
Al	-0.3975	0.0661	0.0612	0.1992	-0.1252	-0.5865	0.4545	0.6750	1.0000	-0.4541
Si/Al	0.0280	0.1988	0.2083	0.1413	0.4632	0.2944	0.0168	-0.0620	-0.4541	1.0000
Mg	0.3644	-0.1119	0.1194	-0.0756	0.6048	0.7318	-0.2882	-0.2484	-0.2062	0.3459
Ca	0.2514	-0.1595	-0.1407	-0.1858	0.3087	0.5275	-0.2699	-0.3062	-0.1659	0.2273
Na	0.6022	-0.2905	-0.1949	-0.3988	0.1358	0.6083	-0.4265	-0.2518	-0.3430	0.1742
K	0.3069	-0.2236	0.1101	-0.0570	0.1581	0.2548	-0.1856	0.3781	0.0953	0.2209
Ti	-0.1156	0.3113	0.3877	0.3162	0.4002	-0.0063	0.3609	0.2673	0.0800	0.0892
P	0.1522	0.0955	-0.2027	-0.2026	0.5074	0.4604	-0.0659	-0.3365	-0.2690	0.3331
As	0.4371	-0.2384	-0.2376	-0.3357	0.0403	0.5707	-0.4737	-0.7408	-0.4902	0.2311
Ba	0.2193	0.0035	0.4119	0.1915	0.6964	0.3726	0.1330	0.0095	-0.0273	0.2537
Cd	0.4337	-0.2930	-0.2532	-0.3750	0.0671	0.7550	-0.6206	-0.5798	-0.3679	0.1886
Co	0.7751	-0.6834	-0.5327	-0.7102	-0.4895	0.6141	-0.8141	-0.6477	-0.4749	-0.0496
Cr	-0.1487	-0.0004	0.0188	0.0240	-0.1084	-0.2394	0.1628	0.2080	0.3305	-0.1176
Cu	-0.1120	-0.0462	0.3393	0.2905	0.2106	-0.0910	0.1221	0.5297	0.3810	-0.0239
Mo	0.5662	-0.3663	-0.0634	-0.2664	0.1229	0.8509	-0.7145	-0.7577	-0.5056	0.2409
Ni	0.7353	-0.6844	-0.4168	-0.6192	-0.4129	0.6691	-0.8895	-0.5509	-0.3720	-0.0137
Pb	0.8257	-0.7278	-0.5965	-0.7659	-0.4602	0.5586	-0.7368	-0.6713	-0.4391	-0.0773
Sr	0.1134	0.1474	-0.0790	-0.0658	0.4117	0.5902	-0.2518	-0.5522	-0.3770	0.1953
V	0.0613	0.0780	-0.0196	0.0230	0.3319	0.3609	-0.1248	-0.3879	-0.3090	0.2604
Zn	0.3310	-0.2387	-0.4111	-0.4620	-0.4326	0.0024	-0.1912	-0.1005	-0.1457	-0.1814
Y	-0.1200	0.2929	-0.0563	0.0645	0.2112	0.2111	-0.0125	-0.4782	-0.4260	0.2993

Supplementary Table 2. Continued

	Mg	Ca	Na	K	Ti	P	As	Ba	Cd	Co
Latitude	0.3644	0.2514	0.6022	0.3069	-0.1156	0.1522	0.4371	0.2193	0.4337	0.7751
Longitude	-0.1119	-0.1595	-0.2905	-0.2236	0.3113	0.0955	-0.2384	0.0035	-0.2930	-0.6834
Depth	0.1194	-0.1407	-0.1949	0.1101	0.3877	-0.2027	-0.2376	0.4119	-0.2532	-0.5327
[Oxy]	-0.0756	-0.1858	-0.3988	-0.0570	0.3162	-0.2026	-0.3357	0.1915	-0.3750	-0.7102
Fe	0.6048	0.3087	0.1358	0.1581	0.4002	0.5074	0.0403	0.6964	0.0671	-0.4895
Mn	0.7318	0.5275	0.6083	0.2548	-0.0063	0.4604	0.5707	0.3726	0.7550	0.6141
Fe/Mn	-0.2882	-0.2699	-0.4265	-0.1856	0.3609	-0.0659	-0.4737	0.1330	-0.6206	-0.8141
Si	-0.2484	-0.3062	-0.2518	0.3781	0.2673	-0.3365	-0.7408	0.0095	-0.5798	-0.6477
Al	-0.2062	-0.1659	-0.3430	0.0953	0.0800	-0.2690	-0.4902	-0.0273	-0.3679	-0.4749
Si/Al	0.3459	0.2273	0.1742	0.2209	0.0892	0.3331	0.2311	0.2537	0.1886	-0.0496
Mg	1.0000	0.4766	0.4862	0.4063	0.1687	0.4644	0.2264	0.6483	0.5882	0.1397
Ca	0.4766	1.0000	0.1106	0.1021	-0.1544	0.5032	0.4305	0.0944	0.4915	0.1816
Na	0.4862	0.1106	1.0000	0.4968	0.2030	0.2794	0.1664	0.2806	0.3741	0.4493
K	0.4063	0.1021	0.4968	1.0000	0.2854	-0.2026	-0.3863	0.2626	0.1320	0.1612
Ti	0.1687	-0.1544	0.2030	0.2854	1.0000	-0.1189	-0.4302	0.4899	-0.0423	-0.1384
P	0.4644	0.5032	0.2794	-0.2026	-0.1189	1.0000	0.6705	0.2474	0.2889	-0.0666
As	0.2264	0.4305	0.1664	-0.3863	-0.4302	0.6705	1.0000	0.0245	0.3403	0.3285
Ba	0.6483	0.0944	0.2806	0.2626	0.4899	0.2474	0.0245	1.0000	0.1165	-0.1907
Cd	0.5882	0.4915	0.3741	0.1320	-0.0423	0.2889	0.3403	0.1165	1.0000	0.5462
Co	0.1397	0.1816	0.4493	0.1612	-0.1384	-0.0666	0.3285	-0.1907	0.5462	1.0000
Cr	-0.0140	-0.2118	-0.1375	0.0404	0.0886	-0.1069	-0.1598	0.0256	-0.0673	-0.1399
Cu	0.1883	-0.0477	0.0114	0.5987	0.2532	-0.3354	-0.5626	0.3704	-0.0937	-0.2575
Mo	0.5530	0.4978	0.3357	-0.0424	-0.2732	0.5010	0.7999	0.2186	0.6210	0.4601
Ni	0.3557	0.2429	0.4230	0.3571	-0.2650	-0.1219	0.2304	-0.0996	0.6244	0.8299
Pb	0.1302	0.1226	0.4389	-0.0181	-0.2667	0.1782	0.5430	-0.1112	0.3977	0.8475
Sr	0.4999	0.6002	0.1963	-0.1320	-0.0098	0.6576	0.5600	0.1688	0.5818	0.1392
V	0.1931	0.3136	0.0491	-0.2726	-0.1594	0.5755	0.6265	0.2193	0.1918	-0.0473
Zn	-0.1828	-0.3579	0.3269	0.1629	0.2241	-0.3824	-0.2019	-0.1219	0.0253	0.4613
Y	-0.0632	0.2532	-0.0815	-0.5684	-0.1395	0.5720	0.6105	-0.1121	0.1277	-0.0316

Supplementary Table 2. Continued

	Cr	Cu	Mo	Ni	Pb	Sr	V	Zn	Y
Latitude	-0.1487	-0.1120	0.5662	0.7353	0.8257	0.1134	0.0613	0.3310	-0.1200
Longitude	-0.0004	-0.0462	-0.3663	-0.6844	-0.7278	0.1474	0.0780	-0.2387	0.2929
Depth	0.0188	0.3393	-0.0634	-0.4168	-0.5965	-0.0790	-0.0196	-0.4111	-0.0563
[Oxy]	0.0240	0.2905	-0.2664	-0.6192	-0.7659	-0.0658	0.0230	-0.4620	0.0645
Fe	-0.1084	0.2106	0.1229	-0.4129	-0.4602	0.4117	0.3319	-0.4326	0.2112
Mn	-0.2394	-0.0910	0.8509	0.6691	0.5586	0.5902	0.3609	0.0024	0.2111
Fe/Mn	0.1628	0.1221	-0.7145	-0.8895	-0.7368	-0.2518	-0.1248	-0.1912	-0.0125
Si	0.2080	0.5297	-0.7577	-0.5509	-0.6713	-0.5522	-0.3879	-0.1005	-0.4782
Al	0.3305	0.3810	-0.5056	-0.3720	-0.4391	-0.3770	-0.3090	-0.1457	-0.4260
Si/Al	-0.1176	-0.0239	0.2409	-0.0137	-0.0773	0.1953	0.2604	-0.1814	0.2993
Mg	-0.0140	0.1883	0.5530	0.3557	0.1302	0.4999	0.1931	-0.1828	-0.0632
Ca	-0.2118	-0.0477	0.4978	0.2429	0.1226	0.6002	0.3136	-0.3579	0.2532
Na	-0.1375	0.0114	0.3357	0.4230	0.4389	0.1963	0.0491	0.3269	-0.0815
K	0.0404	0.5987	-0.0424	0.3571	-0.0181	-0.1320	-0.2726	0.1629	-0.5684
Ti	0.0886	0.2532	-0.2732	-0.2650	-0.2667	-0.0098	-0.1594	0.2241	-0.1395
P	-0.1069	-0.3354	0.5010	-0.1219	0.1782	0.6576	0.5755	-0.3824	0.5720
As	-0.1598	-0.5626	0.7999	0.2304	0.5430	0.5600	0.6265	-0.2019	0.6105
Ba	0.0256	0.3704	0.2186	-0.0996	-0.1112	0.1688	0.2193	-0.1219	-0.1121
Cd	-0.0673	-0.0937	0.6210	0.6244	0.3977	0.5818	0.1918	0.0253	0.1277
Co	-0.1399	-0.2575	0.4601	0.8299	0.8475	0.1392	-0.0473	0.4613	-0.0316
Cr	1.0000	-0.0751	-0.2318	-0.1444	-0.0546	-0.2756	-0.2247	-0.0094	-0.2572
Cu	-0.0751	1.0000	-0.2171	0.0044	-0.3665	-0.2334	-0.1901	-0.0610	-0.5745
Mo	-0.2318	-0.2171	1.0000	0.5622	0.5360	0.6236	0.5659	-0.2007	0.3421
Ni	-0.1444	0.0044	0.5622	1.0000	0.6976	0.1499	-0.0712	0.3895	-0.2480
Pb	-0.0546	-0.3665	0.5360	0.6976	1.0000	0.1691	0.1663	0.4085	0.0462
Sr	-0.2756	-0.2334	0.6236	0.1499	0.1691	1.0000	0.5180	-0.3180	0.5291
V	-0.2247	-0.1901	0.5659	-0.0712	0.1663	0.5180	1.0000	-0.3017	0.5922
Zn	-0.0094	-0.0610	-0.2007	0.3895	0.4085	-0.3180	-0.3017	1.0000	-0.3249
Y	-0.2572	-0.5745	0.3421	-0.2480	0.0462	0.5291	0.5922	-0.3249	1.0000

[1] The 95% and 99% Confidence Levels for this correlation coefficient matrix based on N value of 57 are 0.2614 and 0.3369, respectively; coefficients above these values are considered significant at that confidence level

Supplementary Table 3. Correlation coefficient matrix for 33 FeMn crust samples from the Marshall-Gilbert-Tuvalu (MGT) region [1]

	Latitude	Longitude	Depth	[Oxygen]	Fe	Mn	Fe/Mn	Si	Al	Si/Al
Latitude	1.0000	0.9666	0.5863	0.7991	0.3797	-0.7339	0.7361	0.5746	0.5780	-0.3826
Longitude	-0.9666	1.0000	0.6099	0.8000	0.4356	-0.6709	0.7213	0.5626	0.5371	-0.3505
Depth	-0.5863	0.6099	1.0000	0.9390	0.4185	-0.3241	0.4031	0.3594	0.2736	-0.1441
[Oxygen]	-0.7991	0.8000	0.9390	1.0000	0.4241	-0.5194	0.5677	0.4412	0.3808	-0.2261
Fe	-0.3797	0.4356	0.4185	0.4241	1.0000	-0.0653	0.6407	0.3507	0.3716	-0.2094
Mn	0.7339	-0.6709	-0.3241	-0.5194	-0.0653	1.0000	-0.7827	-0.7448	-0.5439	0.1637
Fe/Mn	-0.7361	0.7213	0.4031	0.5677	0.6407	-0.7827	1.0000	0.7312	0.6351	-0.2814
Si	-0.5746	0.5626	0.3594	0.4412	0.3507	-0.7448	0.7312	1.0000	0.7441	-0.1315
Al	-0.5780	0.5371	0.2736	0.3808	0.3716	-0.5439	0.6351	0.7441	1.0000	-0.7198
Si/Al	0.3826	-0.3505	-0.1441	-0.2261	-0.2094	0.1637	-0.2814	-0.1315	-0.7198	1.0000
Mg	0.1620	-0.1035	0.0460	-0.0952	0.5482	0.4592	-0.0077	-0.0882	0.2032	-0.3228
Ca	-0.0364	0.0402	-0.1821	-0.1252	0.2112	0.1723	0.0672	-0.2049	0.0221	-0.1943
Na	0.7919	-0.7170	-0.3401	-0.5415	-0.0766	0.6566	-0.5232	-0.2323	-0.2762	0.3148
K	0.1288	-0.0783	0.1338	-0.0034	0.0547	-0.0721	0.0361	0.5811	0.3299	0.1457
Ti	0.1147	-0.0245	0.3537	0.1625	0.4332	0.3260	-0.0260	0.1303	0.1295	0.0301
P	0.2190	-0.2184	-0.3657	-0.3320	0.3661	0.3942	-0.0536	-0.2804	-0.0475	-0.1732
As	0.4628	-0.4689	-0.4514	-0.4535	-0.2284	0.5772	-0.5372	-0.7710	-0.4768	-0.0321
Ba	0.1366	-0.1238	0.2522	0.0824	0.6708	0.2909	0.1873	0.0842	0.2377	-0.1970
Cd	0.3212	-0.3425	-0.2991	-0.3624	-0.1749	0.7115	-0.6322	-0.5990	-0.3402	0.0525
Co	0.7841	-0.7433	-0.5703	-0.6947	-0.5990	0.6949	-0.8380	-0.7070	-0.6846	0.4015
Cr	-0.1116	0.0356	0.0909	0.0400	0.0845	-0.1010	0.1253	0.1547	0.2832	-0.2698
Cu	-0.3894	0.3801	0.4499	0.4426	0.3745	-0.3320	0.4082	0.6572	0.5293	-0.1335
Mo	0.4491	-0.4319	-0.2059	-0.2989	-0.1643	0.7793	-0.7058	-0.7980	-0.4549	-0.0741
Ni	0.6778	-0.6611	-0.4605	-0.6101	-0.6702	0.6015	-0.8540	-0.5776	-0.5357	0.2600
Pb	0.8809	-0.8764	-0.6602	-0.7848	-0.5190	0.7038	-0.7993	-0.7337	-0.6512	0.3265
Sr	0.1701	-0.1588	-0.1485	-0.1408	0.1893	0.5932	-0.3312	-0.6487	-0.3132	-0.1336
V	0.1563	-0.1793	-0.0780	-0.0709	0.2357	0.5317	-0.2838	-0.4900	-0.2808	-0.0022
Zn	0.6207	-0.6015	-0.5253	-0.6149	-0.5346	0.3567	-0.5395	-0.2777	-0.3737	0.3230
Y	0.0714	-0.0352	-0.1262	-0.0547	0.0298	0.3809	-0.2450	-0.5970	-0.4349	-0.0049

Supplementary Table 3. Continued

	Mg	Ca	Na	K	Ti	P	As	Ba	Cd	Co
Latitude	0.1620	-0.0364	0.7919	0.1288	0.1147	0.2190	0.4628	0.1366	0.3212	0.7841
Longitude	-0.1035	0.0402	-0.7170	-0.0783	-0.0245	-0.2184	-0.4689	-0.1238	-0.3425	-0.7433
Depth	0.0460	-0.1821	-0.3401	0.1338	0.3537	-0.3657	-0.4514	0.2522	-0.2991	-0.5703
[Oxy]	-0.0952	-0.1252	-0.5415	-0.0034	0.1625	-0.3320	-0.4535	0.0824	-0.3624	-0.6947
Fe	0.5482	0.2112	-0.0766	0.0547	0.4332	0.3661	-0.2284	0.6708	-0.1749	-0.5990
Mn	0.4592	0.1723	0.6566	-0.0721	0.3260	0.3942	0.5772	0.2909	0.7115	0.6949
Fe/Mn	-0.0077	0.0672	-0.5232	0.0361	-0.0260	-0.0536	-0.5372	0.1873	-0.6322	-0.8380
Si	-0.0882	-0.2049	-0.2323	0.5811	0.1303	-0.2804	-0.7710	0.0842	-0.5990	-0.7070
Al	0.2032	0.0221	-0.2762	0.3299	0.1295	-0.0475	-0.4768	0.2377	-0.3402	-0.6846
Si/Al	-0.3228	-0.1943	0.3148	0.1457	0.0301	-0.1732	-0.0321	-0.1970	0.0525	0.4015
Mg	1.0000	0.0241	0.3372	0.1424	0.5335	0.3594	0.0177	0.7565	0.3519	-0.0164
Ca	0.0241	1.0000	-0.1608	-0.3254	-0.0253	0.4804	0.3942	-0.0777	0.2351	-0.0013
Na	0.3372	-0.1608	1.0000	0.4872	0.4034	0.1762	0.1620	0.3088	0.2438	0.5573
K	0.1424	-0.3254	0.4872	1.0000	0.5848	-0.3802	-0.6197	0.2325	-0.1774	-0.0117
Ti	0.5335	-0.0253	0.4034	0.5848	1.0000	-0.1767	-0.4078	0.6748	0.1835	0.0614
P	0.3594	0.4804	0.1762	-0.3802	-0.1767	1.0000	0.6877	0.1875	0.1239	-0.0246
As	0.0177	0.3942	0.1620	-0.6197	-0.4078	0.6877	1.0000	-0.2106	0.3386	0.4304
Ba	0.7565	-0.0777	0.3088	0.2325	0.6748	0.1875	-0.2106	1.0000	0.0572	-0.2058
Cd	0.3519	0.2351	0.2438	-0.1774	0.1835	0.1239	0.3386	0.0572	1.0000	0.5667
Co	-0.0164	-0.0013	0.5573	-0.0117	0.0614	-0.0246	0.4304	-0.2058	0.5667	1.0000
Cr	0.3063	-0.0815	-0.0805	0.1553	0.0330	0.0119	-0.0589	0.1580	0.0912	-0.1507
Cu	0.1159	-0.2309	-0.0341	0.5847	0.5636	-0.3355	-0.7320	0.4284	-0.2596	-0.4780
Mo	0.2447	0.2219	0.2833	-0.4376	-0.0786	0.5089	0.8232	0.0015	0.5950	0.4595
Ni	0.0624	-0.1946	0.4902	0.1252	0.0423	-0.2138	0.2419	-0.1899	0.5689	0.8207
Pb	0.0962	0.0102	0.5912	-0.1517	-0.1311	0.3112	0.6697	-0.1062	0.4483	0.8421
Sr	0.2480	0.5428	0.0110	-0.5578	-0.0054	0.6557	0.7682	0.0886	0.4892	0.2177
V	0.1423	0.3264	0.1400	-0.4587	-0.1016	0.6586	0.6871	0.1397	0.3687	0.0551
Zn	0.0257	-0.2475	0.5309	0.3351	0.1089	-0.3135	-0.0320	-0.1263	0.3039	0.6718
Y	-0.1592	0.3831	-0.1137	-0.7153	-0.3312	0.5168	0.7066	-0.2162	0.2078	0.1583

Supplementary Table 3. Continued

	Cr	Cu	Mo	Ni	Pb	Sr	V	Zn	Y
Latitude	-0.1116	-0.3894	0.4491	0.6778	0.8809	0.1701	0.1563	0.6207	0.0714
Longitude	0.0356	0.3801	-0.4319	-0.6611	-0.8764	-0.1588	-0.1793	-0.6015	-0.0352
Depth	0.0909	0.4499	-0.2059	-0.4605	-0.6602	-0.1485	-0.0780	-0.5253	-0.1262
[Oxy]	0.0400	0.4426	-0.2989	-0.6101	-0.7848	-0.1408	-0.0709	-0.6149	-0.0547
Fe	0.0845	0.3745	-0.1643	-0.6702	-0.5190	0.1893	0.2357	-0.5346	0.0298
Mn	-0.1010	-0.3320	0.7793	0.6015	0.7038	0.5932	0.5317	0.3567	0.3809
Fe/Mn	0.1253	0.4082	-0.7058	-0.8540	-0.7993	-0.3312	-0.2838	-0.5395	-0.2450
Si	0.1547	0.6572	-0.7980	-0.5776	-0.7337	-0.6487	-0.4900	-0.2777	-0.5970
Al	0.2832	0.5293	-0.4549	-0.5357	-0.6512	-0.3132	-0.2808	-0.3737	-0.4349
Si/Al	-0.2698	-0.1335	-0.0741	0.2600	0.3265	-0.1336	-0.0022	0.3230	-0.0049
Mg	0.3063	0.1159	0.2447	0.0624	0.0962	0.2480	0.1423	0.0257	-0.1592
Ca	-0.0815	-0.2309	0.2219	-0.1946	0.0102	0.5428	0.3264	-0.2475	0.3831
Na	-0.0805	-0.0341	0.2833	0.4902	0.5912	0.0110	0.1400	0.5309	-0.1137
K	0.1553	0.5847	-0.4376	0.1252	-0.1517	-0.5578	-0.4587	0.3351	-0.7153
Ti	0.0330	0.5636	-0.0786	0.0423	-0.1311	-0.0054	-0.1016	0.1089	-0.3312
P	0.0119	-0.3355	0.5089	-0.2138	0.3112	0.6557	0.6586	-0.3135	0.5168
As	-0.0589	-0.7320	0.8232	0.2419	0.6697	0.7682	0.6871	-0.0320	0.7066
Ba	0.1580	0.4284	0.0015	-0.1899	-0.1062	0.0886	0.1397	-0.1263	-0.2162
Cd	0.0912	-0.2596	0.5950	0.5689	0.4483	0.4892	0.3687	0.3039	0.2078
Co	-0.1507	-0.4780	0.4595	0.8207	0.8421	0.2177	0.0551	0.6718	0.1583
Cr	1.0000	-0.0522	-0.0908	-0.1028	-0.0587	-0.1603	-0.1735	-0.1394	-0.2779
Cu	-0.0522	1.0000	-0.4926	-0.2965	-0.5611	-0.3620	-0.2333	-0.0893	-0.5434
Mo	-0.0908	-0.4926	1.0000	0.4468	0.6077	0.8011	0.7618	0.0183	0.5649
Ni	-0.1028	-0.2965	0.4468	1.0000	0.7151	0.0472	-0.0342	0.8055	-0.1052
Pb	-0.0587	-0.5611	0.6077	0.7151	1.0000	0.3486	0.2611	0.5602	0.2099
Sr	-0.1603	-0.3620	0.8011	0.0472	0.3486	1.0000	0.8093	-0.2263	0.6622
V	-0.1735	-0.2333	0.7618	-0.0342	0.2611	0.8093	1.0000	-0.2796	0.6077
Zn	-0.1394	-0.0893	0.0183	0.8055	0.5602	-0.2263	-0.2796	1.0000	-0.3019
Y	-0.2779	-0.5434	0.5649	-0.1052	0.2099	0.6622	0.6077	-0.3019	1.0000

[1] The 95% and 99% Confidence Levels for this correlation coefficient matrix based on N value of 33 are 0.3444 and 0.4384, respectively; coefficients above these values are considered significant at that confidence level

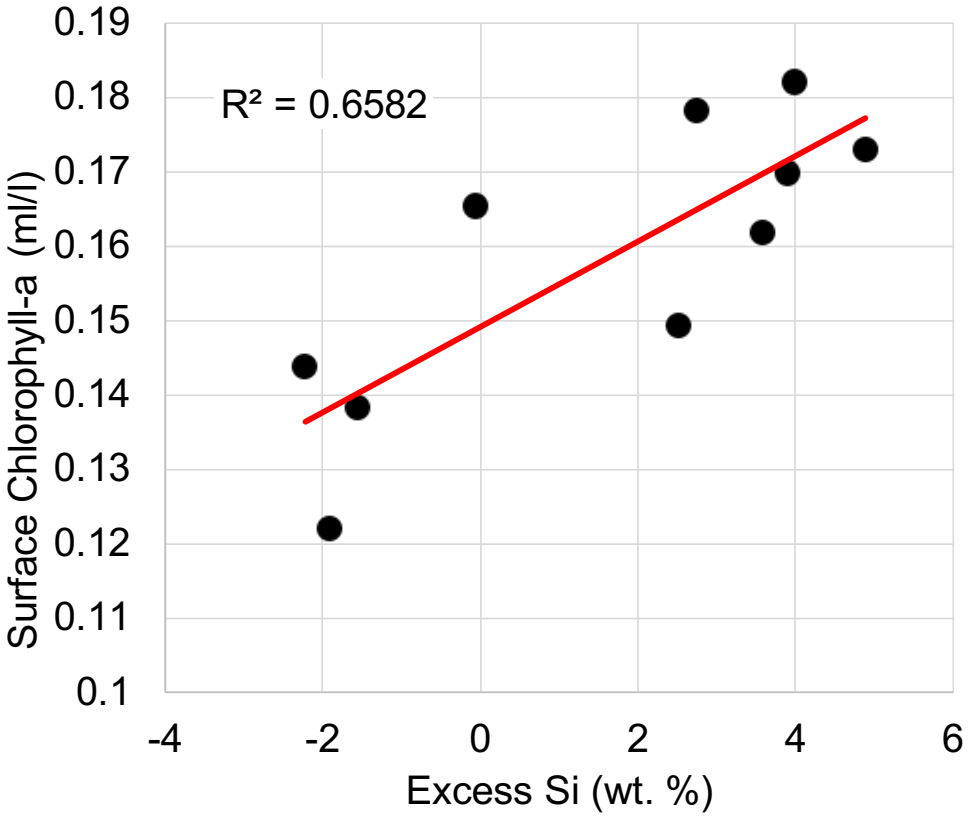

Figure S1. Plot of surface chlorophyll values (NASA MODIS Aqua, April 2019) versus excess silica for the ten FeMn crust samples within the EUZ. Excess silica was calculated by multiplying the Si/Al for average ocean island basalt (3.37; Dasgupta, Jackson, and Lee 2010) by the Al concentration for each FeMn crust and then subtracting this theoretical Si concentration from the measured Si concentration for each FeMn crust. Negative values thereby signify samples with no excess contribution to the total Si concentration in the crust beyond the expected detrital input whereas positive values do exceed the expected contribution.

Chapter 2.

Mineral associations and speciation of Pb in phosphatized ferromanganese crusts from the Pacific Ocean

Abstract

The older layers of most thick FeMn crusts from the central Pacific Ocean have undergone diagenetic phosphatization, during which carbonate-fluorapatite (CFA) filled fractures and pore spaces and replaced carbonates in the FeMn crusts. The effects of phosphatization on individual trace metal concentrations, speciation, and phase associations in FeMn crusts remain poorly understood. Sequential leaching provides a primary determination of the host phase for elements in FeMn crusts. Such leaching has indicated that Pb may be transferred from the oxide phases to diagenetic CFA in phosphatized crusts. Consequently, this study was initiated to determine whether the mineral associations of Pb in the phosphatized portion of FeMn crusts differ from those in non-phosphatized layers and to determine whether Pb-bearing minerals form during phosphatization. Seven phosphatized FeMn crust layers from 3 different thick crusts from the Pacific were analyzed. The concentration of Pb in bulk ferromanganese crust layers correlates with Mn and anticorrelates with P and Ca. μ-XRF mapping in-situ of FeMn crusts in thin-section confirm correlation of Pb with Mn as well as Fe and verifies anticorrelation of Pb with Ca, especially in CFA-rich fracture fill and veins. Both XANES and EXAFS measurements reveal that Pb speciation in bulk phosphatized FeMn crust layers are very similar to non-phosphatized layers and nullifies the hypothesis that Pb undergoes a major phase

transfer or change in speciation during diagenetic phosphatization. We propose that the high Pb concentration measured in the residual CFA fraction during sequential leaching is due to re-adsorption of Pb during the preceding reductive steps to remove Mn oxides and Fe oxyhydroxides. Small differences in the EXAFS spectra for one highly phosphatized layer (43% CFA) compared with other phosphatized layers, and linear combination fitting of leached CFA data, indicate that small amounts of Pb phosphate or other unidentified Pb mineral may form and contribute to the mass balance of Pb in phosphatized FeMn crusts. Further research is required to confirm the precise speciation of Pb in phosphatized FeMn crusts.

1. Introduction

Ferromanganese (FeMn) crusts form by precipitation of iron and manganese oxides from seawater onto a rock substrate and are therefore considered hydrogenetic in origin. However, diagenetic processes also affect the crusts primarily through phosphatization. During phosphatization, abundant dissolved phosphate in seawater replaces the carbonate (mostly biogenic calcite) that fills pore space and fractures to form carbonate fluorapatite (CFA). There is also direct precipitation of CFA within the FeMn matrix pore-space that is likely accompanied by the partial dissolution or replacement of the framework oxide phases (Koschinsky et al. 1997) . Phosphatization occurs in the lower (older) layers of thick crusts, especially in the central Pacific Ocean where two major phosphatization events have been dated and described, one from 39 to 34 Myr ago and another from 27 to 21 Myr ago (Hein et al.

1993). Phosphatization is evident in FeMn crusts simply by measuring the sharp increase in phosphorus concentration when crossing the phosphatization boundary within the crust stratigraphic section (Ling et al. 1997). As a result of these diagenetic processes, sorbed trace elements may be released and either be depleted or enriched in the phosphatized crust layers.

The mineral associations of Pb may be uniquely affected by phosphatization. Sequential leaching experiments revealed the association of Pb with the iron oxyhydroxide (FeOOH) phase in purely hydrogenetic (non-phosphatized) FeMn crust layers (Koschinsky and Hein 2003). This association was explained by the dominant complexation of Pb with carbonate or chloride in seawater (Byrne 2002) and therefore forms a neutrally charged complex that is attracted to the slightly positively charged surface of FeOOH at the pH of seawater. However, statistical correlations for the bulk element concentration of crusts from throughout the Pacific Ocean show Pb concentrations correlate with both Fe and Mn concentrations, suggesting that Pb sorption to the Mn-oxide phase is also possible (Hein et al. 2000). The uptake of Pb by Mn-oxide has been well-documented in contaminated soil environments (Ross et al. 2000) as well as reported for laboratory studies of both biogenic and synthetic Mn-oxides (Villalobos et al. 2005), so the sorption of Pb onto the Mn-oxide phase of FeMn crusts is a viable process, especially when Pb^{2+} is available. Takahashi et al. (2007) confirmed that Pb is indeed associated with both the Fe and Mn phases of FeMn crusts through a detailed study of Pb speciation in non-phosphatized FeMn crust layers using x-ray absorption spectroscopy. Takahashi et al. (2007) found that

Pb can bind to both the tridentate sites at chain terminations in Fe oxides as well as at layer edges in Mn-oxide phyllomanganates, and suggested that the degree to which Pb associates with Fe or Mn can be related not only to the charge of the Pb species, but also to shifts in chemical equilibria between the Mn and Fe binding sites, and/ or the growth rate of the crusts.

In contrast to the association of Pb with Fe or Mn in non-phosphatized FeMn crusts, more than 95% of Pb in phosphatized crust layers was measured in the residual fraction dominantly composed of CFA during sequential leaching experiments (Koschinsky and Halbach 1995; Koschinsky and Hein 2003). The association of Pb with CFA in phosphatized FeMn crust layers means that Pb may vacate the FeOOH phase during diagenesis, which is in part evidenced by the decrease of FeOOH in phosphatized crust layers in leaching experiments (Koschinsky and Halbach 1995). Lead may then either replace Ca in the CFA structure or co-precipitate as stable lead phosphate, in accordance with other CFA studies (e.g. Nathan 1984). Lead isotopic data measured in FeMn crusts show that phosphatization occurs rapidly and in a nearly closed system, since Pb isotopic ratios do not deviate across the phosphatization boundary between hydrogenetic crust layers and phosphatized crust layers (e.g., Christensen et al. 1997). This further supports the notion of phase transfer for Pb since the enrichment of Pb in the CFA fraction cannot be explained by further addition of Pb from seawater during diagenesis.

While the sequential leaching experiments create impetus to study the speciation of lead and its potential transfer from the oxide phase to the CFA phase during

phosphatization of FeMn crusts, it is possible that chemical processes during the leaching have instead determined the mineral associations of Pb. Notably, Pb is a highly reactive element and the re-adsorption of dissolved ions onto residual solid phases during sequential leaching experiments can occur (Rendell and Batley 1980; Gilmore et al. 2001), and apatite in soils effectively sorbs Pb(II) from aqueous solutions (Kaludjerovic-Radoicic and Raicevic 2010). This type of sorption reaction is possible for FeMn crust leaching when Pb is released into solution after reduction of the oxide phases, which could then sorb onto the solid, residual CFA particles in the reaction vessel.

In order to reconcile the mineral associations of Pb in phosphatized crusts and to investigate the potential effects of sequential leaching on Pb associations in experimental settings, we employ synchrotron-based x-ray absorption and fluorescence techniques in this study. By researching the effects of phosphatization on Pb in FeMn crusts, we elucidate a process by which diagenesis may control trace element accumulation and speciation. This provides an important contribution to a more complete genetic model for metal acquisition and preservation in FeMn crusts at quantities far beyond that of average crustal abundance and seawater concentrations.

2. Samples

FeMn crusts studied here include three phosphatized samples from the Pacific Ocean seamount sites (Table 1). Phosphatized and non-phosphatized crusts and crust layers were determined using visual textural characteristics as well as mineralogy

from x-ray diffraction and chemical analyses including P content. All FeMn crust samples consist principally of poorly crystalline Mn-oxide (δ-MnO_2, vernadite), x-ray amorphous FeOOH, and minor (<10%) goethite and or detrital components (quartz, plagioclase, pyroxene). The phosphatized crust layers also contain CFA (Table 2). The P concentration in all phosphatized crusts in this study is greater than or equal to 3.31 wt. %, whereas non-phosphatized crusts have a mean P concentration of 0.51 wt. % (Table 1).

3. Methods

3.1. Preparation of Pb-sorbed end-member model compounds

To emulate the sorption of Pb onto the three main mineral phases in phosphatized FeMn crusts, we prepared three sorption samples that would contain sufficient total Pb for synchrotron analyses: (1) synthetic δ-MnO_2 (vernadite), (2) synthetic δ-FeOOH (feroxyhyte), and (3) natural, pure CFA from a seamount in the equatorial Pacific. These substrates are representative end-member phases for those that occur in the Fe-rich and Mn-rich crust layers (Varentsov et al. 1991; Hein et al. 2000), as well as phosphatized layers. For the CFA, we used the CFA substrate of a Mn crust and leached the minor Mn- and Fe-oxide phases from the sample with hydroxylamine hydrochloride followed by oxalate buffer (Koschinsky and Halbach 1995).

δ-MnO_2 was prepared similar to procedures described in Catts and Langmuir (1986) and Luo and Suib (1997). The following solutions were prepared: (1) 75.14 g $MnCl_2 \cdot 4H_2O$ in 1280 mL ultrapure (UP) water, (2) 40.00 g $KMnO_4$ in 1280 mL UP

water, and (3) 28 g NaOH in 1440 mL UP water. Solution (2) was added slowly (5 min total time) to solution (3) while stirring vigorously. Solution (1) was added slowly (35 min total time) to the above mixture while stirring vigorously to form a black precipitate (approximately 50 g). The suspension was left to settle and, after 4 h, the supernatant solution was siphoned. The pH was 7.0. The remaining suspension was transferred to centrifuge bottles and centrifuged for 20 min at room temperature. The supernatant solution was discarded. The centrifuged paste was mixed with 1 mol/L NaCl, shaken for 1 h and centrifuged, then the supernatant solution was discarded. This was repeated five times. The centrifuged paste was combined with UP water, shaken for 1 h and centrifuged; then the supernatant solution was discarded. The wash cycle was repeated 10 times. The final pH value after washings was adjusted to 8.0 using NaOH. The precipitate was finally centrifuged, air-dried, and stored under ambient conditions. It is generally determined that δ-MnO_2 is predominantly, but not entirely Mn^{4+}; its average mean oxidation state has been reported to range from 3.6-4.0 in natural and lab-produced samples (Stashchuk et al., 1994; Manceau et al., 2014; Grangeon et al., 2017; Zhu et al., 2017), which increases with time in natural Fe-Mn crust samples when stored in air and analyzed shore-based rather than ship-based immediately when collected (Stashchuk et al., 1994).

Feroxyhyte is a poorly ordered form of δ-FeO(OH) whose synthesis conditions are most similar to what might exist in seawater or at the seawater-sediment interface; poorly ordered feroxyhyte and ferrihydrite are difficult to distinguish (Murad and Schwertmann 1988) and when clearly identified commonly occur together in natural

FeMn deposits (Marcus et al. 2015; Maciąg et al. 2019). Feroxyhyte was synthesized according to the following method (Schwertmann and Cornell 2000): 5M NaOH was added dropwise to a vigorously stirred, 0.1 M Fe^{2+}-Cl solution (300 ml volume, made by dissolving fresh $Fe^{2+}Cl_2*4H_2O$ crystals in acidified water), then filtered. The initial solution pH was 3; when it reached 8, a green precipitate formed. After rapid addition of 40 ml of 30% H_2O_2 to the mixture, it turned from green to reddish-brown in a violent reaction, and the pH dropped. The pH was raised back to 8 by dropwise addition of 5M NaOH (with stirring), after which the precipitate was washed thoroughly with UP water, centrifuged, and air-dried. Unlike with δ-MnO_2, feroxyhyte prepared in this manner has no detectable less-oxidized phase (Fe^{2+}) remaining, all was oxidized to Fe^{3+}.

For the sorption procedure, 0.5 g each of lab-made feroxyhyte, lab-made MnO_2, and seamount CFA were added to their own respective polyethylene bottles containing 0.5 L of filtered seawater spiked to a final concentration of 50 μM Pb(II) and adjusted to pH 7.5. The bottles were placed on a shaker for 3 days, after which samples were filtered and the mineral solids were air dried in a desiccator.

3.2. Lead and major element concentration in bulk FeMn crust layers

Layers for each FeMn crust were sampled with a knife based on visual textural delineation and then ground to ~75 μm with an agate mortar and pestle. The chemical composition of the Fe-Mn crusts was determined at SGS Labs, Canada. Iron, Mn, Ca, and P were determined by X-Ray Fluorescence (XRF) on borate fused disks, and Pb

by inductively coupled plasma mass spectrometry and atomic emission spectroscopy (ICP-MS and ICP-AES) following a 4-acid digest. The water content (H_2O^-) of each FeMn crust sample was determined by gravimetric analysis at 105° C for 24 hours, and the weight percent sorbed water was then used to correct element concentrations in each sample to sorbed-water-free values. Water corrections were not performed for CFA samples due to minimal sorbed-water content.

3.3. X-ray diffraction mineralogy

X-ray diffraction mineralogy was determined using a Panalytical X'Pert^3 Powder diffractometer with Cu-kα radiation and graphite monochromator. Diffraction peaks were identified and mineral patterns were matched using Phillips X'Pert High Score software. Semiquantitative mineral percentages were calculated by using peak intensities and weighting factors relative to quartz set as 1 (Cook et al., 1975; Hein et al., 1988). The detection limit for each mineral is between about 0.2% and 1.0%, except for the manganese minerals, for which the limits are greater, probably as much as 10% for δ-MnO_2.

3.4. Bulk x-ray absorption spectroscopy collection

The speciation of Pb in Fe-Mn crusts was investigated with Pb LIII-edge (E_0 = 13035 eV) x-ray absorption spectroscopy (XAS). XANES and EXAFS data were collected at Beam Line 11-2 at Stanford Synchrotron Radiation Lightsource (SSRL) for Pb in hydrogenetic and phosphatized FeMn crust samples and a variety of model

compounds, including Pb sorbed onto synthetic iron and manganese oxides and marine CFA as well as Pb-phosphate and Pb-oxide compounds (Table 3). BL11-2 was equipped with collimating and focusing optics, a "double double" Si(220) LN2-cooled monochromator, and a 100-pixel monolithic solid state Ge detector array. Monochromator energy was calibrated by collecting the absorption edge of a lead foil standard, where the first maximum of the first derivative spectrum was defined as 13035 eV. However, in all XANES plots, spectra were shifted 4eV higher in order to compare with data from Takahashi et al. (2007) and Bargar et al. (1998) to account for differences in energy calibration. The XAS data collected by Takahashi et al. (2007) was calibrated to the energy of the absorption maxima of PbO_2, which was 13061.5 eV in their study and 13057.6 in the current study (~4 eV less). All FeMn samples and mineral model compounds were run in powder form, diluted with powdered sugar when necessary, and packed in a sample holder with Kapton tape on either side. A minimum of three scans were collected in fluorescence mode for all samples.

3.5. Microfocused x-ray fluorescence mapping and x-ray absorption spectroscopy collection

Microfocused x-ray fluorescence (XRF) maps and XAS of samples in polished thin section (PTS; 30 μm thick) were collected on beamline 2-3 at SSRL using a water-cooled double crystal monochromator with either a Si(111), Si(220), or Si(400) crystal and a vortex single element detector (SII Nano Technology, Northridge, CA).

Monochromator energy was calibrated by collecting the absorption edge of a lead foil standard, where the first maximum of the first derivative spectrum was defined as 13035 eV. Element mapping was performed with a microfocused beam (~2x2 μm) provided by a Pt-coated Kirkpatrick-Baez mirror pair (Xradia Inc.), with 25-ms dwell time, and in 20 μm steps for coarse maps and 3 μm steps for fine maps. A thin section was placed directly in front of the X-ray beam tuned to 13,500 eV, above the Pb LIII absorption edge. The XRF maps were analyzed using the Sam's Microprobe Analysis Toolkit (SMAK), version 1.5 (S. M. Webb, n.d.). Each map was linearly scaled from lowest counts (black) to highest counts (white). The highest intensities for Pb, Fe, Mn, and Ca were 500, 14,800, 7400, and 2700 cps, respectively. Microfocused XAS data were collected over an extended XANES region (12,804− 13,304 eV) using the same beam conditions as for the mapping.

3.6. XAS Data Analysis

XAS spectra were analyzed using SIXPACK (version 1.4; S. Webb, n.d.). Spectra were averaged and then the absorption edge (XANES) and extended X-ray absorption fine structure (EXAFS) portions of the spectra were extracted for analysis. Backgrounds were subtracted using a linear fit to the pre-edge region (-210 to -100 eV below edge for bulk samples and -210 to -30 for μXAS samples) that was extended through the spectrum. Spectral step heights were normalized using a quadratic post-edge correction (100 or 125 to 570 eV for bulk and 5 to 250 eV for μXAS above edge. Normalized micro-scale XANES spectra were smoothed using the

boxcar average algorithm in Athena with a kernel size of five (Ravel and Newville 2005). Linear combination fitting (LCF) of EXAFS data was performed from 1 to 8.35 $Å^{-1}$, negative fits were not allowed and the components were not summed to one. Energy shifting of the data was permitted in SIXPACK to correct for insufficient energy calibration during data collection; the maximum shift was -0.029 eV. Several iterations of LCF were performed in order to minimize chi-squared values and thereby improve the fits. In the first fit of the series, all model compounds were included, and in subsequent fits, model compounds with component fractions less than 0.001 were removed and the fit was run again with remaining model compounds; this process was repeated six times. Once the combination of model compounds that generated the best fit to the data were identified, those components alone were reloaded and fit to the data, and this sum, chi-squared, and fit pattern were used for the final results.

4. Results

4.1. Pb content and correlations in bulk non-phosphatized and phosphatized layers of FeMn crusts

In the older, phosphatized sections of the FeMn crusts in this study (D11-1, D11-3, and CD29-2), the average concentrations of Fe, Mn, and Pb, as determined by XRF or ICP-MS and ICP-AES of bulk powders, for all three samples decreased by 36%, 25%, and 21%, respectively, from the average composition of the entire younger, non-phosphatized sections (Table 4). The phosphatized section of D11-3 shows the

largest decrease in Fe concentration (-42%) from its non-phosphatized section, while D11-1 shows the largest decrease in both Mn and Pb concentrations (-35% and -36%, respectively). To test if the decrease of Fe, Mn, and Pb concentrations is simply due to dilution from the addition of CFA to the FeMn crust matrix, a conservative two-component-mixing calculation was made with non-phosphatized Fe-Mn crust material and seamount CFA from the north-central Pacific (NCP; Halbach et al. 1987) as end-members. Based on the P concentration of the respective average phosphatized crust, we calculated mixing ratios between average non-phosphatized crust and NCP CFA of 1 : 0.55 for D11-3, 1 : 0.86 for D11-1, and 1 : 0.44 for CD29-2 (see Table 4 for equation). The calculated theoretical Pb, Mn, and Fe concentrations were less than the actual average concentration for the entire non-phosphatized section of each respective crust, except Fe in D11-3, which was more depleted than the expected value by 1.41 wt. % (Table 4). Depletion of Fe, Mn, and Pb that is less than expected may indicate one or more of the following: CFA precipitated within the FeMn crust matrix can actually contain more Fe, Mn, and Pb than the NCP CFA endmember taken from a seamount, which would elevate the contribution to element totals from CFA; the concentration of P observed in the phosphatized layers is not entirely due to formation of CFA, and phosphate may be sorbed to Mn-oxide or incorporated into other minor element phases that are measured in bulk analyses; Fe, Mn, and Pb are forming additional minor mineral phases that enrich their concentration beyond that of a two-component mixture.

Bulk concentrations of Fe, Mn, Pb, Ca, and P from stratigraphic layers (10s of mm thick; Figure 1A). The patterns seen in the concentrations of Fe, Mn, and Pb suggest that Pb may be correlated with either Mn or Fe in the non-phosphatized layers, depending on the sample. No significant correlations were observed in scatter plots for all non-phosphatized crust layers combined. In contrast, Pb changes with the same pattern as Mn in the phosphatized layers. Further, in the sublayers of the phosphatized portion of crusts D11-1 and CD29-2, Pb is anticorrelated with Ca and P. Correlation plots also show that Pb has a strong correlation with Mn (99% confidence level) and the Mn/Fe ratio (95% confidence level), while there is no correlation of Pb with Fe and anticorrelation of Pb with Ca and P in the phosphatized layers of the FeMn crusts (Figure 1B). For all samples, Pb is less concentrated in the phosphatized layers. The layer concentration data therefore imply that Pb may not be enriched in the CFA fraction of the crusts, contrary to the results from sequential leaching, and that Pb may be more associated with the Mn phase than the Fe phase in the phosphatized FeMn crusts studied here.

4.2. Element correlations from μXRF maps

μXRF mapping of polished thin sections provide further evidence that Pb is not associated with the CFA phase in phosphatized FeMn crusts. Zones of high lead concentration co-occur with Fe and/or Mn (Figure 2). Calcium, which was chosen as the representative element for the CFA phase, is instead highly concentrated in places where little to no Pb can be detected. Correlation plots of the intensity for Pb, Mn, Fe,

and Ca at each pixel confirm the visual interpretations of the μXRF maps. Lead is highly correlated with Fe in the maps for CD29-2 and D11-3. In the map for D11-1, there is no significant correlation of Fe with Pb for pixels in the Fe and Mn-rich laminae; however, Fe is positively correlated Pb in the cracks and fractures filled with CFA (yellow outline in Figure 2). Manganese shows a strong positive correlation with Pb in D11-3 yet no significant correlation with Pb in CD29-2, and similar to Fe, Mn is only correlated with Pb in the CFA cracks and fractures of D11-1. Calcium has no significant correlation with Pb in CD29-2, Ca is anti-correlated with Pb in the CFA-rich fractures in D11-1, and Ca appears to anti-correlate with Pb in D11-3, however the R^2 value is low. While these in-situ and micro-scale measurements provide visual confirmation and pixel intensity correlations that indicate that Pb does not correlate with Ca, and thereby CFA, XAS is required for more definitive characterization of Pb speciation in phosphatized FeMn crusts.

4.3. Pb speciation of bulk phosphatized FeMn crust layers from XANES

XANES of the Pb LIII edge in FeMn crusts are nearly featureless and therefore hold little information about lead mineralogy and coordination environment; however, the XANES spectra are important for determining the oxidation state of Pb in the FeMn crust layers through comparison with mineral model compounds of known Pb oxidation states. First derivative plots of the XANES spectra for phosphatized and non-phosphatized FeMn crust layer samples as well as PbO (orthorhombic) and PbO_2, show that the FeMn samples resemble PbO (Figure 3).

Orthorhombic PbO is a Pb(II) mineral species while PbO_2 is a Pb(IV) species. The evidence for this speciation can be seen in the first derivative plots of the XANES spectra. PbO_2 undergoes an electron transition from 2p → 6s levels during XAS due to its Pb(IV) speciation, which shows a characteristic peak at approximately 13.03 keV (Takahashi et al. 2007; Bargar et al. 1998). In contrast, PbO cannot undergo this electron transition due to being a Pb(II) species and therefore has both 6s levels filled. Since all of the FeMn crust spectra do not contain the characteristic peak at 13.03 keV and instead resemble PbO, it is confirmed that the oxidation state of Pb in phosphatized FeMn crust layers remains as Pb(II), its speciation in seawater and in non-phosphatized crusts. The speciation of Pb as Pb (II) in non-phosphatized layers of FeMn crusts was first confirmed by Takahashi et al. (2007).

4.4. Characterization of non-phosphatized FeMn crust and synthesized mineral model compounds

In order to determine if Pb speciation changes between the non-phosphatized and the phosphatized portion of FeMn crusts, we measured Pb LIII-edge EXAFS of a non-phosphatized and phosphatized FeMn crust as well as Pb sorbed to synthetic FeOOH and MnO_2. We first determine if EXAFS of phosphatized crust exhibit differences from non-phosphatized crusts. We then examine whether potential variations seen in the EXAFS of phosphatized crusts might be explained by changes in the dominant association of Pb with Fe or Mn, as seen previously for non-phosphatized crusts (e.g. Takahashi et al. 2007), or instead due to a true change in

speciation such as transfer to the CFA phase. The stacked EXAFS spectra (Figure 4) for non-phosphatized and synthetic samples illustrates that each of the three patterns are distinct, especially between 4.5 and 5.8 $Å^{-1}$. The synthetic Pb-sorbed MnO_2 sample (PB_MNO2L) has a pattern that is the most unique in this group, with a second peak that is shifted to higher k compared to the other two samples as well as a broad shoulder in the third peak at approximately 5.2 $Å^{-1}$. This synthetic MnO_2 sample resembles a synthetic δ-MnO_2 spectra from Takahashi et al. (2007) that is characterized as a well-crystallized birnessite (PbBi31). The LCF of D11-1B using the two lab-synthesized model compounds (PB_MNO2L and PB_FEOOHL) results in a poor fit with chi-squared of 0.016 and sum of 0.527 (Figure 4). Thus, the natural non-phosphatized crust sample, D11-1B, is not well-described by the lab compounds and is valid as a model compound itself. The spectral variety demonstrated in our natural and synthetic non-phosphatized samples confirm that end-members for Pb sorption onto Fe oxides (PB_FEOOHL) and a relatively crystalline Mn oxide (PB_MNO2L), as well as a natural mixture of poorly crystalline Mn and Fe oxides (D11-1B) are represented in the library of model compounds.

4.5. Pb speciation of bulk phosphatized FeMn crust layers from EXAFS

Stacked plots of Pb LIII-edge EXAFS spectra in k-space in Figure 5 illustrate that all phosphatized crust layers have similar oscillations, except D11-1G which shows a shifted oscillation between 7 and 8 $Å^{-1}$ that is unique from the rest. Iterative LCF of each spectra revealed that phosphatized crust samples D11-1E, D11-1F, D11-1H,

CD29-2D, and CD29-2E were best fit (chi-squared minimized) by a linear combination of non-phosphatized FeMn crust layer D11-1B (>0.70 for all) and the mineral PbO (<0.28 for all; Table 5). This two-component fit also maximized the sum of the fractions. However, fitting the samples with D11-1B alone only slightly increased the chi-squared values (max 3.6E-03) and marginally decreased the sum of fractions (max 0.07). Indeed, the visual similarity of the non-phosphatized D11-1B EXAFS with the EXAFS of phosphatized layers is evident (Figure 5). These data provide strong evidence that the speciation of Pb did not change during the diagenetic process of phosphatization. The exception is layer D11-1G, for which the spectra is best fit by a linear combination of D11-1B, leached CFA sample D11-3-6, and the mineral boleite ($KPb_{26}Ag_9Cu_{24}(OH)_{48}Cl_{62}$). However, the sum of the fractions for these components is only 0.80 (Table 5), and the EXAFS oscillations for boleite are quite different (Figure 5). When D11-1G is fit with the non-phosphatized layer, D11-1B, alone, the fit is worse but the sum is increased to 0.82. The low sum and high residual for the fitting of D11-1G indicates that this layer is not only different from other phosphatized layers but may have a different Pb speciation than the non-phosphatized layers. In addition, the library of model compounds does not include a mineral that matches the Pb species observed in D11-1G.

4.6. Pb speciation in leached residuals from phosphatized FeMn crusts

Samples D11-3-6 and D11-3-7 are the residual fractions of two layers of a phosphatized FeMn crust that have had the Fe and Mn oxides reductively removed;

both are composed of predominantly CFA (Table 2). The EXAFS spectra of these samples show distinctly different oscillation patterns compared to the bulk phosphatized FeMn crusts, especially the addition of a shoulder peak at ~4.7 $Å^{-1}$ (Figure 6). In addition, although the samples are from different individual layers, their spectra are similar, suggesting homogeneity in the bulk residual fraction among the phosphatized layers. Iterative LCF of the spectra determined that a three-component fit composed of PbO and synthetic lead phosphate ($Pb_3(PO_4)_2$) and the lab prepared model compound, Pb-sorbed to seamount CFA (Table 6). The fraction of Pb-sorbed CFA is 0.67 for D11-3-7 and only 0.48 for D11-3-6, which provides evidence that Pb may form Pb minerals during phosphatization, instead of simply undergoing sorption processes at the surface of CFA during phosphatization or during the experimental sequential leaching procedure.

5. Discussion

5.1. Contribution of PbO to linear combination fits

The best fit for all phosphatized FeMn crust layers, except D11-1G, included orthorhombic PbO as one of the two components. PbO, also called massicot or β-PbO is a rare natural mineral that can be produced as a minor oxidation product of galena and other lead-bearing minerals (Anthony et al., n.d.). PbO is not reported as a mineral found commonly in marine settings and has never been identified in FeMn crusts using x-ray diffraction or other mineralogy techniques, therefore we do not suggest that PbO is forming in FeMn crusts during phosphatization. Instead, the

contribution of PbO to the EXAFS spectra of Pb species in phosphatized FeMn crusts is attributed to the coordination of Pb with oxygen in the Pb-Mn-oxide and Pb-Fe-oxide structures. Takahashi et al. (2007) reported that EXAFS analysis of Pb in non-phosphatized FeMn crusts yielded Pb–O distances that are similar to those in β-PbO (2.21 and 2.49 Å; Leciejewicz 1961), and thereby interpreted that lead atoms are likely coordinated at the apex of a distorted pyramid, similar to that of orthorhombic PbO. Because we have found no major difference between the EXAFS for non-phosphatized and most phosphatized crusts, we assume that Pb coordination in our samples is also similar to β-PbO in alignment with the conclusions of Takahashi et al. (2007).

5.2. Possibility of micro-scale changes in Pb speciation

The XAS measurements in this study are of bulk powders of phosphatized FeMn crust layers, which means that the contribution of small scale, individual Pb-rich spots in-situ within crusts may be overwhelmed by the bulk material. In order to observe variability in Pb speciation throughout the phosphatized layers on a finer scale, μXANES of various Pb-rich locations determined by XRF mapping throughout polished thin sections of FeMn crusts were measured at SSRL beamline 2-3. Plots of five μXANES from the phosphatized portion of sample D11-3 are shown in Figure 7. The overall shape of the main peak is similar to the bulk XANES spectrum of D11-1H, a typical phosphatized crust layer in this study, which suggests that no major changes to Pb speciation occur at the micro-scale. However, two samples exhibit

slight shoulder peaks at approximately 13,034 eV (spot 35 and 36), and one sample has a shoulder peak at approximately 13,032 eV (spot 38), which is close to the 2p → 6s transition peak seen in PbO_2 that is a signature of Pb(IV) speciation at 13,029 eV (Figure 3). The signal to noise ratio for these microscale scans is low as evidenced by the jagged nature of the spectra even with boxcar average smoothing, so visual feature identification from the spectra is not definitive and LCF fitting was not warranted. Further research to produce XANES spectra with increased signal to noise ratio and quality data in the EXAFS region may show slight variations in Pb speciation in phosphatized FeMn crusts on the micro-scale, but no major deviation from bulk layers is observed in these data.

5.3. Lead speciation related to the degree of phosphatization

The majority of phosphatized FeMn crust samples studied here fit well with the spectra of non-phosphatized crust layer D11-1B, indicating that phosphatization does not change the speciation of Pb for most FeMn crust samples. D11-1G is the only sample to deviate significantly from this pattern and is also the layer that has been the most heavily phosphatized, as evidenced by the highest Ca and P concentrations (21.3 and 8.45 wt. %, respectively) as well as the highest percentage of CFA (43%) determined by XRD. This suggests that there may be a threshold for the degree of phosphatization that can alter the speciation of Pb in the crust matrix. If the degree of phosphatization is simply cumulative over time, older FeMn crust layers with more phosphatization events incurred since their deposition will experience a higher degree

of phosphatization. In contrast to this expectation, layer D11-1H, the deepest and oldest layer of FeMn crust D11-1, does not contain more CFA, P or Ca than younger layer D11-1G or the other phosphatized layers D11-1E and D11-1F. The degree of phosphatization may also be caused by the amount of carbonate sediment originally entrained in a FeMn crust at the onset of phosphatization – more carbonate material can lead to more diagenetic replacement by CFA. Higher carbonate contents can reflect greater porosity of the primary FeMn crust or may be caused higher deposition rates of biogenic calcite during primary crust formation.

Furthermore, the degree of phosphatization may be influenced by the oceanographic conditions during the phosphatization event, such as the extent of the oxygen minimum zone and associated reducing conditions or extreme seawater phosphate concentrations. Two major episodes of phosphatization have been described by Hein et al. (1993) in phosphorites from equatorial Pacific Seamounts. The first occurred at ~37 Ma near the late Eocene/ earliest Oligocene boundary, while the second episode took place at ~25 Ma near the late Oligocene/ early Miocene boundary. Minor events were also suggested from Sr isotope dating of phosphorite material at 71 Ma, 31 Ma, and 15 Ma (Hein et al. 1993). The age model developed for FeMn crust D11-1 indicates that layer D11-1G, which occurs at a depth below the surface of the crust between 95-135 mm, spans an approximate age of 61 to 42 Myr from the base of the layer to the top of the layer (Nielsen et al. 2009). This layer age range ensures that layer D11-1G was deposited before both major phosphatization

events, as well as two of the minor events, recorded by Hein et al. (1993). In order to determine if the intensity of a phosphatization event is the potential cause for changes in Pb-speciation in phosphatized crusts, precise ages throughout the stratigraphic section encapsulated by layer D11-1G must be measured. These ages can then be correlated with other paleoceanographic records that can explain which oceanographic conditions may have led to more intense phosphatization, and the associated textural features that would promote strong phosphatization.

5.4. Mass balance of Pb between mineral phases in phosphatized FeMn crusts

5.4.1. Lead speciation and enrichment in phosphatized layers

The similarity of Pb EXAFS spectra for non-phosphatized and phosphatized FeMn crust layers provides strong evidence that the speciation of Pb does not undergo a major change in speciation or mineral association during phosphatization, contrary to the results of sequential leaching studies (Koschinsky and Halbach, 1995, Koschinsky and Hein 2003). We interpret the occurrence of >90% of the total Pb in the residual CFA fraction after sequential leaching to be the result of re-adsorption of Pb, that was put into the aqueous phase during reduction of the Fe- and Mn-oxides in the previous reductive leaching steps, to the surface of CFA. Gilmore et al. (2001) also found through Pb tracer experiments that up to 85% of Pb originating in the Fe and Mn-oxide phases of Pb-contaminated soils was re-adsorbed to residual phases during reductive leaching by hydroxylamine hydrochloride. Kinetic studies of Pb sorption to both hydroxyapatite and Lisina apatite (mostly composed of fluorapatite)

show that the majority of Pb is sorbed from solution in the first 5 minutes and reaches steady state in approximately 2 hours (Kaludjerovic-Radoicic and Raicevic 2010). The reductive leaching steps employed for the study of FeMn crusts include 24 hour and 12 hour stirring periods for the reduction of Mn and Fe-oxides, respectively, providing ample time for reabsorption to residual phases. In addition to EXAFS results, μXRF mapping of in-situ phosphatized FeMn crusts also revealed very low association of Pb with CFA-rich areas. Therefore, we conclude that sequential leaching generates a false association of Pb with the CFA phase in phosphatized FeMn crusts. Despite this conclusion, mass-balance equations (Table 4) determine that Pb in phosphatized crusts is generally less diluted by the addition of CFA to the oxide matrix than expected, and that small contributions of Pb beyond the original non-phosphatized crust and pure CFA may exist. Furthermore, the poor fit of EXAFS for the leached, residual CFA samples with the lab-made, Pb-sorbed CFA demonstrate the possible presence of non-reducible Pb species other than Pb sorbed to the surface of CFA.

5.4.2. Potential for the formation of Pb-phosphates

Samples D11-3-6 and D11-3-7 are the residual fractions from the reductive leaching of Fe and Mn oxides from two phosphatized FeMn crust layers. Their mineral composition was identified using powder XRD as containing more than 93% CFA and the remainder pyroxene (Table 2). From XRD, we assumed that the majority of Pb in the residual fractions is sorbed to the surface of CFA or substituted

for Ca^{2+} in CFA during phosphatization, or sorbed to CFA during reductive leaching when Pb^{2+} was put into solution. However, the EXAFS spectra of D11-3-6 and D11-3-7 were fit with a linear combination of Pb-sorbed CFA (48 and 67%), PbO (47 and 15%), and lead phosphate ($Pb_3(PO4)_2$; 39 and 52%; Table 6). The formation of lead phosphate minerals during phosphatization has been proposed (Koschinsky et al. 1997; Koschinsky and Hein 2003), and thermodynamic considerations indicate that the formation of the nearly insoluble Pb phosphate, (chloro-pyromorphite ($Pb_5(PO_4)_3CI$), is most probable (Koschinsky 1994), though formation of $Pb_3(PO4)_2$ is also possible in soil when Pb(II) is available (e.g. Cao et al. 2008). The formation of pyromorphite in nature is almost exclusively reported for soil systems in which the kinetics are controlled by pH and the formation of pyromorphite is increased under acidic conditions below that of seawater (Miretzky and Fernandez-Cirelli 2008). However, the formation of (chloro- or hydroxy-pyromorphite was measured in chlorinated drinking water at ~pH 8 when phosphate was supplied to solution (Lytle et al. 2009). Due to the varying pH, ionic strength, and concentrations and forms of Pb and phosphate supplied to solution being very different for soil and seawater systems, pyromorphite formation in soils is prudently considered a model for pyromorphite formation in FeMn crusts.

To date, neither pyromorphite nor other lead phosphates have been identified in FeMn crusts using XRD, Raman spectroscopy, SEM-EDX, or XAS. XRD analyses of marine phosphorites from throughout Pacific, formed by diagenetic phosphatization that is not associated with FeMn crusts, also did not identify lead phosphate minerals

(Hein et al. 1993); Hein et al. 2016; Benninger and Hein 2000). The overlay of the three-component fit with EXAFS spectra of D11-3-6 and D11-3-7 show that residuals are high (Figure 6), and the sum of the fit is also >1 for both samples (Table 6). In addition, Figure 6 shows that EXAFS oscillations for pyromorphite (sample PbPO4Cl) are generally dissimilar to EXAFS of the leached CFA samples, and that lead phosphate EXAFS (sample Pb_Phate), though more similar to CFA leaches, has key features that are absent in D11-3-6 and -7 such as the small shoulder peak at ~5.2 Å. Thus, the speciation of Pb in these samples does not definitively include lead phosphates. However, if lead phosphate does form during phosphatization it would be an important mineral sink for Pb in seawater and would contribute to the preservation of Pb in FeMn crusts over millions of years. Further investigation to confirm the presence of lead phosphate is defensible, including improved LCF with additional model compounds and shell-fitting XAS analysis.

5.4.3. Formation of other Pb-rich minerals

Phosphatized FeMn crusts may also contain a Pb species not included in the model compounds library used for LCF. For example, Pb^{2+} can also substitute for Ca^{2+} in the apatite structure of CFA due to their similar ionic radii (Pb^{2+} =119; Ca^{2+} = 100; (Nathan 1984), but there is not a model compound representing a Pb-rich CFA or apatite. Notably, the reference phosphorite, NCP CFA, used in the mass-balance calculations (See Section 4.1), contains only 15 ppm Pb (Halbach et al. 1987), and the mean concentration of Pb in phosphorite from open ocean seamounts is just 7 ppm

(Hein et al. 2016). The low concentration of Pb in these diagenetic phosphorites suggests that Pb substitution in CFA is not a significant contributor to total Pb concentration in phosphatized FeMn crusts, unless Pb substitution is more favorable within the chemical environment of the FeMn crust matrix during suboxic diagenesis compared to the non-FeMn-oxide rich environments.

6. Summary and Conclusions

Lead concentration and speciation in the hydrogenetic, non-phosphatized layers and the diagenetic, phosphatized layers of three FeMn crusts from the north central Pacific were investigated in this paper to address the potential transfer of Pb to diagenetic CFA phases during phosphatization as suggested using sequential leaching studies (Koschinsky and Halbach 1995; Koschinsky and Hein 2003). Bulk concentration data for the different crust layers show that Pb correlates with Fe and Mn in the non-phosphatized sections while Pb correlates with just Mn and anticorrelates with Ca and P (the main constituents of CFA) in phosphatized layers. μXRF mapping of in-situ polished thin sections of the phosphatized portion of FeMn crusts confirms anticorrelation of Pb with Ca, and correlations of Pb with both Fe and Mn in phosphatized layers. Statistical correlations from both bulk crust layers and micro-scale XRF measurements suggest that Pb is not enriched in CFA and can be associated with both the Fe and Mn phase in phosphatized layers.

XANES spectra illustrate that the oxidation state of Pb is Pb(II) in both non-phosphatized and phosphatized crusts. EXAFS spectra of six phosphatized older

layers from two FeMn crusts fit well with the spectra of a non-phosphatized crust layer and therefore demonstrate no major changes in the speciation of Pb in the phosphatized portions. We conclude from these XAS data that the association of Pb with the CFA phase seen in sequential leaching experiments is artificial and caused by the re-adsportion of Pb supplied by Mn and Fe oxides to residual CFA during the preceding reductive leaching steps.

One phosphatized crust layer, D11-1G, does exhibit minor differences in its EXAFS spectra compared to other layers. The chi-squared values for linear combination fits of D11-1G were minimized when the Pb-oxychloride mineral, boleite, and leached CFA residuals were included, which provides evidence that minor amounts of Pb phases may be present in some phosphatized layers that differ from those in non-phosphatized FeMn crusts. D11-1G is also the FeMn crust layer that was the most heavily phosphatized, which warrants further investigation into how the degree of phosphatization of a crust can affect the speciation of Pb and other trace metals.

Two samples of residual CFA that were obtained from phosphatized FeMn crusts using reductive leaching to remove Fe- and Mn-oxides are composed of >93% CFA as determined by XRD. In accordance with the conclusion that Pb will re-adsorb to CFA during reductive leaching, the residual CFA samples were expected to have the same Pb speciation as Pb-sorbed CFA that was created in the lab. However, the spectra for residual CFA samples are not identical to the Pb-sorbed CFA model compound, and the LCF that minimized chi-squared includes lead phosphate. The

possible inclusion of minor amounts of Pb phosphate or oxychloride minerals in the residual (non-reducible) portion of phosphatized FeMn crusts, as determined by LCF of EXAFS for highly phosphatized layer D11-1G and CFA residuals, is supported by mixing calculations. The expected concentration of Pb in phosphatized layers due to dilution, that is calculated from conservative mixing of non-phosphatized FeMn crust and diagenetic CFA from a nearby seamount, is lower than the actual concentration of Pb in the phosphatized portions of the three samples studied here. Thus, the intermediate depletion of Pb concentration suggests that minor Pb phases may be contributing to the total Pb concentration in phosphatized FeMn crust layers. However, EXAFS data presented here do not definitively define which Pb species are present in phosphatized crusts layers and instead show that large differences in Pb speciation do not exist between non-phosphatized and phosphatized crusts.

7. Acknowledgements

I would like to thank Dr. Andrea Koschinsky for her contributions to the initial experimental design and for preparation of laboratory-made mineral samples. I also thank Dr. Tracey Conrad, Lia Klofas, and Samantha Whisman for her their huge contributions to sample preparations and synchrotron data collection.

8. References

Anthony, J.W., Bideaux, R. A., Bladh, K. W., and Nichols., M. C. n.d. *Handbook of Mineralogy*. Chantilly, VA 20151-1110, US: Mineralogical Society of America. http://www.handbookofmineralogy.org.

Bargar, J. R., Brown, G. E., and Parks, G.A. 1998. "Surface Complexation of Pb(II) at Oxide-Water Interfaces: III. XAFS Determination of Pb(II) and Pb(II)-Chloro Adsorption Complexes on Goethite and Alumina." *Geochimica et Cosmochimica Acta* 62 (2): 193–207. https://doi.org/10.1016/S0016-7037(97)00334-7.

Benninger, L. M., and Hein, J. R. 2000. "Diagenetic Evolution of Seamount Phosphorite." *Marine Authigenesis: From Global to Microbial*, no. 66: 245–56. https://doi.org/10.2110/pec.00.66.0245.

Byrne, R. H. 2002. "Inorganic Speciation of Dissolved Elements in Seawater: The Influence of PH on Concentration Ratios." *Geochemical Transactions* 3 (1): 11–16. https://doi.org/10.1039/b109732f.

Cao, X., Ma, L. Q., Singh, S. P., and Zhou, Q. 2008. "Phosphate-Induced Lead Immobilization from Different Lead Minerals in Soils under Varying PH Conditions." *Environmental Pollution* 152 (1): 184–92. https://doi.org/10.1016/j.envpol.2007.05.008.

Catts, J. G., and Langmuir, D. 1986. "Adsorption of Cu, Pb and Zn by ΔMnO2: Applicability of the Site Binding-Surface Complexation Model." *Applied Geochemistry* 1 (2): 255–64. https://doi.org/10.1016/0883-2927(86)90010-7.

Christensen, J. N., Halliday, A. N., Godfrey, L. V., Hein, J. R., and Rea, D. K. 1997. "Climate and Ocean Dynamics and the Lead Isotopic Records in Pacific Ferromanganese Crusts." *Science* 277: 913–18. https://science.sciencemag.org/content/sci/277/5328/913.full.pdf.

Cook, H. E., Johnson, P. D., Matti, J. C., and Zemmels, I. 1975. Methods of sample preparation and X-ray diffraction data analysis (X-ray mineralogy laboratory, Deep Sea Drilling Project, Univ. of California Riverside), Initial Rep. Deep Sea Drill. Proj., 28, 999–1007.

Gilmore, E. A., Evans, G. J., and Ho, M. D. 2001. "Radiochemical Assessment of the Readsorption and Redistribution of Lead in the SM&T Sequential Extraction Procedure." *Analytica Chimica Acta* 439: 139–51. https://doi.org/10.1016/S0003-2670(01)01011-X.

Grangeon, S., Fernandez-Martinez, A., Claret, F., Marty, N., Tournassat, C., Warmont, F., and Gloter, A. 2017. "In-Situ Determination of the Kinetics and Mechanisms of Nickel Adsorption by Nanocrystalline Vernadite." *Chemical Geology* 459 (May): 24–31. https://doi.org/10.1016/j.chemgeo.2017.03.035.

Halbach, P., et al. 1987. "Untersuchung Der Co-Reichen Und Pt-Halti- Gen Erzkrusten in Den Submarinen Gebirgen Des Zentralpazi- Fi.~chen Beckens. Technical Cruise Report of the MIDP AC 3-SO 46 Research Project (BMFT, Project No. 03 R 373 A 8)."

Hein, J. R., Koschinsky, A., Bau, M., Manheim, F. T., Kang, J.-K., and Roberts, L. 2000. "Cobalt-Rich Ferromanganese Crusts in the Pacific." *CRC Marine Science Series* 17.

Hein, J. R., Koschinsky, A., Mikesell, M., Mizell, K., Glenn, C., and Wood, R. 2016. "Marine Phosphorites as Potential Resources for Heavy Rare Earth Elements and Yttrium." *Minerals* 6 (4): 88. https://doi.org/10.3390/min6030088.

Hein, J. R., Koschinsky, A., Bau, M., Manheim, F. T., Kang, J.-K. and Roberts, L. 2000. "Cobalt-Rich Ferromanganese Crusts in the Pacific." In *Handbook of Marine Mineral Deposits*, 17:239–79.

Hein, J. R., Yeh, H.-W., Gunn, S. H., Sliter, W. V., Benninger, L. M., and Wang, C.-H. 1993. "Two Major Cenozoic Episodes of Phosphogenesis Recorded in Equatorial Pacific Seamount Deposits." *Palaeogeography and Palaeoclimatology* 8 (2): 293–311.

Hein, J. R., Schwab, W. C., and Davis, A. S. 1988. "Cobalt- and Platinum-Rich Ferromanganese Crusts and Associated Substrate Rocks from the Marshall Islands." *Marine Geology* 78 (3–4): 255–83. https://doi.org/10.1016/0025-3227(88)90113-2.

Kaludjerovic-Radoicic, T., and Raicevic, S. 2010. "Aqueous Pb Sorption by Synthetic and Natural Apatite: Kinetics, Equilibrium and Thermodynamic Studies." *Chemical Engineering Journal* 160 (2): 503–10. https://doi.org/10.1016/J.CEJ.2010.03.061.

Koschinsky, A. 1994. "Geochemische Krustenprofile Und Sequentielle Laugungsversuche an Manganerzkrusten Aus Dem Zentralpazifik Zur Klaung von Genese Und Elementassoziationen." *Berliner Geowiss. Abh* A158: 192 pp.

Koschinsky, A., Stascheit, A., Bau, M., and Halbach, P. 1997. "Effects of Phosphatization on the Geochemical and Mineralogical Composition of Marine

Ferromanganese Crusts." *Geochimica Et Cosmochimica Acta* 61 (19): 4079–94. https://doi.org/Doi 10.1016/S0016-7037(97)00231-7.

Koschinsky, A., and Halbach, P. 1995. "Sequential Leaching of Marine Ferromanganese Precipitates: Genetic Implications." *Geochimica et Cosmochimica Acta* 59 (24): 5113–32. https://doi.org/10.1016/0016-7037(95)00358-4.

Koschinsky, A., and Hein, J. R. 2003. "Uptake of Elements from Seawater by Ferromanganese Crusts: Solid-Phase Associations and Seawater Speciation." *Marine Geology* 198 (3–4): 331–51. https://doi.org/10.1016/S0025-3227(03)00122-1.

Leciejewicz, J. 1961. "On the Crystal Structure of Tetragonal (Red) PbO." *Acta Crystallographica* 14 (12): 1304–1304. https://doi.org/10.1107/S0365110X61003892.

Ling, H. F., Burton, K. W., O'Nions, R. K., Kamber, B. S., von Blanckenburg, F., Gibb, A. J., and Hein, J. R. 1997. "Evolution of Nd and Pb Isotopes in Central Pacific Seawater from Ferromanganese Crusts." *Earth and Planetary Science Letters* 146 (1–2): 1–12. https://doi.org/10.1016/S0012-821X(96)00224-5.

Luo, J., and Suib, S. L. 1997. "Preparative Parameters, Magnesium Effects, and Anion Effects in the Crystallization of Birnessites." *J. Phys. Chem. B* 101 (49): 10403–13. https://doi.org/10.1021/JP9720449.

Lytle, D. A., Schock, M. R., and Scheckel, K. 2009. "The Inhibition of Pb(IV) Oxide Formation in Chlorinated Water by Orthophosphate." *Environmental Science & Technology* 43 (17): 6624–31. https://doi.org/10.1021/es900399m.

Maciąg, Ł., Zawadzki, D., Kozub-Budzyń, G. A. A., Piestrzyński, A., Kotliński, R. A. A.. and Wróbel, R. J. J. 2019. "Mineralogy of Cobalt-Rich Ferromanganese Crusts from the Perth Abyssal Plain (E Indian Ocean)." *Minerals* 9 (2): 84. https://doi.org/10.3390/min9020084.

Manceau, A., Lanson, M., and Takahashi, Y. 2014. "Mineralogy and Crystal Chemistry of Mn, Fe, Co, Ni, and Cu in a Deep-Sea Pacific Polymetallic Nodule." *American Mineralogist* 99 (10): 2068–83. https://doi.org/10.2138/am-2014-4742.

Marcus, M. A., Edwards, K. J., Gueguen, B., Fakra, S. C., Horn, G., Jelinski, N. A., Rouxel, O., Sorensen, J., and Toner, B. M. 2015. "Iron Mineral Structure, Reactivity, and Isotopic Composition in a South Pacific Gyre Ferromanganese Nodule over 4 Ma." *Geochimica et Cosmochimica Acta* 171 (December): 61–79.

https://doi.org/10.1016/J.GCA.2015.08.021.

Miretzky, P., and Fernandez-Cirelli, A. 2008. “Phosphates for Pb Immobilization in Soils: A Review.” *Environmental Chemistry Letters* 6 (3): 121–33. https://doi.org/10.1007/s10311-007-0133-y.

Murad, E., and Schwertmann, U. 1988. “Iron Oxide Mineralogy of Some Deep-Sea Ferromanganese Crusts.” *American Mineralogist* 73: 1395–1400.

Nathan, Y. 1984. “The Mineralogy and Geochemistry of Phosphorites.” In *Photosphate Minerals*, 275–91. Berlin, Heidelberg: Springer Berlin Heidelberg. https://doi.org/10.1007/978-3-642-61736-2_8.

Nielsen, S. G., Mar-Gerrison, S., Gannoun, A., LaRowe, D., Klemm, V., Halliday, A. N., Burton, K. W., and Hein, J. R. 2009. “Thallium Isotope Evidence for a Permanent Increase in Marine Organic Carbon Export in the Early Eocene.” *Earth and Planetary Science Letters* 278 (3–4): 297–307. https://doi.org/10.1016/j.epsl.2008.12.010.

Ravel, B., and Newville, M. 2005. “ATHENA, ARTEMIS, HEPHAESTUS: Data Analysis for X-Ray Absorption Spectroscopy Using IFEFFIT.” *Journal of Synchrotron Radiation* 12 (4): 537–41. https://doi.org/10.1107/S0909049505012719.

Rendell, P. S., and Batley, G. E. 1980. “Adsorption as a Control of Metal Concentrations in Sediment Extracts.” *Environmental Science & Technology* 14 (3): 314–18. https://pubs.acs.org/doi/pdf/10.1021/es60163a002.

Ross, D.S., Negra, C., and Lanzirotti, A. 2000. *Association of Lead with Soil Manganese Oxides*. *NSLS Activity Report 2000*. NSLS.

Schwertmann, U., and Cornell, R. M. 2000. *Chapter 7: Feroxyhyte*. *Iron Oxides in the Laboratory: Preparation and Characterization*. Weinheim: Wiley VCH.

Stashchuk, M. F., Chervonetsky, D. V., Kaplun, E. V., Chichkin, R. V., Avramenko, V. A., Tishchenko, P. Y., and Gramm-Osipov, L. M. 2014. “Adsoption Properties of Ferromanganese Crusts and Nodules.” In *Data and Results from R.V. Aleksandr Vinogradov Cruises 91-AV-19/1, North Pacific Hydrochemistry Transect; 91-AV-19/2, North Equatorial Pacific Karin Ridge Fe-Mn Crust Studies; and 91-AV-19/4, Northwest Pacific and Bering Sea Sediment Geochemistry and Pal*, edited by James R. Hein, A.S. Bychkov, and A.E. Gibbs, 93–98.

Takahashi, Y., Manceau, A., Geoffroy, N., Marcus, M. A., and Usui, A. 2007.

"Chemical and Structural Control of the Partitioning of Co, Ce, and Pb in Marine Ferromanganese Oxides." *Geochimica et Cosmochimica Acta* 71 (4): 984–1008. https://doi.org/10.1016/j.gca.2006.11.016.

Varentsov, I. M., Drits, V.A. A., Gorshkov, A.I. I., Sivtsov, A.V. V., and Sakharov, B.A. A. 1991. "Mn-Fe Oxyhydroxide Crusts from Krylov Seamount (Eastern Atlantic): Mineralogy, Geochemistry and Genesis." *Marine Geology* 96 (1–2): 53–70. https://doi.org/10.1016/0025-3227(91)90201-E.

Villalobos, M., Bargar, J., and Sposito, G. 2005. "Mechanisms of Pb(II) Sorption on a Biogenic Manganese Oxide." *Environ. Sci. Technol.* 39: 569–76. https://pubs.acs.org/doi/pdf/10.1021/es049434a.

Webb, S. n.d. "Sam's Interface for XAS Package (SIXPACK)." https://www.sams-xrays.com/sixpack.

Webb, S. n.d. "MicroAnalysis Toolkit." https://www.sams-xrays.com/smak.

Zhu, Y., Liang, X., Zhao, H., Yin, H., Liu, M., Liu, F., and Feng, X. 2017. "Rapid Determination of the Mn Average Oxidation State of Mn Oxides with a Novel Two-Step Colorimetric Method." *Analytical Methods* 9 (1): 103–9. https://doi.org/10.1039/C6AY02472F.

Table 1. Location information and element concentrations for FeMn crust layers and leached samples

Cruise ID	F10-89-CP	F10-89-CP	F10-89-CP	F10-89-CP	F10-89-CP	F10-89-CP	F10-89-CP	F10-89-CP
Sample Name	D11-3B	D11-3C	D11-3D	D11-1B	D11-1C	D11-1D	D11-1E	D11-1F
Layer Interval (mm)	0-25	25-45	45-79	0-9	9-35	35-43	43-65	65-95
Phosphatized	No	No	Yes	No	No	No	Yes	Yes
Longitude	161˚40.5'E	161˚40.5'E	161˚40.5'E	161˚40.5'E	161˚40.5'E	161˚40.5'E	161˚40.5'E	161˚40.5'E
Latitude	11˚38.9'N	11˚38.9'N	11˚38.9'N	11˚38.9'N	11˚38.9'N	11˚38.9'N	11˚38.9'N	11˚38.9'N
Avg Water Depth	1780	1780	1780	1780	1780	1780	1780	1780
Ocean	WC Pacific	WC Pacific	WC Pacific	WC Pacific	WC Pacific	WC Pacific	WC Pacific	WC Pacific
Fe (wt. %)	18.4	21.3	11.6	22.3	23.9	22.9	18.2	12.5
Mn	23.9	23.6	18.2	30.7	26.3	30.7	12.8	24.0
Mn/Fe	1.3	1.1	1.6	1.4	1.1	1.3	0.7	1.9
Ca	2.51	2.62	14.5	3.01	2.71	3.26	17.5	15.6
P	0.42	0.47	5.06	0.58	0.48	0.56	7.02	5.79
$H2O^-$	21.0	21.3	17.0	18.3	16.8	17.6	8.70	11.8
Pb (ppm)	1772	1398	1325	1983	1623	1687	612	1247

Table 1. Continued

Cruise ID	F10-89-CP	F10-89-CP	F7-86-HW	F7-86-HW	F7-86-HW	F7-86-HW	F10-89-CP	F10-89-CP
Sample Name	D11-1G	D11-1H	CD29-2B	CD29-2C	CD29-2D	CD29-2E	D11-3-6	D11-3-7
Layer Interval (mm)	95-135	135-180	0-9	9-49	49-76	76-105	54-60	56-74
Phosphatized	Yes	Yes	No	No	Yes	Yes	Leached CFA	Leached CFA
Longitude	161˚40.5'E	161˚40.5'E	168˚14.2'W	168˚14.2'W	168˚14.2'W	168˚14.2'W	161˚40.5'E	161˚40.5'E
Latitude	11˚38.9'N	11˚38.9'N	16˚42.4'N	16˚42.4'N	16˚42.4'N	16˚42.4'N	11˚38.9'N	11˚38.9'N
Avg Water Depth	1780	1780	2180	2180	2180	2180	1780	1780
Ocean	WC Pacific	WC Pacific	C Pacific	C Pacific	C Pacific	C Pacific	WC Pacific	WC Pacific
Fe (wt. %)	13.5	14.0	23.5	21.1	15.3	16.1	0.8	1.0
Mn	12.4	26.8	26.9	33.3	19.0	31.1	0.0	0.1
Mn/Fe	0.9	1.9	1.1	1.6	1.2	1.9	NA	NA
Ca	21.3	13.5	3.03	3.34	15.1	10.6	33.9	32.0
P	8.45	4.78	0.56	0.50	5.69	3.31	15.18	12.91
$H2O^-$	7.10	13.5	17.1	21.6	11.8	19.5	NA	NA
Pb (ppm)	873	1803	1966	1390	1007	1950	1648	3194

Table 2. X-ray diffraction mineralogy for crystalline phases of ferromanganese crust samples and residual isolates from leaching experiments reported as percentages

Sample Number	Layer Interval (mm)	δ-MnO_2 [1]	CFA [2]	Others	Type/Comments
		Cruise F7-86-HW			
CD29-2D	L49-76	81	17	3 - plagioclase	phosph. crust
CD29-2E	L76-105	88	12	0	phosph. crust
		Cruise F10-89-CP			
D11-1B	L0-9	96	0	4 - quartz	non-phosph. crust
D11-1E	L43-65	59	32	6 - goethite, 3 - pyroxene	phosph. crust
D11-1F	L65-95	70	28	2 - pyroxene	phosph. crust
D11-1G	L95-135	51	43	3 - goethite, 3 - pyroxene	phosph. crust
D11-1H	L135-180	73	27	0	phosph. crust
D11-3-6	L54-60	0	93	7 - pyroxene	Residual isolate
D11-3-7	L56-74	0	94	6 - pyroxene	Residual isolate

[1] turbostratically disordered hexagonal birnessite

[2] carbonate fluorapatite

Table 3. Model compounds used to fit phosphatized FeMn crust and leached residual carbonate fluorapatite samples

Type	Short Name	Description
Non-phosphatized	D11-1B	FeMn crust layer D11-1B (0-9 mm); Central Pacific
Pb sorbed to mineral substrates	Pb_FeOOHL	Pb sorbed onto lab produced FeO(OH) (feroxyhyte)
	Pb_MnO2L	Pb sorbed onto lab produced MnO_2 (turbostratically disordered hexagonal birnessite)
	Pb_CFA	Pb sorbed onto natural seamount carbonate fluorapatite, Pb_CFA
Pb minerals and compounds	PbPO4Cl	Pyromorphite; $Pb_5(PO_4)_3Cl$
	PbO_Orth	Lead monoxide (massicot); PbO, orthorhombic
	Boelite	Boleite; $Pb_{26}Cu_{24}Ag_{10}Cl_{62}(OH)_{48*}3H_2O$ diluted 15:70 ratio with powdered sugar
	Pb_Phate	Lead Phosphate; $Pb_3(PO_4)_2$ diluted 15:70 ratio with powdered sugar
	Pb_Pyrophate	Lead Pyrophosphate; $Pb_2P_2O_7$ diluted 15:70 ratio with powdered sugar

Table 4. Calculated values for the average concentration of elements in the enitre phosphatized portion of FeMn crusts [1,2]

		Fe	Mn	Pb*100	P	Ca
D11-1	% Difference from avg. non-P	-37%	-35%	-36%	1106%	466%
	Actual	14.54	18.99	11.34	--	--
	Theoretical	12.61	15.89	9.56	--	--
	Actual - Theoretical	1.93	3.11	1.78	--	--
D11-3	% Difference from avg. non-P	-42%	-23%	-16%	1040%	464%
	Actual	11.57	18.19	13.25	--	--
	Theoretical	12.97	15.47	10.28	--	--
	Actual - Theoretical	-1.41	2.72	2.97	--	--
CD29-2	% Difference from avg. non-P	-30%	-17%	-12%	750%	303%
	Actual	15.69	25.02	14.79	--	--
	Theoretical	15.56	20.97	11.67	--	--
	Actual - Theoretical	0.13	4.06	3.11	--	--

[1] All concentration values are in wt. %; non-P = non-phosphatized

[2] Equation for theoretical element concentration : ([non-P] + [NCP CFA]*mixing ratio) / (1 + mixing ratio) ; the mixing ratio was calculated by setting this equation equal to the P concentration in phosphatized crust, and values for [NCP CFA] for P, Fe, Mn, and Pb*100 are 13.46, 0.46, 0.36, 0.15 wt. %, respectively (Halbach et al. 1987)

Table 5. Linear combination fit results of bulk phosphatized FeMn crust layer EXAFS spectra for multi-component fits as well as single component fits with non-phosphatized FeMn crust layer D11-1B [1]

	Multi-component Fit				Single-component fit		
Sample	D11-1B	PbO	Sum	chi-sq.	D11-1B	Sum	chi-sq.
CD29-2D	0.74 (0.018)	0.24 (0.014)	0.98	1.31E-03	0.91 (0.027)	0.91	4.14E-03
CD29-2E	0.79 (0.016)	0.15 (0.012)	0.94	1.03E-03	0.90 (0.019)	0.90	2.09E-03
D11-1E	0.71 (0.016)	0.27 (0.011)	0.98	9.27E-04	0.91 (0.029)	0.91	4.53E-03
D11-1F	0.79 (0.017)	0.19 (0.012)	0.98	1.09E-03	0.93 (0.022)	0.93	2.91E-03
D11-1H	0.80 (0.016)	0.17 (0.012)	0.97	1.06E-03	0.93 (0.020)	0.93	2.51E-03
D11-1G [2]	0.56 (0.055)	Boleite: 0.13 (0.026); D11-3-6: 0.10 (0.034)	0.80	1.06E-03	0.82 (0.015)	0.82	1.32E-03

[1] Error associtiated with each calculated fraction is listed in parentheses

[2] D11-1G is the only sample for which a two component fit with D11-1B and PbO did not minimize chi-squared; the mineral components combined with D11-1B for the best fit are instead listed in the PbO column

Table 6. Linear combination fit results of EXAFS of the residual material produced from the reductive leaching of Fe and Mn oxides from phosphatized layers of FeMn crust D11-3

Sample	Pb-sorbed to CFA	PbO	$Pb_3(PO_4)_2$	Sum	chi-sq.
D11-3-6	0.48 (0.050)	0.47 (0.024)	0.39 (0.046)	1.3	1.62E-03
D11-3-7	0.67 (0.048)	0.15 (0.022)	0.52 (0.044)	1.3	1.58E-03

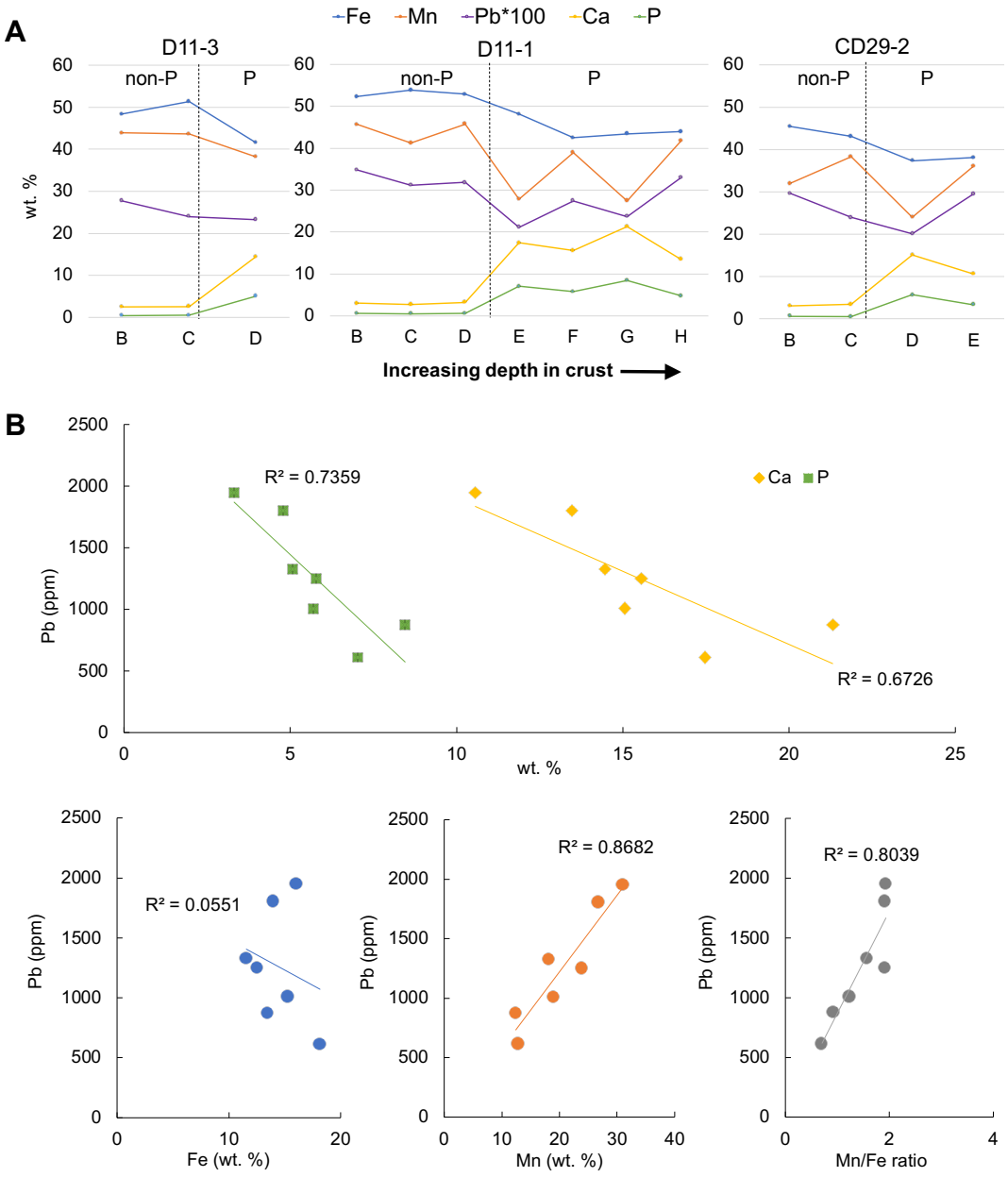

Figure 1. (A) Line plots showing changes in the concentration of Fe, Mn, Pb, Ca, and P throughout the individual bulk layers of FeMn crusts D11-3, D11-1, and CD29-2; layers for each sample increase in age and depth from the surface of the crust from left to right, and specific layer intervals are listed in Table 1; vertical dashed lines represent the onset of phosphatization – layers to the left of the line are non-phosphatized (non-P) and layers to the right are phosphatized (P). (B) Scatter plots of element concentrations and ratios in bulk phosphatized layers versus Pb concentration in the same layers; trendlines and R-squared values illustrate the strength of correlation between Pb and each element or ratio.

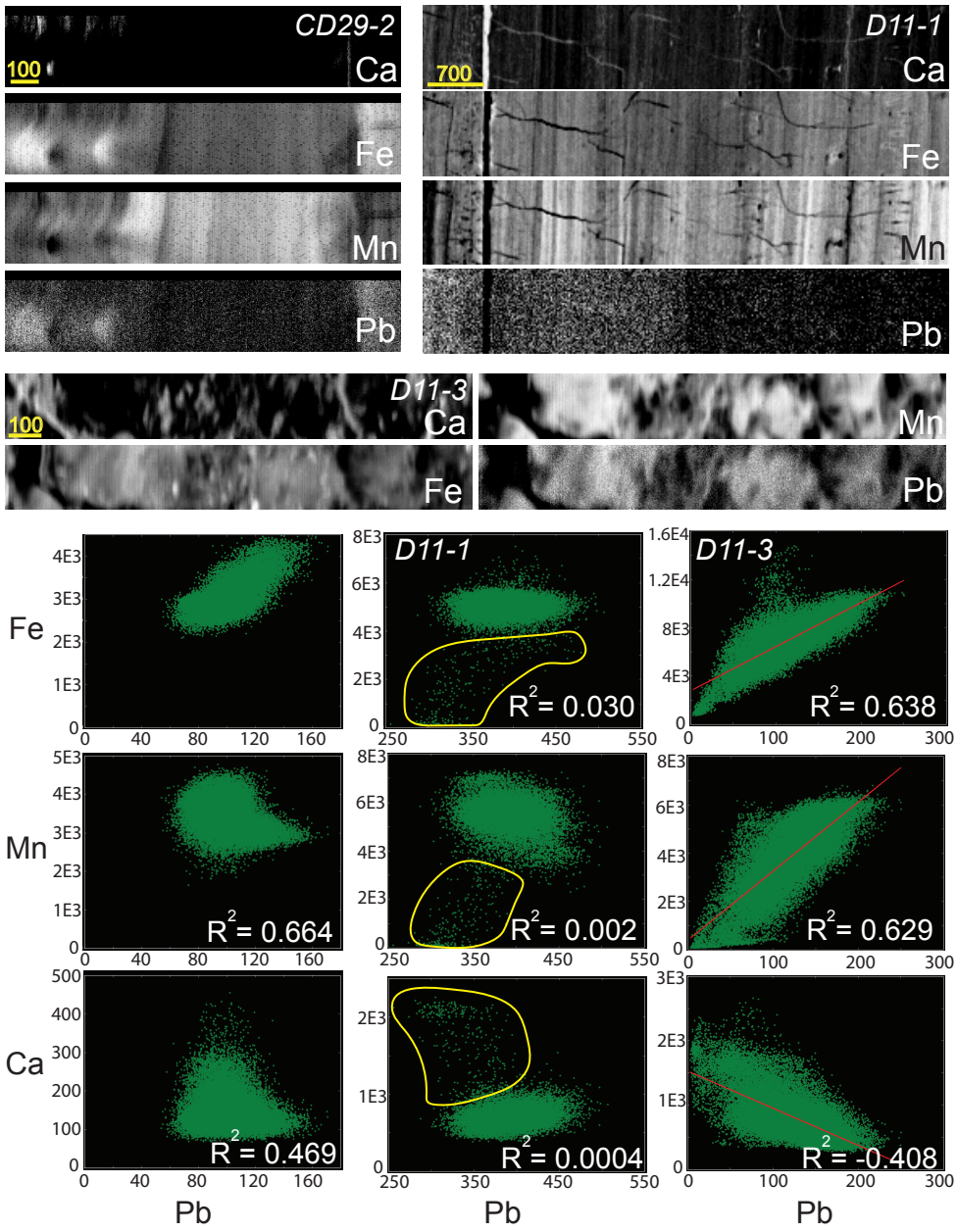

Figure 2. (Upper) XRF Maps of Ca, Fe, Mn, and Pb from thin sections of in-situ phosphatized FeMn crusts, CD29-2, D11-1, and D11-3, with white representing higher concentrations and yellow scale bars in micrometers; note that each map was scaled differently to maximize image clarity and therefore brightness intensities are not comparable between samples. (Lower) Element correlation plots generated from each respective XRF map above with data points representing fluorescence intensity for elements at each pixel; R^2 values illustrate the strength of correlation and trendlines are included in plots with clear and dominant linear trends; yellow outlines for D11-1 encompass pixels measured from CFA-filled cracks and fractures that distinctly fall outside the typically trend for the rest of the mapped areas.

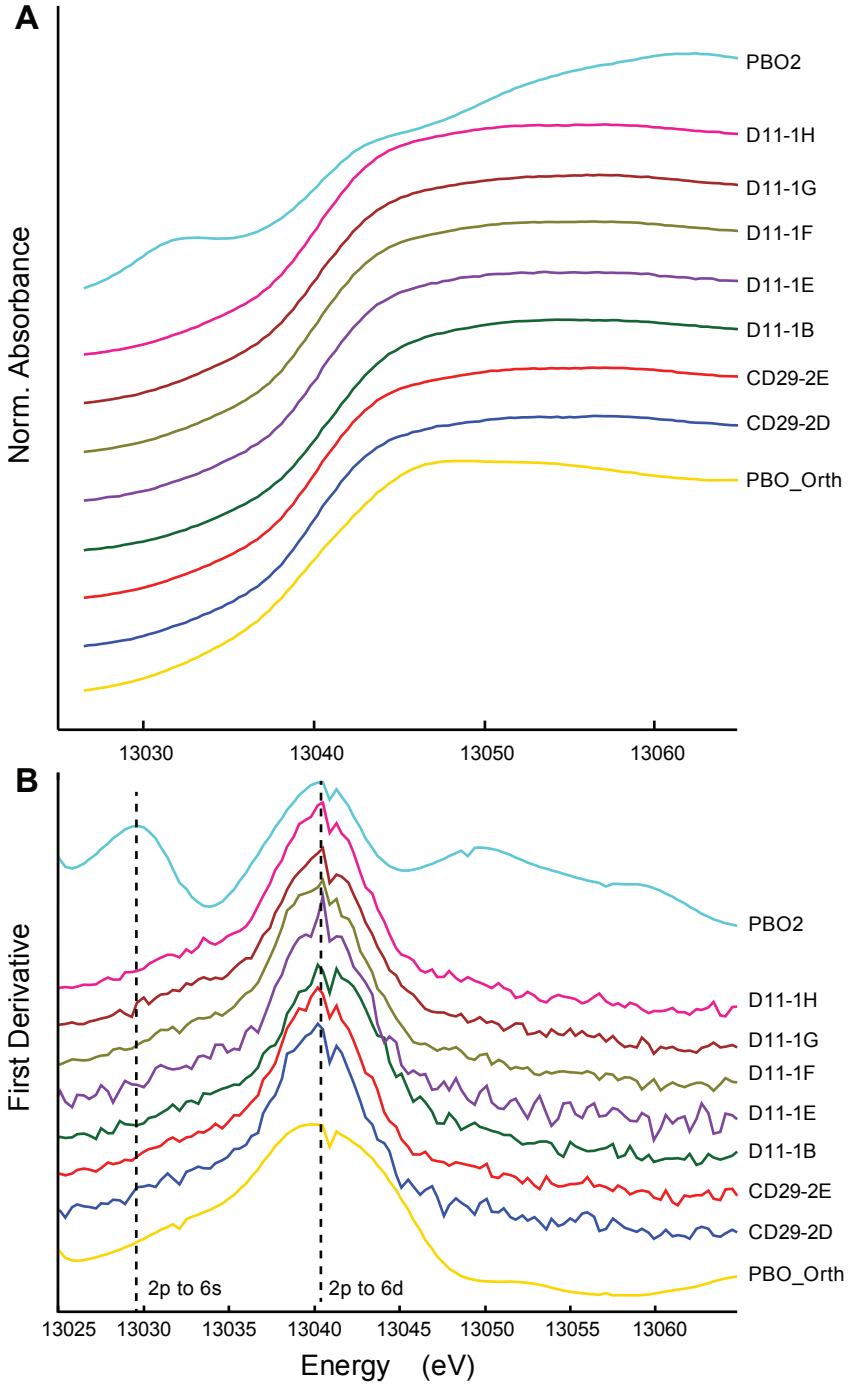

Figure 3. (A) Lead LIII-edge XANES spectra of non-phosphatized and phosphatized bulk FeMn crust powers and model compounds. (B) First derivative of XANES spectra from (A) with dashed lines that show energies where features occur that indicate signature electronic transitions.

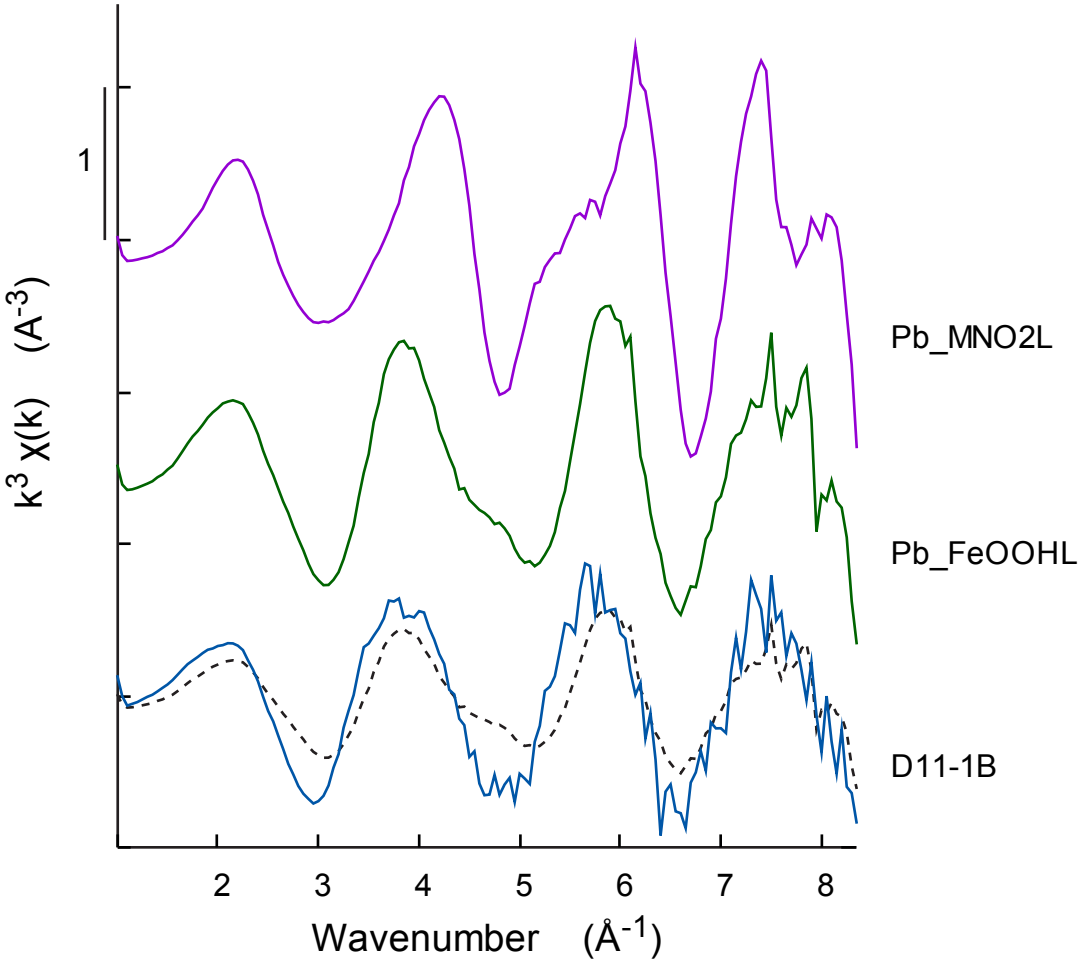

Figure 4. Lead LIII-edge EXAFS spectra for hydrogenetic, non-phosphatized crust D11-1B and end-member model compounds of Pb sorbed to lab-made MnO2 (Pb_MnO2L) and lab-made feroxyhyte (Pb_FeOOHL); LCF fit of D11-1B using Pb_MnO2L and Pb_FeOOHL as the components is shown in the dashed black line; the distance between tick marks for the vertical axis represent 1 $Å^{-3}$.

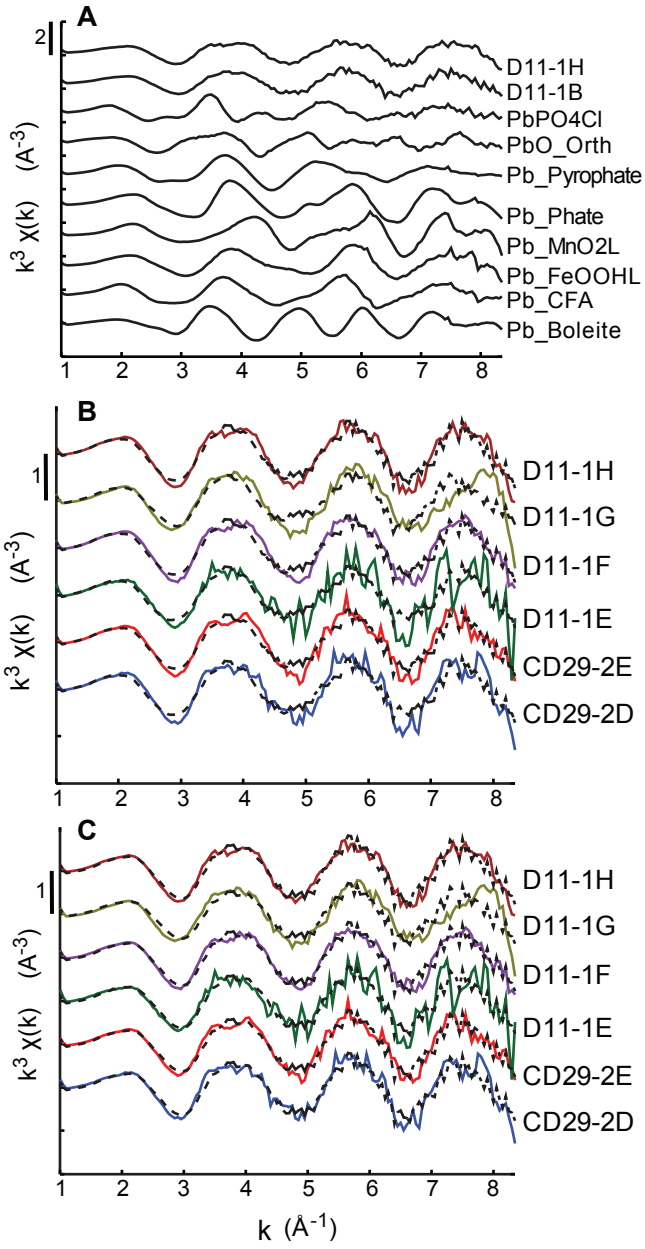

Figure 5. (A) Lead LIII-edge EXAFS spectra of model compounds (see Table 3 for descriptions) used for LCF of phosphatized FeMn crust layers and the spectra of a typical bulk phosphatized (D11-1H) and non-phosphatized (D11-1B) crust layer, for comparison; the distance between tick marks for the vertical axis represent 2 $Å^{-3}$; (B) EXAFS spectra for six bulk phosphatized FeMn crust layers (solid, colored lines) with the best 2-component fits (3-component fits for D11-1G) shown in dashed black lines; the distance between tick marks for the vertical axis represent 1 $Å^{-3}$; fit parameters in Table 5; (C) EXAFS spectra for the same six bulk phosphatized FeMn crust layers but with a single component fit of the non-phosphatized layer, D11-1B, shown in dashed lines; the distance between tick marks for the vertical axis represent 1 $Å^{-3}$.

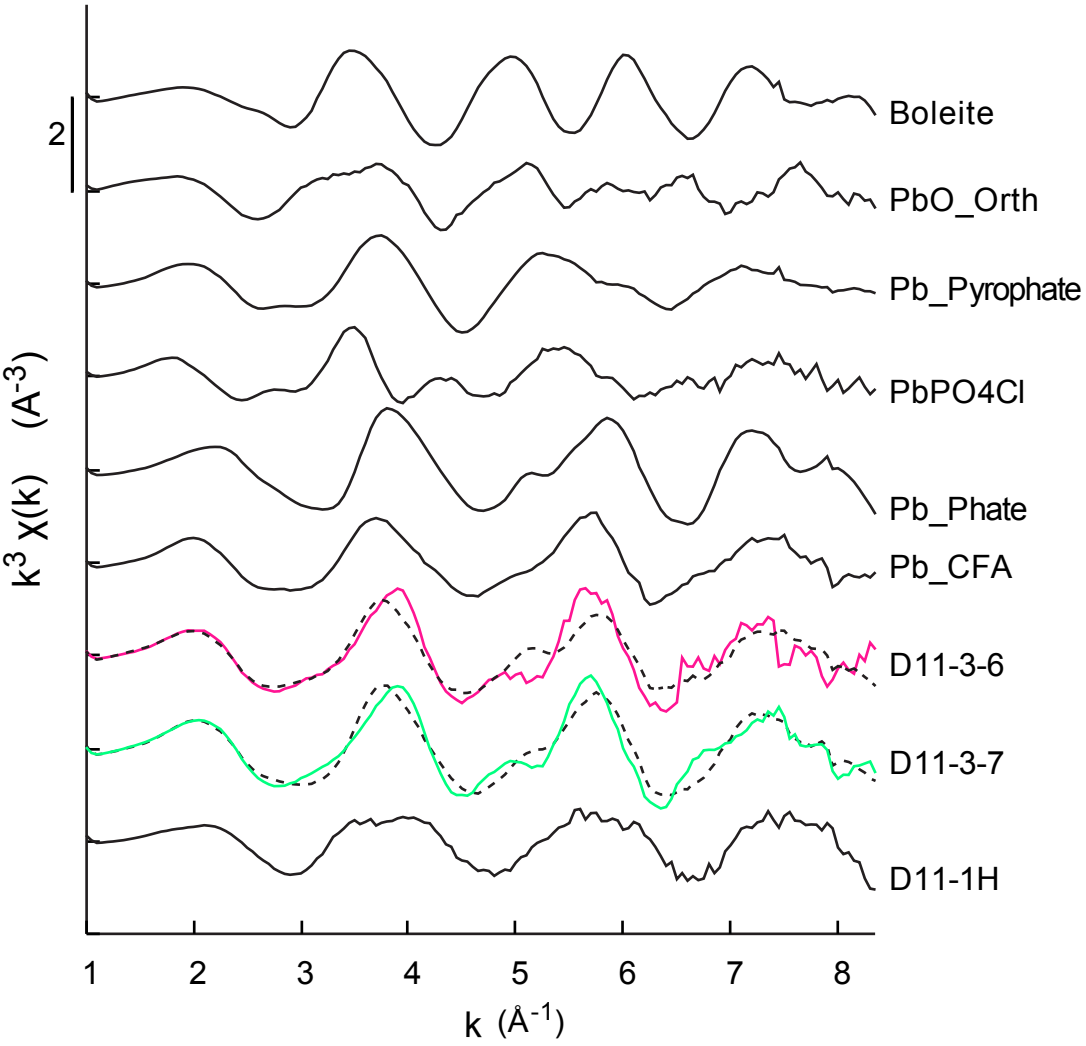

Figure 6. Lead LIII-edge EXAFS spectra of two leached residual samples, D11-3-6 and D11-3-7, with 3-component LCF shown in dashed lines and EXAFS spectra of model compounds used for the LCF as well as a representative bulk phosphatized crust layer, D11-1H, for comparison; the distance between tick marks for the vertical axis represent 2 $Å^{-3}$.

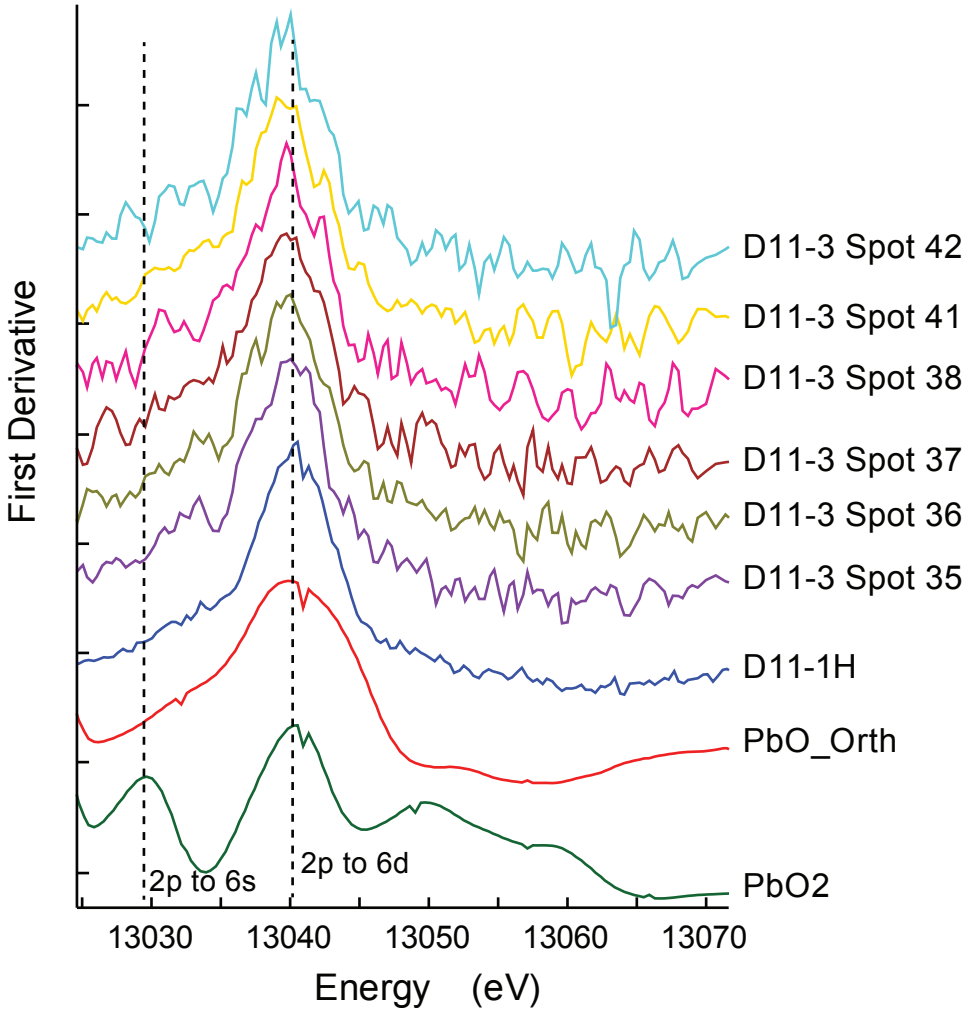

Figure 7. First derivative plots of lead LIII-edge XANES spectra for μXAS measurements of Pb-rich spots throughout a thin section of phosphatized crust, D11-3, typical phosphatized bulk FeMn crust layer, D11-1H, and model compounds; dashed lines show energies where features occur that indicate signature electronic transitions.

Chapter 3.

Ferromanganese Crusts from the Tuvalu Exclusive Economic Zone: Composition, Evolution, and Critical-Metal Resource Considerations

Abstract

This study expands on previous reconnaissance reports for ferromanganese (FeMn) crusts in the Tuvalu EEZ and provides a detailed characterization of genetic controls, mineralization processes, and critical mineral resource potential of Tuvalu FeMn crusts. Fifty-four FeMn samples from water depths between 2286 and 4110 m throughout the EEZ were analyzed. Tuvalu crusts are dominantly hydrogenetic and compositions are generally similar to those from the Prime Crust Zone (PCZ) in the northwest equatorial Pacific, where most studies have been conducted. FeMn crusts from Tuvalu show slight enrichments over the PCZ of Hg, Ag, Li, and Sc, the latter two of which are considered metals of critical importance. Lithium enrichment compared to PCZ crusts is attributed to the occurrence of Li-rich phillipsite, while higher Sc concentrations are likely due to increased dissolved Sc at the comparably deeper depths for crusts collected from Tuvalu. Within the Tuvalu EEZ, FeMn crusts at lower latitudes have slower growth rates and higher concentrations of Mn and Mn-oxide-associated metals, including Co, Ni, Cu, Te, Bi, Cd, and Te, related to the presence of a sustained oxygen minimum zone near the equator. Phosphatization was observed in one sample from a water depth of 3582 m, which is deeper than the depth limit (2500 m) of phosphatization in the Tuvalu region reported in other studies. FeMn crusts from shallower water depths in the Tuvalu EEZ have higher

concentrations of Mn, Co, Ni, and V than deeper-water crusts despite many shallow-water samples containing phosphatized layers. A permissive region for FeMn crusts of economic interest that warrants further exploration occurs in the southeastern portion of the EEZ where an extensive plateau presents reasonably flat and continuous summit areas between 500 and 3000 m water depths. A stratabound hydrothermal Mn sample was also collected from the southern portion of Tuvalu EEZ, which is composed of hydrothermally mineralized foraminifera ooze that is rich in Mn, Li, and Cd. The sediment was dated using biostratigraphy of the foraminifera, which provides an early Eocene age (~54 to 46 Ma) and suggests hydrothermal mineralization may have occurred shortly after seamount formation ~50 Myr ago, or during rejuvenation of volcanic activity associated with the Samoan Hotspot ~15 Myr ago.

1. Introduction

1.1 Ferromanganese crust characteristics

Ferromanganese (FeMn) crusts grow on the exposed, sediment-free surfaces of volcanic edifices throughout the global ocean. The primary mode of formation for FeMn crusts is hydrogenetic whereby colloidal hydrated metal oxides sourced from seawater accrete onto hard-rock surfaces. Hydrogenetic precipitation is very slow, with average growth rates of crusts being 1-10 mm/Myr (Hein et al. 2000). The extremely slow growth rates for crusts generate nanometer-structured iron and

manganese oxides with high specific surface area that creates a large capacity for the sorption and co-precipitation of additional metals. Thus, hydrogenetic FeMn crusts are on average enriched in critical metal concentrations ranging from ~10^5 to ~10^9 times that of seawater concentrations for As and Co, respectively, and ~5 to 10^4 times that of Earth's crust concentrations for Ti and Te, respectively (Hein and Koschinsky 2014). The degree of enrichment for individual trace metals is based on a variety of factors. The concentration of elements in the water masses that bathe the crusts can influence their composition. Proximity to an oxygen minimum zone that acts as a reservoir for dissolved Mn increases Mn contents and may decrease growth rates (Conrad et al. 2017; Mizell et al. *in review*), although that idea is still controversial for open-ocean seamount areas (Usui et al. 2017). The input of detrital material, if high enough, can increase growth rates and dilute trace-metal concentrations (Hein et al. 2017; Konstantinova et al. 2017).

1.2 Development of FeMn crust exploration

Due to their vast distribution and high concentrations of rare and critical metals, FeMn crusts are of interest as a potential mineral resource for critical metals. In July of 2012, the International Seabed Authority (ISA) passed regulations for the exploration of FeMn crusts in Areas Beyond National Jurisdiction (ABNJ) in accordance with the United Nations Convention for the Law of the Sea (UNCLOS), and exploitation regulations are set for release in the early 2020s. Many marine mineral deposits also exist within Exclusive Economic Zones (EEZs), such as those

of Tuvalu discussed here, and countries will likely use the regulations from the ISA as a model for their own marine mineral extraction protocols, since they have been rigorously developed. The Pacific Ocean has been best studied among the ocean basins for FeMn crusts because of the large number of seamounts scattered throughout the west-central part of the basin due to extensive hotspot volcanism since the Jurassic. The Prime Crust Zone (PCZ; Hein et al. 2009) encompasses an area of the western subtropical north Pacific where FeMn crusts are thick (up to 20 cm) and have high metal contents (summarized in Hein et al. 2013). Currently, there are four contracts with the ISA for exploration within the PCZ and one in the Atlantic, which demonstrates active interest in the resource potential of FeMn crusts. However, FeMn crust deposits are highly heterogeneous, even within the region of a single seamount or ridge (e.g. Yeo et al. 2019; Hein et al. 2016; Usui et al. 2017). Therefore, detailed studies that cover a wide range of locations and water-depths within an EEZ or lease area are required in order to determine resource potential based on crust thickness, distribution, and concentration of metals of interest.

1.3 Geological and oceanographic features of Tuvalu seamounts

The seamounts within the Tuvalu EEZ (Figure 1) are part of the Tuvalu chain formed by the Rurutu hotspot starting in the Ellice Basin around 60 Myr ago with the southernmost seamounts in the Tuvalu EEZ dated to be ~50 Ma old (Finlayson et al. 2018). The Tuvalu seamount ages provide ample time for the growth of thick crusts. For reference, the thickest FeMn crust recovered to date from the northwest Pacific is

more than 200 mm thick with a date for the initiation of crust growth of ~70 Myr ago (crust D11-1; Nielsen et al. 2009; Josso et al. 2019). For the southern seamounts of the Tuvalu EEZ, there may also be the potential for hydrothermal input to FeMn crusts because the Samoa Hotspot track crossed the Rurutu track ~15 Myr ago (Finlayson et al. 2018). FeMn crusts with hydrothermal input have a different mineralogy and typically contain higher amounts of Mn, V, and Li, but lesser amounts of the metals typically of economic interest in hydrogenetic crusts, Co, Cu, Ni, Te, and rare earth elements plus yttrium (REY; Hein et al. 2003). The major water mass reaching water depths of FeMn crusts in this study (>2200 m) is Antarctic Bottom water, which is cold and well-oxygenated. There is a slight gradient of increasing oxygen concentration with water depth from ~150-200 μmol/L within the depth range of FeMn crust locations (Garcia et al. 2014). A weak oxygen minimum zone, with oxygen concentrations as low as 100 μmol/L is present in the northern portion of the study area. This OMZ is the distal end of the Eastern Tropical South Pacific Oxygen Deficient Zone that is maintained along the equator due to slow ventilation (Figure 2). This OMZ may cause increased Mn and Mn-oxide associated elements in the crusts forming below it, as discussed above.

1.4 Previous studies

Limited composition and resource potential estimates of FeMn crusts from the Tuvalu seamounts were reported by Cronan and Hodkinson (1993). Their study included analyses of sixty samples from fourteen locations, but only mean

concentrations of Mn, Fe, Co, Ni, Cu, and Pt were reported. De Carlo et al. (1987) also reported chemical data for 12 elements for 18 FeMn crusts from two dredge sites in the Tuvalu EEZ. The study presented here expands upon these preliminary reports by the inclusion of more than sixty major and trace element concentrations in FeMn crusts from 21 dredge sites that cover a broad geographic range (Figure 1). Comparisons of new Tuvalu data with the well-characterized PCZ will expand on the resource estimation calculated by Cronan and Hodkinson (1993) and further investigate compositional variation and controls for FeMn crust throughout the Pacific Ocean. We also report data for a hydrothermally mineralized Mn-oxide sample, which broadens the understanding of mineralization processes in the Tuvalu region. By comparing with and combining data from Cronan and Hodkinson (1993) and De Carlo et al. (1987) where possible, the present study provides a modern and more complete characterization and resource evaluation for FeMn crusts in the Tuvalu EEZ.

2. Samples and Methods

2.1 Samples

FeMn crusts analyzed in this study were collected by dredge during cruise RR1310 aboard the R/V Roger Revelle in 2013. Sampling covered a wide range of seamounts, ridges, and guyots between the latitude of 5°S and 12°S and the longitudes of 175°E and 179°E (Figure 1). Each dredge latitude, longitude, and water

depth were calculated from shipboard dredge log records to account for the length of wire out, movement by the ship, approximate seamount slope, and multiple "bites" of the dredge in order to maximize location accuracy. Each FeMn crust was cut with a wet saw perpendicular to the growth axis, and the surface and internal structure were described in detail. The majority of FeMn crust surfaces are botryoidal, with the botryoids of some samples being smoothed or subdued by bottom currents. Smaller-scale textures, such as granular and lizard-skin, were also observed in 30% of samples, and encrusting foraminifera were also commonly found on the crust surfaces. Major depositional layers were distinguished by visual changes in growth structure, texture, and color, and layers were sampled separately when enough material was available. The dominant internal structure for Tuvalu crusts is columnar with sediment infill between columns as well as vugs where sediment has washed out or prevented from filling those void spaces. Individual layers have textures that are massive, laminated, or mottled (Figure 3). A single spherical FeMn-oxide rock is included in the sample set (D20-54_nodule) which was cemented inside the substrate of a FeMn crust; this sample is labeled as a nodule due to its spherical shape, however it is not meant for comparison to well-known Mn-nodules from deep-sea abyssal plains. Bulk and layer samples were taken from each rock sample using a ceramic knife or Dremel after they were soaked in distilled water for 16-24 hours to remove salts. Subsamples were powdered to a fineness of approximately 75 μm in a mechanical shatterbox with ceramic grinding bowl and puck.

2.2 Methods

2.2.1 Mineralogy

Mineralogy was determined using a Panalytical X'Pert^3 x-ray diffractometer with CuKα radiation and graphite monochromator; measurements were taken at intervals of 0.2° 2θ between 4° and 70° 2θ at 40 kV and 45 mA. Diffraction reflections from the digital scan data were identified using Phillips X'Pert High Score software, and mineral patterns were matched to patterns from the ICDD PDF4+ 2018 database. Semiquantitative mineral percentages were calculated by using peak intensities and weighting factors relative to quartz set as 1 (Cook et al., 1975; Hein et al. 1988). The detection limit for each mineral is between about 0.2% and 1.0%, except for the manganese minerals, for which the limits are greater, probably as much as 10% for the broad, low-intensity reflections typical of δ-MnO_2.

2.2.2 Chemical composition and element correlations

The chemical composition of FeMn crusts and layers was determined at SGS Laboratories, Canada and for platinum group metals (PGM) and gold at Intertek Genalysis, Western Australia. The 10 major elements were determined by X-Ray Fluorescence (XRF) on borate fused disks; Co, Mo, Ni, Rb, U, V, W, Zr, and REY were determined by Inductively Coupled Plasma Mass Spectrometry (ICP-MS) using lithium-metaborate fused disks; Ag, As, Ba, Be, Bi, Cd, Cr, Cs, Cu, Ga, Ge, Hf, In, Li, Nb, Pb, S, Sb, Sc, Sn, Sr, Ta, Th, Tl, and Zn were determined by ICP-MS using a four-acid digest (hydrochloric, hydrofluoric, nitric, perchloric acids); Te and Se were

determined by hydride generation and graphite furnace Atomic-Absorption Spectrometry (AAS); Hg by cold vapor AAS; H_2O^- by gravimetric analysis, $H2O^+$ by penfield-infrared; Cl and F by specific-ion electrode; and platinum group elements (PGE) by fire assay nickel sulfide collection and ICP-MS. Reproducibility based on duplicate analyses of individual samples was better than 5% for all analytes except Te (6%), Ta (7%), Hf (7%), Cd (11%), Bi (11%), Li (14%), Be (20%), Hg (28%), and Ag (43%). Accuracy was calculated by comparing measured values to published values for certified reference materials. Accuracy was better than 15% for all elements except V (16%), Ni (17%), Be (17%), Co (17%), Li (18%), W (18%), Sc (19%), and $H2O^-$ (29%). Certified reference materials used to determine accuracy included: SY-4, NODA-1, NODP-1, OREAS 171, OREAS 405, OREAS 903, SARM42, and RTS-3A. Note that some certified standards measured for accuracy calculations are dissimilar to FeMn crust matrix and may not closely reflect the accuracy for the FeMn crust measurements presented here.

REY plots are normalized to Post-Archean Australian Shale (PAAS; McLennan, 1989). The Ce anomaly (Ce_{SN}) was calculated as $Ce_{SN} = 2Ce_{SN}/(La_{SN}+Pr_{SN})$ with PAAS-normalized values. Pearson correlation coefficient matrices (CCM) were calculated in MatLab from the chemical data to measure the strength of linear dependence between any two elements. For samples with element concentrations measured below the detection limit, values were estimated for inclusion in the CCM by multiplying the detection limit by 0.75. Statistical significance of correlation coefficients is specified at either a 99% or 95% Confidence

Level (CL) based on the n-value. Growth rates (GR) were calculated using the following empirical equations: (1) GR = 1.28 / ([Co]-0.24) from (Puteanus and Halbach 1988); (2) GR = 0.68 * (([Fe]+[Mn] / (50*[Co]))1.67) from (Manheim and Lane-Bostwick 1988).

3. Results

3.1 Mineralogy

FeMn crusts from the Tuvalu EEZ are dominantly composed of δ-MnO_2 (vernadite) and X-ray amorphous iron oxyhydroxide (FeOOH), and three samples also contain >25% birnessite (Table S1). The moderately abundant (5 - 25%) mineral phases include birnessite, goethite, calcite, plagioclase, K-feldspar, phillipsite, and for one sample (D22-03_B0-12), a 10Å manganate phase (todorokite, asbolane, or buserite). The majority of samples contain only minor amounts (<5%) of one or more of plagioclase, quartz, K-feldspar, and several samples also contain minor calcite, or goethite. A single phosphatized layer has a different mineralogy and contains moderate amounts of carbonate fluorapatite (CFA) and minor amounts of 10Å manganate, smectite, pyroxene, and quartz (discussed further in section 3.1.4).

3.2 Fe and Mn contents and genetic discrimination

Iron concentrations in bulk FeMn crusts from Tuvalu range from 14.1 to 23.8 wt. % with a mean concentration of 19.8 wt. % (Table S2; Table 1). Individual non-phosphatized layers contain 15.9 to 26.8 wt. % Fe, and a single phosphatized layer,

D11-17_L41-56, contains the overall minimum Fe concentration of 10.9 wt. % (Table 2). Mn has a broader range of concentrations than Fe in bulk crusts; the lowest Mn content of 13.3 wt. % occurs in a bulk sample containing a single phosphatized layer, while the maximum Mn content in bulk crusts is 29.8 wt. %, and the mean is 19.8 wt. % (Table 1). A single phosphatized layer contains the overall minimum Mn concentration of 8.8 wt. % (Table 2). These Fe and Mn concentrations yield very similar Fe/Mn ratios for both bulk crusts and layers, including the phosphatized layer. Fe/Mn ratios for all bulk and layer samples range from 0.5 to 1.7 wt. % with mean ratios of 1.0, and the phosphatized layer has a Fe/Mn ratio of 1.2. These mean Fe/Mn ratios are typical of hydrogenetic crusts, which generally range between 0.4 and 1.2 (Hein and Koschinsky 2014), and are supported by REY discrimination plots (Figure 4).

3.3 Detrital elements

Silicon, Al, and K are the elements considered to represent detrital input to FeMn crusts. The Si and Al content in bulk crusts from Tuvalu vary by factors of 5 and 10, respectively (Table 1), which suggests variable amounts of detritus delivered to the FeMn crusts. However, the average Si and Al content in bulk crusts of 5.7 and 1.6 wt. %, respectively, illustrate little dilution of the FeMn-oxide phases by detritus. The two samples with the highest Si and Al contents are the phosphatized crust layer of crust D11-17_L41-56 and the bulk crust itself, D11-17_B0-56 (Table 2, Table S1), indicating that this crust may have been growing at a location with higher

aluminosilicate sedimentation rates than other samples or that Si and Al concentrations were affected by phosphatization. Si/Al ratios vary from 2.9 to 5.8 in bulk samples, which encompass the Si/Al ratios of endmembers for detrital input to crusts in this region: 2.8 for oceanic arcs (Arculus 1981) and >4 for aeolian quartz or pelagic biogenic silica.

3.4 Phosphatization

Phosphatization of FeMn crusts occurs in the paleoceanographic record when extremely high surface productivity from upwelling expands and intensifies the oxygen minimum zone, increasing dissolved phosphate concentrations in seawater (Hein et al. 1993). During these events, phosphate replaces carbonates in the pelagic fraction of crusts as well as directly precipitates within the Fe-Mn matrix pore space as carbonate fluorapatite (CFA). Phosphatization is widely observed in the older (>10 Myr) layers of FeMn crusts throughout the global ocean. Phosphatization is important to the characterization of FeMn crusts because it can dilute the Fe and Mn concentrations and may also decrease the concentration or change the speciation of elements of economic interest (Koschinsky et al. 1997; Pan et al. 2003); Chapter 2). Of the 29 bulk FeMn crusts from 20 dredge locations from the Tuvalu EEZ, only a single crust, D11-17, contains a phosphatized layer, D11-17_L41-56. The chemistry of layer D11-17_L41-56 is unique from the other layer samples (Table 2). Mn, Fe, S, As, Ba, Bi, Cd, Co, Mo, Pb, Sb, Se, Sr, U, V, W, Zn, and Zr decrease in the phosphatized layer, whereas Si, Al, Ca, P, K, Cr, F, Li, Rb, and Sc are enriched over

non-phosphatized layer samples. The high detrital elements contents reflect the minerals phillipsite, quartz, plagioclase, and pyroxene determined by XRD (Table S1). In the bulk D11-17 crust sample, 40% of the same elements show maximum or minimum contents relative to other bulk crust samples, which is likely due to the phosphatized layer: Mn, S, Cd, Sb, Sr, and U are also the lowest in D11-17, while only Si, Al, K, and Sc are also the most enriched in the phosphatized bulk sample. Due to the different chemical compositions of the phosphatized layer and its bulk crust, they are not included in correlation matrices. Previous studies of FeMn crusts in the Tuvalu region found that phosphatization typically occurs in crusts from modern water depths above 2500 m, where they were within the expanded OMZ during phosphatization events (De Carlo et al. 1987; De Carlo and Fraley 1990). Contrary to this depth limit, D11-17 was collected at 3582 m water depth. The shallowest dredge for FeMn samples in this study is from a water depth of 2286 m, thus the overall deep-water depths (mean 3262 m) for the sample set presented here explain the lack of phosphatization observed in the crusts. Dredge 11 is near the middle of the latitude range (Figure 1), so a meridional control on phosphatization at this deep-water depth does not seem likely. Phosphatization is important for shallower-water crusts where mining might take place, and comparisons with data from shallower depths within the Tuvalu EEZ are discussed in Section 4.2.

3.5 Interelement relationships of the main mineral phases

The main elements representative of each FeMn crust mineral phase have positive correlation coefficients at a greater than 95% confidence level (CL) as follows (based on 51 non-phosphatized bulk and layer samples): Fe-oxyhydroxide (Fe): P, As, Be, V, REY (except Ce), and the complement of heavy REY (HREY) to the total REY content; Mn-oxide (Mn): Si/Al, Mg, S, Bi, Cd, Co, Mo, Ni, Pb, Sn, Sr, Te, Tl, U, and W; silica-aluminosilicates (both Si and Al): Fe/Mn, Na, K, Ag, Cr, Cu, Li, Rb, Ta, Zr (Table S3). The major-phase elements also exhibit important relationships with one another. Manganese is anticorrelated at the 99% CL with Fe, Si, and Al, demonstrating the dilution of the Mn-oxide phases by detrital input as well as the preferential growth of Mn-oxides under conditions that do not necessarily promote FeOOH precipitation. In Mizell et al. (submitted; Chapter 1), oxygen concentration affected Mn-oxide precipitation more than FeOOH, which may also be the case for bulk FeMn crusts in the Tuvalu region.

3.6 Estimated growth rates

Growth rates were estimated using the cobalt chronometer calculations from both Manheim and Lane-Bostwick (1988) and Puteanus and Halbach (1988). Both methods assume Co is sourced only from seawater and were developed by comparing element concentrations with radiometric dates to derive an empirical equation; Puteanus and Halbach (1988) used only data from FeMn crusts to develop their equation whereas Manheim and Lane-Bostwick (1988) included data from a broader range of Fe-Mn oxide-bearing deposit types such as hydrothermal deposits and

pelagic sediments to derive the growth rate relationship. Both equations generate ages that are correlated with each other and have individually been found in agreement with other dating methods in varied FeMn crust environments (summarized by Josso et al. 2019). However, in the absence of radiometric dates for comparison and validation of the two equations, as is the case for this study, reporting growth rate estimates from one equation over the other is arbitrary (Josso et al. 2019). Therefore, we report the growth rates from both equations and only emphasize element correlations that were significant with both growth rate estimates (Table 3; Table S3). Growth rates for Tuvalu crusts have significant positive correlations with the concentrations of Fe, Fe/Mn, P, and %HREY complement. Conversely, growth rates have strong anticorrelations with Mn, Ti, Ba, Bi, Co, Mo, Ce, Ni, Pb, and Tl. Many of the elements anticorrelated with growth rate are sorbed by, oxidized by, or co-precipitated with Mn-oxides and therefore their trends are closely related to Mn-oxide precipitation. For the eight crusts that were sub-sampled for layers, growth rates are slowest in the oldest layers. The increase in growth rates since the initiation of growth is especially pronounced in sample D20-39 for which the growth rate of the youngest layer increased by factors of 5.5 and 15.5 from the oldest layer, based on the Manheim and Lane-Bostwick (1988) and Puteanus and Halbach (1988) equations, respectively. Concentrations of Bi, Te, Co, Cu, Ni, and Ce decreased overall since the initiation of crust growth in the layer samples, which confirms their anticorrelation with growth rate throughout the duration of crust growth.

3.7 Geographic correlations from CCM

Mn and several of the key Mn-associated elements (Co, Ni, Mo, Bi, Cd, and Te) are positively correlated with latitude, meaning Mn-oxide content increases toward the equator. Notably, growth rates decrease toward the equator (anticorrelate with latitude) as well as Fe and all REY except Ce. This suggests that growth rate is a meridional control on crusts composition in the Tuvalu EEZ, causing increased Mn-oxide contents toward the equator and increased Fe and REY toward the south. REY, Sc, Ta, Th, In, and Be have significant positive correlations with water depth. Water depth is anticorrelated with latitude, which likely explains REY having significant relationships to both depth and latitude. However, the correlation of Sc, Ta, Th, In, and Be with only water depth suggests independent controls from latitude as well as growth rate.

3.8 Metals traditionally of economic interest

Twenty-two elements are enriched on average in bulk FeMn crusts from Tuvalu by a factor of 10 or more compared to average concentrations in continental crust (Rudnick and Gao 2003; Taylor and McLennan 1985), the majority of which commonly show enrichment in FeMn crusts throughout the global oceans (Figure 5; Hein and Koschinsky, 2014). This includes the traditional elements of economic interest, Co, Ni, and Cu, for which the average concentrations in bulk crusts are enriched over continental crust by factors of 304, 82, and 49, respectively. Cobalt in bulk FeMn crusts varies from 0.234 wt. % to 1.28 wt. % with an average

concentration of 0.527 wt. % (Table 1). Cu in bulk crusts is highly variable; the minimum Cu concentration in bulk crusts is 554 ppm while the maximum is five times higher at 2520 ppm, with an average of 1380 ppm. Ni concentrations in the 31 bulk FeMn crusts varies by a factor of four with an average concentration of 3861 ppm. The concentrations of Co, Ni, and Cu in individual layers fall within the range of the bulk concentrations.

3.9 Rare earth elements

Plots of REY from bulk crusts normalized to Post-Archean Australian Shale (PAAS) illustrate that Tuvalu FeMn crusts are enriched in REY to a factor of approximately 10 over the average concentration of REY in PAAS (Figure 6). Most bulk FeMn crusts also exhibit positive Ce anomalies, which is typical for FeMn crusts of hydrogenetic origin and is caused by the preferential retention of Ce relative to other REY through surface oxidation (Bau and Koschinsky 2009). Six samples do not have positive Ce anomalies (Figure 6), and five of these occur in the southern-most portion of the sample sites, which may be indicative of the high growth rates estimated for these crusts (Table 3). Negative Y anomalies are also present in the PAAS-normalized REY patterns, except for sample D04-22; the three other samples from dredge D04 exhibit negative Y anomalies, so this characteristic does not appear to be related to the location of D04-22. The mean ∑REY content for all bulk crusts is 1468 ppm and the maximum is 2213 ppm (Table 2 bulk). The ∑REY concentrations in all crust layer samples fall within the range for bulk samples, except the

phosphatized layer D11-17_L41-56, which has the highest Y concentration (300 ppm) of all crust samples in this study. The heavy REY (Eu through Lu plus Y: HREY) complement of the total REY are enriched compared to the light REY (La though Sm: LREY) complement, and the %HREY complement is 100 times higher in Tuvalu crusts than in continental crust (Figure 5).

3.10 Additional critical metals of interest

The critical metals Te, Bi, and four of the six platinum group metals (PGM), Pt, Ir, Os, and Ru, are highly enriched in bulk Tuvalu crusts compared to average continental crust (Figure 5). The average Te and Bi concentrations in bulk FeMn crusts are 46 and 17 ppm with maxima of 158 and 43 ppm, respectively. Both Bi and Te concentrations tend to increase toward the equator along with Mn, as seen in the CCM (Table S3). The concentrations of the PGM in bulk Tuvalu crusts are as follows (mean, maximum): Pt (278, 395 ppb), Ru (21, 29 ppb), Ir (8, 11 ppb), Pd (6, 9 ppb), and Os (4, 8 ppb). Platinum concentrations in two FeMn crust layer samples exceed the range of the bulk samples, D20-39_L56-72 (428 ppb) and D16-31_(2)_L26-38 (800 ppb). Both of the high platinum layer samples are the oldest layers in their respective crusts and have slow estimated growth rates compared with other samples in Tuvalu (Table 3). Platinum is dominantly enriched in FeMn crusts through oxidation at the surface of Mn-oxides (Koschinsky et al. accepted; Maeno et al. 2016) and therefore favors slower growth rates.

3.11 Hydrothermally mineralized Mn-oxide sample

One sample from the dataset, D28A-01, is a hydrothermally mineralized foraminifera ooze. Three different layers were taken from this 39 mm-thick mineralized sedimentary rock, based on growth texture and structure. The upper layer of D28A-01 has a botryoidal surface that is more typical of hydrogenetic FeMn crust growth. This upper hydrogenetic layer may have been weakly hydrothermally mineralized (see below). The two lower layers are separated by a foraminifera-rich, white layer; the lower layer appears more dense and subtle laminations follow bedding, while the upper layer has a more chaotic and porous texture (Figure 3). The lower hydrothermal layers are composed of birnessite, 10Å manganate, and calcite with minor amounts of magnetite and quartz (Table S1). The lowest layer contains more 10Å manganate than the middle layer as well as less calcite, which suggests more pervasive hydrothermal mineralization of the lowermost layer. The mineralogy of the uppermost layer is dominated by δ-MnO_2 with moderate amounts of birnessite and calcite like other hydrogenetic layers from Tuvalu; however, a trace of 10Å manganate was also found in this layer, which may be due to slight hydrothermal input or more likely from contamination from the layer below during sampling. The chemistry confirms that the uppermost layer is predominantly hydrogenetic (Figure 4 Bau diagram). Fe and Mn concentrations are 15.8 and 22.2 wt. %, respectively, and the Fe/Mn ratio is 0.71; all of these values fall within the range for the bulk and layer samples of the hydrogenetic crusts. In addition, the Co content of the uppermost layer, which is known to be a marker for hydrogenetic origin due to its sole source

from seawater and enrichment in slow-growing open-ocean crusts (Hein et al. 2000), is also within the range of the hydrogenetic crusts. The two hydrothermal layers have low Fe contents and Fe/Mn values of 0.19 for the lower layer and 0.03 for the middle layer, which are very low compared to the hydrogenetic crusts from Tuvalu (Table 4); this fractionation of Fe and Mn is typical for hydrothermal Mn and Fe deposits (Hein et al. 1997).

Both the middle and lower hydrothermal layers are enriched in Li 60 times and in Cd 4-5 times more than the average bulk hydrogenetic crust from Tuvalu (Figure 7). Enrichment of Li in this deposit is consistent with some other hydrothermal Mn-oxide deposits (e.g., Hein et al. 2008; Glasby et al. 1997) due to the high Li contents of hydrothermal fluids that leach newly formed ocean crust (Chan and Hein 2007). The lower hydrothermal layer also contains 2-2.5 times more Ni, Se, Cu, and Zn than the hydrogenetic crusts and layers. High Cd, Ni, Cu, and Zn concentrations were also observed in hydrothermal Mn deposits from the Izu-Bonin-Mariana Arc in the northwest Pacific (Hein et al 2008). However, most elements are actually depleted in the hydrothermal layers compared to hydrogenetic crusts, and the middle layer is more depleted than the lower layer, likely due to its high calcite (foraminifera) content. Depleted metal concentrations are attributed to the fast growth rates, which are estimated by the equation of Manheim and Lane-Bostwick (1988) to be 48.8 mm/Myr for the lower layer and 1395 mm/Myr for the middle layer (Table 3). These growth rates are much higher than those for hydrogenetic deposits from

Tuvalu (average 2 mm/Myr), but well within the range recorded for a variety of hydrothermal Mn deposits (Hein et al 1997).

REY are also generally low in the hydrothermal layers, consistent with a hydrothermal origin (Hein et al. 2008). PAAS normalized plots for the hydrothermal layers show that REY relative enrichment corresponds to the growth rate of each layer, with the upper layer having the highest REY content and the middle layer the lowest (Figure 6). The upper layer and the lower layer exhibit similar enrichment patterns, including no Ce anomaly and a negative Y anomaly. The middle layer, instead shows a strong negative Ce anomaly and no Y anomaly. A negative Ce anomaly is associated with faster growth rates and the slow oxidation of Ce during incorporation. The middle layer plots well within the hydrothermal field, and the lower layer plots at the margin of the hydrothermal field in a discrimination diagram of normalized Ce vs Nd_{SN}, however they plot in the hydrogenetic field in the diagram for Y_{SN}/Ho_{SN} vs normalized Ce, which illustrate higher Ce and Nd and lower Y than other hydrothermal Mn deposits (Figure 4; Bau et al. 2014).

4. Discussion

4.1 Spatial controls on growth rates and Mn contents for Tuvalu crusts

Estimated growth rates for bulk and layer samples of FeMn crusts from the Tuvalu EEZ decrease toward the equator. Two major oceanographic features occur in the region near the equator: increased productivity due to equatorial upwelling and a weak OMZ that is the distal end of the Eastern Tropical South Pacific Oxygen

Deficient Zone (ETSPODZ; Figure 2). The decrease of growth rates toward these features demonstrate that low-oxygen concentrations in and near the OMZ, that is enhanced by increased productivity, is concomitant with slow crust growth. The factors that cause slower growth rates in low-oxygen environments are still not well understood. One possibility in the Tuvalu region is that FeMn crusts that are near the OMZ are from shallower water depth. Shallower crusts will experience more rapid currents as they move up the slopes and over seamounts. Faster currents will cause decreased sedimentation and may also cause winnowing of some of the new oxide precipitates which can mechanically decrease growth rates. Alternatively, chemical controls on crust growth rates near the OMZ may exist. Both dissolved Fe and Mn can be higher in the OMZ than in seawater above and below the OMZ (Landing and Bruland 1987). However, Fe has a shorter residence time in the OMZ due to more efficient scavenging by sinking particles, and the increased Fe concentration in OMZs in the Pacific is dominantly the result of horizontal transport of Fe which may be variable throughout the Pacific Ocean (Landing and Bruland 1987). In contrast, increased dissolved Mn in the OMZ is dominantly caused by high remineralization rates (Chen and Wu 2019) and maintained by decreased oxidation rates (Johnson et al. 1996). These factors could cause less available dissolved Fe than Mn just below the OMZ where Tuvalu FeMn crusts are forming and lead to a smaller contribution of Fe-oxides to the growing crust matrix and therefore slower growth rates. In support of the hypothesis that less dissolved Fe and more dissolved Mn is provided at the lower extents of and just below the OMZ, Mn and Mn-oxide associated metals (Co, Ni, Te,

Bi) increase toward the equator. Many previous studies have also found Mn-oxide contents to increase near OMZs (Hein et al. 2000; Halbach and Puteanus 1984). Mizell et al. (submitted, Chapter 1) found that modern oxygen concentrations had high anticorrelations with Mn concentrations in the upper 15 mm (recent growth) of FeMn crusts from a seamount chain along 4N to 14S, which encompasses the Tuvalu seamounts. The study presented here for bulk crusts that integrate millions of years suggests that proximity to the OMZ at the equator is a dominant geographic control on crust composition through time within the Tuvalu EEZ and is not a recent phenomenon. More detailed study of dissolved Mn concentrations throughout the depth range of crust formation may also elucidate fluctuations in the strength of the ETSPODZ in this region throughout the ~40 Ma growth history.

4.2 Comparisons with Tuvalu crusts from shallower water depths

DeCarlo et al. (1987) characterized 18 bulk FeMn crusts from two dredges in the Tuvalu EEZ, one from 1230 m and the other from 1690 m. Dredges included in the study presented here have a minimum water depth of 2286 m, which is nearly ~1000 m and ~600 m below the dredges from DeCarlo et al. (1987). In order to further investigate the effects of water depth on FeMn crusts composition within the Tuvalu region, we compare the chemistry and mineralogy of the crust groups. FeMn crusts from DeCarlo et al. (1987) will be called in this section, “shallow” crusts, and FeMn crusts from this study will be called, “deep” crusts. A key characteristic of the shallow crusts, is that 11 out of the 18 are phosphatized, as evidenced by CFA in the

reported mineralogy and P concentrations above 0.57 wt. %. This high occurrence of phosphatization is congruent with reports that phosphatization is common in the Pacific Ocean above 2800 m due to crust growth within the expanded oxygen minimum zone during phosphatization events (Koschinsky et al. 1997; Hein et al. 2000).

The shallow-water crusts also contain more Mn and Mn-oxide-associated elements, Co, Ni, and V, but less Fe and FeOOH-associated elements, Cu and Ti, than the deep crusts (Figure 8). This likely reflects two primary factors. First, there is increased Fe, Ti, and Cu contents in FeMn crusts with increasing water depth in the equatorial Pacific and other regions due to increased oxygen concentrations in Antarctic Bottom Water, increased carbonate concentrations and therefore pH, and increased Fe supply at depth, which promotes FeOOH precipitation (Mizell et al. submitted, Chapter 1; Hein et al. 2016; Halbach and Puteanus 1984). Second, there is often high dissolved Mn concentrations in the oxygen depleted waters at shallower depths in the Pacific (as discussed above), which promotes Mn-oxide precipitation and accumulation of elements like Co, Ni, and V that preferentially sorb to Mn-oxides (Mizell et al. submitted). Oxygen concentrations are lower at shallow depths in the Pacific in contrast to the recently ventilated Antarctic Bottom Water that is present at deeper depths. In addition, oxygen may be slightly decreased closer to the summit of seamounts where small-scale increases in productivity are spurred by obstructional upwelling as currents flow past the seamount (Hein et al. 1987; Gall et al. 2013). We hypothesize that Mn enrichment varies primarily with latitude in this

region, which is as a proxy for horizontal variations in oxygen concentration. Despite the higher Mn content of shallow-water crusts from the De Carlo et al. (1987) study, the vertical variation in modern oxygen concentrations (Figure 2) is not reflected in a vertical variation in Mn enrichment when just the deep samples characteristic of this study are considered. This may be evidence that locally produced OMZs are not always strong enough to cause changes in Mn supply or oxidation rates as a function of water depth. Or it may indicate that changes in oxygen concentrations with depth from the base to the summit of the seamounts have been more dynamic over the millions of years of crust growth than the meridional changes in oxygen concentration.

Additionally, the deeper crusts contain more Si and Al overall, which is likely the result of weathering and mass movement of debris down the flanks of seamounts. The Si/Al ratio is very similar for both shallow and deep crusts therefore detrital sources likely do not change. Overall, depth comparisons demonstrate that while phosphatization is more prevalent at shallower depths in the Tuvalu region, the degree of phosphatization is not high enough to impact the enrichment of Mn, Co, Ni and V in the FeMn crusts.

4.3 Comparisons with the Prime Crust Zone

The PCZ is considered the most prospective area for the economic recovery of FeMn crusts (Hein et al. 2013; Hein and Koschinsky 2014), and is the area where four exploration contracts with the International Seabed Authority are located. FeMn

crusts from the PCZ are thick (up to 260 mm; high tonnage) and contain high concentrations of critical and valuable metals (high grade). The PCZ also contains huge guyots with gentle summit slopes where crust growth is abundant, and these types of summit regions are the most prospective area for crusts (Hein et al. 2009). The concentrations of most elements are comparable (within a factor of 1.5) between PCZ (from Hein et al. 2013) and the Tuvalu crusts (Figure 9). Mean concentrations for Mn, Fe, Co, Ni, Cu, SI, Al, Ti, V, P, Ca, and Mg from DeCarlo et al. (1987) were combined with mean data for the crusts presented here to calculate a weighted average for these elements to compare with the PCZ; the weighted average is representative of a mean composition from a broader range of water depths (see Section 4.2). The weighted average for most elements is closer to PCZ averages, except Ni and V for which the weighted averages are further enriched over the PCZ but still within a factor of 1.5. The PCZ is enriched beyond a factor of 1.5 in the critical elements Bi (2.5x), Hf (2.5x), Rb (2.3x), In (1.8), As (1.8x), Pt (1.7x), and REY (1.7x) and therefore has better resource potential for these elements.

However, the mean concentration of Hg (7.6x), Ag (2.2x), Os (1.9x), Li (1.9x), and Sc (1.8x) are higher in bulk FeMn crusts from Tuvalu than mean concentrations in the PCZ. Mercury concentrations in Tuvalu crusts and crust layers are highly variable, ranging from <5 ppb (below detection limit) to 1020 ppb, with mean 55 ppb (Table S2). Mercury shows no correlation with water depth, latitude, or growth rate, and shows no temporal patterns throughout crust layers; therefore, the reason for the Hg enrichments, its host phase, and its input source are difficult to

pinpoint. Based on Hg inorganic speciation in seawater (Byrne 2002), it should be associated with the FeOOH, but Hg does not correlate with Fe in Tuvalu crusts (Table S3). The accumulation of Hg in hydrogenetic crusts typically requires additional inputs by hydrothermal fluids that have leached Hg from organic-rich sediments (Hein et al. 2005; Mikhailik et al. 2018). Rejuvenated volcanism that correspond with the age of the crusts in the Tuvalu seamounts has been recorded (Jackson et al. 2010; Finlayson et al. 2018), but the contribution of this hydrothermal activity to hydrogenetic FeMn crust contents requires further study. Highly variable Hg concentrations have also been found in hydrogenetic FeMn crusts from the North Pacific (e.g. Hein et al. 2012) and the Arctic Ocean (Hein et al. 2017), and mechanisms of enrichment were speculative. Mercury enrichment in hydrogenetic Tuvalu crusts warrants further investigation.

The moderate enrichment of Ag in Tuvalu crusts compared with PCZ is also of interest. Modern depth profiles of dissolved Ag in the Pacific Ocean show that Ag has a nutrient-like chemical behavior in the water column with a maximum concentration in profiles from stations in the equatorial and subtropical north Pacific at approximately 2500 m (Kramer et al. 2011). These authors also found a depletion in Ag when oxygen was low, due to potential precipitation of Ag-sulfides and enhanced particle scavenging in lower oxygen environments (Kramer et al. 2011). The Tuvalu samples are from an average water depth of 3127 m, where waters are relatively well oxygenated, whereas the data compiled by Hein et al. (2013) for the average PCZ composition includes samples from many water depths, including

numerous samples from 1000 to 2000 m water depth where dissolved Ag is depleted due to low oxygen concentrations. Higher dissolved Ag concentrations in seawater in deeper, more oxygenated waters may explain Ag enrichment in the deeper Tuvalu crusts reported here. Alternatively, the accumulation of Ag in marine sediments above lithogenic contribution may be attributed to scavenging of Ag from seawater by organic matter in the water column, and delivery to deep waters by sinking particles (McKay and Pedersen 2008). However, Ag is not more enriched in Tuvalu crusts closer to the equator, where biological activity is higher due to equatorial upwelling, arguing against the notion that Ag enrichment is due to higher overlying productivity.

Lithium and Sc are both considered to be critical metals as defined by the United States Department of the Interior; critical metals are defined as mineral commodities that are vital to the Nation's security and economic prosperity. The enrichment of Li and Sc in Tuvalu is therefore important to their resource potential. The major sources of Li to the oceans are rivers (Huh et al. 1998) and hydrothermal fluids that have leached Li from oceanic crust (Von Damm et al. 1985; Chan et al. 1993). Lithium has a conservative profile in seawater and a very long residence time (2.8 Myr), therefore local changes in the Li concentration of seawater are not the major cause for variable Li contents in hydrogenetic FeMn crusts. Lithium in FeMn crusts is primarily associated with the MnO_2 fraction since the hydrated cationic species of Li is dominant in seawater (Byrne 2002) and forms electrostatic bonds at the negatively charged surface of MnO_2. Specifically, the 10Å manganate mineral,

todorokite, has a tunnel structure that accommodates Li and thereby enrich Li when present in FeMn deposits (Hein and Koschinsky 2014; Jiang et al. 2007). However, Tuvalu crusts are not more enriched in Mn than PCZ crusts, and todorokite was not confirmed to be the 10Å phase present in Tuvalu crusts. Therefore, the sorption of Li to various Mn-oxides is not the definitive cause of Li enrichment. Another possibility is that ~15% of Li is measured in the non-reducible fraction of FeMn crusts, which is largely composed of alumino-silicate minerals in hydrogenetic crusts (Koschinsky and Hein 2003). Li correlates with Si and Al in FeMn crust samples from Tuvalu, and concentrations of Li are higher (>10 ppm) in crusts that contain phillipsite and/ or a 10Å manganate (Table S2; Table S1). Phillipsite is an authigenic zeolite shown to play an important role in the mass balance of lithium in the oceans through removal of Li from seawater by isomorphic substitutions in layer silicates (Pistiner and Henderson 2003; Chan et al. 1992). Therefore, we attribute slight Li enrichment in Tuvalu crusts over crusts from the PCZ to the common inclusion of moderate amounts of phillipsite as well as a small contribution from 10Å manganates in some crusts; this confirms results for the Li contribution to a hydrogenetic crust studied by (Jiang et al. 2007).

Scandium forms the neutrally charged dissolved complex, $Sc(OH)_3$, in seawater (Byrne 2002) that should sorb onto the Fe oxyhydroxides based on the electrochemical model (Koschinsky and Halbach 1995; Koschinsky & Hein, 2003). Scandium concentrations in bulk Tuvalu crusts anticorrelate with Mn, which supports association with the Fe phase. Parker et al. (2016) reported that dissolved Sc in the

Atlantic and Pacific Oceans is a hybrid-type element with both nutrient and scavenged behavior in the water column. Scandium concentrations typically increase with depth, and Sc is scavenged from deep water with a residence time on the order of a thousand years Parker et al. (2016). Scandium correlates at the 99% CL with water depth in Tuvalu crusts, and since the average depth of FeMn crusts in this study are quite deep, we attribute Sc enrichment in Tuvalu crusts over PCZ crusts to the increasing Sc concentrations at greater water depth.

4.4 Mechanism and potential distribution of hydrothermal mineralization

We interpret that sample D28A-01 was formed by hydrothermal fluids that infiltrated a foraminifera-rich biogenic sediment that had built up on the flanks of the seamount where it was dredged. This type of sediment-hosted stratabound hydrothermal Mn deposit is more commonly found in volcanic arc settings (e.g. Hein et al. 2008). However, sediment-hosted stratabound Mn deposits have been associated with large midplate volcanic edifices, e.g. along Haleakala Ridge off Maui Island and Puna Ridge off of Hawaii Island (Hein et al. 1996), the axis of the northeast rift zone of the Gardner Pinnacles, Hawaiian Archipelago (De Carlo et al. 1987; De Carlo and McMurtry 1992), at South Johnston Island Ridge (Hein et al. 1990a), and on Lajutokwa Seamount, Marshall Islands (Hein et al. 1990b). The formation mechanism for mid-plate stratabound hydrothermal deposits requires hydrothermal activity after both the initial formation of the seamount and the deposition of the host sediment; this mineralization occurred during or following submarine flank fissure

eruptions in other mid-plate locations. Sample D28A-01 was collected from Bayonnaise seamount in the southern portion of the Tuvalu EEZ (Figure 1) where the older Rurutu hotspot track (~50 Myr) is crossed by the younger Samoa hotspot track (~10 Myr; Finlayson et al. 2018). Foraminifera biostratigraphic dating determined that the host foraminifera ooze for sample D28A-01 has an early Eocene age of ~54 to 46 Ma (Appendix 1). This sediment age suggests that Bayonnaise seamount was formed by Rurutu lavas in the Eocene and that foraminifera-rich biogenic sediments built up on the flanks of the seamount soon after. Hydrothermal mineralization of the sediment may have occurred during the shield-building phase of the seamount or possibly during rejuvenation of volcanism and hydrothermal activity from the Samoa hotspot. Hydrothermal activity related to rejuvenation of volcanism has been reported for some of the older Rurutu-generated seamounts (Jackson et al. 2010; Finlayson et al. 2018). Dredge 27, collected from nearby Niulakita seamount, contained lavas with ages 45-42 Ma and Rurutu compositions that define the base of the volcano as well as lavas from reactivation at ~15 Myr with Samoa-like compositions (Finlayson et al. 2018). A basalt from Dredge 28B at Bayonnaise seamount, very close to where the mineralized sediment D28A-01 was collected, has a Samoa-like composition (Finlayson et al. 2018) as do other samples from Bayonnaise seamount (Jackson et al. 2010), which suggests reactivation of volcanism and hydrothermal activity may have occurred at Bayonnaise seamount ~15 Myr ago.

Because only a single stratabound sample was recovered, the extent of this deposit type in Tuvalu is not known. Several measurements in future work are needed

to determine the size of the reservoir in which stratabound Mn oxides accumulated and the extent of mineralization that occurred on this and other seamounts, such as the thickness of the sediment on the seamount and the thickness of the sedimentary sections that were mineralized.

4.5 Resource considerations for FeMn crusts from the Tuvalu EEZ

The main characteristics that determine the mining potential of FeMn crust deposits are metal concentrations (grade), crust thickness (tonnage), extent of the deposit, small-scale topography, and degree of slope of the topography. In terms of grade, FeMn crusts from the Tuvalu EEZ on average have similar enrichments of critical metals to crusts in the Prime Crust Zone, which is the area considered to have the most mineral resource potential for crusts in the global ocean (Hein et al. 2013). The PCZ has better resource potential than Tuvalu for REY, Pt, and especially Bi; however, Tuvalu crusts contain high grades of Co, Mn, Cu, Ni, and V that are subequal to PCZ crusts, and they are more enriched in the critical metals Pd, Sc, and Li than the PCZ deposits (Figure 9). Manganese, Co, Cu, Ni, Bi, and Te are more enriched in crusts in the northern portion of the EEZ, whereas Sc and REY grades increase to the south.

Hein et al. (2009) defined the ideal minimum crust thickness for a potential mine site to be 40 mm, and that areas with mean crust thicknesses ≥30 mm should be considered for exploration. This thickness allows recovery of substantial tonnages and accounts for collection efficiency (Morgan 2008). Crust thicknesses are variable

for our data from Tuvalu, ranging from 1 mm to 72 mm, mean 26 mm. There is no overall correlation of sample thickness with latitude or water depth, however the thickest crust (D20-39; 72 mm) was collected at the deepest dredge site (4110 m). Tuvalu crust data compiled by Cronan and Hodkinson (1993) showed an average thickness of 11 mm with the thickest crusts occurring in the north of the EEZ and within a depth range of 1700-2000 m. For the Tuvalu crusts reported by DeCarlo et al. (1987) from two dredges collected near Dredge 16 in this study (Figure 1), the average thickness for 18 crusts was 37 mm; for Dredge 4RD-007 from a depth of 1690 m, 14 of 16 crusts were thicker than 35 mm. These combined data demonstrate that thick FeMn crusts can occur at various latitudes and water depths in the Tuvalu EEZ, but crusts >30 mm thick may be more consistently found above 2500 m.

Regarding distribution, the primary parameters to optimize a potential mine-site area are water depth and summit area. The depth cut-off chosen here is 3000 m, which allows large summit areas of seamounts, guyots, and ridges to be located and is within the current operation limits of crust mining prototypes. In addition, edifice slopes tend to be more rugged below 3000 m, and crust thicknesses and the grades of Mn-oxide hosted metals, such as Mn, Co, Ni, Te, Bi, and others can decrease with water depth as seen in this study and throughout the Pacific (Usui and Someya 1997; Hein et al. 2000; Zhang et al. 2008). An upper bound of 500 m water depth is also used as a constraint, since sedimentation rates above 500 m are generally too high to permit FeMn crust growth. Figure 10 shows the bathymetric map of areas within the Tuvalu EEZ that lie between 500 and 3000 m water depth. The only large area that

occurs within this depth range is in the southeastern portion of the EEZ. The summits of the seamounts and guyots in this permissive region are quite shallow, with large areas above 500 m. Cullen and Burnett (1986) found that several of the seamounts in this region are capped with thick sediment sections (maximum ~800 m) with an uppermost unit composed of smoothed, hardened outcrops of massive reef-building coral (~20 m). Beyond the shallow extremes of the summits, many large areas exist with near-uniform depths that warrant exploration. The entire permissive area in the southeastern portion of the Tuvalu EEZ encompasses more than 40,000 km^2. Exploration contracts for FeMn crusts distributed by the International Seabed Authority allocate a maximum of 3000 km^2 consisting of 150 blocks of no more than 20 km^2 each. Narrowing the permissive region in Tuvalu to 3,000 km^2 would allow for 92.5% of the area to be ruled out due to thick sediment cover, roughness of topography, thin crusts, etc. In order to refine this permissive area, further data collection is required. This should include detailed bathymetric mapping to determine large flat areas and areas to avoid with steep slopes, backscatter data to estimate sediment extent, seismic surveys to determine sediment thickness, and detailed sampling of FeMn crusts from a wide range of locations and water depths to better estimate grades. The eight bulk FeMn crust sampled from seven dredges within this region (Figure 10) have an average thickness of only 14 mm and lower Mn, Co, Ni, and Te concentrations than the average for the entire EEZ, however REY concentrations are slightly higher, and numerous portions of the permissive area and water depth range have not been sampled. In addition, the stratabound hydrothermal

manganese sample, D28A-01, was collected in this permissive region, and contains high enrichments of Li, Cd, Ni, and especially Mn (Figure 7). If hydrothermally mineralized sediments are discovered to be widespread, they may constitute a separate critical mineral resource, in addition to the hydrogenetic crusts in the Tuvalu EEZ.

5. Summary and Conclusions

Ferromanganese crusts were sampled throughout the Tuvalu EEZ from water depths between 2286 and 4110 m. The crusts collected are relatively thin, averaging 14 mm, however 39% of samples were >30 mm thick. The dominant compositional control in the region is the OMZ that is strongest near the equator. Proximity to the OMZ correlates with decreased growth rates and enrichment of Mn, Co, Ni, Bi, Cu, Cd, and Te in FeMn crusts from the northern portion of the Tuvalu EEZ. Despite previous studies showing little to no phosphatization in the Tuvalu region below 2500 m (De Carlo et al., 1987; De Carlo and Fraley 1990), a sample containing a phosphatized lower layer was collected from 3582 m water depth. The phosphatized layer has highly depleted Fe and Mn contents but elevated concentrations of Li, Rb, and Y compared to non-phosphatized crusts and crust layers. When the chemistry of the deep-water and minimally-phosphatized crusts from this study are compared with shallower crusts that have a high occurrence of phosphatization (De Carlo et al. 1987), Mn, Co, Ni, and V concentrations are higher in shallow crusts. Thus,

phosphatization does not cause major dilution of the primary metals of economic interest for Tuvalu crusts.

Comparison of Tuvalu crusts with crusts from the PCZ reveal similar average concentrations for most elements. Tuvalu crusts are enriched, however, in Hg, Li, Ag, and Sc compared to PCZ crusts, while PCZ crusts have a higher resource potential for REY, Pt, Bi, and As. Based on water depth criteria, we determined that the most prospective region for further crust exploration lies in the southeastern portion of the Tuvalu EEZ where several large seamounts and guyots are grouped and present reasonably flat and continuous summit areas across an extensive plateau (Figure 10). Crusts recovered from within this permissive region are relatively thin, with an average thickness of only 14 mm. The Mn, Co, Ni, and Te concentrations are lower for these crusts than the average for the entire EEZ; however, they are still within the range of potential economic interest, and REY concentrations are slightly higher in this permissive area than elsewhere in Tuvalu. Further data are required to refine the permissive region presented here, but there is ample expanse to delineate priority areas for exploration.

In addition to the hydrogenetic FeMn crusts collected, a stratabound hydrothermal Mn sample (D28A-01) was collected from the southern portion of Tuvalu EEZ. Sample D28A-01 is a hydrothermally mineralized foraminifera ooze that is rich in Mn, Li, and Cd, and the lower layer is also enriched in Ni, Se, Cu, and Zn. The foraminiferal sediment that was hydrothermally mineralized was dated using biostratigraphy to have an early Eocene age ~54 to 46 Ma. This age allows that the

sediment could have been mineralized shortly after the formation of the Eocene seamount (~50 Myr ago) during the shield-building stage; alternatively, mineralization may have occurred during rejuvenation of volcanic activity associated with the Samoan Hotspot ~15 Myr ago. The extent of sediment-hosted, stratabound hydrothermal Mn deposits is not known, since only a single sample was collected. However, this type of hydrothermal mineralization provides key information regarding seamount formation and rejuvenation events and warrants continued research. Further, if this deposit type is widespread or hosted within a large sediment body, it may be of economic interest.

6. Acknowledgements

I would like to thank Dr. Anthony Koppers and the Marine and Geology Repository, College of Earth, Ocean, and Atmospheric Sciences, Oregon State University for providing rock samples.

7. References

Arculus, R. J. 1981. "Island Arc Magmatism in Relation to the Evolution of the Crust and the Mantle." *Tectonophysics* 75: 113–33.

Bau, M., Schmidt, K., Koschinsky, A., Hein, J. R., Kuhn, T., and Usui, A. 2014. "Discriminating between Different Genetic Types of Marine Ferro-Manganese Crusts and Nodules Based on Rare Earth Elements and Yttrium." *Chemical Geology* 381: 1–9. https://doi.org/10.1016/j.chemgeo.2014.05.004.

Bau, M., and Koschinsky, A. 2009. "Oxidative Scavenging of Cerium on Hydrous Fe Oxide: Evidence from the Distribution of Rare Earth Elements and Yttrium between Fe Oxides and Mn Oxides in Hydrogenetic Ferromanganese Crusts." *Geochemical Journal* 43 (1): 37–47.

Byrne, R. H. 2002. "Inorganic Speciation of Dissolved Elements in Seawater: The Influence of PH on Concentration Ratios." *Geochemical Transactions* 3 (1): 11–16. https://doi.org/10.1039/b109732f.

Chan, L. H., Edmond, J. M., Thompson, G., and Gillis, K. 1992. "Lithium Isotopic Composition of Submarine Basalts: Implications for the Lithium Cycle in the Oceans." *Earth and Planetary Science Letters* 108 (1–3): 151–60. https://doi.org/10.1016/0012-821X(92)90067-6.

Chan, L-H., Edmond, J. M., and Thompson, G. 1993. "A Lithium Isotope Study of Hot Springs and Metabasalts from Mid- Ocean Ridge Hydrothermal Systems." *Journal of Geophysical Research* 98 (B6): 9653–59. https://doi.org/10.1029/92jb00840.

Chan, L. H., and Hein, J. R. 2007. "Lithium Contents and Isotopic Compositions of Ferromanganese Deposits from the Global Ocean." *Deep-Sea Research Part II: Topical Studies in Oceanography* 54 (11–13): 1147–62. https://doi.org/10.1016/j.dsr2.2007.04.003.

Chen, G., and Wu, J. 2019. "Meridional Distribution of Dissolved Manganese in the Tropical and Equatorial Pacific." *Geochimica et Cosmochimica Acta* 263 (October): 50–67. https://doi.org/10.1016/j.gca.2019.06.048.

Conrad, T., Hein, J. R., Paytan, A., and Clague, D. A. 2017. "Formation of Fe-Mn Crusts within a Continental Margin Environment." *Ore Geology Reviews* 87: 25–40. https://doi.org/10.1016/j.oregeorev.2016.09.010.

Cook, H. E., Johnson, P. D., Matti, J. C., and Zemmels, I. 1975. Methods of sample preparation and X-ray diffraction data analysis (X-ray mineralogy laboratory, Deep Sea Drilling Project, Univ. of California Riverside), Initial Rep. Deep Sea Drill. Proj., 28, 999–1007.

Cronan, D.S. and Hodkinson, R.A. 1993. "An Evaluation of Manganese Nodules and Cobalt-rich Crusts in South Pacific Exclusive Economic Zones.Part III. Nodules and Crusts in the EEZ of Tuvalu (Ellice Islands)." *Marine Georesources & Geotechnology* 11: 153–74.

Cullen, D. J., and Burnett, W. C. 1986. "Phosphorite Associations on Seamounts in the Tropical Southwest Pacific Ocean." *Marine Geology* 71 (3–4): 215–36. https://doi.org/10.1016/0025-3227(86)90071-X.

De Carlo E. H. and Fraley, C. M. 1990. Chemistry and mineralogy of ferromanganese deposits from the equatorial Pacific Ocean. In Geology and Offshore Mineral Resources of the central Pacific Basin (ed. B. H. Keating and B. R. Bolton), pp. 225-245. Earth Science Series, vol. 15. Circum-Pacific Council for Energy and Mineral Resources.

De Carlo, Heinen, E., and McMurtry, G. M. 1992. "Rare-Earth Element Geochemistry of Ferromanganese Crusts from the Hawaiian Archipelago, Central Pacific." *Chemical Geology* 95 (3–4): 235–50. https://doi.org/10.1016/0009-2541(92)90014-V.

De Carlo, E. H., Mcmurtry, G. M., and Kim, K. H. 1987. "Geochemistry of Ferromanganese Crusts from the Hawaiian Archipelago I. Northern Survey Areas." *Deep-Sea Research* 3487 (3): 441–67.

De Carlo, E. H., Pennywell, P. A., and Fraley, C. M. 1987. "Geochemistry of Ferromanganese Deposits from the Kiribati and Tuvalu Region of the West Central Pacific Ocean." *Marine Mining* 6: 301 pp.

Finlayson, V. A., Konter, J. G., Konrad, K., Koppers, A. A.P, Jackson, M. G., and

Rooney, T. O. 2018. “Sr–Pb–Nd–Hf Isotopes and 40Ar/39Ar Ages Reveal a Hawaii–Emperor-Style Bend in the Rurutu Hotspot.” *Earth and Planetary Science Letters* 500: 168–79. https://doi.org/10.1016/j.epsl.2018.08.020.

Gall, L., Williams, H. M., Siebert, C. Halliday, A. N., Herrington, R. J., and Hein, J. R. 2013. “Nickel Isotopic Compositions of Ferromanganese Crusts and the Constancy of Deep Ocean Inputs and Continental Weathering Effects over the Cenozoic.” *Earth and Planetary Science Letters* 375: 148–55. https://doi.org/10.1016/j.epsl.2013.05.019.

Garcia, H. E., Locarnini, R. A., Boyer, T. P., Antonov, J. I., Baranova, O. K., Zweng, M. M., … Johnson, D. R. 2014. *World Ocean Atlas 2013, Volume 3: Dissolved Oxygen, Apparent Oxygen Utilization, and Oxygen Saturation*. (S. (Ed. . Levitus & A. (Technical E. . Mishonov, Eds.). NOAA Atlas NESDIS 75.

Glasby, G. P., Stüben, D., Jeschke, G., Stoffers, P., and Garbe-Schönberg, C. D. 1997. “A Model for the Formation of Hydrothermal Manganese Crusts from the Pitcairn Island Hotspot.” *Geochimica et Cosmochimica Acta* 61 (21): 4583–97. https://doi.org/10.1016/s0016-7037(97)00262-7.

Halbach, P. and Puteanus, D. 1984. “The Influence of the Carbonate Dissolution Rate on the Growth and Composition of Co-Rich Ferromanganese Crusts from Central Pacific Seamount Areas.” *Earth and Planetary Science Letters* 68 (1): 73–87. https://doi.org/10.1016/0012-821X(84)90141-9.

Hein, J. R., Conrad, T. A. and Dunham, R. E. 2009. “Seamount Characteristics and Mine-Site Model Applied to Exploration- and Mining-Lease-Block Selection for Cobalt-Rich Ferromanganese Crusts.” *Marine Georesources and Geotechnology* 27 (2): 160–76. https://doi.org/10.1080/10641190902852485.

Hein, J. R., Conrad, T. A. Frank, M. Christl, M. and Sager, W. W. 2012. “Copper-Nickel-Rich, Amalgamated Ferromanganese Crust-Nodule Deposits from Shatsky Rise, NW Pacific.” *Geochemistry, Geophysics, Geosystems* 13 (10). https://doi.org/10.1029/2012GC004286.

Hein, J. R., Conrad, T., Mizell, K., Banakar, V. K., Frey, F. A., and Sager, W. W. 2016. “Controls on Ferromanganese Crust Composition and Reconnaissance Resource Potential, Ninetyeast Ridge, Indian Ocean.” *Deep-Sea Research Part I: Oceanographic Research Papers* 110: 1–19.

https://doi.org/10.1016/j.dsr.2015.11.006.

Hein, J. R., Gibbs, A. E., Clague, D. A., and Torresan, M. 1996. "Hydrothermal Mineralization along Submarine Rift Zones, Hawaii." *Marine Georesources and Geotechnology* 14 (2): 177–203. https://doi.org/10.1080/10641199609388310.

Hein, J. R., Kang, J-K., Schulz, M. S., Park, B-K., Kirschenbaum, H., Yoon, S-H., Olson, R. L., Smith, V. K., Park, D-W., Riddle, G. O., Quinterno, P. J., Lee, Y-O., Davis, A. S., Kim, S. R., Pringle, M. S., Choi, D-L., Pickthorn, L. B., Schlanger, S. O., Duennebier, F. K., Bergersen, D. D., and Lincoln, J. M., 1990b. Geological, geochemical, geophysical, and oceanographic data and interpretations of seamounts and Co-rich ferromanganese crusts from the Marshall Islands, KORDI-USGS R.V. Farnella Cruise F10-89-CP. U.S. Geological Survey Open File Report 90-407, 246 p.

Hein, J. R., Kirschenbaum, H., Schwab, W. C., Usui, A., Taggart, J. E., Stewart, K. C., Davis, A. S., Terashima, S., Quinterno, P. J., Olson, R. L., Pickthorn, L. G., Schulz, M. S., Morgan, C. L., 1990a. Mineralogy and geochemistry of Co-rich ferromanganese crusts and substrate rocks from Karin Ridge and Johnston Island, Farnella Cruise F7-86-HW. U.S. Geological Survey Open File Report 90-298, 80 p.

Hein, J. R., Konstantinova, K., Mikesell, M., Mizell, K., Fitzsimmons, J. N., Lam, P. J., Jensen, L. T. et al. 2017. "Arctic Deep Water Ferromanganese-Oxide Deposits Reflect the Unique Characteristics of the Arctic Ocean." *Geochemistry, Geophysics, Geosystems* 18 (11): 3771–3800. https://doi.org/10.1002/2017GC007186.

Hein, J. R., and Koschinsky, A. 2014. *Deep-Ocean Ferromanganese Crusts and Nodules*. *Treatise on Geochemistry: Second Edition*. 2nd ed. Vol. 13. Published by Elsevier Inc. https://doi.org/10.1016/B978-0-08-095975-7.01111-6.

Hein, J. R., Koschinsky, A., Bau, M., Manheim, F. T., Kang, J-K., and Roberts, L. 2000. "Cobalt-Rich Ferromanganese Crusts in the Pacific." In *Handbook of Marine Mineral Deposits*, 17:239–79.

Hein, J. R., Koschinsky, A., Halbach, P., Manheim, F. T., Bau, M., Kang, J-K., and Lubick, N. 1997. "Iron and Manganese Oxide Mineralization in the Pacific." *Geological Society, London, Special Publications* 119 (1): 123 LP – 138.

https://doi.org/10.1144/GSL.SP.1997.119.01.09.

Hein, J. R., Koschinsky, A., and Halliday, A. N. 2003. "Global Occurrence of Tellurium-Rich Ferromanganese Crusts and a Model for the Enrichment of Tellurium." *Geochimica et Cosmochimica Acta* 67 (6): 1117–27. https://doi.org/10.1016/S0016-7037(00)01279-6.

Hein, J. R., Koschinsky, A., and McIntyre, B. R. 2005. "Mercury- and Silver-Rich Ferromanganese Oxides, Southern California Borderland: Deposit Model and Environmental Implications." *Economic Geology* 100 (6): 1151–68. https://doi.org/10.2113/gsecongeo.100.6.1151.

Hein, J. R., Mizell, K., Koschinsky, A., and Conrad, T, A. 2013. "Deep-Ocean Mineral Deposits as a Source of Critical Metals for High- and Green-Technology Applications: Comparison with Land-Based Resources." *Ore Geology Reviews* 51 (June): 1–14. https://doi.org/10.1016/J.OREGEOREV.2012.12.001.

Hein, J. R., Morgenson, L. A., Clague, D. A., and Koski, R. A., 1987. Cobalt-rich ferromanganese crusts from the Exclusive Economic Zone of the United States and nodules from the oceanic Pacific. In Scholl, D.W., Grantz, A., and Vedder, J.G. (eds.), Geology and Resource Potential of the Continental Margin of Western North America and Adjacent Ocean Basins - Beaufort Sea to Baja California. Circum-Pacific Council for Energy and Mineral Resources, Earth Sci. Series v. 6, Houston, Texas, p. 753-771.

Hein, J. R., Schulz, M. S., Dunham, R. E., Stern, R. J., and Bloomer, S. H. 2008. "Diffuse Flow Hydrothermal Manganese Mineralization along the Active Mariana and Southern Izu-Bonin Arc System, Western Pacific." *Journal of Geophysical Research: Solid Earth* 113 (8). https://doi.org/10.1029/2007JB005432.

Hein, J. R., Schwab, W. C., and Davis, A. S. 1988. "Cobalt- and Platinum-Rich Ferromanganese Crusts and Associated Substrate Rocks from the Marshall Islands." *Marine Geology* 78 (3–4): 255–83. https://doi.org/10.1016/0025-3227(88)90113-2.

Hein, J. R., Yeh, H-W., Gunn, S. H., Sliter, W. V., Benninger, L. M., and Wang, C-H. 1993. "Two Major Cenozoic Episodes of Phosphogenesis Recorded in

Equatorial Pacific Seamount Deposits." *Palaeogeography and Palaeoclimatology* 8 (2): 293–311.

Huh, Y., Chan, L. H., Zhang, L., and Edmond, J. M. 1998. "Lithium and Its Isotopes in Major World Rivers: Implications for Weathering and the Oceanic Budget." *Geochimica et Cosmochimica Acta* 62 (12): 2039–51. https://doi.org/10.1016/S0016-7037(98)00126-4.

Jackson, M. G., Hart, S. R., Konter, J. G., Koppers, A. A.P., Staudigel, H., Kurz, M. D., Blusztajn, J., and Sinton, J. M. 2010. "Samoan Hot Spot Track on a 'Hot Spot Highway': Implications for Mantle Plumes and a Deep Samoan Mantle Source." *Geochemistry, Geophysics, Geosystems* 11 (12). https://doi.org/10.1029/2010GC003232.

Jiahua, P., De Carlo, E. H., and Liu, S. 2003. "Effect of Phosphatization on Element Concentration of Cobalt-Rich Ferromanganese Crusts." In *Proceedings of the ISOPE Ocean Mining Symposium*, 20–26. https://doi.org/10.1111/j.1755-6724.2005.tb00900.x.

Jiang, X., Lin, X., Yao, D., Zhai, S., and Guo, W. 2007. "Geochemistry of Lithium in Marine Ferromanganese Oxide Deposits." *Deep-Sea Research Part I: Oceanographic Research Papers* 54 (1): 85–98. https://doi.org/10.1016/j.dsr.2006.10.004.

Johnson, K. S., Coale, K. H., Berelson, W. M., and Gordon, R. M. 1996. "On the Formation of the Manganese Maximum in the Oxygen Minimum." *Geochimica et Cosmochimica Acta*. https://doi.org/10.1016/0016-7037(96)00005-1.

Josso, P., Parkinson, I., Horstwood, M., Lusty, P., Chenery, S., and Murton, B. 2019. "Improving Confidence in Ferromanganese Crust Age Models: A Composite Geochemical Approach." *Chemical Geology* 513: 108–19. https://doi.org/10.1016/j.chemgeo.2019.03.003.

Konstantinova, N., Cherkashov, G., Hein, J. R., Mirão, J., Dias, L., Madureira, P., Kuznetsov, V., and Maksimov, F. 2017. "Composition and Characteristics of the Ferromanganese Crusts from the Western Arctic Ocean." *Ore Geology Reviews* 87 (July): 88–99. https://doi.org/10.1016/j.oregeorev.2016.09.011.

Koschinsky, A., Stascheit, A., Bau, M., and Halbach, P. 1997. "Effects of Phosphatization on the Geochemical and Mineralogical Composition of Marine Ferromanganese Crusts." *Geochimica Et Cosmochimica Acta* 61 (19): 4079–94. https://doi.org/Doi 10.1016/S0016-7037(97)00231-7.

Koschinsky, A. and Halbach, P. 1995. "Sequential Leaching of Marine Ferromanganese Precipitates: Genetic Implications." *Geochimica et Cosmochimica Acta* 59 (24): 5113–32. https://doi.org/10.1016/0016-7037(95)00358-4.

Koschinsky, A. and Hein, James R. 2003. "Uptake of Elements from Seawater by Ferromanganese Crusts: Solid-Phase Associations and Seawater Speciation." *Marine Geology* 198 (3–4): 331–51. https://doi.org/10.1016/S0025-3227(03)00122-1.

Koschinsky, A., Hein, J. R., Kraemer, D., Foster, A. L., Kuhn, T., and Halbach, P. (Accepted to Geochim. Cosmochim. Acta October 2019). Platinum enrichment and phase associations in marine ferromanganese crusts and nodules based on a multi-method approach.

Kramer, D., Cullen, J. T., Christian, J. R., Johnson, W. K., and Pedersen, T. F. 2011. "Silver in the Subarctic Northeast Pacific Ocean: Explaining the Basin Scale Distribution of Silver." *Marine Chemistry*. https://doi.org/10.1016/j.marchem.2010.11.002.

Landing, W. M., and Bruland K. W. 1987. "The Contrasting Biogeochemistry of Iron and Manganese in the Pacific Ocean." *Geochimica et Cosmochimica Acta* 51 (1): 29–43. https://doi.org/10.1016/0016-7037(87)90004-4.

Maeno, M. Y., Ohashi, H., Yonezu, K., Miyazaki, A., Okaue, Y., Watanabe, K., Ishida, T., Tokunaga, M., and Yokoyama, T. 2016. "Sorption Behavior of the Pt(II) Complex Anion on Manganese Dioxide (δ-MnO2): A Model Reaction to Elucidate the Mechanism by Which Pt Is Concentrated into a Marine Ferromanganese Crust." *Mineralium Deposita* 51 (2): 211–18. https://doi.org/10.1007/s00126-015-0599-7.

Manheim, F. T. and Lane-Bostwick, C. M. 1988. "Cobalt in Ferromanganese Crusts as a Monitor of Hydrothermal Discharge on the Pacific Sea Floor." *Nature 1988 335:6185* 335 (6185): 59. https://doi.org/10.1038/335059a0.

McKay, J. L. and T. F. Pedersen. 2008. “The Accumulation of Silver in Marine Sediments: A Link to Biogenic Ba and Marine Productivity.” *Global Biogeochemical Cycles* 22 (4). https://doi.org/10.1029/2007GB003136.

McLennan, S. M. (1989), Rare earth elements in sedimentary rocks: Influence of provenance and sedimentary processes, in Geochemistry and Mineralogy of Rare Earth Elements, Rev. Mineral., vol. 21, edited by B. R. Lipin and G. A. McKay, pp. 169–200, Mineral. Soc. of Am., Washington, D. C.

Mikhailik, P. E., Khanchuk, A. I., Mikhailik, E. V., Ivanov, M. V., Rashidov, V. A., Zarubina, N. V., Blokhin, M. G., Barinov, N. N., and Pletnev, S. P. 2018. “Abnormally High Mercury Contents in Hydrogenic Ferromanganese Crusts from Seth Guyot (Northwestern Pacific).” *Russian Geology and Geophysics* 59 (3): 217–25. https://doi.org/10.1016/j.rgg.2018.03.001.

Morgan, C. 2008. Mining development scenario summary (cobalt-rich ferromanganese crusts deposits). In: Mining Cobalt-rich Ferromanganese Crusts and Polymetallic Sulphides Deposits: Technological and Economic Considerations. Proceedings of the International Seabed Authority’s Workshop, Kingston, Jamaica, 31 July–4 August 2006, 131–207.

Nielsen, Sune G., Mar-Gerrison, S., Gannoun, A., LaRowe, D., Klemm, V., Halliday, A. N., Burton, K. W., and Hein, J. R. 2009. “Thallium Isotope Evidence for a Permanent Increase in Marine Organic Carbon Export in the Early Eocene.” *Earth and Planetary Science Letters* 278 (3–4): 297–307. https://doi.org/10.1016/j.epsl.2008.12.010.

Parker, C. E., Brown, M. T., and Bruland, K. W. 2016. “Scandium in the Open Ocean: A Comparison with Other Group 3 Trivalent Metals.” *Geophysical Research Letters* 43 (6): 2758–64. https://doi.org/10.1002/2016GL067827.

Pistiner, J. S. and Henderson, G. M. 2003. “Lithium-Isotope Fractionation during Continental Weathering Processes.” *Earth and Planetary Science Letters* 214 (1–2): 327–39. https://doi.org/10.1016/S0012-821X(03)00348-0.

Puteanus, D. and Halbach, P. 1988. “Correlation of Co Concentration and Growth Rate - A Method for Age Determination of Ferromanganese Crusts.” *Chemical Geology* 69 (1–2): 73–85. https://doi.org/10.1016/0009-2541(88)90159-3.

Rudnick, R. L., and Gao, S. 2003. *Treatise on Geochemistry*. *Treatise on Geochemistry*. https://doi.org/10.1016/B0-08-043751-6/03016-4.

Schlitzer, R., Ocean Data View, odv.awi.de, 2018.

Taylor, S. R., and McLennan, S. M. 1985. *The Continental Crust: Its Composition and Evolution: An Examination of the Geochemical Record Preserved in Sedimentary Rocks (GT)*. Edited by S.R. Taylor and S.M. McLennan. *The Continental Crust: Its Composition and Evolution. An Examination of the Geochemical Record Preserved in Sedimentary Rocks.* Blackwell Scientific Pub.,Palo Alto, CA. https://doi.org/10.1017/S0016756800032167.

Usui, A., Nishi, K., Sato, H., Nakasato, Y., Thornton, B. Kashiwabara, T., Tokumaru, A. et al. 2017. "Continuous Growth of Hydrogenetic Ferromanganese Crusts since 17 Myr Ago on Takuyo-Daigo Seamount, NW Pacific, at Water Depths of 800–5500 M." *Ore Geology Reviews* 87 (July): 71–87. https://doi.org/10.1016/J.OREGEOREV.2016.09.032.

Usui, A., and Someya, M. 1997. "Distribution and Composition of Marine Hydrogenetic and Hydrothermal Manganese Deposits in the Northwest Pacific." *Geological Society, London, Special Publications* 119 (1): 177–98. https://doi.org/10.1144/gsl.sp.1997.119.01.12.

Von Damm, K. L., Edmond, J. M., Grant, B., Measures, C. I., Walden, B., and Weiss, R. F. 1985. "Chemistry of Submarine Hydrothermal Solutions at 21 °N, East Pacific Rise." *Geochimica et Cosmochimica Acta* 49 (11): 2197–2220. https://doi.org/10.1016/0016-7037(85)90222-4.

Yeo, I. A., Howarth, S. A., Spearman, J., Cooper, A., Crossouard, N., Taylor, J., Turnbull, M., and Murton. B. J. 2019. "Distribution of and Hydrographic Controls on Ferromanganese Crusts: Tropic Seamount, Atlantic." *Ore Geology Reviews* 114 (November): 103131. https://doi.org/10.1016/j.oregeorev.2019.103131.

Zhang, F., Zhang, W., Zhu, K., Gao, S., Zhang, H., Zhang, X., and Zhu, B. 2008. Distribution characteristics of cobalt-rich ferromanganese crust resources on submarine seamounts in the western Pacific. Acta Geologica Sinica 82: 796–803.

Table 1. Statistics for bulk ferromanganese crusts from the Tuvalu EEZ [1,2,3]

	N	Mean	Median	StDev	Min	Max
Fe wt. %	31	19.8	19.6	2.37	14.1	23.8
Mn	31	19.8	19.3	3.69	13.3	29.8
Fe/Mn	31	1.04	0.98	0.26	0.47	1.67
Si	31	5.69	5.63	1.80	1.80	10.3
Al	31	1.65	1.52	0.69	0.34	3.35
Si/Al	31	3.69	3.49	0.74	2.89	5.84
Mg	31	1.16	1.14	0.08	1.03	1.33
Ca	31	2.69	2.53	0.46	2.26	4.32
Na	31	1.30	1.30	0.29	0.38	1.77
K	31	0.56	0.52	0.21	0.31	1.34
Ti	31	1.22	1.18	0.27	0.84	1.74
P	31	0.40	0.40	0.07	0.28	0.52
S	30	0.18	0.18	0.05	0.09	0.29
CO_2	31	0.71	0.56	0.53	0.27	2.64
LOI[1]	31	34.8	34.4	2.19	28.8	38.5
H_2O^-	31	22.0	21.7	2.02	17.5	26.6
H_2O^+	31	12.0	12.3	2.78	7.10	17.0
Ag ppm	31	0.24	0.19	0.24	0.04	1.3
As	31	220	224	39	144	308
Ba	31	1493	1461	243	1074	2047
Be	31	5.4	5.2	0.98	3.9	7.5
Bi	31	17	17	8.3	5.1	43
Cd	31	4.0	3.9	0.90	2.5	6.7
Cl	30	3998	3836	2290	574	8723
Co	31	5270	4984	2390	2337	12808
Cr	29	20	15	21	5.1	108
Cu	31	1380	1372	470	554	2520
F	31	331	334	130	148	733
Hf	31	3.7	2.6	2.8	0.51	11
Hg ppb	24	71	24	203	8.9	1020
In ppm	31	0.33	0.31	0.09	0.20	0.54
Li	31	6.3	5.1	4.0	1.3	17
Mo	31	407	392	108	224	631
Nb	31	70	71	17	39	125
Ni	31	3861	3595	1321	2149	7554
Pb	31	1077	1069	177	728	1546
Rb	31	6.0	5.1	3.8	2.5	22
Sb	31	50	49	12	37	89
Sc	31	12	13	2.4	8.1	17

Table 1. Continued

	N	Mean	Median	StDev	Min	Max
Se	28	2.8	2.6	2.07	0.3	6.3
Sn	31	11	9.0	9.1	5.7	56
Sr	31	1493	1496	146	1087	1741
Ta	31	0.92	0.72	0.67	0.12	3.2
Te	31	46	42	30	19	158
Th	31	6.3	5.1	2.66	3.2	13
Tl	31	146	138	50	80	292
U	31	12	13	1.41	8.9	15
V	31	659	651	88	483	824
W	31	73	70	19	41	112
Zn	31	612	605	58	514	734
Zr	31	677	688	89	495	853
La	31	229	228	47.4	133	319
Ce	31	668	620	240	329	1283
Pr	31	39.9	40.4	10.6	18.6	60.4
Nd	31	164	158	45.67	74.2	253
Sm	31	32.4	31.2	9.52	14.0	51.3
Eu	31	8.64	8.51	2.29	4.16	12.5
Gd	31	40.2	39.0	9.93	20.9	57.4
Tb	31	6.12	6.18	1.47	3.29	8.5
Dy	31	39.8	39.9	8.91	22.7	55.2
Y	31	175	175	31	103	230
Ho	31	8.68	8.83	1.74	5.50	11.51
Er	31	24.7	24.4	5.01	14.9	33.8
Tm	31	3.75	3.81	0.68	2.33	5.01
Yb	31	23.8	23.6	4.20	14.8	32.0
Lu	31	3.86	3.95	0.60	2.30	5.11
∑REY[2]	31	1468	1443	314	1000	2213
%HREY[3]	31	23	24	5	16	32
Au ppb	10	29	22	25	17	101
Ir	10	8	8	2	6	11
Os	10	4	4	2	2	8
Pd	9	6	7	2	3	9
Pt	10	278	317	94.7	128	395
Rh	10	20	22	4.9	12	25
Ru	10	21	21	6	12	29

[1]Loss on ignition at 1000°C

[2]∑ REY = Sum of rare earth elements plus yttrium

[3]Percent of heavy REY (Eu-Lu, +Y) of the total sum of REY

Table 2. Statistics for layers samples from ferromanganese crusts compared to a layer that is phosphatized

	N	Mean	Median	StDev	Min	Max	Phosphatized D11-17_L41-56
Fe wt. %	21	19.8	19.4	2.79	15.9	26.8	10.9
Mn	21	19.9	19.8	2.70	15.1	24.9	8.79
Fe/Mn	21	1.02	0.94	0.25	0.64	1.66	1.24
Si	21	5.52	5.65	1.44	3.06	7.99	14.7
Al	21	1.60	1.72	0.62	0.66	2.69	5.27
Si/Al	21	3.66	3.45	0.71	2.72	5.65	2.79
Mg	21	1.13	1.13	0.08	0.99	1.27	1.10
Ca	21	2.51	2.52	0.20	2.02	2.83	3.85
Na	21	1.42	1.44	0.16	1.08	1.73	2.29
K	21	0.55	0.56	0.17	0.32	1.03	2.53
Ti	21	1.29	1.21	0.40	0.80	2.17	0.93
P	21	0.40	0.42	0.06	0.31	0.50	1.16
S	21	0.19	0.19	0.03	0.13	0.26	0.12
CO_2	21	0.50	0.46	0.16	0.29	0.94	0.54
LOI[1]	21	35.7	35.0	3.04	31.1	46.2	26.3
H_2O^-	21	22.2	21.9	1.44	19.3	25.3	16.0
H_2O^+	21	12.7	12.10	3.53	9.10	25.3	9.90
Ag ppm	21	0.20	0.17	0.12	0.04	0.46	0.23
As	21	214	207	41	157	288	80
Ba	21	1563	1490	261	1192	2074	885
Be	21	5.7	5.7	1.2	3.7	8.2	3.8
Bi	21	17	15	5.2	10	29	7.3
Cd	21	3.8	3.8	0.87	2.5	5.7	2.0
Cl	21	5194	4915	2245	1930	9180	2529
Co	21	5211	5606	1630	2644	8511	2455
Cr	21	13	13	7.6	1.3	24	30
Cu	21	1441	1504	488	700	2425	1350
F	21	379	321	181	150	926	3438
Hf	21	5.6	4.6	4.25	0.6	15.2	2.1
Hg ppb	18	36	29	24	12	99	26
In ppm	21	0.34	0.32	0.13	0.17	0.68	0.27
Li	21	6.4	6.2	3.6	2.6	14	27
Mo	21	436	418	92	281	617	138
Nb	21	71	70	17	41	99	61
Ni	21	3764	3654	1310	1571	6168	2218
Pb	21	1102	1107	135	796	1380	460
Rb	21	5.6	5.2	2.94	2.3	13.5	41
Sb	21	51.8	49.9	10.83	34.8	81.1	30
Sc	21	12	12	2.3	8.4	16	18

Table 2. Continued

	N	Mean	Median	StDev	Min	Max	Phosphatized D11-17_L41-56
Se	17	3.6	3.8	1.7	0.39	6.5	<2
Sn	21	11	10.1	3.5	5.5	19	7.3
Sr	21	1486	1478	140	1220	1739	702
Ta	21	1.2	0.71	1.1	0.27	4.2	0.38
Te	21	40	38	15	19	73	28
Th	21	6.7	6.0	3.8	1.8	17	4.2
Tl	21	145	144	45	45	219	71
U	21	13	13	1	10	15	5.2
V	21	685	665	105	519	862	311
W	21	81	80	16	53	106	29
Zn	21	611	593	64	507	763	395
Zr	21	688	696	103	499	906	477
La	21	248	263	58.4	155	338	231
Ce	21	752	720	271	289	1302	508
Pr	21	44.0	45.7	14.74	21.3	63.5	44.0
Nd	21	182	191	60.8	90.2	269	176
Sm	21	35.8	37.5	12.95	17.0	56.1	33.6
Eu	21	9.3	10.0	2.95	4.9	13.7	8.76
Gd	21	43.2	44.5	12.6	23.7	62.2	43.8
Tb	21	6.55	6.96	1.84	3.66	9.39	6.23
Dy	21	42.6	43.4	10.82	24.7	58.0	39.3
Y	21	187	186	33.6	137	240	300
Ho	21	9.28	9.49	2.02	5.81	12.3	8.57
Er	21	26.7	26.0	5.58	16.6	35.3	23.8
Tm	21	3.96	3.97	0.68	2.67	4.94	3.43
Yb	21	25.0	24.7	4.00	17.3	31.0	21.2
Lu	21	4.01	4.10	0.49	3.20	4.77	3.33
∑REY[2]	21	1619	1745	429	966	2375	1452
%HREY[3]	21	23	23	4	16	35	32
Au ppb	6	23	22	4	18	30	--
Ir	6	8	8	2	6	12	--
Os	6	4	4	1	3	5	--
Pd	6	6	6	2	3	9	--
Pt	6	325	230	261.4	109	800	--
Rh	6	22	20	11.8	10	40	--
Ru	6	20	18	8	10	32	--

[1]Loss on ignition at 1000°C

[2]∑ REY = Sum of rare earth elements plus yttrium

[3]Percent of heavy REY (Eu-Lu, +Y) of the total sum of REY

Table 3. Growth rates and ages estimated using Co-chronomoter equations from Manheim and Lane-Bostwick (1988) and Puteanus and Halbach (1988) [1]

Sample ID	Bulk/Layer	sample thickness (mm)	Manheim and Lane-Bostwick (1988)		Puteanus + Halbach (1988)	
			Rate mm/My	age (My)	Rate mm/My	age (My)
D04-02	B0-60	60	1.16	51.6	3.8	15.6
D04-02	L0-10	10	2.37	4.2	10.4	0.96
D04-02	L10-55	45	1.04	43.5	3.4	13.2
D04-14	B0-30	30	0.36	82.2	1.2	24.3
D04-22	B0-30	30	1.20	25.1	4.0	7.5
D04-24	B0-23	23	0.38	61.3	1.2	18.7
D05-27	B0-37	37	1.74	21.2	6.3	5.8
D06-08	B0-65	65	1.18	55.3	5.0	13.1
D07-33	B0-18	18	0.96	18.7	3.1	5.9
D08-10	B0-2	2	1.02	2.0	2.8	0.7
D09-12	B0-25	25	1.30	19.2	4.4	5.7
D09-12	L0-10	10	1.20	8.3	3.7	2.7
D09-12	L10-20	10	1.00	10.0	3.5	2.9
D10-54	B0-5	5	1.85	2.7	6.9	0.73
D11-17	B0-56	56	2.16	25.9	16.3	3.4
D11-17	L0-25	25	1.50	16.6	5.5	4.6
D11-17	L25-41	16	1.01	15.9	4.2	3.9
D11-17	L41-56	15	1.50	10.0	233.7	0.06
D16-30	B0-42	42	1.41	29.7	4.7	8.9
D16-31 (2)	B0-35	35	1.13	31.0	3.7	9.6
D16-31 (2)	L0-14	14	2.08	6.7	8.4	1.7
D16-31 (2)	L14-26	12	1.13	10.6	4.0	3.0
D16-31 (2)	L26-38	12	0.86	13.9	2.7	4.4
D16-34	B0-12	12	1.03	11.6	3.1	3.9
D16-37	B0-45	45	1.09	41.3	3.4	13.4
D16-37	L0-10	10	1.13	8.9	3.2	3.1
D16-37	L10-20	10	3.18	3.1	17.9	0.6
D16-37	L20-30	10	0.88	11.4	2.8	3.6
D16-37	L30-45	15	0.63	23.7	2.1	7.2
D17-07	B0-24	24	1.69	14.2	7.1	3.4
D17-27	B0-22	22	1.78	12.4	5.8	3.8
D17-30	B0-32*	32	0.98	32.6	3.3	9.8
D17-30	L0-10	10	0.95	10.5	2.8	3.6
D17-30	L10-32	22	1.00	22.0	3.6	6.1
D18-20	B0-1	1	1.50	0.7	4.6	0.2
D19-33	B0-13	13	1.92	6.8	10.7	1.2
D20-39	B0-72*	72	2.13	33.8	8.4	8.6
D20-39	L0-26	26	4.86	5.3	52.5	0.49
D20-39	L26-56	30	2.03	14.8	9.0	3.3
D20-39	L56-72	16	0.88	18.2	3.4	4.7
D20-54	B0-20	20	2.65	7.6	9.3	2.2
D20-54	L0-3	3	3.55	0.8	15.4	0.2
D20-54	L3-16	13	3.50	3.7	14.8	0.9
D20-54	L16-21	5	2.46	2.0	9.5	0.5
D20-54	nodule	10	0.95	10.5	3.7	2.7
D22-03	B0-12	12	1.66	7.2	5.1	2.3
D22-26	B0-15	15	0.95	15.7	3.1	4.8
D23-21	B0-30	30	2.09	14.4	7.6	4.0
D25-27	B0-15	15	3.37	4.4	16.0	0.94
D26-04	B0-10	10	2.55	3.9	10.3	0.97
D27-04	B0-10	10	4.58	2.2	549	0.02
D28B-01	B0-5	5	4.93	1.0	NA	NA
D30-02	B0-15	15	4.97	3.0	345	0.04
D28A-01	L3_UPPER	5	4.71	1.1	NA	NA
D28A-01	L1_LOWER	12	48.8	0.2	NA	NA
D28A-01	L2_MIDDLE	22	1395	0.02	NA	NA

[1] The growth rate calculation from Puteanus and Halbach (1988) is only applicable to crusts with Co concentrations between 0.24 and 2 wt. %; samples with Co values outside this range are marked with NA

Table 4. Water-normalized chemistry for a sediment-hosted stratabound hydrothermal Mn sample from the Tuvalu EEZ [1,2,3]

Sample No.	TE-44C	TE-44A	TE-44B
Cruise ID	RR1310	RR1310	RR1310
Sample ID	D28A-01	D28A-01	D28A-01
Bulk/Layer	L3_UPPER	L1_LOWER	L2_MIDDLE
Latitude	-11.33	-11.33	-11.33
Longitude	179.87	179.87	179.87
Water Depth (m)	2842	2842	2842
Fe wt%	15.8	5.98	0.65
Mn	22.2	31.4	21.3
Fe/Mn	0.71	0.19	0.03
Si	3.90	1.78	0.42
Al	1.11	0.70	0.30
Si/Al	3.51	2.55	1.41
Mg	1.46	1.86	1.59
Ca	5.33	7.12	21.4
Na	1.55	2.14	0.94
K	0.58	0.87	0.78
Ti	0.66	0.21	0.03
P	0.37	0.15	0.03
S	0.10	0.08	0.05
CO_2	4.06	6.50	22.7
LOI[1]	45.9	33.7	35.8
H_2O^-	20.4	10.6	5.00
H_2O^+	10.3	9.17	4.74
Ag ppm	0.10	0.03	0.02
As	191	70	9.5
Ba	990	813	405
Be	3.8	1.3	0.2
Bi	5.6	1.9	0.16
Cd	9.3	20	14
Cl	10496	12768	6883
Co	2386	578	46
Cr	3.8	3.4	1.1
Cu	1471	2881	1253
F	210	276	280
Hf	1.3	1.7	0.42
Hg ppb	10	8.9	3.8

Table 4. Continued

Sample No.	TE-44C	TE-44A	TE-44B
Cruise ID	RR1310	RR1310	RR1310
Sample ID	D28A-01	D28A-01	D28A-01
Bulk/Layer	L3_UPPER	L1_LOWER	L2_MIDDLE
Latitude	-11.33	-11.33	-11.33
Longitude	179.87	179.87	179.87
Water Depth (m)	2842	2842	2842
In ppm	0.25	0.09	0.02
Li	138	403	401
Mo	264	179	152
Nb	35	12	2.1
Ni	6879	>10000	4349
Pb	707	230	21
Rb	3.6	4.0	3.2
Sb	41	89	47
Sc	12	4.7	2.0
Se	5.0	6.7	1.5
Sn	5.0	2.3	0.95
Sr	1239	884	963
Ta	0.16	0.10	0.0375
Te	18	6	1
Th	6.0	1.8	0.21
Tl	216	253	143
U	11	8.7	2.8
V	529	366	168
W	45	51	24
Zn	844	1223	1068
Zr	412	149	19
La	188	61.7	11.9
Ce	343	102	8.00
Pr	35.6	11.3	2.00
Nd	152	50.4	9.37
Sm	31.7	10.5	2.00
Eu	8.30	2.74	0.57
Gd	37.4	12.9	2.80
Tb	5.64	1.96	0.41
Dy	35.4	12.4	2.85
Y	161	57.5	18.4
Ho	7.55	2.64	0.71
Er	21.9	7.62	1.95
Tm	3.12	1.11	0.28
Yb	19.7	7.05	1.79
Lu	3.09	1.12	0.31
∑REY[2]	1054	343	63
%HREY[3]	28.8	31.2	47.5

[1]Loss on ignition at 1000°C

[2]∑REY = Sum of rare earth elements plus yttrium

[3]Percent of heavy REY (Eu-Lu, +Y) of the total sum of REY

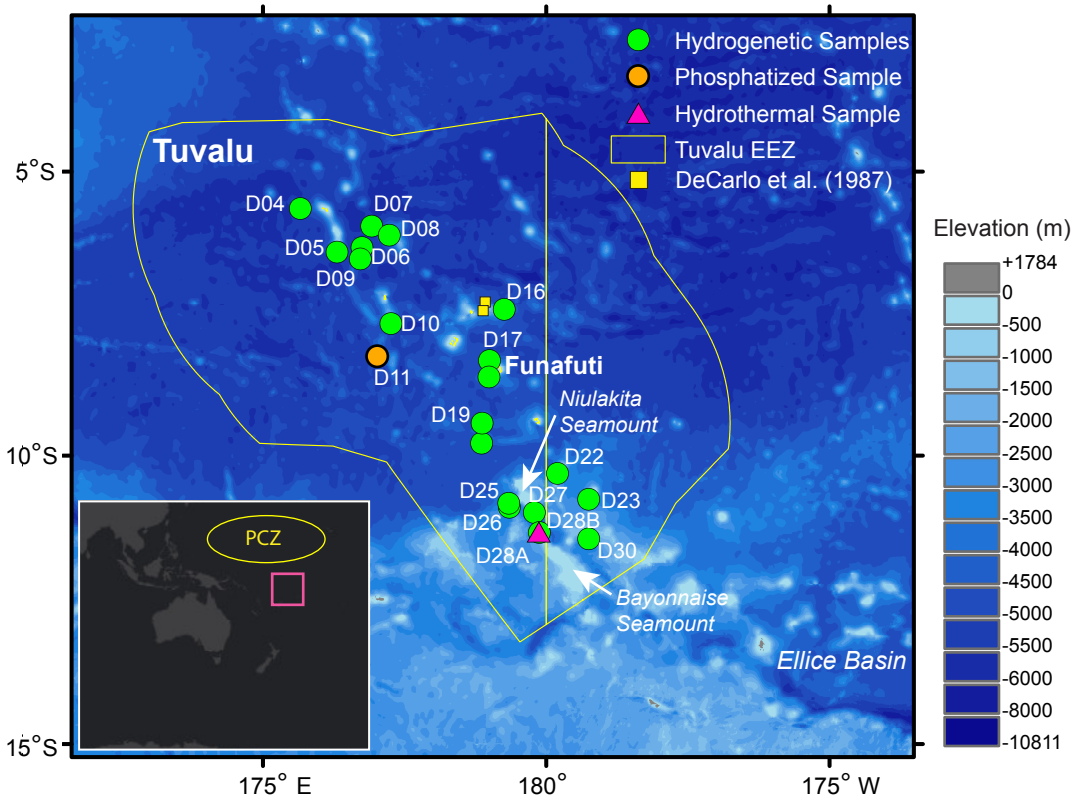

Figure 1. Dredge sites for FeMn samples in the Tuvalu EEZ and prominent seafloor features; inset map shows the general location of Tuvalu within the Pacific Ocean (pink square) as well as the approximate location of the Prime Crust Zone (PCZ from Hein et al. 2009; yellow oval) which is used for chemical comparisons; locations of two dredge sites from DeCarlo et al. (1987) are also included (yellow boxes).

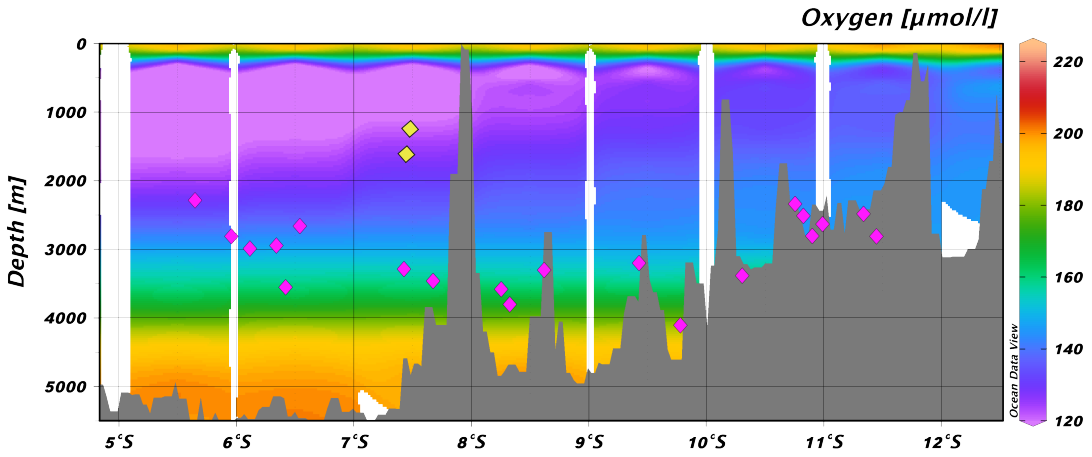

Figure 2. Depth section of seawater oxygen concentrations with sample locations plotted from this study (pink) and DeCarlo et al. (1987) (yellow); the plot was created in Ocean Data View (Schlitzer 2018) using oceanographic data from the World Ocean Atlas (Garcia et al. 2014). The scale bar for oxygen has a minimum value of 120 µmol/l and a maximum value of 225 µmol/l.

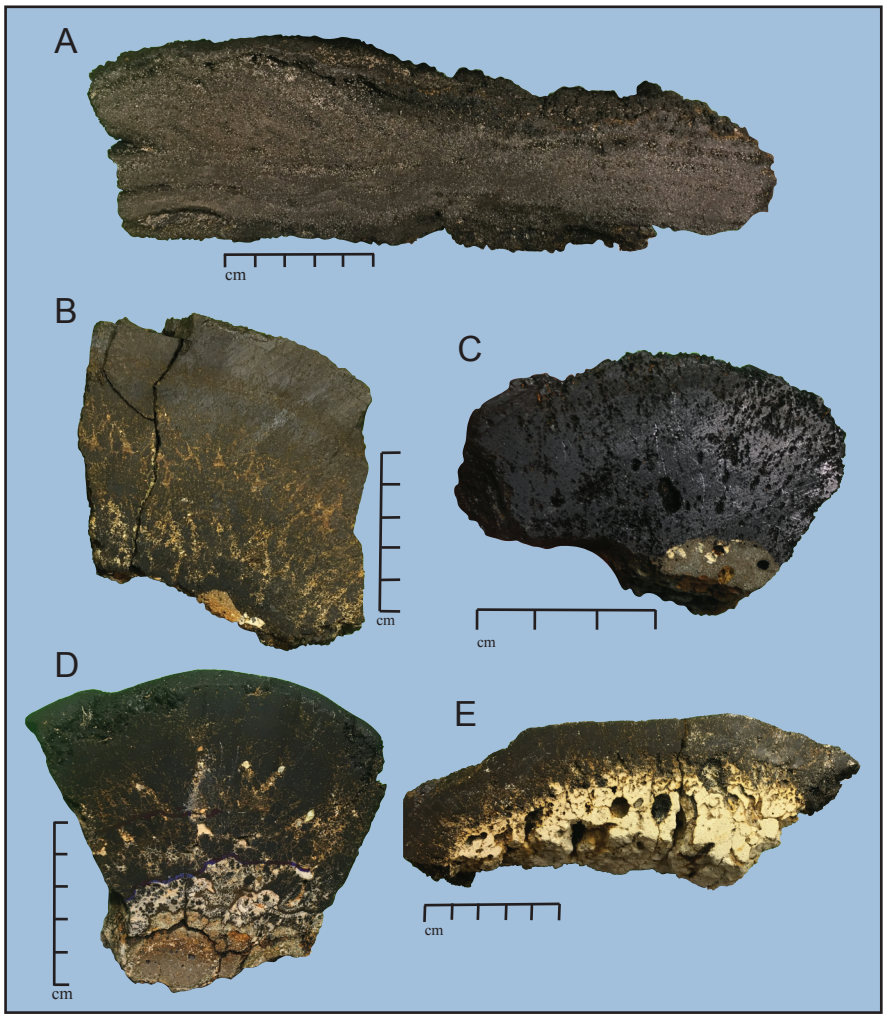

Figure 3. FeMn crust photos with centimeter scale bars. (A) Sample D28A-01 from sediment-hosted stratabound hydrothermal Mn deposit; (B) Sample D20-39 is the thickest crust collected (72 mm) and shows 3 distinct growth layers that were sub-sampled; (C) Sample D04-14 is purely hydrogenetic with no trace detrital minerals detected by XRD and contains very high concentrations of Mn and Co (29.8 and 1.28 wt. %, respectively); (D) Sample D11-17 is the only phosphatized sample collected; lenses of yellow-white carbonate fluorapatite can be seen throughout the lower layer and in the substrate breccia; (E) Sample D20-39 was dredged from the southeastern portion of the Tuvalu EEZ and is formed on a cemented pelagic carbonate substrate that has been partially mineralized by Mn.

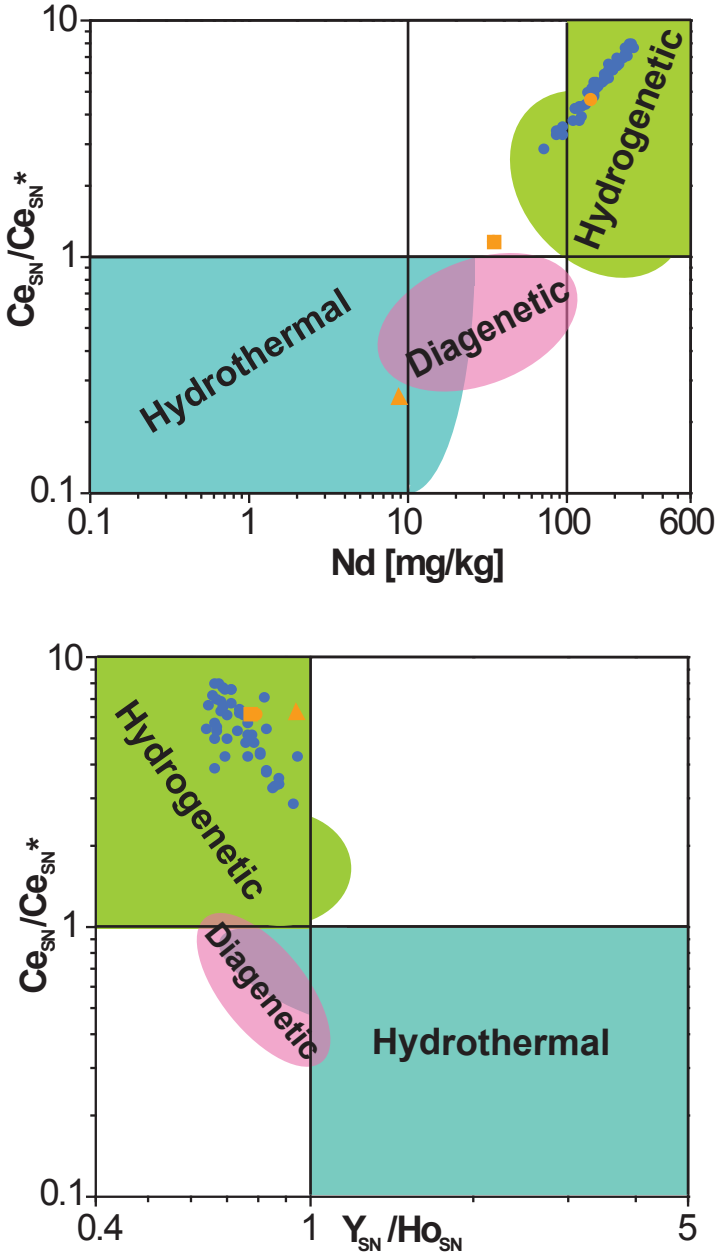

Figure 4. Data for Tuvalu hydrogenetic crust and crust layer samples (blue circles) and the sediment-hosted hydrothermal Mn sample layers (upper = orange circle, middle = orange triangle, lower = orange square) plotted on discrimination graphs developed by Bau et al. (2014); these discrimination plots were not developed to include phosphatized ferromanganese samples, so sample D11-17_L41-56 has been not been included.

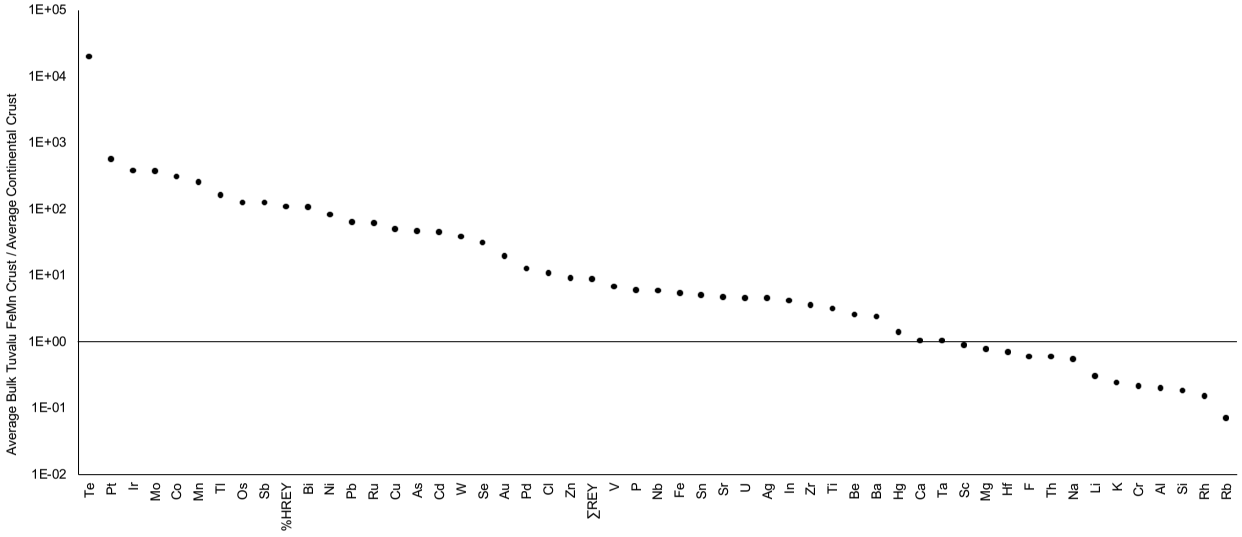

Figure 5. Element enrichment diagram for the average bulk composition of Tuvalu crusts relative to the average composition of continental crust (Rudnick and Gao 2003; Taylor and McLennan 1985); element ratios greater than 1 are enriched in Tuvalu crusts and those below 1 are enriched in continental crust.

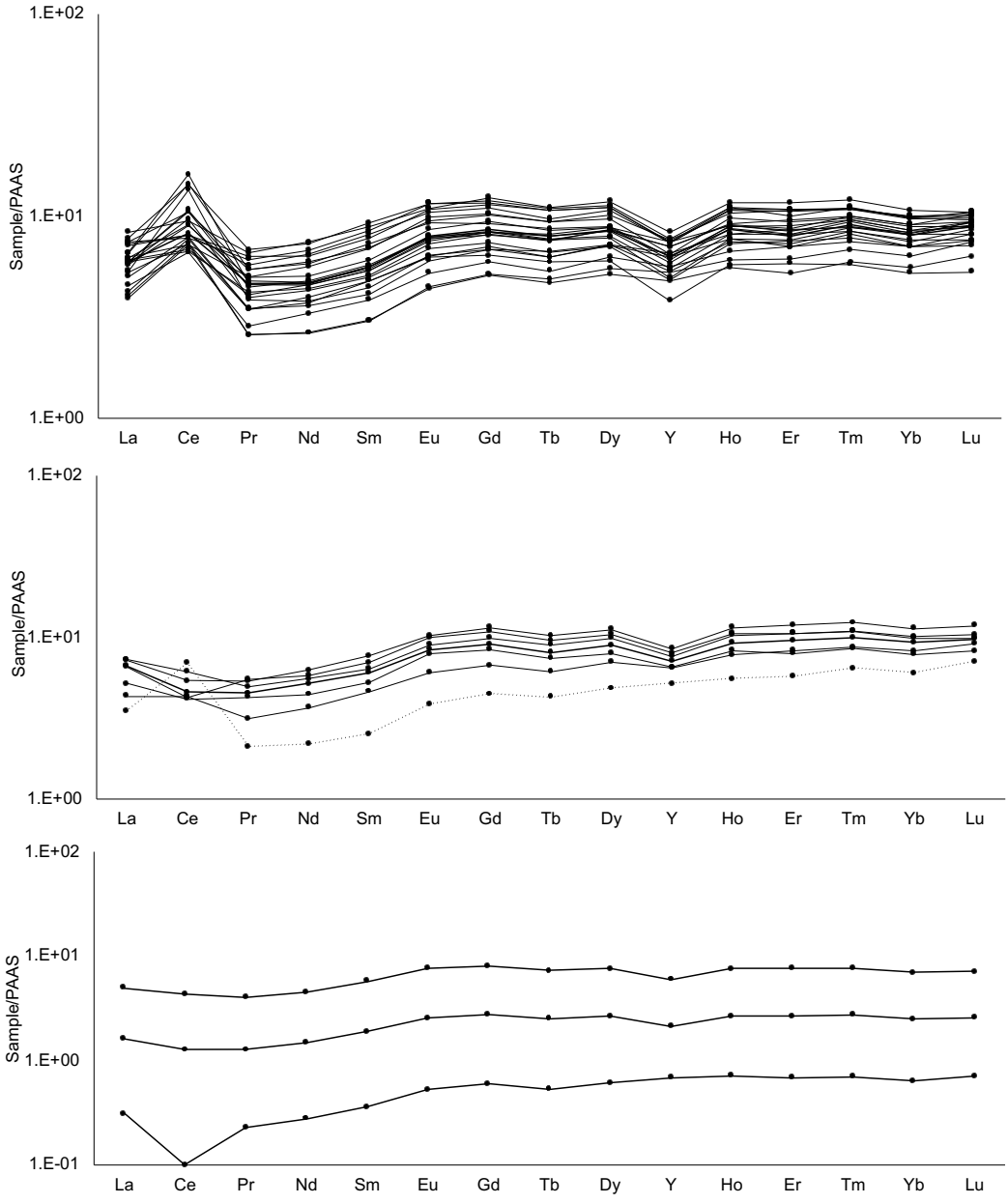

Figure 6. PAAS shale-normalized rare earth element plots for bulk Tuvalu crusts; (A) shows large positive Ce anomalies and large negative Y anomalies for the majority of samples, characteristic of hydrogenetic precipitation; (B) shows samples that lack a positive Ce anomaly, indicating fast growth rate (D25-27, D30-02, D17-27, D28B-01, D27-04) and one sample without a negative Y anomaly (D04-22); (C) shows the upper, middle, and lower layers of the hydrothermally mineralized sample D28A-01, with overall low REY enrichments and a negative Ce anomaly for the lower layer which has the highest degree of mineralization and the fastest growth rates.

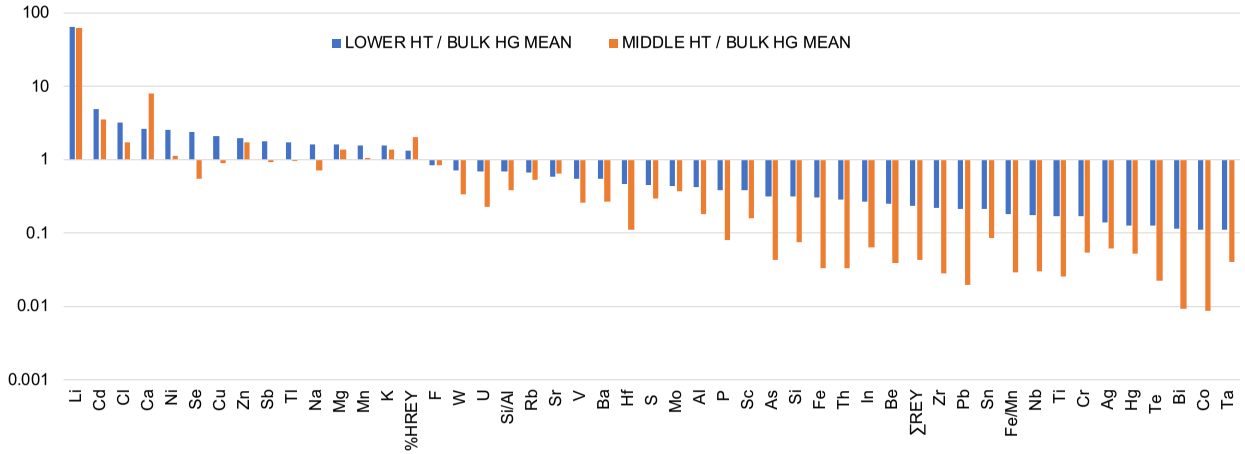

Figure 7. Element enrichment diagram for the composition of the middle layer (orange) and the lower layer (blue) from the hydrothermally (HT) mineralized sample, D28A-01, relative to the mean bulk composition of Tuvalu hydrogenetic (HG) crusts; element ratios greater than 1 are enriched in the hydrothermal layer and those below 1 are enriched in hydrogenetic crusts.

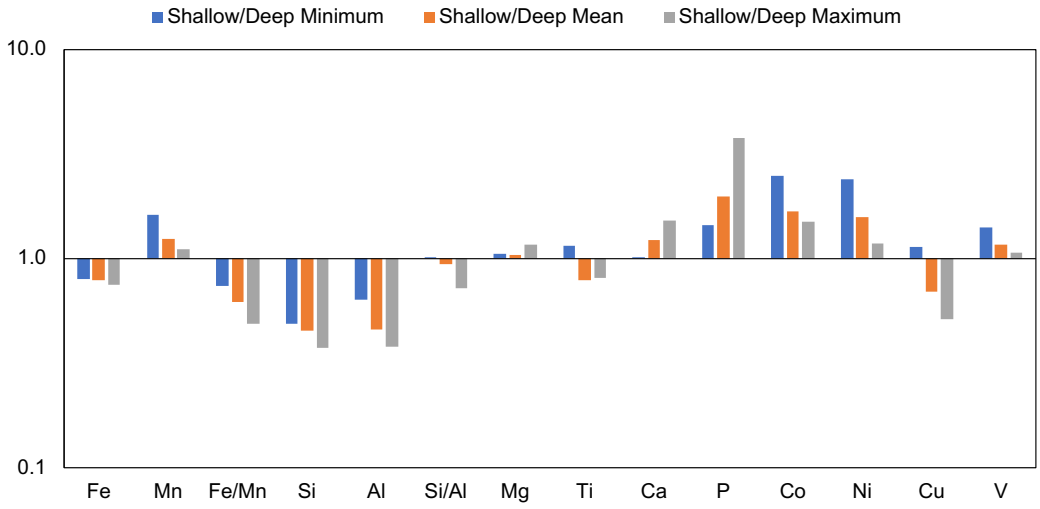

Figure 8. Element enrichment diagram for the average composition of FeMn crusts from water depths above 1700 m (called Shallow) reported by DeCarlo et al. (1987) relative to the minimum (blue), maximum (gray), and mean (orange) composition of bulk hydrogenetic crusts from this study, which were collected between 2286 and 4110 m (called Deep); element ratios greater than 1 are enriched in in the FeMn crusts from shallow depths and those below 1 are enriched in crusts from deeper depths.

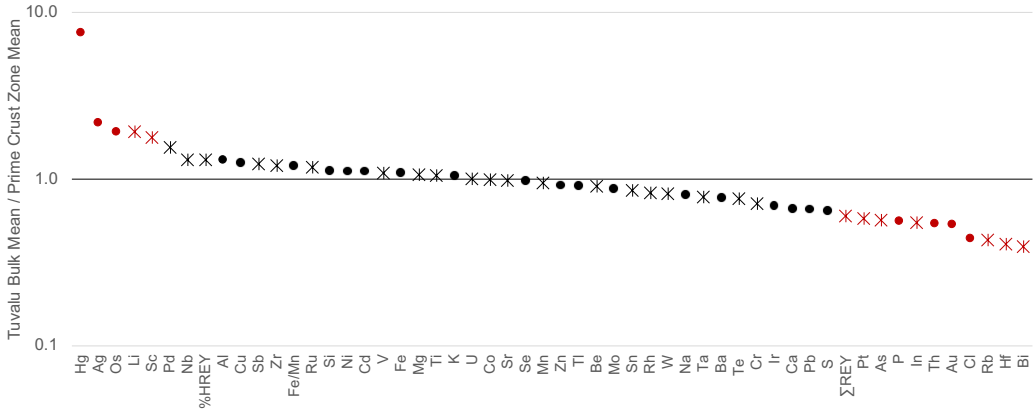

Figure 9. Element enrichment diagram for the average composition of Tuvalu bulk crusts relative to the average composition of crusts from the Prime Crust Zone (compiled by Hein et al. 2013); element ratios greater than 1 are enriched in Tuvalu crusts and those below 1 are enriched in the Prime Crust Zone. Elements marked by an asterisk are considered critical elements as defined by the United States Department of the Interior; elements in red are enriched in either Tuvalu crusts or PCZ crusts by a factor of 1.6 or more.

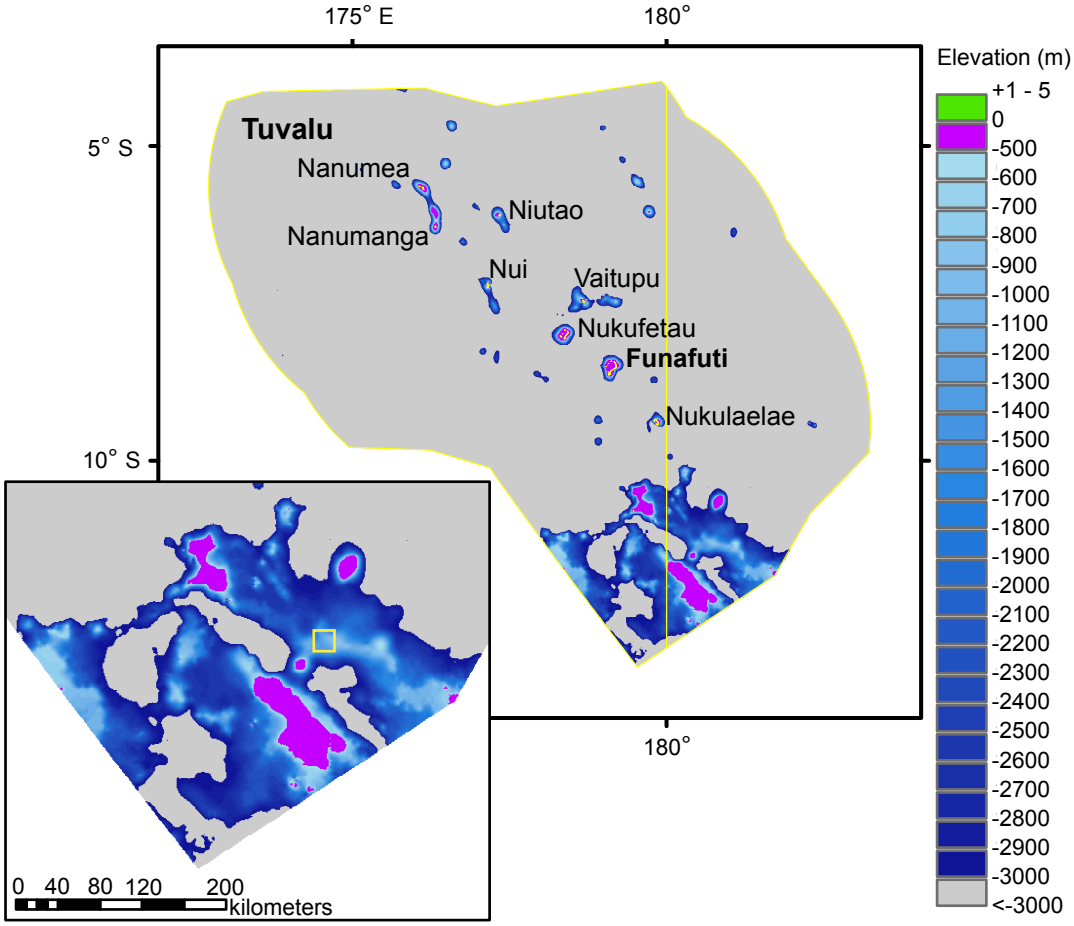

Figure 10. Map of areas within the Tuvalu EEZ that occur between 500 and 3000 m water depth, which is the depth criteria used to delineate regions that are permissive for FeMn crusts of potential economic interest; the inset shows the region with the highest potential; a 20 km^2 block is included (yellow outline) to illustrate the size of the sub-blocks that are used to define regions of interest for exploration by contractors with the International Seabed Authority.

Table S1. Mineralogy of crystalline phases in FeMn deposits from the Tuvalu EEZ[1,2,3]

Sample	Layer Interval	Major	Moderate	Minor
D04-02	B0-60	δ-MnO_2	goethite	K-feldspar, quartz
D04-02	L0-10	δ-MnO_2	plagioclase	
D04-02	L10-55	δ-MnO_2		plagioclase, quartz
D04-14	B0-30	δ-MnO_2		
D04-22	B0-30	δ-MnO_2	birnessite	plagioclase, quartz
D04-24	B0-23	δ-MnO_2		goethite
D05-27	B0-37	δ-MnO_2	K-feldspar	plagioclase, quartz
D06-08	B0-65	δ-MnO_2	phillipsite	plagioclase, calcite, quartz
D07-33	B0-18	δ-MnO_2	K-feldspar	quartz
D08-10	B0-2	δ-MnO_2		plagioclase
D09-12	B0-25	δ-MnO_2	phillipsite	calcite
D09-12	L0-10	δ-MnO_2	phillipsite	calcite, plagioclase
D09-12	L10-20	δ-MnO_2, birnessite	quartz	10Å manganate, plagioclase
D10-54	B0-5	δ-MnO_2	birnessite	plagioclase, calcite, quartz
D11-17	B0-56	δ-MnO_2	phillipsite, K-feldspar	quartz
D11-17	L0-25	δ-MnO_2		plagioclase, quartz
D11-17	L25-41	δ-MnO_2	phillipsite	quartz
D11-17	L41-56	δ-MnO_2	CFA, phillipsite, plagioclase	10Å manganate, smectite, pyroxene, quartz
D16-30	B0-42	δ-MnO_2		plagioclase, quartz
D16-31 (2)	B0-35	δ-MnO_2	goethite	plagioclase, quartz
D16-31 (2)	L0-14	δ-MnO_2		plagioclase, quartz
D16-31 (2)	L14-26	δ-MnO_2		plagioclase, quartz
D16-31 (2)	L26-38	δ-MnO_2		plagioclase, quartz
D16-34	B0-12	δ-MnO_2		plagioclase, quartz
D16-37	B0-45	δ-MnO_2		plagioclase
D16-37	L0-10	δ-MnO_2		plagioclase
D16-37	L10-20	δ-MnO_2	goethite	K-feldspar
D16-37	L20-30	δ-MnO_2		plagioclase
D16-37	L30-45	δ-MnO_2		plagioclase

Table S1. Continued

Sample	Layer Interval	Major	Moderate	Minor
D17-07	B0-24	δ-MnO_2	plagioclase	quartz
D17-27	B0-22	δ-MnO_2		plagioclase, quartz
D17-30	L0-10	δ-MnO_2		plagioclase
D17-30	L10-32	δ-MnO_2		plagioclase, quartz
D18-20	B0-1	δ-MnO_2	plagioclase, calcite	
D19-33	B0-13	δ-MnO_2	phillipsite, plagioclase	quartz
D20-39	L0-26	δ-MnO_2		plagioclase, quartz
D20-39	L26-56	δ-MnO_2	plagioclase	quartz
D20-39	L56-72	δ-MnO_2, birnessite	goethite	plagioclase, quartz
D20-54	B0-20	δ-MnO_2	K-feldspar	
D20-54	L0-3	δ-MnO_2	plagioclase	
D20-54	L3-16	δ-MnO_2		plagioclase
D20-54	L16-21	δ-MnO_2	K-feldspar	
D20-54	nodule	δ-MnO_2	birnessite, plagioclase	quartz
D22-03	B0-12	δ-MnO_2	10Å manganate	plagioclase
D22-26	B0-15	δ-MnO_2		plagioclase, calcite
D23-21	B0-30	δ-MnO_2		plagioclase, calcite, quartz
D25-27	B0-15	δ-MnO_2	K-feldspar	plagioclase, calcite, quartz
D26-04	B0-10	δ-MnO_2	calcite	quartz
D27-04	B0-10	δ-MnO_2	calcite	plagioclase
D28B-01	B0-5	δ-MnO_2	birnessite	plagioclase
D30-02	B0-15	δ-MnO_2		calcite, plagioclase, quartz
D28A-01	Upper	δ-MnO_2	birnessite, calcite, 10Å manganate	plagioclase
D28A-01	Middle	birnessite, calcite	10Å manganate	magnetite, quartz
D28A-01	Lower	birnessite, 10Å manganate	calcite	magnetite, quartz

[1] Mineralogy was determined by x-ray diffraction (XRD) and verified with chemistry; poorly crystalline FeOOH is also present in the majority of samples but is not detected by XRD

[2] Major = >25%, Moderate = 5-25%, Minor = <5%

[3] 10Å manganate = todorokite, asbolane, or buserite

Table S2. Chemical composition of ferromanganese crusts from the Tuvalu EEZ, normlizaed to 0% H_2O^-

Sample ID	D04-02	D04-02	D04-02	D04-14	D04-22	D04-24	D05-27	D06-08	D07-33	D08-10
Bulk/Layer Interval [4]	B0-60	L0-10	L10-55	B0-30	B0-30	B0-23	B0-37	B0-65	B0-18	B0-2
Latitude	-5.648	-5.648	-5.648	-5.648	-5.648	-5.648	-6.42	-6.34	-5.96	-6.12
Longitude	175.661	175.661	175.661	175.661	175.661	175.661	176.31	176.75	176.92	177.23
Water Depth (m)	2286	2286	2286	2286	2286	2286	3555	2950	2813	2989
Fe wt. %	19.1	20.2	18.6	14.1	18.7	15.4	19.9	17.7	18.5	20.1
Mn	20.5	18.1	21.0	29.8	20.6	29.4	18.9	16.9	22.0	24.4
Fe/Mn	0.93	1.12	0.89	0.47	0.91	0.52	1.05	1.04	0.84	0.82
Si	5.95	6.97	5.69	1.80	6.42	1.96	6.52	8.62	5.50	3.79
Al	1.78	2.16	1.72	0.37	1.94	0.34	1.94	2.75	1.53	0.65
Si/Al	3.35	3.23	3.31	4.83	3.30	5.72	3.37	3.13	3.60	5.84
Mg	1.13	1.07	1.13	1.27	1.13	1.24	1.10	1.03	1.06	1.16
Ca	2.40	2.52	2.40	2.80	2.47	2.80	2.72	2.77	2.45	2.93
Na	1.61	1.52	1.58	1.45	1.49	1.21	1.33	1.59	1.45	0.87
K	0.61	0.56	0.61	0.45	0.69	0.45	0.57	1.03	0.63	0.37
Ti	1.22	0.87	1.39	1.44	1.10	1.62	1.18	1.18	1.47	0.96
P	0.39	0.47	0.39	0.28	0.41	0.29	0.44	0.35	0.30	0.52
S	0.24	0.19	0.26	0.29	0.21	0.25	0.18	0.18	0.22	0.11
CO_2	0.43	0.46	0.36	0.50	0.38	0.52	0.70	0.95	0.36	0.64
LOI[1]	33.2	33.7	35.0	37.5	35.6	36.5	33.9	32.8	34.4	38.5
H_2O^-	20.7	21.5	22.4	23.3	24.25	22.9	21.8	20.8	22.3	26.6
H_2O^+	8.40	9.20	9.10	12.26	8.60	10.51	8.60	7.50	7.10	8.30
Ag ppm	0.21	0.15	0.21	0.26	0.20	0.31	0.17	0.77	0.19	0.29
As	207	237	207	219	205	224	210	170	199	308
Ba	1660	1320	1821	1836	1469	2047	1477	1500	2012	1198
Be	5.2	4.3	5.7	3.9	4.2	4.4	6.0	4.8	7.5	4.5
Bi	21	15	24	39	24	43	18	19	21	18
Cd	4.0	3.7	4.4	6.7	4.5	6.6	3.6	3.4	3.7	4.3
Cl	6467	4915	7063	5037	4114	1965	2210	2191	4846	582
Co	5735	3625	6147	12752	5592	12808	4421	4984	6570	6969
Cr	14	13	12	<1	15	<1	6.4	10	5.1	6.8
Cu	1660	1094	1762	1608	1537	1180	1535	1479	2453	608
F	463	427	464	359	544	361	474	434	318	733
Hf	11	4.6	3.5	4.7	2.0	4.9	2.2	3.0	4.1	6.0
Hg ppb	<5	<5	66	<5	<5	40	23	16	50	23
In ppm	0.21	0.17	0.23	0.46	0.28	0.54	0.27	0.21	0.22	0.27
Li	8.8	6.4	7.7	2.6	9.2	1.3	3.8	8.8	6.4	2.7
Mo	444	399	433	631	417	573	384	309	471	609
Nb	73	52	79	91	71	125	62	71	80	44
Ni	4721	3566	4424	7554	4791	7066	3116	3436	4238	4191
Pb	1037	967	1080	1505	1064	1546	1119	917	1170	1274
Rb	5.4	5.1	5.5	2.9	6.9	3.2	5.1	13	5.9	3.1
Sb	49	39	51	58	42	76	38	49	49	37
Sc	9.0	9.3	9.3	8.1	8.6	9.5	12	10	11	13

Table S2. Continued

Sample ID	D04-02	D04-02	D04-02	D04-14	D04-22	D04-24	D05-27	D06-08	D07-33	D08-10
Bulk/Layer Interval [4]	B0-60	L0-10	L10-55	B0-30	B0-30	B0-23	B0-37	B0-65	B0-18	B0-2
Latitude	-5.648	-5.648	-5.648	-5.648	-5.648	-5.648	-6.42	-6.34	-5.96	-6.12
Longitude	175.661	175.661	175.661	175.661	175.661	175.661	176.31	176.75	176.92	177.23
Water Depth (m)	2286	2286	2286	2286	2286	2286	3555	2950	2813	2989
Se	0.25	0.76	<0.2	0.65	0.40	0.78	0.51	0.25	0.26	1.5
Sn	12	6.4	12	15	10	26	7.8	9.6	12	7.1
Sr	1498	1442	1554	1726	1467	1722	1451	1264	1530	1741
Ta	1.1	0.66	0.54	0.96	0.36	1.17	0.64	1.1	0.82	0.87
Te	43	23	63	141	58	158	42	55	57	37
Th	3.3	3.1	3.2	7.0	3.6	7.5	5.1	3.7	3.9	11
Tl	153	127	157	292	166	258	133	148	203	154
U	13	13	13	13	12	14	12	10	14	15
V	724	735	702	695	698	651	692	585	764	824
W	71	59	72	112	66	102	60	45	82	82
Zn	661	585	669	711	605	711	554	514	676	569
Zr	806	670	906	574	643	636	625	688	853	495
La	155	162	156	205	133	253	226	150	227	281
Ce	585	375	669	1072	552	1283	653	574	852	640
Pr	23.0	23.9	23.1	34.0	18.6	41.1	40.8	22.9	42.3	55.9
Nd	89.7	96.3	90.2	128.7	74.2	158.2	157	89.8	160	215
Sm	16.9	18.5	17.0	24.6	14.0	30.5	31.2	17.0	31.3	43.3
Eu	4.82	5.38	4.87	6.90	4.16	8.51	8.61	4.72	8.39	11.7
Gd	24.0	26.6	23.7	31.8	20.9	38.8	40.0	23.9	37.5	53.1
Tb	3.78	4.20	3.66	5.19	3.29	6.29	6.18	3.61	5.89	8.30
Dy	25.7	29.3	24.7	33.8	22.7	41.0	39.8	24.1	36.7	51.9
Y	142	169	139	145	140	165	172	129	134	202
Ho	5.99	7.11	5.81	7.37	5.50	8.86	8.56	5.51	7.64	11.0
Er	17.5	20.1	16.6	20.9	16.4	24.0	22.7	14.9	20.1	28.5
Tm	2.76	3.29	2.67	3.42	2.61	3.90	3.68	2.40	3.29	4.50
Yb	17.9	21.4	17.3	21.0	17.0	24.0	22.8	15.7	19.9	27.7
Lu	3.23	3.90	3.20	3.72	3.08	4.05	3.87	2.75	3.53	4.55
∑REY[2]	1118	966	1197	1742	1027	2090	1437	1081	1588	1638
%HREY[3]	22.2	30.1	20.2	16.0	22.9	15.5	22.8	20.9	17.4	24.6
Au ppb	101	--	--	--	--	--	--	--	--	--
Ir	9	--	--	--	--	--	--	--	--	--
Os	3	--	--	--	--	--	--	--	--	--
Pd	9	--	--	--	--	--	--	--	--	--
Pt	395	--	--	--	--	--	--	--	--	--
Rh	24	--	--	--	--	--	--	--	--	--
Ru	29	--	--	--	--	--	--	--	--	--

Table S2. Continued

Sample ID	D09-12	D09-12	D10-54	D11-17	D11-17	D11-17	D11-17	D16-30	D16-31 (2)	D16-31 (2)
Bulk/Layer Interval [4]	L0-10	L10-20	B0-5	B0-56	L0-25	L25-41	L41-56	B0-42	B0-35	L0-14
Latitude	-6.54	-6.54	-7.68	-8.26	-8.26	-8.26	-8.26	-7.43	-7.43	-7.43
Longitude	176.72	176.72	177.26	177.02	177.02	177.02	177.02	179.26	179.26	179.26
Water Depth (m)	2665	2665	3463	3582	3582	3582	3582	3289	3289	3289
Fe wt. %	19.4	17.2	20.2	18.5	20.1	17.8	10.9	20.6	19.0	20.7
Mn	21.8	21.2	18.6	13.3	17.9	17.0	8.79	19.0	21.0	17.7
Fe/Mn	0.89	0.81	1.09	1.39	1.12	1.05	1.24	1.09	0.91	1.17
Si	4.79	5.82	6.11	10.3	6.40	7.99	14.7	6.47	5.84	7.09
Al	1.39	1.92	1.52	3.35	2.01	2.69	5.27	1.85	1.51	1.98
Si/Al	3.45	3.03	4.01	3.07	3.18	2.97	2.79	3.49	3.86	3.59
Mg	1.25	1.27	1.12	1.21	1.15	1.10	1.10	1.09	1.09	1.07
Ca	2.58	2.77	2.77	2.29	2.63	2.31	3.85	2.47	2.53	2.51
Na	1.18	1.36	1.30	1.69	1.46	1.60	2.29	1.25	1.68	1.61
K	0.50	0.71	0.66	1.34	0.60	1.03	2.53	0.56	0.57	0.60
Ti	0.95	1.07	1.06	1.28	1.26	1.58	0.93	1.29	1.39	0.90
P	0.42	0.46	0.43	0.40	0.45	0.35	1.16	0.37	0.34	0.36
S	0.16	0.19	0.15	0.13	0.17	0.14	0.12	0.18	0.24	0.19
CO_2	0.64	0.62	0.98	0.35	0.52	0.40	0.54	0.62	0.43	0.56
LOI[1]	38.6	38.2	34.4	28.8	34.9	34.7	26.3	33.0	34.0	32.2
H_2O^-	25.3	25.3	21.2	17.5	21.9	22.8	16.0	21.2	21.7	20.2
H_2O^+	10.6	10.4	12.1	9.80	11.2	10.9	9.90	9.10	11.2	11.2
Ag ppm	0.24	0.46	0.13	0.17	0.27	0.40	0.23	0.28	0.18	0.16
As	217	175	256	152	200	157	80	230	197	201
Ba	1424	1434	1074	1310	1366	1500	885	1581	1768	1450
Be	4.4	3.7	4.2	6.1	5.2	6.1	3.8	5.1	6.0	5.8
Bi	16	18	13	11	13	13	7.3	19	21	14
Cd	4.6	4.6	3.9	2.5	3.2	3.1	2.0	3.5	4.1	3.2
Cl	1930	2135	5124	4280	3948	3670	2529	2028	8723	6268
Co	5862	6104	4260	3183	4736	5482	2455	5105	5905	3927
Cr	9.4	21	108	58	23	23	30	14	17	16
Cu	1521	1866	769	1401	1090	1316	1350	1363	2313	2425
F	286	697	221	561	455	460	3438	334	363	248
Hf	4.9	0.64	2.4	2.4	5.1	14	2.1	2.2	5.4	8.3
Hg ppb	29	23	8.9	13	12	16	26	<5	41	25
In ppm	0.24	0.21	0.32	0.39	0.46	0.44	0.27	0.29	0.31	0.20
Li	12	13	5.1	16	6.4	12	27	5.1	3.8	3.8
Mo	447	406	377	250	357	285	138	379	392	365
Nb	63	71	53	78	70	98	61	79	80	60
Ni	5416	6035	3039	2269	2597	2980	2218	3434	4055	3357
Pb	1165	1027	1014	817	1035	970	460	1061	1065	1013
Rb	4.7	8.4	8.9	22	6.5	14	41	5.7	5.4	5.3
Sb	45	42	37	37	48	48	30	49	50	45
Sc	9.4	8.4	16	17	14	15	18	13	13	11

Table S2. Continued

Sample ID	D09-12	D09-12	D10-54	D11-17	D11-17	D11-17	D11-17	D16-30	D16-31 (2)	D16-31 (2)
Bulk/Layer Interval [4]	L0-10	L10-20	B0-5	B0-56	L0-25	L25-41	L41-56	B0-42	B0-35	L0-14
Latitude	-6.54	-6.54	-7.68	-8.26	-8.26	-8.26	-8.26	-7.43	-7.43	-7.43
Longitude	176.72	176.72	177.26	177.02	177.02	177.02	177.02	179.26	179.26	179.26
Water Depth (m)	2665	2665	3463	3582	3582	3582	3582	3289	3289	3289
Se	<2	<2	6.3	2.4	3.8	3.9	<2	0.38	0.38	0.50
Sn	19	16	6.7	7.8	10	12	7.3	10	12	9.5
Sr	1478	1299	1447	1087	1355	1220	702	1456	1496	1452
Ta	0.67	0.27	0.47	1.2	1.5	2.8	0.4	0.58	1.3	1.1
Te	38	48	23	27	27	36	28	51	56	35
Th	4.4	2.9	8.5	7.0	10	9.6	4.2	4.2	4.6	2.3
Tl	185	205	112	100	110	129	71	170	123	95
U	12	10	12	8.9	11	11	5.2	13	13	11
V	632	564	626	505	603	540	311	671	806	796
W	76	78	58	47	68	56	29	65	93	80
Zn	691	680	558	576	549	566	395	551	593	625
Zr	703	653	626	722	624	755	477	788	829	638
La	216	155	239	219	268	242	231	192	236	193
Ce	533	550	576	715	800	964	508	627	719	395
Pr	34.4	21.3	44.2	44.0	55.2	50.3	44.0	30.8	40.4	29.3
Nd	151	97	190	171	215	193	176	122	155	116
Sm	29.6	18.5	38.6	33.7	42.4	38.1	33.6	22.8	30.0	21.7
Eu	7.58	4.91	10.7	9.30	11.4	10.2	8.76	6.52	8.29	6.05
Gd	36.7	24.5	47.8	43.9	52.9	46.4	43.8	32.0	38.8	30.2
Tb	5.57	3.72	7.27	6.58	8.02	6.98	6.23	4.87	6.19	4.67
Dy	37.6	25.7	45.3	41.2	50.1	43.0	39.3	33.5	39.2	31.7
Y	171	143	175	201	207	186	300	169	158	137
Ho	8.29	6.14	9.67	8.88	10.6	9.04	8.57	7.66	8.66	7.17
Er	25.2	19.8	26.8	24.4	29.4	24.7	23.8	21.7	23.1	19.5
Tm	3.67	2.89	3.97	3.60	4.49	3.81	3.43	3.58	3.81	3.17
Yb	24.2	19.7	25.0	22.9	28.0	24.2	21.2	22.8	23.2	19.3
Lu	3.92	3.25	3.85	3.53	4.39	3.75	3.33	4.06	4.04	3.35
∑REY[2]	1288	1096	1443	1549	1787	1846	1452	1300	1494	1017
%HREY[3]	25.2	23.2	24.6	23.6	22.8	19.4	31.6	23.5	21.0	25.7
Au ppb	--	--	--	--	--	--	--	19	23	21
Ir	--	--	--	--	--	--	--	10	10	6
Os	--	--	--	--	--	--	--	5	4	5
Pd	--	--	--	--	--	--	--	4	9	4
Pt	--	--	--	--	--	--	--	341	379	157
Rh	--	--	--	--	--	--	--	24	23	11
Ru	--	--	--	--	--	--	--	28	20	26

Table S2. Continued

Sample ID	D16-31 (2)	D16-34	D16-37	D16-37	D16-37	D16-37	D17-07	D17-27	D17-30	D17-30
Bulk/Layer Interval [4]	L26-38	B0-12	B0-45	L0-10	L10-20	L20-30	B0-24	B0-22	B0-32 [4]	L0-10
Latitude	-7.43	-7.43	-7.43	-7.43	-7.43	-7.43	-8.33	-8.33	-8.33	-8.33
Longitude	179.26	179.26	179.26	179.26	179.26	179.26	179.00	179.00	179.00	179.00
Water Depth (m)	3289	3289	3289	3289	3289	3289	3808	3808	3808	3808
Fe wt. %	18.8	19.6	18.1	19.4	21.1	16.4	19.5	20.2	18.3	19.8
Mn	21.9	22.3	23.2	23.8	18.2	24.2	16.8	20.6	21.0	23.2
Fe/Mn	0.86	0.88	0.78	0.82	1.16	0.68	1.16	0.98	0.87	0.85
Si	5.15	4.95	4.04	3.34	5.65	4.16	7.54	4.52	4.95	3.06
Al	1.27	1.37	1.13	0.74	1.84	1.16	2.29	1.16	1.40	0.66
Si/Al	4.05	3.62	3.59	4.52	3.07	3.59	3.29	3.88	3.53	4.67
Mg	1.08	1.17	1.19	1.14	1.19	1.20	1.09	1.20	1.23	1.14
Ca	2.51	2.43	2.70	2.61	2.77	2.62	2.26	2.49	2.76	2.60
Na	1.55	1.29	1.38	1.26	1.31	1.48	1.62	1.46	1.26	1.19
K	0.60	0.52	0.47	0.40	0.51	0.51	0.65	0.46	0.50	0.36
Ti	1.68	1.06	1.04	0.92	0.80	1.16	1.45	0.91	1.48	1.21
P	0.32	0.39	0.41	0.42	0.48	0.34	0.31	0.41	0.38	0.42
S	0.26	0.21	0.19	0.19	0.18	0.21	0.14	0.20	0.14	0.17
CO_2	0.39	0.46	0.65	0.59	0.94	0.54	0.34	0.66	0.75	0.66
LOI[1]	35.0	38.0	36.1	36.5	34.3	36.5	31.9	36.6	34.9	36.8
H_2O^-	23.0	26.5	22.4	22.5	21.1	22.4	20.0	23.1	21.3	22.5
H_2O^+	9.70	9.00	12.2	13.2	12.7	13.0	12.6	14.0	15.2	15.1
Ag ppm	0.36	0.24	0.19	0.12	0.04	0.12	0.23	0.04	0.1	0.08
As	200	244	240	277	243	209	173	231	199	263
Ba	2066	1416	1378	1263	1204	1504	1683	1451	1461	1399
Be	6.8	5.0	4.6	4.8	5.6	4.1	6.5	6.0	5.6	5.3
Bi	23	18	21	19	11	24	16	17	20.4	20
Cd	3.8	4.6	4.9	4.8	3.8	5.7	3.7	4.1	4.2	4.2
Cl	6103	2199	6420	5086	4777	6839	7213	7702	3528	4217
Co	7064	6527	6220	6378	3117	6985	4208	4597	6303	7037
Cr	18	5.4	7.7	3.9	13	9.0	25	12	18.1	5.2
Cu	2419	1420	1188	794	1074	1518	1825	1529	1419	1141
F	312	256	370	270	421	383	253	268	394	236
Hf	6.0	9.0	2.6	3.0	4.1	5.3	1.3	0.79	1.9	3.7
Hg ppb	32	1020	40	99	77	41	<5	<5	<5	<5
In ppm	0.34	0.31	0.30	0.35	0.28	0.22	0.46	0.27	0.4	0.45
Li	5.2	4.8	3.9	3.9	6.3	3.9	7.5	5.2	5.1	2.6
Mo	413	501	575	617	465	571	308	538	446	555
Nb	99	64	62	46	65	66	79	48	77	68
Ni	3682	5001	5184	4813	3654	6168	3165	4092	4069	3880
Pb	1177	1127	1101	1143	796	1144	1053	1126	1131	1274
Rb	6.6	4.5	4.1	2.6	4.7	4.1	7.6	4.0	4.9	2.5
Sb	59	50	56	50	81	50	53	53	65	71
Sc	15	13	12	12	14	10	15	14	15	14

Table S2. Continued

Sample ID	D16-31 (2)	D16-34	D16-37	D16-37	D16-37	D16-37	D17-07	D17-27	D17-30	D17-30
Bulk/Layer Interval [4]	L26-38	B0-12	B0-45	L0-10	L10-20	L20-30	B0-24	B0-22	B0-32 [4]	L0-10
Latitude	-7.43	-7.43	-7.43	-7.43	-7.43	-7.43	-8.33	-8.33	-8.33	-8.33
Longitude	179.26	179.26	179.26	179.26	179.26	179.26	179.00	179.00	179.00	179.00
Water Depth (m)	3289	3289	3289	3289	3289	3289	3808	3808	3808	3808
Se	0.39	0.54	5.2	5.2	3.8	2.6	3.8	5.2	5.5	6.5
Sn	16	8.4	8.2	6.5	11	13	9.0	10	8.7	8.3
Sr	1700	1491	1589	1739	1437	1570	1338	1546	1506	1675
Ta	1.4	1.1	0.35	0.40	0.33	0.71	1.2	0.23	0.5	0.68
Te	65	49	41	42	30	50	42	32	46	49
Th	6.2	4.7	4.0	5.4	1.8	3.1	8.8	3.9	8.3	10
Tl	136	193	207	181	183	211	133	153	164	156
U	15	13	13	14	11	13	11	13	13	14
V	831	773	651	706	616	626	593	769	565	665
W	96	83	98	99	81	102	58	95	89	105
Zn	627	572	566	583	531	593	619	609	533	507
Zr	905	682	619	525	696	642	705	553	706	653
La	278	227	233	274	208	197	228	278	286	338
Ce	970	532	548	535	289	588	838	490	834	793
Pr	50.5	37.1	36.1	45.7	26.2	29.4	39.4	43.7	48.0	59.7
Nd	191	148	156	197	117	126	163	189	202	252
Sm	37.5	28.3	29.8	38.5	21.3	24.2	31.9	35.6	38.9	49.0
Eu	9.96	7.90	8.14	10.5	6.07	6.57	8.54	9.73	10.3	13.0
Gd	44.5	38.1	38.9	47.7	31.6	31.6	39.4	46.0	47.4	58.2
Tb	6.96	5.84	5.90	7.16	4.65	4.86	5.98	6.96	7.28	8.78
Dy	44.3	40.1	39.9	47.0	33.8	32.1	37.3	46.3	47.4	56.2
Y	168	192	191	190	215	155	149	205	205	218
Ho	9.49	9.01	9.10	10.2	8.33	7.42	8.09	10.2	10.3	12.0
Er	25.6	24.9	27.3	29.7	26.0	22.4	23.1	30.0	30.4	34.4
Tm	3.97	4.07	4.05	4.41	3.80	3.45	3.40	4.40	4.43	4.92
Yb	24.7	25.7	25.6	27.0	24.7	22.2	21.6	27.8	28.1	31.0
Lu	4.21	4.41	4.07	4.32	4.11	3.52	3.30	4.29	4.34	4.77
∑REY [2]	1868	1325	1357	1468	1020	1253	1598	1428	1804	1932
%HREY [3]	18.3	26.6	26.1	25.7	35.1	23.0	18.7	27.4	21.9	22.8
Au ppb	30	--	--	--	--	--	--	--	--	--
Ir	12	--	--	--	--	--	--	--	--	--
Os	5	--	--	--	--	--	--	--	--	--
Pd	3	--	--	--	--	--	--	--	--	--
Pt	800	--	--	--	--	--	--	--	--	--
Rh	40	--	--	--	--	--	--	--	--	--
Ru	32	--	--	--	--	--	--	--	--	--

Table S2. Continued

Sample ID	D17-30	D18-20	D19-33	D20-39	D20-39	D20-39	D20-39	D20-54	D20-54	D20-54
Bulk/Layer Interval [4]	L10-32	B0-1	B0-13	B0-72 [4]	L0-26	L26-56	L56-72	B0-20	L0-3	L3-16
Latitude	-8.33	-8.62	-9.43	-9.78	-9.78	-9.78	-9.78	-9.78	-9.78	-9.78
Longitude	179.00	178.99	178.87	178.86	178.86	178.86	178.86	178.86	178.86	178.86
Water Depth (m)	3808	3302	3202	4110	4110	4110	4110	4110	4110	4110
Fe wt. %	17.6	20.2	17.2	22.3	26.8	21.8	16.2	23.4	23.3	24.2
Mn	20.0	21.6	16.2	16.5	16.1	15.1	19.8	19.3	20.2	19.4
Fe/Mn	0.88	0.94	1.06	1.35	1.66	1.44	0.82	1.22	1.15	1.24
Si	5.81	4.61	8.76	6.66	5.23	7.65	7.11	4.66	4.28	3.93
Al	1.74	0.88	2.89	2.13	1.33	2.56	2.62	1.18	0.76	0.86
Si/Al	3.33	5.25	3.03	3.13	3.93	2.99	2.72	3.95	5.65	4.55
Mg	1.26	1.28	1.33	1.04	1.00	0.99	1.19	1.07	1.08	1.07
Ca	2.83	2.95	2.36	2.32	2.02	2.37	2.70	2.28	2.36	2.24
Na	1.29	0.87	1.56	1.30	1.08	1.38	1.51	1.36	1.44	1.39
K	0.56	0.33	0.89	0.54	0.35	0.57	0.81	0.37	0.35	0.32
Ti	1.60	0.84	1.52	1.63	1.13	2.17	1.41	1.25	0.83	1.02
P	0.37	0.45	0.30	0.41	0.46	0.34	0.48	0.43	0.50	0.45
S	0.13	0.09	0.12	0.16	0.15	0.15	0.19	0.20	0.18	0.22
CO_2	0.80	0.70	0.27	0.34	0.40	0.29	0.35	0.40	0.47	0.38
LOI[1]	34.1	36.5	31.5	33.0	34.2	31.1	34.4	36.5	37.8	36.9
H_2O^-	20.8	22.8	19.4	20.7	21.7	19.3	21.8	23.2	23.9	22.7
H_2O^+	15.2	17.0	13.7	12.7	13.4	12.5	12.0	12.7	25.3	12.8
Ag ppm	0.04	0.09	0.07	0.3	0.23	0.33	0.17	0.16	0.07	0.05
As	170	281	144	208	272	178	161	249	288	266
Ba	1490	1118	1527	1741	1770	1864	1465	1685	1192	1730
Be	5.8	5.2	5.0	7.1	7.4	7.3	6.0	7.0	5.4	7.2
Bi	21	15	15	12	10	12	15	13	12	13
Cd	4.2	4.8	4.1	2.8	2.5	2.5	3.8	3.3	3.4	3.2
Cl	3215	1246	5308	2833	2295	2617	4114	5934	8752	9180
Co	5970	5212	3592	3922	2644	3825	6178	3780	3229	3266
Cr	24	30	32	15	5.1	24	17	6.5	1.3	2.6
Cu	1545	554	2520	1012	700	918	1697	1217	903	1354
F	466	148	370	379	194	247	926	194	150	265
Hf	1.0	2.9	1.9	8.9	6.3	15	1.0	0.51	4.6	0.72
Hg ppb	<5	9.1	9.9	42	49	36	43	9.1	25	16
In ppm	0.39	0.38	0.35	0.5	0.43	0.57	0.68	0.30	0.32	0.30
Li	6.3	2.6	17.4	6.6	2.6	6.2	14	3.9	2.6	2.6
Mo	396	470	233	379	467	281	418	499	457	602
Nb	81	39	62	82	72	88	88	55	41	45
Ni	4155	3595	4373	2149	1571	1862	3628	2753	2377	2682
Pb	1067	1259	927	1081	1162	1107	902	1225	1246	1273
Rb	6.1	3.5	12	6.6	2.8	7.1	12	3.0	2.4	2.3
Sb	62	37	47	47	51	46	43	52	35	58
Sc	16	17	14	14	12	14	16	12	12	11

Table S2. Continued

Sample ID	D17-30	D18-20	D19-33	D20-39	D20-39	D20-39	D20-39	D20-54	D20-54	D20-54
Bulk/Layer Interval [4]	L10-32	B0-1	B0-13	B0-72 [4]	L0-26	L26-56	L56-72	B0-20	L0-3	L3-16
Latitude	-8.33	-8.62	-9.43	-9.78	-9.78	-9.78	-9.78	-9.78	-9.78	-9.78
Longitude	179.00	178.99	178.87	178.86	178.86	178.86	178.86	178.86	178.86	178.86
Water Depth (m)	3808	3302	3202	4110	4110	4110	4110	4110	4110	4110
Se	5.1	5.2	2.5	3.8	3.8	3.7	3.8	5.2	3.9	3.9
Sn	9.0	5.7	8.2	8.3	6.9	8.6	10	6.3	5.5	8.2
Sr	1429	1631	1242	1383	1484	1357	1269	1551	1535	1591
Ta	0.44	0.40	1.9	2.4	1.5	4.2	0.74	0.72	0.74	0.60
Te	44	23	34	32	25	29	51	29	19	24
Th	7.3	11	7.3	13	8.9	17	11	7.0	11	4.8
Tl	168	127	119	81	45	69	162	138	110	144
U	12	13	9.8	12	13	12	10	14	14	14
V	519	703	483	695	843	617	602	788	811	862
W	82	70	41	71	87	53	78	87	70	106
Zn	544	575	721	623	637	646	556	656	558	680
Zr	730	496	603	729	731	739	707	587	527	499
La	263	285	161	297	327	284	273	319	306	326
Ce	852	620	615	1139	865	1290	1302	758	720	673
Pr	42.7	53.8	30.5	60.4	62.2	59.4	59.6	58.2	63.5	56.7
Nd	179	231	127	249	262	240	244	253	269	243
Sm	34.3	47.2	26.6	51.3	53.0	50.1	50.9	49.1	56.1	47.0
Eu	9.07	12.5	6.80	12.5	13.2	11.9	12.3	11.8	13.7	11.5
Gd	42.4	54.1	29.8	55.6	61.0	51.2	55.1	57.4	62.2	56.3
Tb	6.60	8.32	4.59	8.4	9.39	7.71	8.16	8.53	9.19	8.20
Dy	43.4	51.7	28.0	52.7	58.0	48.5	52.1	55.2	56.8	55.8
Y	199	199	103	209	227	176	240	225	219	230
Ho	9.51	10.7	5.68	10.9	12.3	9.81	10.7	11.5	11.7	12.1
Er	28.5	30.7	16.6	30.7	35.0	27.0	30.7	33.2	32.5	35.3
Tm	4.20	4.38	2.33	4.4	4.94	4.00	4.26	4.86	4.61	4.88
Yb	26.8	27.5	14.8	27.5	30.5	25.0	27.4	30.1	28.5	30.5
Lu	4.14	4.25	2.30	4.1	4.61	3.73	4.10	4.54	4.40	4.77
∑REY[2]	1745	1641	1174	2213	2025	2288	2375	1879	1858	1795
%HREY[3]	21.4	24.6	18.2	18.8	22.5	15.9	18.7	23.5	23.8	25.0
Au ppb	--	--	--	22	20	24	23	18	--	--
Ir	--	--	--	7	6	7	9	7	--	--
Os	--	--	--	3	3	4	3	8	--	--
Pd	--	--	--	7	6	7	9	--	--	--
Pt	--	--	--	198	109	152	428	128	--	--
Rh	--	--	--	16	10	15	29	12	--	--
Ru	--	--	--	16	15	19	10	12	--	--

Table S2. Continued

Sample ID	D20-54	D20-54	D22-03	D22-26	D23-21	D25-27	D26-04	D27-04	D28B-01	D30-02
Bulk/Layer Interval [4]	L16-21	nodule	B0-12	B0-15	B0-30	B0-15	B0-10	B0-10	B0-5	B0-15
Latitude	-9.78	-9.78	-10.31	-10.31	-10.76	-10.83	-10.90	-10.99	-11.34	-11.45
Longitude	178.86	178.86	-179.80	-179.80	-179.25	179.34	179.35	179.79	179.88	-179.25
Water Depth (m)	4110	4110	3384	3384	2342	2513	2806	2636	2485	2812
Fe wt. %	22.7	17.4	20.3	18.0	21.9	23.2	23.5	23.8	22.5	23.1
Mn	17.8	18.5	21.4	21.7	18.2	18.6	16.6	14.2	15.8	17.0
Fe/Mn	1.28	0.94	0.95	0.83	1.21	1.25	1.42	1.67	1.42	1.36
Si	5.26	7.31	4.41	4.41	5.63	5.23	4.47	7.17	6.75	5.09
Al	1.32	2.53	1.29	1.27	1.74	1.41	1.27	2.24	2.06	1.39
Si/Al	3.98	2.89	3.41	3.47	3.23	3.71	3.53	3.20	3.27	3.65
Mg	1.05	1.14	1.33	1.28	1.13	1.11	1.07	1.12	1.15	1.15
Ca	2.31	2.41	2.33	2.94	2.62	2.57	4.32	4.02	2.47	3.26
Na	1.51	1.77	1.05	1.13	1.18	0.91	0.38	1.20	1.22	1.13
K	0.40	0.74	0.45	0.52	0.46	0.36	0.31	0.47	0.46	0.36
Ti	2.14	1.74	1.18	1.73	1.15	0.87	0.98	0.90	0.86	0.93
P	0.39	0.28	0.40	0.34	0.45	0.51	0.48	0.46	0.47	0.51
S	0.20	0.20	0.15	0.15	0.18	0.10	<0.01	0.13	0.13	0.20
CO_2	0.33	0.28	0.47	0.90	0.66	0.56	2.64	2.28	0.69	1.50
LOI[1]	34.1	34.1	33.5	35.5	36.1	34.4	33.9	32.6	35.7	37.8
H_2O^-	21.1	21.3	19.8	21.3	22.8	21.2	18.9	21.1	23.1	24.5
H_2O^+	12.1	13.8	15.3	15.1	15.9	16.2	12.3	15.4	11.7	12.9
Ag ppm	0.28	1.33	0.22	0.05	0.08	0.11	0.16	0.24	0.42	0.09
As	208	147	228	206	234	270	263	224	228	272
Ba	2074	1676	1418	1629	1451	1341	1264	1167	1316	1189
Be	8.2	6.6	4.6	6.4	5.7	6.0	5.7	5.4	4.0	4.8
Bi	14	16	10	18	11	8.2	6.2	6.7	5.2	5.1
Cd	2.9	3.7	4.7	4.0	3.5	3.6	3.8	3.3	3.5	3.0
Cl	8976	8609	1714	3975	2096	574	<50	2667	2333	3698
Co	3744	5887	4893	6501	4092	3201	3644	2423	2337	2437
Cr	11	22	17	41	21	5.1	6.2	20	10	7.9
Cu	1506	1372	1283	1447	1153	994	801	807	1350	1270
F	231	357	192	295	231	168	190	275	224	208
Hf	9.1	7.0	0.84	1.3	0.75	4.1	0.5	7.1	8.9	1.7
Hg ppb	15	11	37	61	66	30	17	76	10	12
In ppm	0.27	0.41	0.32	0.33	0.31	0.32	0.44	0.27	0.26	0.28
Li	3.8	10	15	5.1	3.9	2.5	2.5	3.8	7.8	4.0
Mo	380	309	404	421	356	373	284	224	280	385
Nb	65	88	71	81	69	58	97	70	55	56
Ni	2530	3079	5057	4474	3201	2794	2543	2288	2289	2494
Pb	1380	1069	989	1147	1133	985	880	891	728	799
Rb	3.5	9.1	4.4	5.5	4.3	3.2	2.5	4.7	5.1	3.6
Sb	57	48	55	73	48	46	89	41	43	46
Sc	12	13	13	12	10	13	15	12	12	13

Table S2. Continued

Sample ID	D20-54	D20-54	D22-03	D22-26	D23-21	D25-27	D26-04	D27-04	D28B-01	D30-02
Bulk/Layer Interval [4]	L16-21	nodule	B0-12	B0-15	B0-30	B0-15	B0-10	B0-10	B0-5	B0-15
Latitude	-9.78	-9.78	-10.31	-10.31	-10.76	-10.83	-10.90	-10.99	-11.34	-11.45
Longitude	178.86	178.86	-179.80	-179.80	-179.25	179.34	179.35	179.79	179.88	-179.25
Water Depth (m)	4110	4110	3384	3384	2342	2513	2806	2636	2485	2812
Se	3.8	<2	5.0	3.8	<2	3.8	4.9	2.5	2.6	4.0
Sn	8.2	9.7	9.1	9.8	11	8.2	10	7.9	6.2	6.2
Sr	1542	1334	1456	1628	1544	1622	1650	1444	1490	1572
Ta	3.7	3.2	0.41	0.66	0.22	0.51	0.12	1.2	1.4	0.53
Te	25	54	38	44	45	29	42	31	24	19
Th	6.8	11	8.7	7.4	5.1	5.2	4.4	3.5	4.0	4.9
Tl	134	92	152	179	118	99	94	111	86	80
U	15	11	12	14	13	13	12	10	10	13
V	749	510	620	565	636	697	610	592	628	699
W	74	66	71	79	70	70	54	42	48	102
Zn	763	591	734	684	630	612	557	593	616	564
Zr	677	705	691	653	716	788	795	689	635	677
La	321	252	274	222	201	275	255	165	198	252
Ce	995	1151	641	771	579	430	365	345	329	338
Pr	58.7	48.2	50.6	34.9	30.6	47.3	40.1	27.8	37.6	48.6
Nd	245	198	221	146	135	212	176	124	151	197
Sm	49.6	40.7	45.3	27.8	26.6	42.8	33.7	25.6	29.1	38.7
Eu	12.0	10.0	11.3	7.51	6.83	11.0	9.08	6.55	8.50	10.8
Gd	54.8	42.9	51.1	34.4	33.0	53.4	42.3	31.3	39.0	50.5
Tb	8.16	6.72	7.53	5.13	4.84	7.89	6.25	4.77	5.76	7.39
Dy	54.1	41.4	49.9	33.0	33.7	52.3	41.8	32.8	37.3	48.7
Y	227	169	200	131	177	230	192	175	177	216
Ho	11.6	8.83	10.6	7.20	8.06	11.3	9.17	7.71	8.22	10.5
Er	33.2	25.7	30.0	21.5	24.6	33.8	27.3	23.6	22.6	30.1
Tm	4.74	3.86	4.39	3.15	3.56	5.01	4.03	3.52	3.46	4.42
Yb	29.7	23.9	28.3	19.9	23.6	32.0	26.1	23.2	22.1	28.5
Lu	4.59	3.81	4.41	3.10	3.91	5.11	4.22	3.95	3.56	4.49
∑REY[2]	2108	2026	1629	1468	1291	1449	1233	1000	1072	1285
%HREY[3]	20.9	16.6	24.4	18.1	24.7	30.5	29.4	31.2	30.6	32.0
Au ppb	--	17	27	--	21	28	--	--	--	--
Ir	--	6	9	--	8	8	--	--	--	--
Os	--	4	2	--	4	3	--	--	--	--
Pd	--	3	9	--	4	8	--	--	--	--
Pt	--	315	318	--	206	165	--	--	--	--
Rh	--	25	22	--	18	13	--	--	--	--
Ru	--	22	20	--	25	13	--	--	--	--

[1] Loss on ignition at 1000°C

[2] ∑ REY = Sum of rare earth elements plus yttrium

[3] Percent of heavy REY (Eu-Lu, +Y) of the total sum of REY

[4] Bulk compoition was calculated from a weighted average of layer samples

Table S3. Pearson correlation coefficiant matrix for element concentrations in hydrogenetic, non-pohsphatized bulk and layer FeMn crusts samples in the Tuvalu EEZ [1,2]

	Latitude	Water Depth (m)	Growth Rate (mm/Ma; M&L-B 1988)	Growth Rate (mm/Ma; P&H 1988)	Fe	Mn	Fe/Mn
Latitude		**-0.3965**	**-0.6441**	**-0.4466**	**-0.5957**	**0.5530**	**-0.6544**
Water Depth (m)	**-0.3965**		0.0687	-0.2403	0.2326	-0.2545	0.2196
Growth Rate (mm/Ma; M&L-B 1988)	**-0.6441**	0.0687		**0.6713**	**0.8457**	**-0.6341**	**0.8545**
Growth Rate (mm/Ma; P&H 1988)	**-0.4466**	-0.2403	**0.6713**		**0.3601**	**-0.3738**	**0.4953**
Fe	**-0.5957**	0.2326	**0.8457**	**0.3601**		**-0.6232**	**0.8823**
Mn	**0.5530**	-0.2545	**-0.6341**	**-0.3738**	**-0.6232**		**-0.8802**
Fe/Mn	**-0.6544**	0.2196	**0.8545**	**0.4953**	**0.8823**	**-0.8802**	
Si	-0.1213	0.1001	0.1597	0.1652	0.0786	**-0.7896**	**0.4545**
Al	-0.1194	0.0623	0.0843	0.1522	-0.0382	**-0.7256**	**0.3716**
Si/Al	0.1461	0.0117	-0.0315	-0.1204	0.0722	**0.5697**	-0.2620
Mg	0.0910	-0.2397	**-0.3513**	-0.0419	**-0.5481**	**0.4919**	**-0.5729**
Ca	-0.1897	**-0.3163**	0.1331	**0.3653**	0.0491	-0.0367	0.1208
Na	**0.3712**	0.1480	**-0.2979**	-0.1632	**-0.4149**	-0.0271	-0.2416
K	**0.3096**	-0.0341	**-0.4021**	-0.1683	**-0.5333**	-0.2293	-0.1866
Ti	-0.0288	**0.3519**	**-0.4023**	**-0.2769**	**-0.3334**	0.0326	-0.1587
P	**-0.3341**	-0.0379	**0.5935**	**0.3021**	**0.6303**	**-0.3002**	**0.4669**
S	**0.5092**	-0.1619	**-0.3076**	-0.1705	**-0.3750**	**0.4598**	**-0.4579**
Ag	0.0575	0.0353	-0.1632	0.0539	-0.2050	-0.1198	-0.0240
As	-0.1595	-0.0774	**0.4339**	0.1344	**0.5732**	0.1676	0.2086
Ba	0.2028	0.1212	**-0.3137**	**-0.2882**	-0.2369	0.2229	-0.2091
Be	**-0.3818**	**0.6145**	0.1917	-0.1618	**0.4130**	**-0.3896**	**0.4215**
Bi	**0.7186**	-0.2581	**-0.7318**	**-0.4118**	**-0.7677**	**0.8267**	**-0.8304**
Cd	**0.5036**	**-0.4267**	**-0.5812**	-0.2162	**-0.7035**	**0.8781**	**-0.8234**
Cl	0.1027	**0.3290**	-0.0809	-0.1707	-0.1187	0.0664	-0.1504
Co	**0.5843**	-0.2564	**-0.7673**	**-0.3706**	**-0.7898**	**0.8958**	**-0.8704**
Cr	-0.0758	0.1121	-0.0924	-0.0442	-0.0887	-0.2484	0.0647
Cu	**0.3153**	-0.1103	**-0.3561**	-0.1588	**-0.4620**	0.0855	**-0.3387**
F	**0.4459**	-0.1020	**-0.4559**	-0.1938	**-0.5506**	0.2038	**-0.4300**
Hf	0.0544	0.0521	0.0271	0.1398	0.0527	-0.1844	0.1816
Hg	0.0498	-0.0078	-0.0792	-0.0234	0.0024	0.1104	-0.0733
In	**-0.3028**	**0.4355**	-0.1486	-0.1482	-0.1290	0.0561	-0.0242
Li	0.0591	-0.0523	-0.2286	-0.0592	**-0.3730**	-0.2041	-0.1347
Mo	**0.4024**	0.0110	**-0.2991**	**-0.3442**	-0.2058	**0.8034**	**-0.5745**
Nb	0.1210	-0.0806	**-0.4138**	-0.1522	**-0.4463**	0.1839	-0.2508
Ni	**0.6355**	**-0.4587**	**-0.6835**	**-0.3186**	**-0.7877**	**0.8491**	**-0.8791**
Pb	**0.3287**	0.1160	**-0.4139**	**-0.4560**	-0.2103	**0.6842**	**-0.4680**
Rb	0.1003	0.0885	**-0.2913**	-0.0965	**-0.4282**	**-0.3466**	-0.0616
Sb	-0.0895	0.0566	-0.1399	-0.1773	-0.1000	0.2411	-0.1482
Sc	**-0.4611**	**0.6015**	0.0818	-0.0073	0.1730	**-0.3253**	0.2408
Se	**-0.5239**	**0.5334**	0.2118	0.0129	0.2634	-0.1085	0.1888
Sn	**0.3485**	**-0.3090**	**-0.3025**	-0.1485	**-0.3226**	**0.2860**	**-0.3227**
Sr	0.0695	-0.2233	-0.0381	-0.0160	0.0708	**0.6251**	**-0.2812**
Ta	-0.1895	**0.3769**	0.0201	0.0291	0.0480	**-0.3411**	0.2688
Te	**0.4792**	**-0.3685**	**-0.5566**	-0.2081	**-0.6607**	**0.7228**	**-0.6592**
Th	**-0.3336**	**0.5912**	-0.0772	-0.1784	0.0578	-0.0741	0.0967
Tl	**0.6097**	**-0.3281**	**-0.6365**	**-0.3017**	**-0.7150**	**0.8397**	**-0.8325**
U	0.1271	0.0815	-0.1335	**-0.3123**	0.1268	**0.5058**	-0.2461
V	0.1478	0.0648	0.2201	-0.0910	**0.4257**	0.1588	0.1059
W	0.2066	0.1043	-0.2417	-0.2589	-0.2109	**0.7112**	**-0.5119**
Zn	0.0012	-0.1812	-0.0439	-0.0653	-0.0679	0.2011	-0.1022
Zr	0.0640	-0.1924	-0.1181	-0.0428	-0.0533	-0.2107	0.0878
La	**-0.4539**	**0.7160**	0.1790	-0.1617	**0.4078**	0.0366	0.1814
Ce	0.0189	**0.4536**	**-0.4188**	**-0.3548**	**-0.3446**	0.2416	-0.2695
Pr	**-0.4899**	**0.7274**	0.2060	-0.0790	**0.3876**	-0.0747	0.2410
N	**-0.5550**	**0.7361**	0.2598	-0.0713	**0.4447**	-0.1009	**0.2819**
Sm	**-0.5644**	**0.7287**	0.2662	-0.0622	**0.4416**	-0.1261	**0.2972**
Eu	**-0.5352**	**0.6962**	0.2581	-0.0371	**0.4258**	-0.0857	0.2654
Gd	**-0.5437**	**0.6927**	**0.3079**	-0.0339	**0.4827**	-0.0981	**0.2974**
Tb	**-0.4951**	**0.6884**	0.2644	-0.0562	**0.4428**	-0.0542	0.2567
Dy	**-0.5111**	**0.6717**	**0.2958**	-0.0460	**0.4836**	-0.0480	0.2720
Y	**-0.4999**	**0.5112**	**0.4275**	0.0673	**0.5600**	-0.1382	**0.3558**
Ho	**-0.5093**	**0.6405**	**0.3333**	-0.0253	**0.5261**	-0.0467	**0.2919**
Er	**-0.5621**	**0.6216**	**0.3623**	-0.0157	**0.5367**	-0.0589	**0.3043**
Tm	**-0.4750**	**0.5754**	**0.3124**	-0.0275	**0.5093**	0.0117	0.2539
Yb	**-0.5074**	**0.5406**	**0.3401**	0.0020	**0.5269**	-0.0201	**0.2793**
Lu	**-0.3610**	**0.3604**	**0.3166**	0.0127	**0.5216**	0.0651	0.2292
∑REY	-0.2614	**0.6766**	-0.1417	**-0.2792**	0.0097	0.1322	-0.0424
%HREY	-0.2499	-0.2501	**0.6226**	**0.4569**	**0.5547**	**-0.3132**	**0.4470**

Table S3. Continued

	Si	Al	Si/Al	Mg	Ca	Na	K	Ti	P	S	Ag	As
Latitude	-0.1213	-0.1194	0.1461	0.0910	-0.1897	**0.3712**	**0.3096**	-0.0288	**-0.3341**	**0.5092**	0.0575	-0.1595
Water Depth (m)	0.1001	0.0623	0.0117	-0.2397	**-0.3163**	0.1480	-0.0341	**0.3519**	-0.0379	-0.1619	0.0353	-0.0774
Growth Rate (mm/Ma; M&L-B 1988)	0.1597	0.0843	-0.0315	**-0.3513**	0.1331	**-0.2979**	**-0.4021**	**-0.4023**	**0.5935**	**-0.3076**	-0.1632	**0.4339**
Growth Rate (mm/Ma; P&H 1988)	0.1652	0.1522	-0.1204	-0.0419	**0.3653**	-0.1632	-0.1683	**-0.2769**	**0.3021**	-0.1705	0.0539	0.1344
Fe	0.0786	-0.0382	0.0722	**-0.5481**	0.0491	**-0.4149**	**-0.5333**	**-0.3334**	**0.6303**	**-0.3750**	-0.2050	**0.5732**
Mn	**-0.7896**	**-0.7256**	**0.5697**	**0.4919**	-0.0367	-0.0271	-0.2293	0.0326	**-0.3002**	**0.4598**	-0.1198	0.1676
Fe/Mn	**0.4545**	**0.3716**	-0.2620	**-0.5729**	0.1208	-0.2416	-0.1866	-0.1587	**0.4669**	**-0.4579**	-0.0240	0.2086
Si		**0.9658**	**-0.7072**	**-0.3222**	-0.1388	**0.4262**	**0.7215**	0.1545	-0.0848	-0.2005	**0.3444**	**-0.6006**
Al	**0.9658**		**-0.8186**	-0.2171	-0.1085	**0.4266**	**0.7677**	0.2122	-0.1241	-0.1687	**0.3900**	**-0.6964**
Si/Al	**-0.7072**	**-0.8186**		0.0642	0.0439	**-0.3045**	**-0.5719**	-0.1899	0.1178	0.0942	-0.2319	**0.6616**
Mg	**-0.3222**	-0.2171	0.0642		0.1548	-0.1573	0.0001	-0.0978	-0.1086	-0.0541	-0.1691	-0.1070
Ca	-0.1388	-0.1085	0.0439	0.1548		**-0.5722**	-0.2134	-0.2593	**0.2847**	**-0.4324**	-0.1061	0.2115
Na	**0.4262**	**0.4266**	**-0.3045**	-0.1573	**-0.5722**		**0.6233**	**0.3605**	**-0.5481**	**0.6670**	**0.3113**	**-0.6555**
K	**0.7215**	**0.7677**	**-0.5719**	0.0001	-0.2134	**0.6233**		**0.3197**	**-0.4545**	0.1406	**0.4468**	**-0.8064**
Ti	0.1545	0.2122	-0.1899	-0.0978	-0.2593	**0.3605**	**0.3197**		**-0.6698**	0.1965	**0.2845**	**-0.6161**
P	-0.0848	-0.1241	0.1178	-0.1086	**0.2847**	**-0.5481**	**-0.4545**	**-0.6698**		**-0.4187**	**-0.3272**	**0.6619**
S	-0.2005	-0.1687	0.0942	-0.0541	**-0.4324**	**0.6670**	0.1406	0.1965	**-0.4187**		0.1231	-0.1965
Ag	**0.3444**	**0.3900**	-0.2319	-0.1691	-0.1061	**0.3113**	**0.4468**	**0.2845**	**-0.3272**	0.1231		**-0.4191**
As	**-0.6006**	**-0.6964**	**0.6616**	-0.1070	0.2115	**-0.6555**	**-0.8064**	**-0.6161**	**0.6619**	-0.1965	**-0.4191**	
Ba	-0.0663	-0.0312	-0.0219	-0.2335	**-0.4334**	**0.4207**	0.1389	**0.7641**	**-0.6840**	**0.5445**	0.2163	**-0.4409**
Be	0.1877	0.1385	-0.1013	**-0.5520**	-0.2555	0.1262	-0.0721	**0.5163**	-0.1380	-0.0212	0.0280	-0.1232
Bi	**-0.4405**	**-0.3795**	**0.3349**	**0.2996**	-0.1342	**0.3151**	0.1323	**0.3349**	**-0.6279**	**0.5960**	0.0525	-0.2377
Cd	**-0.6246**	**-0.5284**	**0.3665**	**0.6822**	0.1400	-0.0707	-0.1033	-0.0672	**-0.3233**	**0.2879**	-0.0875	0.0334
Cl	0.0019	-0.0414	0.0416	-0.1719	**-0.4095**	**0.7204**	0.0863	0.2208	**-0.3514**	**0.5589**	0.0251	-0.2181
Co	**-0.5528**	**-0.4527**	**0.3697**	**0.4228**	0.0033	0.1165	0.0709	**0.3191**	**-0.5506**	**0.4630**	0.1116	-0.1663
Cr	**0.3400**	**0.2829**	-0.1945	0.1193	0.0542	0.0822	**0.3291**	0.1238	-0.0882	-0.2127	-0.0109	-0.1839
Cu	**0.2772**	**0.2809**	**-0.3164**	0.1019	**-0.2966**	**0.6261**	**0.4913**	**0.3113**	**-0.5940**	**0.4729**	0.0539	**-0.6530**
F	0.1821	**0.2901**	-0.2335	0.2017	0.0157	0.2646	**0.4935**	0.1315	0.0166	0.1703	0.1573	**-0.4055**
Hf	**0.2854**	0.2511	-0.0709	**-0.3841**	-0.2347	**0.3107**	0.2002	**0.3299**	-0.2493	0.1421	**0.3034**	-0.2213
Hg	-0.0751	-0.0633	-0.0218	0.0399	-0.0493	-0.0504	-0.0390	-0.0896	-0.0085	0.1081	-0.0132	0.1142
In	-0.0770	0.0202	0.0568	0.0240	0.0356	-0.1335	0.0179	**0.4656**	-0.1399	-0.1900	0.0490	-0.1554
Li	**0.5230**	**0.6286**	**-0.6112**	**0.3784**	-0.2545	**0.3309**	**0.6852**	0.1575	-0.1897	-0.0362	**0.2838**	**-0.6440**
Mo	**-0.8339**	**-0.8112**	**0.6391**	0.2293	-0.1609	-0.1072	**-0.4826**	-0.2027	0.0488	**0.4052**	**-0.3049**	**0.5010**
Nb	0.0266	0.1549	-0.2252	-0.0020	0.1152	0.1272	**0.3390**	**0.6585**	**-0.5930**	0.1804	**0.3105**	**-0.5517**
Ni	**-0.4969**	**-0.3856**	0.1872	**0.6722**	-0.0062	0.1185	0.0848	0.0153	**-0.4259**	**0.4364**	-0.0528	-0.1607
Pb	**-0.6521**	**-0.6736**	**0.6936**	0.0764	-0.2451	0.0209	**-0.3534**	**0.3097**	**-0.3223**	**0.3819**	-0.0682	0.1981
Rb	**0.7610**	**0.8063**	**-0.5823**	0.0106	-0.1604	**0.4998**	**0.9595**	**0.3386**	**-0.3407**	-0.0301	**0.4370**	**-0.7634**
Sb	**-0.4236**	**-0.3220**	0.0502	0.1517	**0.2970**	**-0.2921**	-0.2389	0.2415	-0.2084	-0.0827	-0.1545	0.0220
Sc	0.1944	0.1338	-0.0073	-0.0221	0.1489	-0.2200	-0.0031	0.1559	0.1115	**-0.5367**	-0.1280	0.0264
Se	-0.2505	-0.2387	0.1025	0.1416	0.1207	**-0.3746**	**-0.3545**	-0.0345	**0.3089**	**-0.4987**	**-0.3549**	**0.2963**
Sn	-0.1079	-0.0350	-0.0536	0.2119	-0.0622	0.1276	0.1468	0.0408	-0.2576	0.2694	0.1152	-0.2523
Sr	**-0.8637**	**-0.8975**	**0.7189**	0.0899	0.2426	**-0.4679**	**-0.7595**	-0.1634	0.1062	0.1292	**-0.3527**	**0.6795**
Ta	**0.4217**	**0.4134**	-0.1809	**-0.3782**	**-0.3170**	**0.3936**	**0.3053**	**0.6948**	**-0.4064**	0.0682	**0.4996**	**-0.4496**
Te	**-0.4250**	**-0.3221**	**0.2787**	**0.2776**	0.0685	0.1299	0.0962	**0.3267**	**-0.5793**	**0.4980**	0.1755	-0.2234
Th	0.0317	0.0330	0.2054	-0.0714	-0.1732	-0.1011	-0.0193	**0.4721**	-0.0446	**-0.2875**	0.1624	-0.0252
Tl	**-0.5539**	**-0.4361**	0.2253	**0.5472**	0.0264	0.0936	0.0273	0.0495	**-0.3572**	**0.4417**	-0.1158	-0.0865
U	**-0.6849**	**-0.7664**	**0.6637**	-0.1555	-0.1434	-0.1785	**-0.5962**	0.1349	-0.0129	**0.2795**	**-0.3205**	**0.5372**
V	**-0.3375**	**-0.4869**	**0.5379**	**-0.4668**	-0.2696	0.0095	**-0.4744**	-0.2376	0.2134	**0.3829**	-0.2616	**0.5515**
W	**-0.7792**	**-0.7410**	**0.4721**	0.1916	-0.1281	0.0125	**-0.4548**	0.0022	-0.1068	**0.5058**	**-0.2790**	**0.2962**
Zn	-0.1875	-0.1452	0.0446	0.2290	**-0.3012**	0.0990	-0.0894	**0.3546**	**-0.3498**	**0.3034**	-0.0085	-0.1734
Zr	**0.3189**	**0.3529**	**-0.5016**	**-0.3011**	-0.0179	0.1593	**0.2990**	**0.3774**	**-0.2876**	0.1293	0.1648	**-0.4089**
La	**-0.3980**	**-0.4460**	**0.4579**	-0.2006	-0.1464	**-0.3010**	**-0.5236**	0.1799	0.2169	-0.2023	-0.1481	**0.4090**
Ce	-0.0593	0.0155	0.0902	-0.0780	**-0.3235**	**0.2803**	0.2014	**0.8104**	**-0.5007**	0.2458	**0.2989**	**-0.4112**
Pr	-0.2143	-0.2657	**0.3875**	-0.2469	-0.1849	-0.2183	**-0.3624**	0.2451	0.2126	-0.2182	-0.0436	**0.3031**
N	-0.2410	**-0.2878**	**0.3723**	-0.2089	-0.1589	**-0.2808**	**-0.4226**	0.1754	**0.2789**	**-0.2812**	-0.0870	**0.3536**
Sm	-0.1991	-0.2459	**0.3553**	-0.2086	-0.1611	-0.2699	**-0.3920**	0.1872	**0.2794**	**-0.2912**	-0.0629	**0.3314**
Eu	-0.2425	**-0.2999**	**0.4089**	-0.1878	-0.1247	**-0.3084**	**-0.4196**	0.1391	**0.2972**	**-0.3050**	-0.0950	**0.3879**
Gd	-0.2655	**-0.3261**	**0.4117**	-0.2113	-0.1291	**-0.3255**	**-0.4620**	0.0754	**0.3589**	**-0.2981**	-0.1380	**0.4383**
Tb	**-0.2824**	**-0.3465**	**0.4453**	-0.2061	-0.1359	**-0.3088**	**-0.4560**	0.1044	**0.3142**	-0.2743	-0.1188	**0.4259**
Dy	**-0.3261**	**-0.3848**	**0.4429**	-0.2006	-0.1142	**-0.3439**	**-0.5186**	0.0573	**0.3663**	-0.2647	-0.1623	**0.4734**
Y	**-0.2845**	**-0.2991**	0.2548	-0.1847	0.0071	**-0.3884**	**-0.5420**	-0.1803	**0.6386**	-0.2618	-0.2177	**0.5350**
Ho	**-0.3622**	**-0.4202**	**0.4428**	-0.2071	-0.0864	**-0.3693**	**-0.5762**	-0.0122	**0.4279**	-0.2555	-0.1933	**0.5321**
Er	**-0.3896**	**-0.4227**	**0.3735**	-0.1310	-0.0372	**-0.4116**	**-0.6145**	-0.0580	**0.4730**	**-0.2966**	-0.2321	**0.5321**
Tm	**-0.4297**	**-0.4746**	**0.4334**	-0.1759	-0.0341	**-0.4055**	**-0.6347**	-0.0592	**0.4391**	-0.2368	-0.2073	**0.5668**
Yb	**-0.4171**	**-0.4490**	**0.3787**	-0.1409	0.0076	**-0.4474**	**-0.6379**	-0.1001	**0.5000**	**-0.2782**	-0.2215	**0.5694**
Lu	**-0.4748**	**-0.5206**	**0.4403**	-0.1915	0.0579	**-0.4463**	**-0.6872**	-0.1898	**0.5154**	-0.1538	-0.2186	**0.6501**
∑REY	-0.2027	-0.1744	0.2683	-0.1616	**-0.2854**	0.0239	-0.1208	**0.6091**	-0.1621	0.0323	0.1328	-0.0586
%HREY	-0.0341	-0.0813	-0.0309	-0.0265	**0.3722**	**-0.4284**	**-0.4141**	**-0.8094**	**0.7502**	**-0.3272**	**-0.3142**	**0.5816**

Table S3. Continued

	Ba	Be	Bi	Cd	Cl	Co	Cr	Cu	F	Hf	Hg	In
Latitude	0.2028	**-0.3818**	**0.7186**	**0.5036**	0.1027	**0.5843**	-0.0758	**0.3153**	**0.4459**	0.0544	0.0498	**-0.3028**
Water Depth (m)	0.1212	**0.6145**	-0.2581	**-0.4267**	**0.3290**	-0.2564	0.1121	-0.1103	-0.1020	0.0521	-0.0078	**0.4355**
Growth Rate (mm/Ma; M&L-B 1988)	**-0.3137**	0.1917	**-0.7318**	**-0.5812**	-0.0809	**-0.7673**	-0.0924	**-0.3561**	**-0.4559**	0.0271	-0.0792	-0.1486
Growth Rate (mm/Ma; P&H 1988)	**-0.2882**	-0.1618	**-0.4118**	-0.2162	-0.1707	**-0.3706**	-0.0442	-0.1588	-0.1938	0.1398	-0.0234	-0.1482
Fe	-0.2369	**0.4130**	**-0.7677**	**-0.7035**	-0.1187	**-0.7898**	-0.0887	**-0.4620**	**-0.5506**	0.0527	0.0024	-0.1290
Mn	0.2229	**-0.3896**	**0.8267**	**0.8781**	0.0664	**0.8958**	-0.2484	0.0855	0.2038	-0.1844	0.1104	0.0561
Fe/Mn	-0.2091	**0.4215**	**-0.8304**	**-0.8234**	-0.1504	**-0.8704**	0.0647	**-0.3387**	**-0.4300**	0.1816	-0.0733	-0.0242
Si	-0.0663	0.1877	**-0.4405**	**-0.6246**	0.0019	**-0.5528**	**0.3400**	**0.2772**	0.1821	**0.2854**	-0.0751	-0.0770
Al	-0.0312	0.1385	**-0.3795**	**-0.5284**	-0.0414	**-0.4527**	**0.2829**	**0.2809**	**0.2901**	0.2511	-0.0633	0.0202
Si/Al	-0.0219	-0.1013	**0.3349**	**0.3665**	0.0416	**0.3697**	-0.1945	**-0.3164**	-0.2335	-0.0709	-0.0218	0.0568
Mg	-0.2335	**-0.5520**	**0.2996**	**0.6822**	-0.1719	**0.4228**	0.1193	0.1019	0.2017	**-0.3841**	0.0399	0.0240
Ca	**-0.4334**	-0.2555	-0.1342	0.1400	**-0.4095**	0.0033	0.0542	**-0.2966**	0.0157	-0.2347	-0.0493	0.0356
Na	**0.4207**	0.1262	**0.3151**	-0.0707	**0.7204**	0.1165	0.0822	**0.6261**	0.2646	**0.3107**	-0.0504	-0.1335
K	0.1389	-0.0721	0.1323	-0.1033	0.0863	0.0709	**0.3291**	**0.4913**	**0.4935**	0.2002	-0.0390	0.0179
Ti	**0.7641**	**0.5163**	**0.3349**	-0.0672	0.2208	**0.3191**	0.1238	**0.3113**	0.1315	**0.3299**	-0.0896	**0.4656**
P	**-0.6840**	-0.1380	**-0.6279**	**-0.3233**	**-0.3514**	**-0.5506**	-0.0882	**-0.5940**	0.0166	-0.2493	-0.0085	-0.1399
S	**0.5445**	-0.0212	**0.5960**	**0.2879**	**0.5589**	**0.4630**	-0.2127	**0.4729**	0.1703	0.1421	0.1081	-0.1900
Ag	0.2163	0.0280	0.0525	-0.0875	0.0251	0.1116	-0.0109	0.0539	0.1573	**0.3034**	-0.0132	0.0490
As	**-0.4409**	-0.1232	-0.2377	0.0334	-0.2181	-0.1663	-0.1839	**-0.6530**	**-0.4055**	-0.2213	0.1142	-0.1554
Ba		**0.5299**	**0.5119**	0.0500	**0.3490**	**0.4059**	-0.2342	**0.5027**	0.0332	0.2586	-0.0588	0.1992
Be	**0.5299**		-0.2616	**-0.6160**	**0.2923**	**-0.3134**	-0.0798	0.1037	-0.2336	0.2066	-0.0465	0.2653
Bi	**0.5119**	-0.2616		**0.7667**	0.1869	**0.9221**	-0.1673	**0.3258**	**0.3215**	-0.0184	0.0111	0.1119
Cd	0.0500	**-0.6160**	**0.7667**		-0.0424	**0.8252**	-0.1277	0.0782	0.1986	-0.2669	0.1084	0.0389
Cl	**0.3490**	**0.2923**	0.1869	-0.0424		0.0040	0.0272	**0.4245**	-0.0645	0.0887	-0.1408	-0.1596
Co	**0.4059**	**-0.3134**	**0.9221**	**0.8252**	0.0040		-0.1548	0.1978	**0.3294**	-0.0170	0.0829	0.2642
Cr	-0.2342	-0.0798	-0.1673	-0.1277	0.0272	-0.1548		-0.0386	-0.0410	-0.0361	-0.1099	0.0457
Cu	**0.5027**	0.1037	**0.3258**	0.0782	**0.4245**	0.1978	-0.0386		0.2074	0.0313	-0.0155	-0.2390
F	0.0332	-0.2336	**0.3215**	0.1986	-0.0645	**0.3294**	-0.0410	0.2074		-0.0602	-0.0846	0.1288
Hf	0.2586	0.2066	-0.0184	-0.2669	0.0887	-0.0170	-0.0361	0.0313	-0.0602		0.1752	0.0607
Hg	-0.0588	-0.0465	0.0111	0.1084	-0.1408	0.0829	-0.1099	-0.0155	-0.0846	0.1752		-0.0314
In	0.1992	0.2653	0.1119	0.0389	-0.1596	0.2642	0.0457	-0.2390	0.1288	0.0607	-0.0314	
Li	-0.0065	-0.2002	-0.1015	-0.0145	-0.0373	-0.0691	0.2037	**0.3920**	**0.4233**	-0.0234	-0.0683	0.0068
Mo	0.0837	-0.1730	**0.5286**	**0.5801**	0.1658	**0.5520**	**-0.3600**	-0.1588	0.0910	-0.2388	0.1304	-0.0241
Nb	**0.6110**	0.1651	**0.4697**	0.2110	-0.1035	**0.5291**	-0.0477	0.2756	0.2369	0.2113	-0.0421	**0.5236**
Ni	0.1695	**-0.5890**	**0.7963**	**0.9190**	0.0175	**0.8233**	-0.1436	**0.3108**	**0.3237**	-0.1885	0.1318	-0.1135
Pb	**0.4875**	0.1351	**0.6447**	**0.4427**	0.1895	**0.6323**	-0.2181	-0.0445	-0.1066	0.0106	0.0213	0.1696
Rb	0.0580	-0.0100	-0.0330	-0.2073	0.0068	-0.0440	**0.4319**	**0.3693**	**0.4672**	0.1651	-0.0781	0.1623
Sb	0.2598	0.1760	0.2317	0.2469	-0.0224	**0.2941**	-0.1940	-0.0121	-0.1315	-0.2081	0.0060	**0.2919**
Sc	-0.2333	**0.3571**	**-0.3823**	**-0.3208**	-0.0949	-0.2738	**0.3805**	-0.1934	-0.1205	-0.0045	0.0204	**0.5068**
Se	**-0.3318**	0.1479	**-0.3407**	-0.0982	0.0096	-0.2354	0.2424	**-0.4959**	-0.2693	-0.2607	-0.1748	**0.3888**
Sn	0.2087	-0.2702	**0.3484**	**0.2930**	-0.0209	**0.3440**	-0.0645	0.2580	0.1216	0.0211	-0.0413	-0.1026
Sr	0.0713	-0.0695	**0.3350**	**0.4520**	-0.0158	**0.3990**	**-0.3110**	-0.2532	**-0.2924**	-0.1837	0.0216	-0.0505
Ta	**0.4767**	**0.4907**	-0.0786	**-0.4017**	0.2171	-0.0886	0.0626	0.0902	-0.0658	**0.7644**	-0.0048	**0.3101**
Te	**0.5082**	-0.2417	**0.8753**	**0.7282**	-0.0244	**0.8959**	-0.2312	0.2518	0.2295	-0.0235	0.0328	**0.2843**
Th	0.0911	**0.3320**	-0.0969	-0.1938	-0.1158	0.0448	0.2044	**-0.3720**	-0.0061	0.2245	-0.0956	**0.7496**
Tl	0.2073	**-0.4293**	**0.7829**	**0.8382**	0.0401	**0.8074**	-0.2185	0.2118	**0.3432**	-0.2681	0.1524	-0.0543
U	**0.3259**	0.2689	**0.3128**	0.1660	0.2165	**0.2972**	-0.2506	-0.1329	-0.2693	-0.0179	0.0640	-0.0800
V	0.2028	**0.2858**	0.0295	-0.1525	0.2733	-0.0680	**-0.3406**	0.0192	-0.2311	0.1458	0.1561	-0.2668
W	0.2687	-0.0010	**0.4994**	**0.4623**	**0.2995**	**0.5339**	**-0.3608**	0.0929	0.0088	-0.1780	0.0690	0.0792
Zn	**0.5820**	0.1592	0.2177	0.2011	0.1666	0.2001	-0.0829	**0.3256**	-0.1417	0.0549	-0.0778	-0.0831
Zr	**0.4412**	**0.3033**	0.0166	-0.2171	-0.0333	-0.0088	0.0058	**0.4013**	0.0501	0.2467	0.0266	0.0053
La	0.1055	**0.5454**	-0.2018	-0.2372	0.0670	-0.0806	-0.1202	**-0.3813**	**-0.3169**	-0.0058	-0.0343	**0.4947**
Ce	**0.6690**	**0.4364**	**0.4272**	0.0698	0.1483	**0.4812**	-0.0043	0.0900	0.2440	0.2425	-0.1006	**0.7378**
Pr	0.0947	**0.5403**	-0.2692	**-0.3376**	0.0347	-0.1320	-0.0522	**-0.3632**	-0.2175	0.1102	-0.0620	**0.5715**
N	0.0228	**0.5215**	**-0.3333**	**-0.3350**	0.0234	-0.1942	-0.0371	**-0.4229**	-0.2750	0.0346	-0.0713	**0.5446**
Sm	0.0153	**0.5156**	**-0.3491**	**-0.3468**	0.0120	-0.2095	-0.0137	**-0.4268**	-0.2594	0.0551	-0.0762	**0.5548**
Eu	-0.0354	**0.4615**	**-0.3298**	**-0.3098**	-0.0152	-0.1798	0.0043	**-0.4479**	-0.2732	0.0475	-0.0651	**0.5478**
Gd	-0.0593	**0.4654**	**-0.3603**	**-0.3324**	-0.0110	-0.2197	-0.0384	**-0.4629**	**-0.2883**	0.0138	-0.0512	**0.5008**
Tb	-0.0241	**0.4640**	**-0.3005**	**-0.2959**	-0.0077	-0.1628	-0.0376	**-0.4481**	-0.2703	0.0368	-0.0509	**0.5188**
Dy	-0.0462	**0.4559**	**-0.3213**	**-0.2928**	-0.0143	-0.1840	-0.0814	**-0.4690**	**-0.2927**	0.0086	-0.0217	**0.4798**
Y	-0.2503	**0.3168**	**-0.4348**	**-0.3116**	-0.0894	**-0.3148**	-0.1964	**-0.5828**	-0.1545	-0.0733	0.0556	**0.3355**
Ho	-0.0900	**0.4325**	**-0.3412**	**-0.2886**	-0.0129	-0.2092	-0.1075	**-0.5060**	**-0.3078**	-0.0156	0.0017	**0.4237**
Er	-0.1427	**0.4042**	**-0.3750**	-0.2592	-0.0170	-0.2415	-0.1121	**-0.5386**	**-0.3189**	-0.1024	-0.0163	**0.4060**
Tm	-0.1140	**0.3833**	**-0.3031**	-0.2192	-0.0395	-0.1655	-0.1570	**-0.5302**	**-0.3194**	-0.0380	0.0459	**0.3813**
Yb	-0.1700	**0.3417**	**-0.3518**	-0.2233	-0.0873	-0.2033	-0.1506	**-0.5612**	**-0.3065**	-0.0756	0.0464	**0.3640**
Lu	-0.1554	**0.2787**	-0.2675	-0.1622	-0.1053	-0.1351	-0.2530	**-0.5231**	**-0.2972**	-0.0460	0.1249	0.2269
∑REY	**0.4518**	**0.5578**	0.1251	-0.1121	0.1059	0.2329	-0.0526	-0.1787	0.0254	0.1686	-0.0858	**0.7682**
%HREY	**-0.7289**	**-0.2869**	**-0.5893**	-0.1967	-0.2252	**-0.5697**	-0.0900	**-0.3854**	-0.2557	-0.1720	0.1272	**-0.4654**

Table S3. Continued

	Li	Mo	Nb	Ni	Pb	Rb	Sb	Sc	Se	Sn	Sr	Ta
Latitude	0.0591	**0.4024**	0.1210	**0.6355**	**0.3287**	0.1003	-0.0895	**-0.4611**	**-0.5239**	**0.3485**	0.0695	-0.1895
Water Depth (m)	-0.0523	0.0110	-0.0806	**-0.4587**	0.1160	0.0885	0.0566	**0.6015**	**0.5334**	**-0.3090**	-0.2233	**0.3769**
Growth Rate (mm/Ma; M&L-B 1988)	-0.2286	**-0.2991**	**-0.4138**	**-0.6835**	**-0.4139**	**-0.2913**	-0.1399	0.0818	0.2118	**-0.3025**	-0.0381	0.0201
Growth Rate (mm/Ma; P&H 1988)	-0.0592	**-0.3442**	-0.1522	**-0.3186**	**-0.4560**	-0.0965	-0.1773	-0.0073	0.0129	-0.1485	-0.0160	0.0291
Fe	**-0.3730**	-0.2058	**-0.4463**	**-0.7877**	-0.2103	**-0.4282**	-0.1000	0.1730	0.2634	**-0.3226**	0.0708	0.0480
Mn	-0.2041	**0.8034**	0.1839	**0.8491**	**0.6842**	**-0.3466**	0.2411	**-0.3253**	-0.1085	**0.2860**	**0.6251**	**-0.3411**
Fe/Mn	-0.1347	**-0.5745**	-0.2508	**-0.8791**	**-0.4680**	-0.0616	-0.1482	0.2408	0.1888	**-0.3227**	**-0.2812**	0.2688
Si	**0.5230**	**-0.8339**	0.0266	**-0.4969**	**-0.6521**	**0.7610**	**-0.4236**	0.1944	-0.2505	-0.1079	**-0.8637**	**0.4217**
Al	**0.6286**	**-0.8112**	0.1549	**-0.3856**	**-0.6736**	**0.8063**	**-0.3220**	0.1338	-0.2387	-0.0350	**-0.8975**	**0.4134**
Si/Al	**-0.6112**	**0.6391**	-0.2252	0.1872	**0.6936**	**-0.5823**	0.0502	-0.0073	0.1025	-0.0536	**0.7189**	-0.1809
Mg	**0.3784**	0.2293	-0.0020	**0.6722**	0.0764	0.0106	0.1517	-0.0221	0.1416	0.2119	0.0899	**-0.3782**
Ca	-0.2545	-0.1609	0.1152	-0.0062	-0.2451	-0.1604	**0.2970**	0.1489	0.1207	-0.0622	0.2426	**-0.3170**
Na	**0.3309**	-0.1072	0.1272	0.1185	0.0209	**0.4998**	**-0.2921**	-0.2200	**-0.3746**	0.1276	**-0.4679**	**0.3936**
K	**0.6852**	**-0.4826**	**0.3390**	0.0848	**-0.3534**	**0.9595**	-0.2389	-0.0031	**-0.3545**	0.1468	**-0.7595**	**0.3053**
Ti	0.1575	-0.2027	**0.6585**	0.0153	**0.3097**	**0.3386**	0.2415	0.1559	-0.0345	0.0408	-0.1634	**0.6948**
P	-0.1897	0.0488	**-0.5930**	**-0.4259**	**-0.3223**	**-0.3407**	-0.2084	0.1115	**0.3089**	-0.2576	0.1062	**-0.4064**
S	-0.0362	**0.4052**	0.1804	**0.4364**	**0.3819**	-0.0301	-0.0827	**-0.5367**	**-0.4987**	0.2694	0.1292	0.0682
Ag	**0.2838**	**-0.3049**	**0.3105**	-0.0528	-0.0682	**0.4370**	-0.1545	-0.1280	**-0.3549**	0.1152	**-0.3527**	**0.4996**
As	**-0.6440**	**0.5010**	**-0.5517**	-0.1607	0.1981	**-0.7634**	0.0220	0.0264	**0.2963**	-0.2523	**0.6795**	**-0.4496**
Ba	-0.0065	0.0837	**0.6110**	0.1695	**0.4875**	0.0580	0.2598	-0.2333	**-0.3318**	0.2087	0.0713	**0.4767**
Be	-0.2002	-0.1730	0.1651	**-0.5890**	0.1351	-0.0100	0.1760	**0.3571**	0.1479	-0.2702	-0.0695	**0.4907**
Bi	-0.1015	**0.5286**	**0.4697**	**0.7963**	**0.6447**	-0.0330	0.2317	**-0.3823**	**-0.3407**	**0.3484**	**0.3350**	-0.0786
Cd	-0.0145	**0.5801**	0.2110	**0.9190**	**0.4427**	-0.2073	0.2469	**-0.3208**	-0.0982	**0.2930**	**0.4520**	**-0.4017**
Cl	-0.0373	0.1658	-0.1035	0.0175	0.1895	0.0068	-0.0224	-0.0949	0.0096	-0.0209	-0.0158	0.2171
Co	-0.0691	**0.5520**	**0.5291**	**0.8233**	**0.6323**	-0.0440	**0.2941**	-0.2738	-0.2354	**0.3440**	**0.3990**	-0.0886
Cr	0.2037	**-0.3600**	-0.0477	-0.1436	-0.2181	**0.4319**	-0.1940	**0.3805**	0.2424	-0.0645	**-0.3110**	0.0626
Cu	**0.3920**	-0.1588	0.2756	**0.3108**	-0.0445	**0.3693**	-0.0121	-0.1934	**-0.4959**	0.2580	-0.2532	0.0902
F	**0.4233**	0.0910	0.2369	**0.3237**	-0.1066	**0.4672**	-0.1315	-0.1205	-0.2693	0.1216	**-0.2924**	-0.0658
Hf	-0.0234	-0.2388	0.2113	-0.1885	0.0106	0.1651	-0.2081	-0.0045	-0.2607	0.0211	-0.1837	**0.7644**
Hg	-0.0683	0.1304	-0.0421	0.1318	0.0213	-0.0781	0.0060	0.0204	-0.1748	-0.0413	0.0216	-0.0048
In	0.0068	-0.0241	**0.5236**	-0.1135	0.1696	0.1623	**0.2919**	**0.5068**	**0.3888**	-0.1026	-0.0505	**0.3101**
Li		**-0.4122**	0.1394	0.1754	**-0.4296**	**0.7155**	-0.2171	-0.0455	-0.1123	0.2175	**-0.6986**	0.1347
Mo	**-0.4122**		-0.1971	**0.5389**	**0.6438**	**-0.5670**	0.1952	-0.2531	0.1166	0.0599	**0.6768**	**-0.4109**
Nb	0.1394	-0.1971		0.2445	0.1184	**0.3084**	**0.4963**	0.0077	-0.2238	0.2613	-0.0837	**0.3163**
Ni	0.1754	**0.5389**	0.2445		**0.4063**	-0.0641	0.1901	**-0.4832**	-0.2666	**0.4451**	**0.2825**	**-0.3415**
Pb	**-0.4296**	**0.6438**	0.1184	**0.4063**		**-0.4278**	0.1264	-0.2461	-0.0560	0.2138	**0.5379**	0.0841
Rb	**0.7155**	**-0.5670**	**0.3084**	-0.0641	**-0.4278**		-0.2557	0.1858	-0.1817	0.0659	**-0.8003**	**0.3480**
Sb	-0.2171	0.1952	**0.4963**	0.1901	0.1264	-0.2557		0.1330	**0.2788**	0.0448	**0.3569**	-0.1268
Sc	-0.0455	-0.2531	0.0077	**-0.4832**	-0.2461	0.1858	0.1330		**0.5802**	**-0.4153**	-0.1260	0.1545
Se	-0.1123	0.1166	-0.2238	-0.2666	-0.0560	-0.1817	**0.2788**	**0.5802**		**-0.2916**	0.1271	-0.1117
Sn	0.2175	0.0599	0.2613	**0.4451**	0.2138	0.0659	0.0448	**-0.4153**	**-0.2916**		-0.0595	-0.0508
Sr	**-0.6986**	**0.6768**	-0.0837	**0.2825**	**0.5379**	**-0.8003**	**0.3569**	-0.1260	0.1271	-0.0595		**-0.3656**
Ta	0.1347	**-0.4109**	**0.3163**	**-0.3415**	0.0841	**0.3480**	-0.1268	0.1545	-0.1117	-0.0508	**-0.3656**	
Te	-0.1010	**0.3501**	**0.6752**	**0.7021**	**0.5215**	-0.0277	**0.3644**	**-0.3566**	**-0.3820**	**0.3274**	**0.3267**	-0.0405
Th	0.0200	-0.0732	0.1554	**-0.3154**	0.2549	0.1485	-0.0901	**0.5282**	**0.4034**	-0.2232	-0.1059	**0.5031**
Tl	0.0367	**0.6262**	0.2403	**0.8964**	**0.4709**	-0.1096	**0.3028**	**-0.4172**	-0.1781	**0.3673**	**0.3249**	**-0.3768**
U	**-0.6272**	**0.6402**	-0.0861	0.1178	**0.6728**	**-0.6468**	0.2148	-0.0603	0.0763	-0.1081	**0.7901**	-0.0889
V	**-0.5507**	**0.4625**	**-0.3360**	-0.1528	**0.3740**	**-0.5412**	-0.1781	-0.1496	-0.2076	-0.1500	**0.4814**	-0.0717
W	**-0.4199**	**0.8361**	0.0421	**0.4668**	**0.5480**	**-0.5233**	**0.3467**	-0.1441	0.1399	0.1038	**0.6317**	**-0.2784**
Zn	0.2400	0.0678	0.1720	**0.3126**	**0.3801**	-0.1192	0.0501	**-0.4474**	-0.2003	0.2362	0.1140	0.2329
Zr	0.1827	**-0.4207**	**0.5987**	-0.0964	**-0.2854**	0.2548	0.1981	0.0209	**-0.3123**	0.1608	-0.1875	0.1853
La	**-0.4065**	**0.3124**	-0.0964	**-0.3840**	**0.3861**	**-0.3831**	0.2122	**0.5403**	**0.6128**	-0.2733	**0.3269**	0.1885
Ce	0.0729	0.0841	**0.6202**	0.0635	**0.5046**	0.2516	0.1276	0.1792	0.0416	0.0766	-0.0770	**0.5558**
Pr	-0.2639	0.1542	-0.0724	**-0.4788**	**0.2945**	-0.1942	0.0075	**0.5771**	**0.5405**	**-0.3141**	0.1588	**0.3332**
N	-0.2585	0.1599	-0.1419	**-0.4868**	0.2690	-0.2416	0.0266	**0.5729**	**0.6272**	**-0.3143**	0.1651	0.2665
Sm	-0.2212	0.1184	-0.1406	**-0.4989**	0.2524	-0.2048	-0.0235	**0.5702**	**0.6061**	**-0.3174**	0.1269	**0.2976**
Eu	**-0.2769**	0.1539	-0.1572	**-0.4829**	0.2449	-0.2355	-0.0075	**0.6133**	**0.6249**	**-0.3378**	0.1875	0.2488
Gd	**-0.3130**	0.1860	-0.2031	**-0.4989**	0.2343	**-0.2838**	0.0078	**0.5849**	**0.6317**	**-0.3419**	0.2022	0.1949
Tb	**-0.3335**	0.2098	-0.1695	**-0.4671**	**0.2804**	**-0.2860**	0.0058	**0.5869**	**0.6025**	**-0.3359**	0.2228	0.2131
Dy	**-0.3640**	0.2461	-0.2021	**-0.4580**	**0.2768**	**-0.3522**	0.0450	**0.5613**	**0.6180**	**-0.3181**	0.2584	0.1660
Y	**-0.3402**	0.2406	**-0.2794**	**-0.4622**	0.0518	**-0.3916**	0.0945	**0.4550**	**0.5891**	**-0.2952**	0.1867	-0.0273
Ho	**-0.4186**	**0.2819**	-0.2383	**-0.4559**	0.2601	**-0.4192**	0.0799	**0.5360**	**0.6221**	**-0.3245**	**0.2956**	0.1073
Er	**-0.3887**	**0.2877**	-0.2607	**-0.4242**	0.2203	**-0.4503**	0.1422	**0.5076**	**0.6976**	**-0.3002**	**0.2916**	0.0320
Tm	**-0.4799**	**0.3329**	-0.2251	**-0.3902**	0.2669	**-0.4978**	0.1331	**0.4958**	**0.6073**	**-0.3004**	**0.3570**	0.0418
Yb	**-0.4373**	**0.3019**	-0.2365	**-0.3901**	0.2102	**-0.4906**	0.1401	**0.4869**	**0.6329**	**-0.2788**	**0.3286**	-0.0020
Lu	**-0.5454**	**0.3636**	-0.2257	**-0.3217**	0.2404	**-0.5933**	0.1367	**0.3699**	**0.4330**	-0.2618	**0.4396**	-0.0791
∑REY	-0.1263	0.1789	**0.3402**	-0.1985	**0.4872**	0.0010	0.1355	**0.4147**	**0.3576**	-0.1096	0.0680	**0.4788**
%HREY	-0.2184	-0.0269	**-0.6000**	-0.2716	**-0.5073**	**-0.3865**	-0.0466	0.0303	0.1782	-0.1760	0.1227	**-0.4593**

Table S3. Continued

	Te	Th	Tl	U	V	W	Zn	Zr	La	Ce	Pr	N
Latitude	**0.4792**	**-0.3336**	**0.6097**	0.1271	0.1478	0.2066	0.0012	0.0640	**-0.4539**	0.0189	**-0.4899**	**-0.5550**
Water Depth (m)	**-0.3685**	**0.5912**	**-0.3281**	0.0815	0.0648	0.1043	-0.1812	-0.1924	**0.7160**	**0.4536**	**0.7274**	**0.7361**
Growth Rate (mm/Ma; M&L-B 1988)	**-0.5566**	-0.0772	**-0.6365**	-0.1335	0.2201	-0.2417	-0.0439	-0.1181	0.1790	**-0.4188**	0.2060	0.2598
Growth Rate (mm/Ma; P&H 1988)	-0.2081	-0.1784	**-0.3017**	**-0.3123**	-0.0910	-0.2589	-0.0653	-0.0428	-0.1617	**-0.3548**	-0.0790	-0.0713
Fe	**-0.6607**	0.0578	**-0.7150**	0.1268	**0.4257**	-0.2109	-0.0679	-0.0533	**0.4078**	**-0.3446**	**0.3876**	**0.4447**
Mn	**0.7228**	-0.0741	**0.8397**	**0.5058**	0.1588	**0.7112**	0.2011	-0.2107	0.0366	0.2416	-0.0747	-0.1009
Fe/Mn	**-0.6592**	0.0967	**-0.8325**	-0.2461	0.1059	**-0.5119**	-0.1022	0.0878	0.1814	-0.2695	0.2410	**0.2819**
Si	**-0.4250**	0.0317	**-0.5539**	**-0.6849**	**-0.3375**	**-0.7792**	-0.1875	**0.3189**	**-0.3980**	-0.0593	-0.2143	-0.2410
Al	**-0.3221**	0.0330	**-0.4361**	**-0.7664**	**-0.4869**	**-0.7410**	-0.1452	**0.3529**	**-0.4460**	0.0155	-0.2657	**-0.2878**
Si/Al	**0.2787**	0.2054	0.2253	**0.6637**	**0.5379**	**0.4721**	0.0446	**-0.5016**	**0.4579**	0.0902	**0.3875**	**0.3723**
Mg	**0.2776**	-0.0714	**0.5472**	-0.1555	**-0.4668**	0.1916	0.2290	**-0.3011**	-0.2006	-0.0780	-0.2469	-0.2089
Ca	0.0685	-0.1732	0.0264	-0.1434	-0.2696	-0.1281	**-0.3012**	-0.0179	-0.1464	**-0.3235**	-0.1849	-0.1589
Na	0.1299	-0.1011	0.0936	-0.1785	0.0095	0.0125	0.0990	0.1593	**-0.3010**	**0.2803**	-0.2183	**-0.2808**
K	0.0962	-0.0193	0.0273	**-0.5962**	**-0.4744**	**-0.4548**	-0.0894	**0.2990**	**-0.5236**	0.2014	**-0.3624**	**-0.4226**
Ti	**0.3267**	**0.4721**	0.0495	0.1349	-0.2376	0.0022	**0.3546**	**0.3774**	0.1799	**0.8104**	0.2451	0.1754
P	**-0.5793**	-0.0446	**-0.3572**	-0.0129	0.2134	-0.1068	**-0.3498**	**-0.2876**	0.2169	**-0.5007**	0.2126	**0.2789**
S	**0.4980**	**-0.2875**	**0.4417**	**0.2795**	**0.3829**	**0.5058**	**0.3034**	0.1293	-0.2023	0.2458	-0.2182	**-0.2812**
Ag	0.1755	0.1624	-0.1158	**-0.3205**	-0.2616	**-0.2790**	-0.0085	0.1648	-0.1481	**0.2989**	-0.0436	-0.0870
As	-0.2234	-0.0252	-0.0865	**0.5372**	**0.5515**	**0.2962**	-0.1734	**-0.4089**	**0.4090**	**-0.4112**	**0.3031**	**0.3536**
Ba	**0.5082**	0.0911	0.2073	**0.3259**	0.2028	0.2687	**0.5820**	**0.4412**	0.1055	**0.6690**	0.0947	0.0228
Be	-0.2417	**0.3320**	**-0.4293**	0.2689	**0.2858**	-0.0010	0.1592	**0.3033**	**0.5454**	**0.4364**	**0.5403**	**0.5215**
Bi	**0.8753**	-0.0969	**0.7829**	**0.3128**	0.0295	**0.4994**	0.2177	0.0166	-0.2018	**0.4272**	-0.2692	**-0.3333**
Cd	**0.7282**	-0.1938	**0.8382**	0.1660	-0.1525	**0.4623**	0.2011	-0.2171	-0.2372	0.0698	**-0.3376**	**-0.3350**
Cl	-0.0244	-0.1158	0.0401	0.2165	0.2733	**0.2995**	0.1666	-0.0333	0.0670	0.1483	0.0347	0.0234
Co	**0.8959**	0.0448	**0.8074**	**0.2972**	-0.0680	**0.5339**	0.2001	-0.0088	-0.0806	**0.4812**	-0.1320	-0.1942
Cr	-0.2312	0.2044	-0.2185	-0.2506	**-0.3406**	**-0.3608**	-0.0829	0.0058	-0.1202	-0.0043	-0.0522	-0.0371
Cu	0.2518	**-0.3720**	0.2118	-0.1329	0.0192	0.0929	**0.3256**	**0.4013**	**-0.3813**	0.0900	**-0.3632**	**-0.4229**
F	0.2295	-0.0061	**0.3432**	-0.2693	-0.2311	0.0088	-0.1417	0.0501	**-0.3169**	0.2440	-0.2175	-0.2750
Hf	-0.0235	0.2245	-0.2681	-0.0179	0.1458	-0.1780	0.0549	0.2467	-0.0058	0.2425	0.1102	0.0346
Hg	0.0328	-0.0956	0.1524	0.0640	0.1561	0.0690	-0.0778	0.0266	-0.0343	-0.1006	-0.0620	-0.0713
In	**0.2843**	**0.7496**	-0.0543	-0.0800	-0.2668	0.0792	-0.0831	0.0053	**0.4947**	**0.7378**	**0.5715**	**0.5446**
Li	-0.1010	0.0200	0.0367	**-0.6272**	**-0.5507**	**-0.4199**	0.2400	0.1827	**-0.4065**	0.0729	-0.2639	-0.2585
Mo	**0.3501**	-0.0732	**0.6262**	**0.6402**	**0.4625**	**0.8361**	0.0678	**-0.4207**	**0.3124**	0.0841	0.1542	0.1599
Nb	**0.6752**	0.1554	0.2403	-0.0861	**-0.3360**	0.0421	0.1720	**0.5987**	-0.0964	**0.6202**	-0.0724	-0.1419
Ni	**0.7021**	**-0.3154**	**0.8964**	0.1178	-0.1528	**0.4668**	**0.3126**	-0.0964	**-0.3840**	0.0635	**-0.4788**	**-0.4868**
Pb	**0.5215**	0.2549	**0.4709**	**0.6728**	**0.3740**	**0.5480**	**0.3801**	**-0.2854**	**0.3861**	**0.5046**	**0.2945**	0.2690
Rb	-0.0277	0.1485	-0.1096	**-0.6468**	**-0.5412**	**-0.5233**	-0.1192	0.2548	**-0.3831**	0.2516	-0.1942	-0.2416
Sb	**0.3644**	-0.0901	**0.3028**	0.2148	-0.1781	**0.3467**	0.0501	0.1981	0.2122	0.1276	0.0075	0.0266
Sc	**-0.3566**	**0.5282**	**-0.4172**	-0.0603	-0.1496	-0.1441	**-0.4474**	0.0209	**0.5403**	0.1792	**0.5771**	**0.5729**
Se	**-0.3820**	**0.4034**	-0.1781	0.0763	-0.2076	0.1399	-0.2003	**-0.3123**	**0.6128**	0.0416	**0.5405**	**0.6272**
Sn	**0.3274**	-0.2232	**0.3673**	-0.1081	-0.1500	0.1038	0.2362	0.1608	-0.2733	0.0766	**-0.3141**	**-0.3143**
Sr	**0.3267**	-0.1059	**0.3249**	**0.7901**	**0.4814**	**0.6317**	0.1140	-0.1875	**0.3269**	-0.0770	0.1588	0.1651
Ta	-0.0405	**0.5031**	**-0.3768**	-0.0889	-0.0717	**-0.2784**	0.2329	0.1853	0.1885	**0.5558**	**0.3332**	0.2665
Te		-0.0659	**0.6898**	0.1608	-0.0706	**0.3946**	0.2730	0.1224	-0.1938	**0.4533**	-0.2381	**-0.3010**
Th	-0.0659		**-0.3044**	0.0689	-0.1280	-0.0971	-0.0481	-0.1705	**0.6150**	**0.6986**	**0.7614**	**0.7311**
Tl	**0.6898**	**-0.3044**		0.2040	-0.1204	**0.5018**	0.2188	-0.1355	-0.2601	0.1307	**-0.3745**	**-0.3833**
U	0.1608	0.0689	0.2040		**0.6467**	**0.6165**	0.1650	-0.0521	**0.4923**	0.1603	**0.3596**	**0.3387**
V	-0.0706	-0.1280	-0.1204	**0.6467**		**0.4238**	0.0953	-0.0828	**0.3403**	-0.0941	**0.2841**	0.2510
W	**0.3946**	-0.0971	**0.5018**	**0.6165**	**0.4238**		0.0918	-0.1611	**0.3884**	0.1879	0.2145	0.2071
Zn	0.2730	-0.0481	0.2188	0.1650	0.0953	0.0918		0.0415	-0.0635	0.2363	-0.0689	-0.0605
Zr	0.1224	-0.1705	-0.1355	-0.0521	-0.0828	-0.1611	0.0415		-0.2272	0.1440	-0.2078	-0.2494
La	-0.1938	**0.6150**	-0.2601	**0.4923**	**0.3403**	**0.3884**	-0.0635	-0.2272		**0.4134**	**0.9466**	**0.9584**
Ce	**0.4533**	**0.6986**	0.1307	0.1603	-0.0941	0.1879	0.2363	0.1440	**0.4134**		**0.5078**	**0.4375**
Pr	-0.2381	**0.7614**	**-0.3745**	**0.3596**	**0.2841**	0.2145	-0.0689	-0.2078	**0.9466**	**0.5078**		**0.9865**
N	**-0.3010**	**0.7311**	**-0.3833**	**0.3387**	0.2510	0.2071	-0.0605	-0.2494	**0.9584**	**0.4375**	**0.9865**	
Sm	**-0.3104**	**0.7611**	**-0.4080**	**0.3046**	0.2296	0.1549	-0.0461	-0.2437	**0.9343**	**0.4533**	**0.9833**	**0.9961**
Eu	**-0.2955**	**0.7425**	**-0.3951**	**0.3359**	0.2474	0.1907	-0.1127	-0.2629	**0.9435**	**0.4094**	**0.9854**	**0.9906**
Gd	**-0.3267**	**0.6793**	**-0.3931**	**0.3520**	**0.2940**	0.2222	-0.1248	**-0.2769**	**0.9549**	**0.3486**	**0.9765**	**0.9893**
Tb	-0.2756	**0.6986**	**-0.3708**	**0.3763**	**0.3104**	0.2463	-0.1228	-0.2696	**0.9588**	**0.3892**	**0.9819**	**0.9860**
Dy	**-0.2911**	**0.6331**	**-0.3466**	**0.4005**	**0.3378**	**0.2877**	-0.1197	**-0.2797**	**0.9689**	**0.3326**	**0.9633**	**0.9781**
Y	**-0.3767**	**0.3534**	**-0.2911**	0.2643	**0.2799**	0.2552	**-0.2839**	-0.2344	**0.7934**	0.0809	**0.7402**	**0.7856**
Ho	**-0.3101**	**0.5531**	**-0.3339**	**0.4223**	**0.3662**	**0.3263**	-0.1557	**-0.2823**	**0.9594**	0.2542	**0.9228**	**0.9466**
Er	**-0.3418**	**0.4867**	**-0.2969**	**0.3773**	**0.2791**	**0.3442**	-0.1432	**-0.2919**	**0.9290**	0.1912	**0.8590**	**0.9107**
Tm	-0.2666	**0.4614**	-0.2612	**0.4511**	**0.3613**	**0.3882**	-0.1848	-0.2585	**0.9290**	0.1938	**0.8561**	**0.8870**
Yb	**-0.3026**	**0.4292**	-0.2614	**0.4043**	**0.3051**	**0.3592**	-0.1968	-0.2426	**0.8974**	0.1435	**0.8183**	**0.8617**
Lu	-0.2038	0.2587	-0.1876	**0.4991**	**0.4482**	**0.4084**	-0.2222	-0.1586	**0.7973**	0.0417	**0.6962**	**0.7234**
∑REY	0.1595	**0.8132**	-0.0872	**0.3114**	0.0916	**0.2765**	0.1020	-0.0314	**0.7889**	**0.8771**	**0.8474**	**0.8089**
%HREY	**-0.5277**	**-0.4821**	-0.2472	-0.1107	0.1508	-0.0961	**-0.3590**	-0.1925	-0.0803	**-0.8557**	-0.1793	-0.1000

Table S3. Continued

	Sm	Eu	Gd	Tb	Dy	Y	Ho	Er	Tm	Yb	Lu	∑REY	%HREY
Latitude	**-0.5644**	**-0.5352**	**-0.5437**	**-0.4951**	**-0.5111**	**-0.4999**	**-0.5093**	**-0.5621**	**-0.4750**	**-0.5074**	**-0.3610**	-0.2614	-0.2499
Water Depth (m)	**0.7287**	**0.6962**	**0.6927**	**0.6884**	**0.6717**	**0.5112**	**0.6405**	**0.6216**	**0.5754**	**0.5406**	**0.3604**	**0.6766**	-0.2501
Growth Rate (mm/Ma; M&L-B 1988)	0.2662	0.2581	**0.3079**	0.2644	**0.2958**	**0.4275**	**0.3333**	**0.3623**	**0.3124**	**0.3401**	**0.3166**	-0.1417	**0.6226**
Growth Rate (mm/Ma; P&H 1988)	-0.0622	-0.0371	-0.0339	-0.0562	-0.0460	0.0673	-0.0253	-0.0157	-0.0275	0.0020	0.0127	**-0.2792**	**0.4569**
Fe	**0.4416**	**0.4258**	**0.4827**	**0.4428**	**0.4836**	**0.5600**	**0.5261**	**0.5367**	**0.5093**	**0.5269**	**0.5216**	0.0097	**0.5547**
Mn	-0.1261	-0.0857	-0.0981	-0.0542	-0.0480	-0.1382	-0.0467	-0.0589	0.0117	-0.0201	0.0651	0.1322	**-0.3132**
Fe/Mn	**0.2972**	0.2654	**0.2974**	0.2567	0.2720	**0.3558**	**0.2919**	**0.3043**	0.2539	**0.2793**	0.2292	-0.0424	**0.4470**
Si	-0.1991	-0.2425	-0.2655	**-0.2824**	**-0.3261**	**-0.2845**	**-0.3622**	**-0.3896**	**-0.4297**	**-0.4171**	**-0.4748**	-0.2027	-0.0341
Al	-0.2459	**-0.2999**	**-0.3261**	**-0.3465**	**-0.3848**	**-0.2991**	**-0.4202**	**-0.4227**	**-0.4746**	**-0.4490**	**-0.5206**	-0.1744	-0.0813
Si/Al	**0.3553**	**0.4089**	**0.4117**	**0.4453**	**0.4429**	0.2548	**0.4428**	**0.3735**	**0.4334**	**0.3787**	**0.4403**	0.2683	-0.0309
Mg	-0.2086	-0.1878	-0.2113	-0.2061	-0.2006	-0.1847	-0.2071	-0.1310	-0.1759	-0.1409	-0.1915	-0.1616	-0.0265
Ca	-0.1611	-0.1247	-0.1291	-0.1359	-0.1142	0.0071	-0.0864	-0.0372	-0.0341	0.0076	0.0579	**-0.2854**	**0.3722**
Na	-0.2699	**-0.3084**	**-0.3255**	**-0.3088**	**-0.3439**	**-0.3884**	**-0.3693**	**-0.4116**	**-0.4055**	**-0.4474**	**-0.4463**	0.0239	**-0.4284**
K	**-0.3920**	**-0.4196**	**-0.4620**	**-0.4560**	**-0.5186**	**-0.5420**	**-0.5762**	**-0.6145**	**-0.6347**	**-0.6379**	**-0.6872**	-0.1208	**-0.4141**
Ti	0.1872	0.1391	0.0754	0.1044	0.0573	-0.1803	-0.0122	-0.0580	-0.0592	-0.1001	-0.1898	**0.6091**	**-0.8094**
P	**0.2794**	**0.2972**	**0.3589**	**0.3142**	**0.3663**	**0.6386**	**0.4279**	**0.4730**	**0.4391**	**0.5000**	**0.5154**	-0.1621	**0.7502**
S	**-0.2912**	**-0.3050**	**-0.2981**	-0.2743	-0.2647	-0.2618	-0.2555	**-0.2966**	-0.2368	**-0.2782**	-0.1538	0.0323	**-0.3272**
Ag	-0.0629	-0.0950	-0.1380	-0.1188	-0.1623	-0.2177	-0.1933	-0.2321	-0.2073	-0.2215	-0.2186	0.1328	**-0.3142**
As	**0.3314**	**0.3879**	**0.4383**	**0.4259**	**0.4734**	**0.5350**	**0.5321**	**0.5321**	**0.5668**	**0.5694**	**0.6501**	-0.0586	**0.5816**
Ba	0.0153	-0.0354	-0.0593	-0.0241	-0.0462	-0.2503	-0.0900	-0.1427	-0.1140	-0.1700	-0.1554	**0.4518**	**-0.7289**
Be	**0.5156**	**0.4615**	**0.4654**	**0.4640**	**0.4559**	**0.3168**	**0.4325**	**0.4042**	**0.3833**	**0.3417**	**0.2787**	**0.5578**	**-0.2869**
Bi	**-0.3491**	**-0.3298**	**-0.3603**	**-0.3005**	**-0.3213**	**-0.4348**	**-0.3412**	**-0.3750**	**-0.3031**	**-0.3518**	-0.2675	0.1251	**-0.5893**
Cd	**-0.3468**	**-0.3098**	**-0.3324**	**-0.2959**	**-0.2928**	**-0.3116**	**-0.2886**	-0.2592	-0.2192	-0.2233	-0.1622	-0.1121	-0.1967
Cl	0.0120	-0.0152	-0.0110	-0.0077	-0.0143	-0.0894	-0.0129	-0.0170	-0.0395	-0.0873	-0.1053	0.1059	-0.2252
Co	-0.2095	-0.1798	-0.2197	-0.1628	-0.1840	**-0.3148**	-0.2092	-0.2415	-0.1655	-0.2033	-0.1351	0.2329	**-0.5697**
Cr	-0.0137	0.0043	-0.0384	-0.0376	-0.0814	-0.1964	-0.1075	-0.1121	-0.1570	-0.1506	-0.2530	-0.0526	-0.0900
Cu	**-0.4268**	**-0.4479**	**-0.4629**	**-0.4481**	**-0.4690**	**-0.5828**	**-0.5060**	**-0.5386**	**-0.5302**	**-0.5612**	**-0.5231**	-0.1787	**-0.3854**
F	-0.2594	-0.2732	**-0.2883**	-0.2703	**-0.2927**	-0.1545	**-0.3078**	**-0.3189**	**-0.3194**	**-0.3065**	**-0.2972**	0.0254	-0.2557
Hf	0.0551	0.0475	0.0138	0.0368	0.0086	-0.0733	-0.0156	-0.1024	-0.0380	-0.0756	-0.0460	0.1686	-0.1720
Hg	-0.0762	-0.0651	-0.0512	-0.0509	-0.0217	0.0556	0.0017	-0.0163	0.0459	0.0464	0.1249	-0.0858	0.1272
In	**0.5548**	**0.5478**	**0.5008**	**0.5188**	**0.4798**	**0.3355**	**0.4237**	**0.4060**	**0.3813**	**0.3640**	0.2269	**0.7682**	**-0.4654**
Li	-0.2212	**-0.2769**	**-0.3130**	**-0.3335**	**-0.3640**	**-0.3402**	**-0.4186**	**-0.3887**	**-0.4799**	**-0.4373**	**-0.5454**	-0.1263	-0.2184
Mo	0.1184	0.1539	0.1860	0.2098	0.2461	0.2406	**0.2819**	**0.2877**	**0.3329**	**0.3019**	**0.3636**	0.1789	-0.0269
Nb	-0.1406	-0.1572	-0.2031	-0.1695	-0.2021	**-0.2794**	-0.2383	-0.2607	-0.2251	-0.2365	-0.2257	**0.3402**	**-0.6000**
Ni	**-0.4989**	**-0.4829**	**-0.4989**	**-0.4671**	**-0.4580**	**-0.4622**	**-0.4559**	**-0.4242**	**-0.3902**	**-0.3901**	**-0.3217**	-0.1985	-0.2716
Pb	0.2524	0.2449	0.2343	**0.2804**	**0.2768**	0.0518	0.2601	0.2203	0.2669	0.2102	0.2404	**0.4872**	**-0.5073**
Rb	-0.2048	-0.2355	**-0.2838**	**-0.2860**	**-0.3522**	**-0.3916**	**-0.4192**	**-0.4503**	**-0.4978**	**-0.4906**	**-0.5933**	0.0010	**-0.3865**
Sb	-0.0235	-0.0075	0.0078	0.0058	0.0450	0.0945	0.0799	0.1422	0.1331	0.1401	0.1367	0.1355	-0.0466
Sc	**0.5702**	**0.6133**	**0.5849**	**0.5869**	**0.5613**	**0.4550**	**0.5360**	**0.5076**	**0.4958**	**0.4869**	**0.3699**	**0.4147**	0.0303
Se	**0.6061**	**0.6249**	**0.6317**	**0.6025**	**0.6180**	**0.5891**	**0.6221**	**0.6976**	**0.6073**	**0.6329**	**0.4330**	**0.3576**	0.1782
Sn	**-0.3174**	**-0.3378**	**-0.3419**	**-0.3359**	**-0.3181**	**-0.2952**	**-0.3245**	**-0.3002**	**-0.3004**	**-0.2788**	-0.2618	-0.1096	-0.1760
Sr	0.1269	0.1875	0.2022	0.2228	0.2584	0.1867	**0.2956**	**0.2916**	**0.3570**	**0.3286**	**0.4396**	0.0680	0.1227
Ta	**0.2976**	0.2488	0.1949	0.2131	0.1660	-0.0273	0.1073	0.0320	0.0418	-0.0020	-0.0791	**0.4788**	**-0.4593**
Te	**-0.3104**	**-0.2955**	**-0.3267**	-0.2756	**-0.2911**	**-0.3767**	**-0.3101**	**-0.3418**	-0.2666	**-0.3026**	-0.2038	0.1595	**-0.5277**
Th	**0.7611**	**0.7425**	**0.6793**	**0.6986**	**0.6331**	**0.3534**	**0.5531**	**0.4867**	**0.4614**	**0.4292**	0.2587	**0.8132**	**-0.4821**
Tl	**-0.4080**	**-0.3951**	**-0.3931**	**-0.3708**	**-0.3466**	**-0.2911**	**-0.3339**	**-0.2969**	-0.2612	-0.2614	-0.1876	-0.0872	-0.2472
U	**0.3046**	**0.3359**	**0.3520**	**0.3763**	**0.4005**	0.2643	**0.4223**	**0.3773**	**0.4511**	**0.4043**	**0.4991**	**0.3114**	-0.1107
V	0.2296	0.2474	**0.2940**	**0.3104**	**0.3378**	**0.2799**	**0.3662**	**0.2791**	**0.3613**	**0.3051**	**0.4482**	0.0916	0.1508
W	0.1549	0.1907	0.2222	0.2463	**0.2877**	0.2552	**0.3263**	**0.3442**	**0.3882**	**0.3592**	**0.4084**	**0.2765**	-0.0961
Zn	-0.0461	-0.1127	-0.1248	-0.1228	-0.1197	**-0.2839**	-0.1557	-0.1432	-0.1848	-0.1968	-0.2222	0.1020	**-0.3590**
Zr	-0.2437	-0.2629	**-0.2769**	-0.2696	**-0.2797**	-0.2344	**-0.2823**	**-0.2919**	-0.2585	-0.2426	-0.1586	-0.0314	-0.1925
La	**0.9343**	**0.9435**	**0.9549**	**0.9588**	**0.9689**	**0.7934**	**0.9594**	**0.9290**	**0.9290**	**0.8974**	**0.7973**	**0.7889**	-0.0803
Ce	**0.4533**	**0.4094**	**0.3486**	**0.3892**	**0.3326**	0.0809	0.2542	0.1912	0.1938	0.1435	0.0417	**0.8771**	**-0.8557**
Pr	**0.9833**	**0.9854**	**0.9765**	**0.9819**	**0.9633**	**0.7402**	**0.9228**	**0.8590**	**0.8561**	**0.8183**	**0.6962**	**0.8474**	-0.1793
N	**0.9961**	**0.9906**	**0.9893**	**0.9860**	**0.9781**	**0.7856**	**0.9466**	**0.9107**	**0.8870**	**0.8617**	**0.7234**	**0.8089**	-0.1000
Sm		**0.9887**	**0.9815**	**0.9783**	**0.9651**	**0.7656**	**0.9280**	**0.8894**	**0.8609**	**0.8363**	**0.6934**	**0.8127**	-0.1184
Eu	**0.9887**		**0.9919**	**0.9927**	**0.9779**	**0.7728**	**0.9445**	**0.8956**	**0.8834**	**0.8549**	**0.7254**	**0.7846**	-0.0761
Gd	**0.9815**	**0.9919**		**0.9957**	**0.9926**	**0.8255**	**0.9709**	**0.9307**	**0.9203**	**0.8965**	**0.7772**	**0.7501**	-0.0020
Tb	**0.9783**	**0.9927**	**0.9957**		**0.9908**	**0.8017**	**0.9659**	**0.9164**	**0.9165**	**0.8855**	**0.7741**	**0.7756**	-0.0483
Dy	**0.9651**	**0.9779**	**0.9926**	**0.9908**		**0.8577**	**0.9897**	**0.9540**	**0.9544**	**0.9319**	**0.8345**	**0.7422**	0.0332
Y	**0.7656**	**0.7728**	**0.8255**	**0.8017**	**0.8577**		**0.9039**	**0.9286**	**0.9203**	**0.9440**	**0.9001**	**0.5041**	**0.3785**
Ho	**0.9280**	**0.9445**	**0.9709**	**0.9659**	**0.9897**	**0.9039**		**0.9780**	**0.9822**	**0.9677**	**0.8916**	**0.6836**	0.1329
Er	**0.8894**	**0.8956**	**0.9307**	**0.9164**	**0.9540**	**0.9286**	**0.9780**		**0.9773**	**0.9815**	**0.8902**	**0.6274**	0.2054
Tm	**0.8609**	**0.8834**	**0.9203**	**0.9165**	**0.9544**	**0.9203**	**0.9822**	**0.9773**		**0.9918**	**0.9468**	**0.6236**	0.2078
Yb	**0.8363**	**0.8549**	**0.8965**	**0.8855**	**0.9319**	**0.9440**	**0.9677**	**0.9815**	**0.9918**		**0.9511**	**0.5794**	0.2710
Lu	**0.6934**	**0.7254**	**0.7772**	**0.7741**	**0.8345**	**0.9001**	**0.8916**	**0.8902**	**0.9468**	**0.9511**		**0.4533**	**0.3602**
∑REY	**0.8127**	**0.7846**	**0.7501**	**0.7756**	**0.7422**	**0.5041**	**0.6836**	**0.6274**	**0.6236**	**0.5794**	**0.4533**		**-0.5833**
%HREY	-0.1184	-0.0761	-0.0020	-0.0483	0.0332	**0.3785**	0.1329	0.2054	0.2078	0.2710	**0.3602**	**-0.5833**	

[1] Correlations significant at the 99% CL are highlighted in green (positive) and orange (negative); correlations significant at the 95% CL are highlighted in blue (positive) and yellow (negative)

[2] Correlations with growth rates calculated by the equations of both Puteanus and Halbach (1988) and Manheim and Lane-Bostwick (1988) are included and labeled as such